Structure and Property Prediction of Novel Materials using Advanced Molecular Dynamics Techniques: Novel Carbons, Germaniums and High-Performance Thermoelectrics

DISSERTATION

zur Erlangung des akademischen Grades
Doctor rerum naturalium
(Dr. rer. nat.)

vorgelegt
der Fakultät Mathematik und Naturwissenschaften
der Technischen Universität Dresden
von

M. Sc. Daniele Selli

geboren am 10.07.1985 in Perugia, Italien

Die Dissertation wurde in der Zeit von Juni 2010 bis
Dezember 2013 am Institut für Physikalische Chemie und Elektrochemie,
Technische Universität Dresden angefertigt.

to my father

Eingereicht am

Gutacher

Publications:

Hierarchical thermoelectrics: Crystal grain boundaries in rocksalt PbSe as scalable phonon scatterers
D. Selli, S. E. Boulfelfel, P. Schapotschnikow, D. Donadio, S. Leoni
in preparation (2013)

PbTe/PbSe Thermoelectric nanocomposites: The impact of length modulations on lowering thermal conductivity
D. Selli, D. Donadio, S. Leoni
in preparation (2013)

Theoretical investigation of the electronic structure and quantum transport in the graphene-C(111) diamond surface system
D. Selli, I. A. Baburin, S. Leoni, Z. Zhu, D. Tomànek, G. Seifert
J. Phy, Condens. Matter. **25**, 435302 (2013)

Novel metastable metallic and semiconducting germaniums
D. Selli, I. A. Baburin, R. Martoňàk, S. Leoni
Sci. Rep. **3**, 1466 (2013)

Optimizing electronic structure and quantum transport at the graphene-Si(111) interface: An ab initio density-functional study
C. Tayran, Z. Zhu, M. Baldoni, D. Selli, G. Seifert, D. Tomànek
Phys. Rev. Lett. **110**, 176805 (2013)

Framework reconstruction between hR8 and cI16 germaniums: A molecular dynamics study
D. Selli, S. E. Boulfelfel, I. A. Baburin, G. Seifert, S. Leoni
RSC Advances **2**, 8833-8839 (2012)

Superhard sp(3) carbon allotropes with odd and even ring topologies
D. Selli, I. A. Baburin, R. Martoňàk, S. Leoni
Phys. Rev. B **84**, 161411 (2011)

Contents

1 Introduction 1
1.1 Motivations . . . 1
1.2 Outline . . . 2

2 Theoretical Background 5
2.1 Molecular Dynamics . . . 5
2.1.1 Periodic Boundary Conditions . . . 6
2.1.2 Potential Energy . . . 8
2.1.3 Kinetic Energy, Temperature and Pressure . . . 11
2.1.4 Integration of the Equations of Motion . . . 12
2.1.5 Beyond the Microcanonical Ensemble . . . 14
2.2 Metadynamics . . . 16
2.2.1 The Choice of Collective Variables . . . 17
2.2.2 Escaping Free-Energy Minima . . . 18
2.3 Transition Path Sampling . . . 23
2.3.1 Rare Event in Complex Systems . . . 23
2.3.2 Transition State Theroy . . . 25
2.3.3 Sampling the Transition Path Ensemble . . . 27
2.4 Density Functional Theory . . . 34
2.4.1 The electron density . . . 34
2.4.2 The Hohenberg-Kohn Theorems . . . 36
2.4.3 The Kohn-Sham Equations . . . 38
2.5 Introduction to The Tight-Binding Approach . . . 42
2.5.1 Standard DFTB, non-SCC Approach . . . 43
2.5.2 Self-Consistent Charge Extension . . . 44
2.5.3 Gradient for the DFTB methods . . . 45

3 Novel carbons 46
3.1 Superhard Carbon Materials: Cold Compression of Graphite . . . 47
3.1.1 Introduction . . . 48

3.1.2 Methods 49
3.1.3 Results and Discussion 51
3.2 Hybrid Graphene-based Systems 58
3.2.1 Graphene@C(111) Interface 58
3.2.2 Methods of Electronic Transport Calculation 59
3.2.3 Results and Discussion 62
3.2.4 Graphene@Si(111) Interface 66
3.2.5 Methods 67
3.2.6 Results and Discussion 67

4 Novel germaniums **76**
4.1 Novel metallic and semiconducting structures prediction 77
4.1.1 Refining the Ge phase diagram 77
4.1.2 Methods 78
4.1.3 Results and Discussion 80
4.2 Unrevealing the interconversion mechanism of Ge($hR8$) and Ge($cI16$) polymorphs 85
4.2.1 Introduction 85
4.2.2 Methods 86
4.2.3 Results and Discussion 88
4.3 High pressure behaviour of Ge($cF136$) clathrate 96
4.3.1 Methods 97
4.3.2 Results and Discussion 99

5 High-Performance Thermoelectric Materials **106**
5.0.3 Lowering the Thermal Lattice Conductivity 107
5.0.4 Lead Chalcogenide in Thermoelectronics 108
5.1 PbTe-PbSe Nanoengineering 109
5.1.1 Methods of Heat Transport Calculation 110
5.1.2 Results and Discussion 114
5.2 Crystal grain boundaries in rocksalt PbSe as scalable phonon scatterers . 124
5.2.1 Introduction 124
5.2.2 B1-B2 Phase Transition in PbSe 125
5.2.3 Results and Discussion 127

Conclusions and Outlook **133**

Bibliography **135**

School participations, Oral presentations 145

Acknowledgements 146

List of Figures

2.1 Periodic replicas (transparent) for a hypothetic binary B1 compound unit cell (solid coloured). Each atom is translationally replicated in each direction ($\pm x$, $\pm y$, $\pm z$). In the figure two illustrative translations are considered, atom i is replicated onto i' and atom j onto j'. Replicas in the $+z$ direction are not reported for clarity. 6
2.2 Two dimensional PBC for a dynamic system. The grey shaded cell is the original one. In each replica positions and velocities (arrows) are the same as the corresponding original cell. $\boldsymbol{r}_{cut}$ represents the cutoff distance for the interaction of one atom with neighbors. 7
2.3 Flow diagram of the *velocity Verlet* algorithm. (a) Given positions, velocities and forces, (b) new positions can be computed. (c) Velocities at half-step are computed and (d) subsequently the forces at the new position. (e) At the end, the velocities are computed at full step and (f) the system advanced to the next time step repeating the procedure. 13
2.4 Three-minima one dimensionall free energy surface exploration: starting from the central basin, a time evolution sum of Gaussian potential functions (thin lines) is shown until all the minima for a certain collective variable (x) are explored. 16
2.5 The effect of neglecting a relevant degree of freedom. (a) Z-shaped two dimensional free energy potential. (b) Meta-trajectory considering only variable CV1. The only way of describing transition from A to B, and *vice versa*, with a single variable, is to induce a strong hysteresis. Figure taken from Ref. [1]. 18
2.6 Flow diagram of a metadynamics simulation: communications between MD integrator and the metadynamics driver are shown. 21
2.7 Energy landscapes for a simple (a) and complex (b) system. In the first case a single stationary point, representing the saddle point of the transition, divides the the attraction basins A and B, whereas in the second case more points become relevant and a single transition pathway is impossible to identify. 23
2.8 Time evolution of a dynamic transition from different states, A and B. Most of the time the system will fluctuate in one basin or the other, and just rarely it will switch between the two states. A and B can be distinguished using an order parameter like the coordination number of an atom. 25

2.9 Ideal illustration of the transition state scheme: reactants and products separated by an highest energy transition state. 26
2.10 In a shooting move, at a random time slice $x_{t'}^{(o)}$ of the old path (solid line), momenta $p_{t'}^{(o)}$ are changed by a small amount δp. Integrating backward and forward the equations of motion starting from the modified state $x_{t'}^{(n)}$, the new trajectory $x^{(n)}(T)$ is yielded (dashed line). (a) If the new trajectory still connect A to B, than is accepted, otherwise (b) is rejected. 33
2.11 Schematic workflow of a Self-Consistent Field (SCF) procedure: iterative resolution of the Kohn-Sham equations. 41

3.1 Example of meta-trajectory. From a quasirandom carbon sp^3 structure at metastep 1 to the final oC16-II at metastep 380, different intermediate modifications are encountered. Each metastep corresponds to 0.5 ps for a total of 190 ps of simulation time. At metastep 350 and 380 two snapshots of the same structures are reported with different orientations. 50
3.2 Crystal structures of unique carbon phases. oC16-I and mC32 are characterized by a 5 + 7 odd-odd ring pattern. mC12 represents a distinct $5+8$ odd-even ring topology, while oC16-II contains even rings only, $4+6+8$. 52
3.3 (a) Enthalpies (relative to graphite) of different carbon allotropes; (b) enthalpies of certain sp^3 carbon allotropes (relative to diamond) in the high-pressure range. The colors (lines) are the same as in (a). 54
3.4 (a) Electronic band structures (top) and phonon dispersion curves (bottom) for (from left to right) mC12, oC16-I,mC32, and oC16-II carbon phases. 55
3.5 Comparison of M-carbon with oC16-I, mC12, and oC16-II with respect to their underlying puckered graphitic stacking. Layers are highlighted in turquoise(mediumgray). 56
3.6 Simulated XRD pattern for oC16-I and oC16-II carbon phases (λ = 0.3329Å). The structural data are those of Table. 3.2. 57
3.7 Optimum geometry of wavy graphene on the C(111) surface. (a) Side view and (b) top view of the equilibrium structure of the slab. The ridges of free-standing C atoms forming polyacetylene chains can be distinguished from sp^3 C atoms covalently bonded to the diamond surface. (c) Perspective view of the hybrid system, illustrating transport direction along the ridges (A) and normal to the ridges (B). 59
3.8 (a) A device in equilibrium. (b) Self-consistent procedure for the analysis of electronic devices in equilibrium. Derivation of the potential can be done applying the Poisson equation, if we referred to a statistical mechanics approach or using directly *ab initio*techniques, as DFT in our case. 60
3.9 (a) A device driven out of equilibrium by two contacts with different chemical potentials μ_1 and μ_2. (b) Self-consistent procedure for determining the density matrix ρ from which all quantities of interest (electron density, current intensity, etc) can be calculated. 62

3.10 Electronic structure of graphene/C(111). (a) Electronic density of states (DOS) of graphene/C(111) (solid black line), free-standing wavy graphene (dashed red line) and free- standing planar graphene (dotted blue line). (b) DOS of graphene/C(111) (solid black line) and the projected electronic density of state (PDOS) onto p_z orbitals of graphene C atoms at the ridge (dashed red line) and in the valley (dotted blue line). (c) Characterization of the ridge and valley sites in the side view of the graphene/C(111) structure. (d) PDOS associated with p_x (red lines), p_y (blue lines) and p_z (black lines) states of graphene C atoms in valley and ridge sites. $E = 0$ denotes the position of the Fermi level in (a), (b) and (d). 64

3.11 Geometry and numerical results of quantum transport calculations. Transport along the ridges in geometry A (a-c) is compared to transport normal to the ridges in geometry B (d-f). (a,d) Top and (b,e) side view of the structure used in the calculations. A central graphene/C(111) scattering region is connected to two semi-infinite leads consisting of free-standing wavy graphene. (c,f) Transmission spectra with drain-source bias $V_{ds} = 0$ for the two geometries, with $E = 0$ representing carriers injected at the Fermi level. 65

3.12 Optimum geometry and electronic structure of wavy graphene on the Si(111) surface. (a) Equilibrium structure of the slab and (b) electron density difference $\Delta n(\mathrm{r})$ in a plane normal to the surface. (c) Top view of the structure. The ridges of C atoms forming paraphenylene chains can be distinguished from sp^3 C atoms covalently bonded to Si and C atoms in butadienelike units that are not covalently bonded to Si. $\mathbf{a}_1$ and $\mathbf{a}_2$ are the Bravais lattice vectors defining the 2×1 surface unit cell. (d) Electronic density of states (DOS) of wavy graphene-Si(111) (solid black line), wavy graphene only (dashed red line), and planar graphene (dotted blue line). $E = 0$ denotes the position of the Fermi level. 68

3.13 Top and side view of the relaxed geometry of 2×1 supercells of wavy graphene on the Si(111) surface at different H coverages. 70

3.14 Setup for the quantum transport calculations for contiguous wavy graphene layers bonded to Si(111). Results for quantum transport normal to the ridges in transport geometry A (a)-(c) are compared to those along the ridges in transport geometry B (d)-(f). (a), (d) Schematic geometry for the calculations distinguishing perfect graphene leads from the central scattering region, with the direction of the current I shown by the arrows. (b), (e) Atomic structure of the scattering region and its connection to the leads in the top and side views. (c), (f) Quantum conductance G in units of the conduction quantum G_0 as a function of injection energy, with $E = 0$ corresponding to the Fermi level. The conductance is given per unit cell normal to the transport direction, shown in panels (b) and (e). 72

3.15 Geometry and quantum transport calculations for semi-infinite wavy graphene layers and graphene nanoribbons bonded to Si(111). Results in (a)-(c) are for transport geometry C analogous to that of Fig. 3.14 (a), with the graphene monolayer disrupted by removing a ridge in the scattering region. Results in (d)-(f) are for transport geometry D analogous to that of Fig. 3.14 (d), where removal of every other ridge resulted in the formation of bent graphene nanoribbons. (a), (d) Schematic geometry for the calculations distinguishing free-standing perfect graphene leads from the central scattering region, with the direction of the current I shown by the arrows. (b), (e) Atomic structure of the scattering region and its connection to the leads in the top and side views. (c), (f) Quantum conductance G in units of the conduction quantum G_0 as a function of injection energy, with $E = 0$ corresponding to the Fermi level. The conductance is given per unit cell normal to the transport direction shown in panels (b) and (e). 74

4.1 Lower pressure region of the phase diagram of Ge, augmented by two novel phases $mC16$ and bct-5, found by *ab initio* metadynamics runs. bct-5 shows characteristic square pyramidal 5-fold coordination of Ge atoms. In monoclinic $mC16$ four-rings are a characteristic feature. The arrows indicate the direction of metadynamics evolution. The pressures were evaluated based on the common tangent construction (see below, Fig. 4.3). 78

4.2 High pressure Ge modifications sequence. $tI4$ and $Imma$ are reported in the same structure because they are visually undistinguishable (transition pressure of the former into the latter is ~10 GPa). From the left to the right all the high-pressure "cascade" is reported: $Imma \rightarrow sh \rightarrow Cmca \rightarrow hcp$. 79

4.3 Equation of states of Ge $mC16$ and bct-5, compared to cubic diamond and β-tin type. bct-5 features a reduced volume per atom compared to diamond type ($cF8$), while the total energy minimum lies lower than β-tin. $mC16$ on the contrary is less dense and energetically close to the diamond type. The tangents used for evaluating equilibrium pressures of Fig. 4.1 are highlighted. 81

4.4 Metadynamics (DFT) runs on a 64 Ge atoms box (P=10.0 GPa, T=300 K). bct-5 appears as a stepwise feature in the enthalpy profile of the run started from diamond (red line). Runs commenced from bct-5 (black line) evolve into β-tin. Configurations corresponding to distinct points along the runs are detailed below the graph. Energy units are eV. . . 82

4.5 Evolution of the bonding situation from diamond to β-tin type over bct-5. The ELF map is showing four bond attractors for diamond Ge (a, η =0.58), one+four bond attractors for bct-5 (b, η =0.53, transparent green isosurface η =0.48), two+four bond attractors for β-tin (c, η =0.51). 83

4.6 Band structures and phonon spectra (0.0 GPa) of mC16 (left) and bct-5 (right). mC16 is a narrow-gap semiconductor (band gap 5 1.43 eV), while bct-5 is metallic. Both are mechanically stable. Brillouin zone choice (bct-5) according to Ref. [2]. 83

4.7 Evolution of ω, λ and T_c as a function of pressure for bct-5 and β-tin, calculated based on the electron-phonon coupling model. The calculated equilibrium pressure between bct-5 and β-tin marks the boundary between the phases. Notice the flattening of bct-5 T_c after 5 GPa as phonons soften. The model predicts an increase of T_c in the lower pressure region. 84

4.8 Crystal structures of the (a) $cI16$ and (b) $hR8$ Ge allotropes ($hR8$ is represented in a pseudo-cubic cell for better comparison with $cI16$). Their networks follow the shape of the gyroid (transparent blue), except for a set of bonds, which trespass the surface in a way that is peculiar for $cI16$ and $hR8$, respectively. Flipping these bonds formally converts $cI16$ into $hR8$. One such flip is visible in the foreground, causing inversion of a Ge tetrahedron. 86

4.9 Enthalpy vs. Pressure of Ge($cI16$) and Ge($hR8$). The intersection point represents the transition pressure within the DFTB potential considered. 87

4.10 Coordination sequence calculated along the time coordinate for the converged transition trajectory. 89

4.11 Configurations appearing along the transformation. (a) Ge($cI16$), (b) reactive intermediate, (c) a novel metastable phase Ge($hR32$) and (d) Ge($hR8$). Bonds changing from one structure to the other are highlighted in blue, while red ones show stretching along the trajectory, but they are never completely broken. (c) and (d) differ only by some bonds. They are nonetheless two distinct local minima on the chemical landscape of Ge. 90

4.12 Phonon dispersion curves (a) were calculated at 0 GPa. No imaginary frequencies were observed throughout the whole Brillouin zone, confirming the dynamical stability of the intermediate $hR32$ structure. Band structure calculations (DFTB+) indicate that $hR32$ is a semiconductor (b). 91

4.13 Transition mechanism for a single reaction chain (in blue in Fig. 4.11). Snapshots of the trajectory are shown at 0.0 (a), 880 (b), 906 (c), 960 (d), 1040 (e), 2000 (f) fs. 92

4.14 Evolution of WFC relative distances, calculated for each bond and each reactive chains (four blue chains in Fig. 4.11 (b)) along the time coordinate of the framework reconstruction transition. Different colors (green, black, purple and turquoise) refer to distinct chains, while distinct symbols (square, circle and triangle) refer to different bonds within a single chain. Inset: potential energy profile with $hR32$ as the intermediate phase. Zeroth time frame is arbitrary set. The y axis corresponds to relative displacements of WFC along the transition and is used here as an order parameter, able to distinguish between initial and final states. 93

4.15 sp^3-projected, maximally-localized Wannier functions for the Ge atom at which the transition is commenced. The evolution of bonds (transparent lobes) and lone pair (opaque lobe) are shown at different snapshots. For clarity, only the positive lobe of the MLWFs is rendered. The chain and time frames are the same as in Fig. 4.13. Zeroth time frame was set at $cI16$. 94

4.16 Meta-trajectories at two different pressure regimes and T=300 K. Starting from the Ge($cF136$) clathrate (a), and depending on the pressure applied, different structure are encountered. At low pressure, an intermediate clathrate Ge($mC68$) is initially found (b1), and then through a large number of amorphous phases, e. g. (c1) and (d1) the system is attracted by the bct-5 basin (e1). The meta-trajectory follows a significantly different path in the case of an high pressure transition: the amorphous structure are relatively larger than in the previous case, e. g. (b2), (c2) and (d2), and the "perfect" Ge($tI4$) structure is caught only after several steps (e2), while the bct-5 one is completely bypassed. 98

4.17 Average circuits size (a), coordination sequence (b) and enthalpy of each meta-trajectory step for β-tin at 300 K and 5 GPa. The blue curve in each graph represent the total percentage % of β-tin in each snapshot and the segments represent a different structural "area". . . 100

4.18 Average circuits size (a), coordination sequence (b) and enthalpy of each meta-trajectory step for bct-5 at 300 K and 2.5 GPa. The blue curve in each graph represent the total percentage % of bct-5 in each snapshot while the segments represent a different structural "area". . . 102

4.19 Average circuits size (a), coordination sequence (b) and enthalpy of each meta-trajectory step for β-tin at 77 K and 5.0 GPa. The blue curve in each graph represents the total percentage % of β-tin in each snapshot and the segments highlight "areas" characterized by a particular structural pattern, including fluctuations. 104

5.1 Maximizing the efficiency (ZT) of a thermoelectric involves a compromise of thermal conductivity (κ; plotted on the y axis from 0 to a top value of 10 W m^{-1} K^{-1}) and Seebeck coefficient (α; 0 to 500 μV K^{-1}) with electrical conductivity (σ; 0 to 5.000 Ω^{-1} cm^{-1}). Good thermoelectric materials are typically heavily doped semiconductors with a carrier concentration between 10^{-19} and 10^{-21} carriers per cm^3. The thermoelectric power factor $\alpha^2\sigma$ maximizes at higher carrier concentration than ZT. The difference between the peak in $\alpha^2\sigma$ and ZT is greater for the newer lower-κ_L materials. Trends shown were modelled from Bi_2Te_3, based on empirical data in Ref. [3] 108

5.2 (a) Layered structure of PbTe (in blue) and PbSe (in red) in their rock-salt modification. Layers are (from, left to right) 25, 12.5 and 6.25 thick. (b) Intercalated PbTe(Se) spheres in a PbSe(Te) matrix. Sphere radii are, from left to right 5, 10, 15 and 20 Å, respectively. (c) 25 Å and 15 Å radius spheres and (d) “eight-in-a-box” spheres of 15 Å radius. 111

5.3 Predicted lattice thermal conductivity of bulk PbTe (a), PbSe (b) and solid solution (c) in comparison with experimental counterpart values [4–6]. 113

5.4 (a) Normalized heat current autocorrelation function of $PbSe_{0.50}Te_{0.50}$ alloy as a function of correlation time at 300K. The inset reports the calculated thermal conductivity as a function of the truncation time. (b) Lattice thermal conductivity as a function of the system size. Values for the best $PbSe_{0.50}Te_{0.50}$ alloy (red), 12.5 Å thickness layer averaged (green) and the z component (blue) and the 20 Å radius PbTe sphere in PbSe matrix (blue) are reported. 115

5.5 κ_L dependence on PbTe(PbSe) nano-dot size in PbSe(PbTe) matrix for 4096 (a) and 10648 (b) atoms systems. The dashed lines represent the κ_L value for the most performing $PbSe_{0.50}Te_{0.50}$ alloys. 117

5.6 (a) Lattice thermal conductivity dependence of PbTe(PbSe) nanocomposites as a function of nano-dot distance d (b). 117

5.7 κ_L temperature dependence of PbTe nano-dots in PbSe matrix and $PbSe_{0.50}Te_{0.50}$ alloy (both systems have 10648 atoms in the unit cell). 118

5.8 Comparison of lattice thermal conductivity dependence on temperature between (a) bulk PbTe, bulk PbSe and $PbSe_{0.50}Te_{0.50}$ alloy, (b) between 20 Å radius PbTe(PbSe) sphere in PbSe(PbTe) matrix and $PbSe_{0.50}Te_{0.50}$ alloy and (c) between the cartesian components of the lattice thermal conductivity of the 12.5 Å thickness layered structure and the $PbSe_{0.50}Te_{0.50}$ alloy. 119

5.9 Calculated amplitude of group velocities as a function of frequency for bulk PbTe sample (a), $PbSe_{0.50}Te_{0.50}$ alloy (b), 20 Å radius PbTe sphere in PbSe matrix and for 12.5 Å thick layered structure (d). . . . 120

5.10 Calculated lifetimes of vibrational modes as a function of frequency for bulk PbTe sample (a), $PbSe_{0.50}Te_{0.50}$ alloy (b), 20 Å radius PbTe sphere in PbSe matrix (c) and for 12.5 Å thick layered structure (d). . 121

5.11 Average mean free path of vibrational modes as a function of frequency for bulk PbTe sample (a), $PbSe_{0.50}Te_{0.50}$ alloy (b), 20 Å radius PbTe sphere in PbSe matrix and directional mean free path for 12.5 Å thick layered structure. 122

5.12 Mean free path of vibrational modes as a function of frequency for 6.25 Å (a) and 12.5 Å (b) thick layered structure. The former shows a lowest average mfp for $\kappa_{\mathrm{L_x}}$ and $\kappa_{\mathrm{L_y}}$ (values in black and red) and the latter shows very low values for $\kappa_{\mathrm{L_z}}$ (in green) confirming not only its strikingly phonon scattering features but also an incredible anisotropy. 123

5.13 Representative path of structural transformation from B1 to B2. The TPS identifies an intermediate of overall B33 structure, showing the typical alternation of triangular and square layers in the chosen projection. The latter can be stabilized in the lower pressure range, while higher pressure favors B2. 125

5.14 Coordination sequence calculated along the time coordinate for the converged transition trajectory. The plateaux marked with the magenta line correspond to the "B33" intermediate. 126

5.15 (a) Structural example of B1 grain boundaries obtained by enlarging the "B33" intermediate of Fig. 5.13 by a factor 1×1×1 (4k atoms), 2×2×2 (32k atoms), 4×4×4 (256k atoms), 6×6×6 (864k atoms) and 12×12×12 (7M atoms), and propagating it in a NpT-MD calculation. (b) Detailed representation of the smallest grain obtained (4k atoms): B1 zones are separated by crossing boundaries. A strong anisotropy can be noticed, since no interfaces are presented in the direction normal to the plane. 128

5.16 κ_{L} values calculated as a function of temperature for B1 and B1 grains (3960 atoms box). Cartesian components $\kappa_{\mathrm{L_x}}$, $\kappa_{\mathrm{L_y}}$ and $\kappa_{\mathrm{L_z}}$ are reported for the grain boundaries case: anisotropy can be noticed since the z component presents lattice thermal conductivity values markedly larger than x and y components. However, the overall value of κ_{L} is noticeably reduced with respect to the B1 pure phase, as temperature dependence is nearly lost. 129

5.17 Mean free path of vibrational modes as a function of frequency for pure B1 (a) B1 grains (b) PbSe structure (3960 atoms box). In the former a frequency gap can be noticed between 4.0 and 4.5 THz. The latter shows a lowest average mfp already for $\kappa_{\mathrm{L_z}}$ (in green) with a particular reduction for $\kappa_{\mathrm{L_x}}$ and $\kappa_{\mathrm{L_y}}$ (values in black and red) that confirms not only its strikingly phonon scattering features but also remarkable anisotropy. 130

5.18 Mean free path reduction factor (RF) resolved in Cartesian directions. In agreement with Fig. 5.17, the reduction factor displays a strong anisotropy since RF_x and RF_y (black and red lines) show similar values, while RF_z (green line) is markedly lower. 131

5.19 κ_L values calculated as a function of temperature for B1 and B1 with grains (3960, 31680 and 253444 atoms boxes). Enlarging the system brings to a direct reduction of the lattice thermal conductivity and to a lower dependence over temperature, nearly lost for the 256k atoms grain. 132

1 Introduction

1.1 Motivations

Ci sono soltanto due possibili conclusioni:
se il risultato conferma le ipotesi,
allora hai appena fatto una misura;
se il risultato è contrario alle ipotesi,
allora hai fatto una scoperta.

There are two possible outcomes:
if the result confirms the hypothesis,
then you've made a measurement;
if the result is contrary to the hypothesis,
then you've made a discovery.

Enrico Fermi

Nowadays, the massive and quick progress in high performance computing allows for *a priori* study of complex structures. Therefore, chemical systems in general and solid states materials in the specific can be studied and understood in depth by means of computational science, which allow for a detailed evaluation of macroscopic properties without reference to any empirical considerations. Parallel to technological improvements, significant progresses have been achieved in method development in chemistry and physics. Molecular and atomistic simulations are based on a great and steadily growing variety of powerful algorithms, which allow for an extensive comprehension of static and dynamic processes in the solid states.

In laboratory experiments, time and space resolutions are limited by device precision and accuracy. On the other hand, theoretical models allow for an atomistic level of detail, i.e. without restrictions on what can be learned on a system of interest. Furthermore, such methods can provide the missing resolution, necessary for understanding experimental issues, the only limitation being the level and kind of theory used. To account for transformations and dynamic changes in molecular and solid state, the properties of a system have to be investigated, while to evaluate stability and mechanical, optical and electronic features, a static approach is usually convenient.

The current technological progress critically depends on the ability of modern science to find novel materials with outstanding properties. Experimental efforts in the quest of novel structures, comprehension of dynamic processes and characterization of materials, can be extremely difficult and generally speaking, expensive. Thus, the role of theoretical and computational sciences is central towards a synergistic strategy, involving also experimental and information sciences, in order to give birth to a new generation of materials meant to improve performances and to be environmental friendly at the same time.

The successful search for novel materials, in a so-called “material genome” prospective, requires an extensive theoretical effort meant at finding novel possible structural modification. To this purpose, it is central to effectively discriminate between all crystalline structural solutions allowed for a given set of system variables (composition, structural constraints, boundary conditions, pressure and temperature), by scanning the potential energy surface associated with that set of variables. In order to efficiently scan an inherently complex potential surface, accelerated molecular dynamics and a quantum mechanic description of the interatomic forces have been merged together, while maintaining an appropriate description of the electronic structure of the compound under study. Following this approach a large number of thermodynamically stable and metastable new phases can be found in a manageable amount of time at an affordable computational cost.

While the prediction of a plausible structural solution represents an important starting point of a possible synthesis route, it does not immediately provide indications on possible experimental protocols for its realization. A commonly used approach to the synthesis of novel phases exploits phase transitions induced by pressure or temperature. Therein, reconstructive transitions stand out as they involve bond breaking, large volume change, latent heat exchange and hysteresis effects. Such so-called first order phase transitions, implying discontinuous behaviour in first order derivatives of the free energy, are markedly different from second order ones, where only small atomic displacements can be observed. Even if different theories allow to capture certain aspect of first-order phase transition, many relevant aspects of their mechanisms remains to be discovered. Gathering evidence for an atomistic mechanism of crystal reconstruction in solid materials entails a deep understanding of local rearrangement, phase coexistence and nucleation and growth events.

1.2 Outline

In this thesis, the applications, the potentialities and the advantages of molecular dynamics techniques will be presented in relation to the quest of novel materials, prediction of feasible synthesis and detailed comprehension of transition mechanisms. The phase diagrams of Group-IVa elements, especially Carbon and Germanium have been studied in great detail and outstanding new structure modifications have been discovered; moreover, their quantum mechanics characterization suggests the possibility to engineer materials with interesting mechanical, electronic and optical properties. On the other hand, extensive efforts have been put in understanding the transition mechanism between different predicted structures, in order to suggest possible synthesis route, that could be investigated experimentally. Among the predicted structures, the ones based on carbon have shown intriguing electron transport properties. Advanced methods of molecular dynamics simulations has been used to rationalize phase transition in lead chalcogenides (PbSe, PbTe), which are extremely promising material for their heat transport properties.

In Chapter 2, an extensive introduction into the use and capabilities of techniques of structure prediction (Metadynamics) and a detailed elucidation of transition mechanisms (Transition Path Sampling) is presented. Additionally, a review of the principal theoretical chemistry methods for the description of time evolution and the representation of atomic interactions and electronic structures by means of *ab initio* laws, is given. At the end, we discuss Density Functional Theory (DFT) and its Tight Binding (DFTB) treatment as approaches to solving the Schrödinger equation. In a nutshell, the principal aspects of a large number of computational theories are illustrated and used here, as they represent the toolbox of computational material sciences.

Chapter 3 and 4 are related by their content while Chapter 5 is self-contained. The formers are focused on the study of tetrels (Carbon, Silicon and Germaniums) and their polymorphism, while the latter is more oriented to the quest of high performance thermoelectric materials based on Lead Selenide and Telluride

In Chapter 3, the problem of the cold compression of graphite, which produces a hard, transparent and still not characterized product is explored by means of metadynamics. Different structural solutions have been found and their characterization and comparison with experimental datas suggest them as potential product candidates of the compression process. Next, the interaction of graphene with bare surfaces of C and Si cubic diamond is reported. The resulting hybrid systems present remarkable electronic properties and extreme anisotropic electron transport channels, which suggests them as outstanding devices for the next generation circuitry.

The alluring properties of Ge modifications, particularly the good tunability of its electronic properties and the existence of metallic, superconducting phases, motivated our interest in the refinement of its phase diagram, as reported in Chapter 4. Systematic metadynamics simulations allowed us to predict two new metastable germaniums. The first one is topologically unprecedented and semiconducting, while the second one is predicted to be the first modification that is metallic at ambient conditions. Thanks to the same technique we investigated the behaviour upon compression of type-II Ge clathrate. This compound transforms into a denser β-tin type structure, with a number of metastable, amorphous phases appearing as intermediates. Metadynamics allowed for a precise investigation of the related transformation pathways, including mechanisms and characterization of amorphous phases. Furthermore, fine-tuning temperature and pressure parameters, a viable synthetic way towards bct-5 was elucidated, as illustrated in detail in the last part of Chapter 4. Further, two other metastable germanium phases were investigated with respect to the mechanism of their interconversion under pressure. Transition path sampling has been successfully applied to the study of the pressure-induced transformation of γ-silicon to $hR8$ germanium phases. This methods allows unraveling the mechanism of a phase transition in great detail. For germanium, a S_N2-like reaction in the solid state is responsible for interconverting the two tetrahedral germaniums. Furthermore, along the transformation pathways, another metastable phase of germanium could be discovered, as an additional member of the Ge phase diagram.

Chapter 5 concentrates on a topic of top priority, the characterization and improved performance of thermoelectric materials. Therein, thermal conductivity of PbSe and PbTe is investigated by means of molecular dynamics techniques. As a strategy towards better thermoelectrics, two approaches were considered. On the one hand, systematic (sub)nanoengineering, on the other, the introduction of grains and grain boundaries into PbSe. A fragmentation into domains typically accompanies structural phase transitions. Investigating the B1-B2 pathway of structure reconstruction induced by pressure we were able to obtain realistic models of grain geometries. The latter strikingly lower thermal conductivity as they scatter phonons over a broader frequency range than just nano-inclusions. Therefore this represents a distinct approach towards an intelligent design of next-generation thermoelectrics.

2 Theoretical Background

Science requires both observation and comprehension [7]. Without observation there are no facts to be comprehended; without comprehension science is mere documentation. The basis for comprehension is theory, and the language of theoretical science is mathematics. Theory is constructed on a foundation of hypothesis; the fewer the hypotheses needed to explain existing observations and predict new phenomena, the more 'elegant' the theory - Occam's razor.

In simulation contest, the comprehension arises from a prediction of experimental measurements based on a plausible mathematical and physical method. Therein, a computer simulation can not be consider as a mere calculation process, but has to be thought of as a virtual laboratory, a numerical experiment. Advances in experimental observations may steer the development of novel theoretical models. On the other hand the systematic application of methods can lead to entirely unexpected results and consequences, not immediately obvious from the formulations of the model itself. As a matter of fact, the history of science is full of examples of theory anticipating experiments, see for example the counter-intuitive prediction of quantum mechanisms, or of relativity theory, which were verified only at a later point.

Computational material sciences dispose of an articulated toolbox of methods, which may contain an explicit reference to dynamical processes over a time coordinate, or may be setup for a sophisticated description of solid state structures. In this work several methods have been combined to shed light on the polymorphism of solids, in the search for novel crystalline modifications, the principle being molecular dynamics (MD), accelerated MD models and quantum mechanic methodologies (DFT, DFTB).

2.1 Molecular Dynamics

In molecular dynamics (MD) simulations, Newton's equations of motion (EOM) are integrated over time for each N interacting object:

$$m_i \frac{\partial^2 \boldsymbol{r}_i}{\partial t^2} = \boldsymbol{F}_i, \qquad i = 1 \dots N \tag{2.1}$$

where m_i and $\boldsymbol{r}_i$ are mass and position of the object i respectively. The forces, which are the quantities that move our system at each time step, are the negative derivatives of a potential function $U(\boldsymbol{r}_1, \boldsymbol{r}_2, \ldots, \boldsymbol{r}_N)$:

$$\boldsymbol{F}_i = -\frac{\partial \boldsymbol{U}}{\partial \boldsymbol{r}_i} \tag{2.2}$$

Once the potential is defined and the forces derived from it, the integration of the previous coupled differential equations (Eqs. (2.1) and (2.2)) should be performed simultaneously. In practice, the EOM are solved by integration on small and finite time intervals and numerical iterative step-by-step techniques have been developed for this prupose [8–11]. In the simulation, the properties of the system under study are assigned at the beginning by defining a specific thermodynamic ensemble (NVE, NVT or NPT). In a specific statistical ensemble, the average (over infinite time) of a conserved observable along the time coordinate at equilibrium, is the same as the average on the total space configurations of the observable itself. This statement, called *ergodic principle* [12], is of central importance for MD simulations as it allows the evaluation of macroscopic properties from averages of microscopic configurations.

In this Section a brief overview on classical interatomic potential, on the calculation of the forces, on the workflow of the *velocity Verlet* algorithm and definition of the principal statistical ensemble will be reported. For an in-depth analysis, general [7,13] and computational oriented [14] books are strongly recommended.

2.1.1 Periodic Boundary Conditions

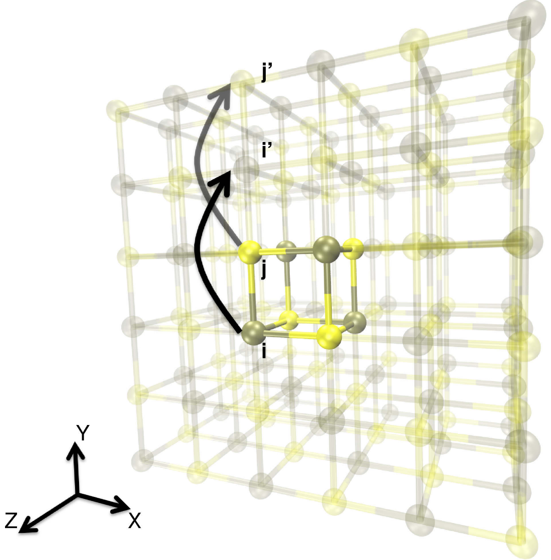

Figure 2.1 – Periodic replicas (transparent) for a hypothetic binary B1 compound unit cell (solid coloured). Each atom is translationally replicated in each direction ($\pm x$, $\pm y$, $\pm z$). In the figure two illustrative translations are considered, atom i is replicated onto i' and atom j onto j'. Replicas in the $+z$ direction are not reported for clarity.

The study of solid state often has to deal with periodic objects. Even if they contain isolated objects, like molecules or clusters, solid state systems tend to be periodic in at least one dimension. The number of atoms that can be treated is in general limited by the computational resources and by the level of theory adopted. The strategy to make periodic solid tractable consists in the application of periodic boundary conditions (PBC). The atoms of the system to be simulated are enclosed into a box, which typically exceeds the unit cell in case of a crystal, and which is surrounded by periodic replicas of itself (Fig. 2.1). There are thus no boundaries and the system will behave as if it was infinite in size. This approach, together with the use of periodic basis set (plane waves) for the representation of the electronic structure of crystalline systems, allows for a quantum mechanic description of any system of interest as bulk material.

In molecular dynamics periodicity is needed also for the correct description of the time evolution of molecules and clusters. Figure 2.2 illustrates the concept of PBC in molecular dynamics simulation. The shaded box represents the system simulated surrounded by exact copies of it self, with same positions and velocities (arrows). Whenever an atom leaves the simulation cell, it is replaced by another one with exactly the same velocity, entering from the opposite cell face. This way the number of atoms in the cell is conserved. In the figure, $\boldsymbol{r}_{cut}$ is the cutoff radius, limiting the region of interest for the calculation of short-range interatomic forces. As can be noticed, an atom may interact with another in the neighboring cell (which is an image

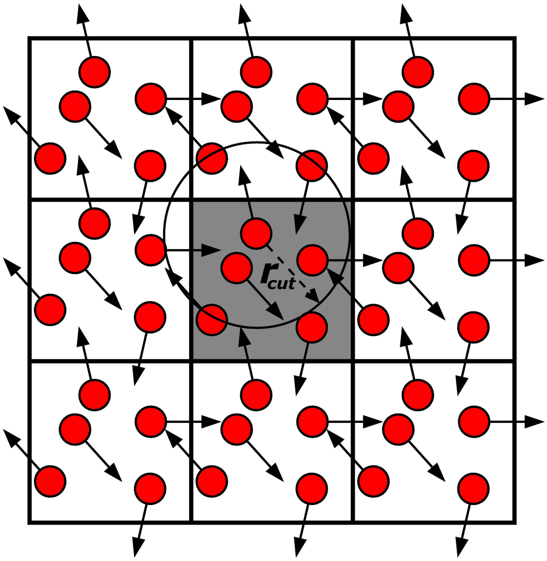

Figure 2.2 – Two dimensional PBC for a dynamic system. The grey shaded cell is the original one. In each replica positions and velocities (arrows) are the same as the corresponding original cell. $\boldsymbol{r}_{cut}$ represents the cutoff distance for the interaction of one atom with neighbors.

of one of the atoms in the simulation cell) because it is within the cutoff radius. It ignores the equivalent atom in the simulation cell because it is too far away. In other cases the interaction comes from an atom in the simulation cell itself. Important is to consider that the cutoff radius has to be chosen so that an atom can interact with only a single 'image' of each atom in the simulation box. For this reason, $\boldsymbol{r}_{cut}$ can not be greater than half of the width of the cell.

The shape of the box can be skew, as well as the periodicity imposed on the system can be other than translational, e.g., think of roto-translation periodicity in twisted carbon nanotubes.

2.1.2 Potential Energy

The total potential energy is a sum of different contribution: an *intra*-molecular one (bonded terms), *inter*-molecular (such as Lennard-Jones) and an electrostatic (Coulomb) term for charged systems. The total configuration energy of a molecular system may be written as:

$$\begin{aligned} U(\boldsymbol{r}_1, \boldsymbol{r}_2, \ldots, \boldsymbol{r}_N) = & \sum_{i_{bond}=1}^{N_{bond}} U_{bond}(i_{bond}, \boldsymbol{r}_a, \boldsymbol{r}_b) \\ & + \sum_{i_{angle}=1}^{N_{angle}} U_{angle}(i_{angle}, \boldsymbol{r}_a, \boldsymbol{r}_b, \boldsymbol{r}_c) \\ & + \sum_{i_{dihed}=1}^{N_{dihed}} U_{dihed}(i_{dihed}, \boldsymbol{r}_a, \boldsymbol{r}_b, \boldsymbol{r}_c, \boldsymbol{r}_d) \\ & + \sum_{i=1}^{N-1} \sum_{j>i}^{N} U_{pair}(i, j, \mid \boldsymbol{r}_i - \boldsymbol{r}_j \mid) \\ & \ldots \end{aligned} \tag{2.3}$$

where U_{bond}, U_{angle}, U_{dihed}, U_{pair} are analytical functions used to describe chemical bonds, valence angles, dihedral angles and pair-body interactions. The first three contributions represent the *intra*-molecular interactions of the system, while the last one is regarded as the *inter*-molecular therm. Eq. (2.3) could hold many others terms such as inversion angles, three-body, Tersoff (many-body covalent), etc.. The positions of the atoms are given by the position vectors $\boldsymbol{r}_a$, $\boldsymbol{r}_b$, $\boldsymbol{r}_c$ and $\boldsymbol{r}_d$. The numbers N_{bond}, N_{angle} and N_{dihed} indicate the total numbers of corresponding interactions present in the simulated system, and the indices i_{bond}, i_{angle} and i_{dihed} uniquely specify an individual interaction of each type, all of which must be individually cited. In the pair-body term, the indices i, j refer to the atoms involved in the interaction. There is normally a very large number of these and they are therefore specified according to atom *types* rather than indices. In general, it is assumed that the pair-body terms arise from van der Waals and/or electrostatic (Coulombic) forces. The former are regarded as short range interactions and the latter as long range ones.

Short Range Potentials

The analytical potentials used to describe short range interactions, are commonly two. The first is the two-boy Lennard-Jones potential:

$$U(r_{ij}) = 4\epsilon \left[\left(\frac{\sigma}{r_{ij}} \right)^{12} - \left(\frac{\sigma}{r_{ij}} \right)^{6} \right] \tag{2.4}$$

where $r_{ij} =\mid \boldsymbol{r}_j - \boldsymbol{r}_i \mid$ refers to the distance between particle i and j, ϵ is the depth of the potential well and σ is the finite distance at which the inter-particle potential is zero. In addition, a more involved potential has been also used for the treatment of covalent, non-charged systems. J. Tersoff [15, 16], abandoned the use of N-body potential forms and proposed a new approach by effectively coupling two body and higher multi atom correlations into the model. The central idea is to consider the *bond order.* The strength of a bond between two atoms is not constant, but depends on the local environment: an atom with many neighbors forms weaker bonds than an atom with few neighbors. This potential has been calibrated for Silicon, Carbon and Germanium and it is extremely efficient in the description of their covalent compounds. It is written in the following form:

$$E = \sum_i E_i = \frac{1}{2} \sum_{i \neq j} V_{ij} \tag{2.5}$$

$$V_{ij} = f_C(r_{ij}) \left[f_R(r_{ij}) + b_{ij} f_A(r_{ij}) \right] \tag{2.6}$$

where the potential energy is decomposed into a site energy E_i and a bonding energy V_{ij}, r_{ij} is the distance between the atoms i and j, f_A and f_R are the attractive and repulsive pair potential respectively, and f_C is a smooth cutoff function.

$$\begin{aligned} f_R(r) &= Ae^{-\lambda_1 r} \\ f_A(r) &= Be^{-\lambda_2 r} \end{aligned} \tag{2.7}$$

$$f_C(r) = \begin{cases} 1, & r < R - D \\ \frac{1}{2} - \frac{1}{2} sin[\frac{\pi}{2}(r - R)/D], & R - D < r < R + D \\ 0, & r < R - D \end{cases} \tag{2.8}$$

It has to be noticed that the parameters R and D are not systematically optimized but are chosen as to include the first-neighbor shell only for several selected high-symmetry bulk structure (diamond, graphite, simple cubic, face-centered cubic structures). Hence, the f_C function decreases from 1 to 0 in the range $R - D < r < R + D$. As explained before, the basic idea is that the strength of each bond depends upon the local environment and is lowered when the number of neighbors is relatively high. This dependence is expressed by b_{ij}, which can accentuate or diminish the attractive force relative to the repulsive force, according to the environment, such that

$$\begin{aligned} b_{ij} &= \frac{1}{\left(1+\beta^n \zeta_{ij}^n\right)^{\frac{1}{2}n}} \\ \zeta_{ij}^n &= \sum_{k \neq i,j} f_C(r_{ij}) g(\theta_{ijk}) e^{\left[\lambda_3^3 (r_{ij}-r_{ik})^3\right]} \\ g(\theta) &= 1+\frac{c^2}{d^2}-\frac{c^2}{d^2+\left(h-cos\theta\right)^2} \end{aligned} \tag{2.9}$$

The term ζ_{ij} defines the effective coordination number of atom i, i.e. the number of nearest neighbors, taken into account the relative distance of two neighbors $r_{ij} - r_{ik}$ and the bond-angle θ. The function $g(\theta)$ has a minimum for $h = \cos(\theta)$, the parameter d determines how sharp the dependence on angle is, and c expresses the strength of the angular effect. All the parameters present in this potential, have been chosen to fit theoretical and experimental data obtained for realistic and hypothetical tetrels configurations.

Long Range Potentials and Ewald Sum

A Coulomb potential has been considered for the interaction of two charged ions:

$$U(r_{ij}) = \frac{1}{4\pi\epsilon_0} \frac{q_i q_j}{r_{ij}} \tag{2.10}$$

Direct summation of Coulomb terms is sometimes necessary for accurate simulation of isolated (non-periodic) systems. However, it is generaly not recommended for periodic systems. In this case the best technique for calculating electrostatic interactions, is the Ewald sum [17]. The basic model for a neutral periodic system is a system of charged point ions mutually interacting via the Coulomb potential. The Ewald method makes two amendments to this simple model. Initially, each ion is effectively neutralized (at long range) by the superposition of a spherical gaussian clouds of opposite charge, centred on the ion. The combined assembly of point ions and gaussian charges becomes the *Real Space* part of the Ewald sum. The second modification is to superimpose a second set of gaussian charges, this time with the same charges as the original point ions and again centred on the point ions (so nullifying the effect of the first set of gaussians). The potential due to these gaussians is obtained from Poissons equation and is solved as a Fourier series in *Reciprocal Space*. The complete Ewald sum requires an additional correction by a constant, known as the self energy correction, which arises from a gaussian acting on its own site. Without giving further details, the general Ewald equation is reported:

$$
\begin{aligned}
U = \frac{1}{2V} \sum_{\boldsymbol{k} \neq 0} \frac{4\pi}{k^2} \mid \rho(\boldsymbol{k}) \mid^2 e^{(-k^2/\alpha)} \\
-(\alpha/\pi)^{1/2} \sum_{i=1}^{N} q_i^2 \\
+\frac{1}{2} \sum_{i \neq j}^{N} \frac{q_i q_j erfc(\sqrt{\alpha} r_{ij})}{r_{ij}}
\end{aligned}
\tag{2.11}
$$

The first term stems from the periodic sum of screening function and it is calculated in reciprocal space, the second one is the correction deriving from the self interaction of the two set of gaussians (calculated in real space) and the last term contains the complementary error function, namely the electrostatic potential due to a point charge q_i surrounded by a gaussian with net charge $-q_i$.

2.1.3 Kinetic Energy, Temperature and Pressure

The temperature is related to the total kinetic energy of the N-particle system:

$$K = \frac{1}{2} \sum_{i=1}^{N} m_i v_i^2 \tag{2.12}$$

where m_i and v_i are atomic masses and velocities, respectively. From this the, absolute temperature T can be computed using:

$$\frac{1}{2} N_{df} k_B T = K \tag{2.13}$$

where k_B is Boltzmann's constant and N_{df} is the number of degrees of freedom which can be computed from:

$$N_{df} = 3N - N_c - N_{com} \tag{2.14}$$

Here N_c is the number of constraints imposed on the system. When performing molecular dynamics $N_{com} = 3$ additional degrees of freedom must be removed, because the three center-of-mass velocities are constants of the motion, which are usually set to zero.

The pressure is another variable that can be extrapolated and controlled during a molecular dynamics simulation. The pressure tensor $\boldsymbol{P}$ is calculated from the difference between the kinetic energy K and the virial Ξ:

$$\boldsymbol{P} = \frac{2}{V} (\boldsymbol{K} - \Xi) \tag{2.15}$$

where V is the volume of the computational box.

Depending on the statistical ensemble in which the simulation is performed, this quantities can be controlled and varied.

2.1.4 Integration of the Equations of Motion

There are different techniques developed during the years to integrate the equation of motions and simulate the time evolution of a system. The basic one is the so-called *Verlet* algorithm [8,9]. The positions, $\boldsymbol{r}(t)$ are expanded in a third-order Taylor series both forward and backward in time:

$$\begin{aligned} \boldsymbol{r}(t+\mathit{\Delta} t) &= \boldsymbol{r}(t) + \boldsymbol{v}(t)\mathit{\Delta} t + (1/2)\boldsymbol{a}(t)\mathit{\Delta} t^2 + O(\mathit{\Delta} t^4) \\ \boldsymbol{r}(t-\mathit{\Delta} t) &= \boldsymbol{r}(t) + \boldsymbol{v}(t)\mathit{\Delta} t - (1/2)\boldsymbol{a}(t)\mathit{\Delta} t^2 + O(\mathit{\Delta} t^4) \end{aligned} \tag{2.16}$$

Adding the previous expression, we have:

$$\boldsymbol{r}(t+\mathit{\Delta} t) = 2\boldsymbol{r}(t) + \boldsymbol{r}(t-\mathit{\Delta} t) + \boldsymbol{a}(t)\mathit{\Delta} t^2 + O(\mathit{\Delta} t^4) \tag{2.17}$$

This is the basic form of the *Verlet* algorithm. Since we are integrating Newton's equations, $\mathbf{a}(t)$ is just the force divided by the mass, and the force is in turn a function of the positions $\mathbf{r}(t)$:

$$\mathbf{a}(t) = -(1/m)\nabla V\left(\mathbf{r}(t)\right) \tag{2.18}$$

It is immediately clear that the truncation error of the algorithm is of the order of Δt^4, even if third derivatives do not appear explicitly. This means that Δt has to be chosen reasonably large to investigate a realistic dynamics in a small simulation time, but on the other end it has to be not too wide to brings to high errors. However, this algorithm is at the same time simple to implement, accurate and stable, explaining its large popularity among molecular dynamics simulators.

The biggest problem with the basic versin of the *Verlet* integration algorithm is that velocities are not directly calculated. Even if their knowledge is not directly needed for the time integration, it is sometimes necessary. Moreover, they are required to compute the kinetic energy K, whose evaluation is necessary to test the conservation of the total energy $E = K + V$. This requirement is one of the most important during MD simulations in the microcanonical ensemble. This is an isolated thermodynamic system that describes a system with a fixed number of particles (N), a fixed volume (V), and a fixed energy (E). That's why we generally refereed to it as NVE ensemble:

$$\mathcal{H}_{\mathrm{NVE}} = U + KE \tag{2.19}$$

Velocities can be computed directly from the positions by using:

$$\mathbf{v}(t) = \frac{\mathbf{r}(t+\Delta t) - \mathbf{r}(t-\Delta t)}{2\Delta t} \tag{2.20}$$

Nonetheless, the total error associated to this expression is of the order of Δt^2 rather than Δt^4. To overcome this difficulty, some variants of the *Verlet* algorithm have been developed. They give rise to exactly the same trajectory, and differ in what variables are stored in memory and at what times. The *leap-frog* algorithm [10] is one of such variant where velocities are handled better, but we will not treat it since an other technique has been used in our calculations. In the algorithm we used, so-called

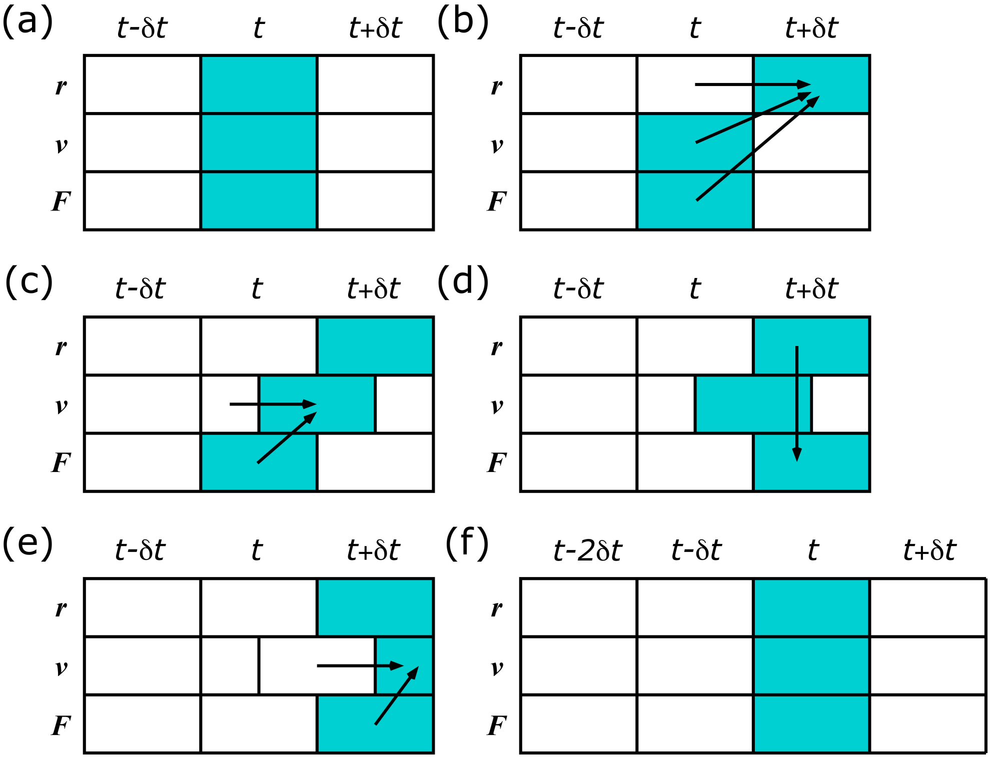

Figure 2.3 – Flow diagram of the *velocity Verlet* algorithm. (a) Given positions, velocities and forces, (b) new positions can be computed. (c) Velocities at half-step are computed and (d) subsequently the forces at the new position. (e) At the end, the velocities are computed at full step and (f) the system advanced to the next time step repeating the procedure.

velocity Verlet scheme [11], positions, velocities and accelerations at time $t + \Delta t$ are obtained from the same quantities at time t in the following way:

$$\begin{aligned} \mathbf{r}(t+\Delta t) &= \mathbf{r}(t) + \mathbf{v}(t)\Delta t + (1/2)\mathbf{a}(t)\Delta t^2 \\ \mathbf{v}(t+\Delta t/2) &= \mathbf{v}(t) + (1/2)\mathbf{a}(t)\Delta t \\ \mathbf{a}(t+\Delta t) &= -(1/m)\nabla V\left(\mathbf{r}(t+\Delta t)\right) \\ \mathbf{v}(t+\Delta t) &= \mathbf{v}(t+\Delta t/2) + (1/2)\mathbf{a}(t+\Delta t)\Delta t \end{aligned} \tag{2.21}$$

The procedure is sketched in Fig. 2.3. Note how we need $9N$ memory locations to save the $3N$ positions, velocities and accelerations, but we never need to have simultaneously stored the values at two different times for any one of these quantities.

2.1.5 Beyond the Microcanonical Ensemble

During the calculations, we would be able to control different parameters related to our systems. For this reason, we might think that the possible way to control the temperature in the system would be simply to set the temperature of the system at every time step exactly to T (i.e. scale atom velocities with a suitable factor). However, for small systems this may cause significant perturbations of the atom trajectories and the overall dynamics of the system. In addition, this totally suppresses any possible natural fluctuations in system temperature and does not provide the correct statistical ensemble, which in this case are the canonical (NVT) or the isothermal-isobaric one (NpT).

Thermostats and Barostats

The most efficient and formally correct way to control macroscopic quantities in our atomic system, is to couple it to a heat bath to ensure that the average system temperature is maintained at the requested temperature, T_{ext}. With a similar purpose, the size and shape of the simulation cell may be dynamically adjusted by coupling the system to a barostat in order to obtain a desired average pressure (P_{ext}) and/or isotropic stress tensor ($\boldsymbol{\sigma}$). Different thermostats and barostats have been developed during the years, but in the following only the basic ideas behind the ones which have been used in this work will be reported.

The Nosé-Hoover thermostat [18,19] is extensively used to control temperature during the simulations. With this method, a frictional term is included in the equations of motion:

$$\begin{aligned} \frac{\partial \boldsymbol{r}(t)}{\partial t} &= \boldsymbol{v}(t) \\ \frac{\partial \boldsymbol{v}(t)}{\partial t} &= \frac{\boldsymbol{f}(t)}{m} - \chi(t)\boldsymbol{v}(t) \end{aligned} \tag{2.22}$$

The friction coefficient, χ, is controlled by the first order differential equation

$$\frac{\partial \chi(t)}{\mathrm{d}t} = \frac{N_f k_B}{Q}(\mathcal{T}(t) - T_{ext}) \tag{2.23}$$

where $Q = N_f k_B T_{\text{ext}} \tau_T^2$ is the effective ‘mass’ of the thermostat, τ_T is a specified time constant (normally in the range $[0.5, 2]$ ps) and N_f is the number of degrees of freedom in the system. $\mathcal{T}(t)$ is the instantaneous temperature of the system at time t. The conserved quantity is derived from the extended Hamiltonian for the system which, to within a constant, is the Helmholtz free energy:

$$\mathcal{H}_{\text{NVT}} = U + KE + \frac{1}{2}Q\chi(t)^2 + \frac{Q}{\tau_T^2}\int_0^t \chi(s)\mathrm{d}s. \tag{2.24}$$

In the Melchionna modification of the Hoover algorithm [20], the equations of motion couple a Nosé-Hoover thermostat with a barostat. For isotropic fluctuations the equations of motion are:

$$
\begin{aligned}
\frac{\mathrm{d}\boldsymbol{r}(t)}{\mathrm{d}t} &= \boldsymbol{v}(t) + \eta(\boldsymbol{r}(t) - \boldsymbol{R}_0) \\
\frac{\mathrm{d}\boldsymbol{v}(t)}{\mathrm{d}t} &= \frac{\boldsymbol{f}(t)}{m} - [\chi(t) + \eta(t)]\boldsymbol{v}(t) \\
\frac{\mathrm{d}\chi(t)}{\mathrm{d}t} &= \frac{N_f k_B}{Q}(\mathcal{T}(t) - T_{\mathrm{ext}}) + \frac{1}{Q}(W_\eta(t)^2 - k_B T_{\mathrm{ext}}) \\
\frac{\mathrm{d}\eta(t)}{\mathrm{d}t} &= \frac{3}{W}V(t)(\mathcal{P} - P_{\mathrm{ext}}) - \chi(t)\eta(t) \\
\frac{\mathrm{d}V(t)}{\mathrm{d}t} &= [3\eta(t)]V(t)
\end{aligned}
\tag{2.25}
$$

where $Q = N_f k_B T_{\mathrm{ext}} \tau_T^2$ is the effective ‘mass’ of the thermostat and $W = N_f k_B T_{\mathrm{ext}} \tau_P^2$ is the effective ‘mass’ of the barostat. N_f is the number of degrees of freedom, η is the barostat friction coefficient, R_0 the system centre of mass, τ_T and τ_P are specified time constants for temperature and pressure fluctuations respectively, $\mathcal{P}(t)$ is the instantaneous pressure and V the system volume.

The conserved quantity is, to within a constant, the Gibbs free energy of the system:

$$
\begin{aligned}
\mathcal{H}_{\mathrm{NPT}} = U + KE + \mathcal{P}_{\mathrm{ext}}V(t) + \frac{1}{2}Q\chi(t)^2 + \\
\frac{1}{2}W\eta(t)^2 + \int_0^t \left(\frac{Q}{\tau_T^2}\chi(s) + k_B \mathcal{T}_{\mathrm{ext}} \right) \mathrm{d}s
\end{aligned}
\tag{2.26}
$$

A different barostat has also been used. Its original formulation is due to Parrinello and Rahman [21] and the novelty of the method stems in the possibility of anisotropic shape change of the simulation cell.

2.2 Metadynamics

Despite important achievements in computational techniques and more performing computational architectures, there are a number of problems that still result of problematic tractability due to intrinsic difficulties. The dynamics of real systems can vary in a range of characteristic times. The integration time step has to be commensurate with the fastest dynamics, typically in the order of fs. For this reason, the feasible total simulation times are of the order of hundreds of nanoseconds for classical molecular dynamics, while the upper limit of a firs-principle MD calculation is in the range of picoseconds. On top of this there is the so-called rare event problematic. Due to the presence of energetic activation barriers, distinct events occur on the time scale of a MD simulation with a very low probability, they are accordingly rare. Examples are chemical reactions and structural phase transitions and, in biophysics, protein folding, protein-protein interactions and molecular recognition. Longer simulation times or coarse-grained models can only partially cure this problem.

A more efficient way consists in enhancing the capabilities of a calculation to collect statistics precisely in the time window relevant for the event in question. Such are methodologies aimed to *accelerating rare events*. Different techniques have been developed based on two principle lines of thought: the first ones are so-called semilocal methods, that start from some low-energy structure (so that minimum effort is wasted on sampling poor regions of the energy surface) and explore the neighborhood of the initial and subsequently found structures, while the second ones are the global methods, that start with randomly generated structures and iteratively focus on the most

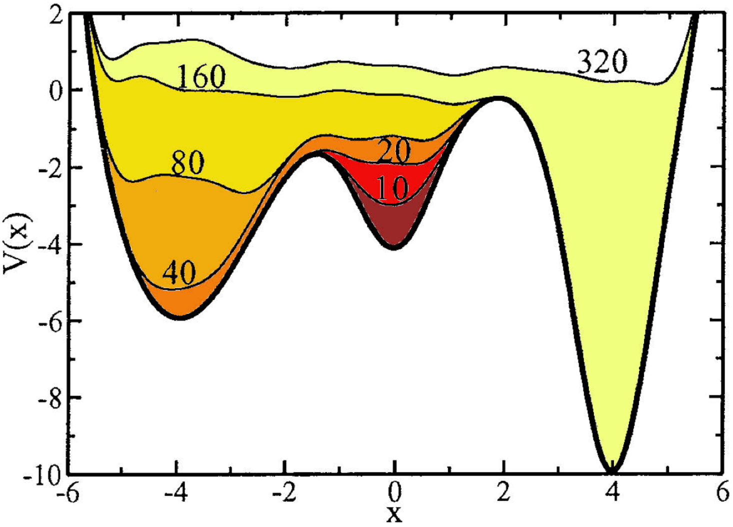

Figure 2.4 – Three-minima one dimensionall free energy surface exploration: starting from the central basin, a time evolution sum of Gaussian potential functions (thin lines) is shown until all the minima for a certain collective variable (x) are explored.

promising areas of the free energy surface until the best structure is found. Metadynamics [22–24], together with basin and minima hopping [25, 26] and simulated annealing [27, 28] represent the first category, while evolutionary algorithms [29–31] belong to the second one.

Among these techniques, metadynamics is aimed at rapidly exploring potential energy surfaces (PES) in the space of a finite number of relevant collective coordinates, called collective variables (CVs). For instance, in a chemical reaction one would choose the distance between two atoms that undergo bond formation or, in the study of nucleation, the size of the nucleus or the density gradient and enhance sampling rate as a function of these coordinates. More detailed description of the choice of a certain CV in reported in Section 2.2.1. Here we mention the choice of the simulation box as a viable CV in metadynmaics simulations of solid state structures. The dynamics in the space of the chosen CVs is biased by a history-dependent potential constructed as a sum of Gaussians centered along the trajectory followed by the CVs. A practical example can give a general outline of the ideas behind method. Imagine a walker who, in the dark of the night, falls into an empty swimming pool. The walls of the swimming pool are too stiff an high (as the energy barriers between potential energy surface minima) to be climbed and without any other help, it is rather unlikely that he will find by chance the shallowest point (lowest saddle). In metadynamics, the walker has access to a large amount of sand: every times he stops somewhere, he tips over a basket of sand (Gaussians). He almost deterministically starts exploring regions that are higher and higher. Sooner or later, the walker is destined to fill sufficiently the pool (potential energy surface minimum) to be able to climb out of it. Furthermore, he will most probably escape the minimum from the initial shallowest point. Figure. 2.4 (taken from Ref. [22]), sketchs the free energy minima flooding process in a metadynamics run.

2.2.1 The Choice of Collective Variables

Similarly to other methods that reconstruct the free energy in a set of generalized coordinates, the reliability of metadynamics is strongly influenced by the choice of the CVs. Their appropriate choice will affect the efficiency of the calculation in terms of accessing transition states and discovering intermediate metastable states. Collective variables should satisfy three main properties:

- **Distinguish** between the initial, the final and (possibly) the intermediate basins.
- **Descibe** all the slow events that are relevant in the transition process.
- **Their number** should not be too large, otherwise it will take a very long time to fill the free energy surface.

Of course, the second and the third request are mutually exclusive, and often to find a good set of CVs can be an involved task. Nonetheless, relevant variables have to be taken in account in order to explicitly bias all the ‘slow’ CVs. Fig. 2.5, highlights a simple metadynamics example to clarify the assumption made above. Let’s consider this Z-shaped, two-dimensional free energy potential. If the filling process of the

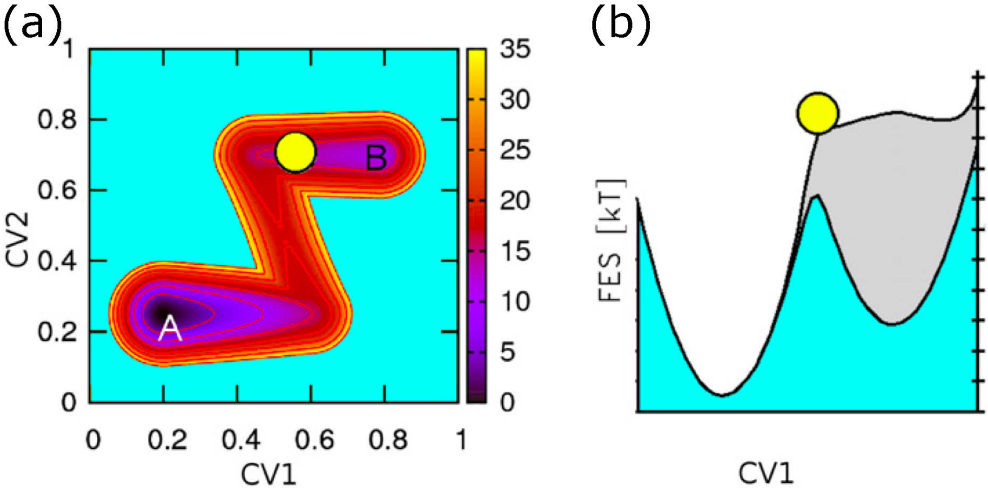

Figure 2.5 – The effect of neglecting a relevant degree of freedom. (a) Z-shaped two dimensional free energy potential. (b) Meta-trajectory considering only variable CV1. The only way of describing transition from A to B, and *vice versa*, with a single variable, is to induce a strong hysteresis. Figure taken from Ref. [1].

starting basin B is done biasing only CV1 and neglecting CV2, the simulation is not able to perform in due time a transition towards A, and metadynamics goes on overfilling this minimum. Actually, a transition will be finally observed, but only when the height of the accumulated Gaussians will largely exceed the true barrier height. Even if there is no *a priori* recipe for finding suitable sets of CVs, several checks can be done *a posteriori*: an ‘hysteretic’ behavior in the free energy reconstruction always signals a missing relevant CV, thus, new ones should be added, on the contrary, if, the free energy grows ‘smoothly’ it is likely that the set of variables is complete.

Depending on which process is under study, some CV can be more suitable than others. They can vary from geometry-related variables, coordination numbers, potential energy, path variables, normal modes, protein-specific variables and many others. In the next Section we will focus on the collective variable more representative and used with success in the simulation of first order phase transition in bulk material, namely the box shape. In relation to the CVs mentioned before, an exhaustive treatment can be found in the review by Laio and Gervasio [1].

2.2.2 Escaping Free-Energy Minima

In this Section we focus on methodological aspects of the metadynamics-based algorithm which was specifically constructed to enable simulations of structural phase transitions in crystals. In the absence of a group-subgroup relation between the limiting modifications, structural phase transitions in solids are often first order. First-order transitions such as crystallization, melting and solid-solid transitions are know to proceed generally via nucleation and growth which involves overcoming of an activation barrier. However, a phase transformation can be observed in MD simulation with a finite probability, only if the activation barrier is of the order $k_{\mathrm{B}}T$ or less.

In the context of first-order transitions, solid-solid transitions represent a special case. Often, these involve a reconstruction of the bonding pattern of the solid which itself might result in a large barrier. The situation in computer simulations is even more difficult given that for crystals one typically applies periodic boundary conditions, which eliminate the surface. This setup suppresses the possibility of a heterogeneous nucleation of a new phase. Overdriving simulation parameters (temperature, pressure), the transitions tend to proceed in a collective way which results in barriers that can be substantially higher than the experimental one. Clearly, this makes the time-scale problem even worse.

Metadynamics has a long record of successes in the prediction of crystals of various kinds [32–35]. As already mentioned, the approach is based on the idea of exploration of the relevant free energy potential surface minima (thermodynamic basins) in the space of a suitable order parameter. In the case of structural phase transitions the three supercell edges $\boldsymbol{a}, \boldsymbol{b}, \boldsymbol{c}$, arranged as a 3×3 box matrix $\boldsymbol{h} = (\boldsymbol{a}, \boldsymbol{b}, \boldsymbol{c})$, has been shown to be a good candidate [36]. In the case of small simulation cells, where it is too energetically expensive to create defects, $\boldsymbol{h}$ is a simple integer multiple of the unit cell $\boldsymbol{u}$. As a consequence, the box matrix can efficiently distinguish between different unit cells and crystal structures. Since only 6 of the 9 degrees of freedom of the matrix $\boldsymbol{h}$ are independent, while the remaining 3 are related to the global rotation of the box, it is convenient [23] to eliminate the last ones. This can be easily done by rotating the system so that the box matrix becomes upper triangular.

The minima of the Gibbs potential energy $\mathcal{G}(\boldsymbol{h}) = F(\boldsymbol{h}) + PV$, where $F(\boldsymbol{h})$ is the Helmholtz free energy of the system at fixed box and $V = det(\boldsymbol{h})$ is the volume of the box, are found for such values of the 6-dimensional order parameter $\boldsymbol{h} = (h_{11}, h_{22}, h_{33}, h_{12}, h_{13}, h_{23})$ that are commensurate with the unit cell of a crystal structure which is stable or metastable at temperature T and pressure P.

One of the biggest advantages of the metadynamics algorithm, is that it does not required a direct calculation of the free energy $\mathcal{G}(\boldsymbol{h})$, that is possible [13] but, in general, cumbersome. In the metadynamics approach it is sufficient to calculate the first derivative of the free energy with respect to the order parameter. In our case such a derivative has a simple form

$$-\frac{\partial \mathcal{G}}{\partial h_{ij}} = V\left[\boldsymbol{h}^{-1}(\boldsymbol{p} - P)\right]_{ij} \tag{2.27}$$

where only the knowledge of the internal pressure tensor $\boldsymbol{p}$, is needed, which can be easily evaluated in MD or Monte Carlo simulations at constant $\boldsymbol{h}$ from the averaged microscopic virial tensor [14].

According to the metadynamics algorithm, the Gibbs potential energy surface is scanned by means of steepest-descent-like dynamics in the space of the $\boldsymbol{h}$ vector

$$\boldsymbol{h}^{t+1} = \boldsymbol{h}^{t} + \delta h \frac{\phi^{t}}{|\phi^{t}|} \tag{2.28}$$

In the last expression the driving force $\phi^t = -\partial \mathcal{G}^t / \partial \boldsymbol{h}$ is derived from a history-dependent Gibbs potential $\mathcal{G}^t$ where a Gaussian has been added to $\mathcal{G}(\boldsymbol{h})$ at every point $\boldsymbol{h}^{t'}$ already visited in order to discourage it from being visited again. Thus, the history-dependent Gibbs potential would be

$$\mathcal{G}^t(\boldsymbol{h}) = \mathcal{G}(\boldsymbol{h}) + \sum_{t'<t} W e^{\frac{|\boldsymbol{h}-\boldsymbol{h}^{t'}|}{2\delta h^2}} \tag{2.29}$$

and so the driving force ϕ^t includes not only the thermodynamic driving force $\boldsymbol{F} = -\partial\mathcal{G}/\partial\boldsymbol{h}$, but also an additional term $\boldsymbol{F_g}$ arising from the history-dependence. As the time evolution proceeds, the history-dependent term in Eq. (2.29) fills the initial well of the free-energy surface and the system explores ever larger deformations. At a certain point, the initial structure is not stable anymore and it enters into the basin of attraction of a new structure and undergoes a pronounced change which corresponds to the structural transformation. Continuing, the system relaxes into the bottom of the new free-energy basin and when this is reached, it starts to fill the new well. In this way, during a single metadynamics simulation a series of transitions might be observed which can correspond either to several new structures or to a single transition proceeding via a number of (metastable) intermediate states. The metadynamics run is stopped when a complete transition has occurred, which can often be detected by a visible change in the configuration. If the entropic contribution to the Gibbs free energy can be neglected, enthalpy typically exhibits a sudden drop that corresponds to the transition.

The metadyamics algorithm can be implemented as follows (Fig. 2.6). The simulation starts from an equilibrated box $\boldsymbol{h}$ containing the structure at a certain critical temperature T and pressure P of the transition we want to study. The pressure tensor $\boldsymbol{p}$ is evaluated in a constant MD run long enough to allow relaxation to equilibrium and sufficient averaging of $\boldsymbol{p}$. Using forces, eq. (2.27) and the metadynamics equation of motion, (2.28), (2.29), the box $\boldsymbol{h}$ is perturbed to the new value $\boldsymbol{h'}$. The particle positions are, then, rescaled in order to fit into the new box using the relation $\boldsymbol{r'} = \boldsymbol{h'}\boldsymbol{h}^{-1}\boldsymbol{r}$. The new positions are relaxed again and the pressure tensor of the new box evaluated: the procedure is iterative and can be stopped anywhere along the transition.

The technique shown above is the original formulation of the metadynamics algorithm applied to first-order phase transitions in solid state as presented in Ref. [23]. More recently, however, an improvement has been proposed [24]. It is well know that the energy costs of a deformation vary significantly depending on the deformation itself. Hence, a large volume change would be energetically costly compared to shear or compression along one dimension accompanied by elongation along a perpendicular direction (in this case the volume is conserved). For this reason, the shape of the potential energy basin in the $\boldsymbol{h}$ space can be strongly anisotropic, similar to a valley having isolines in the shape of hyperellipsoids with their shortest semi-axis in the direction of volume change. The natural choice is therefore a Gaussian with a δh proportional to the length of the respective semi-axis in each dimension, whereas a symmetric Gaussian would drive the exploration of such kind of free energy surface too strongly into the direction of volume changes or would take too long to fill up the perpendicular directions. To include some informations on the shape of the initial well, it is worth expanding the Gibbs free energy up to the second order term around

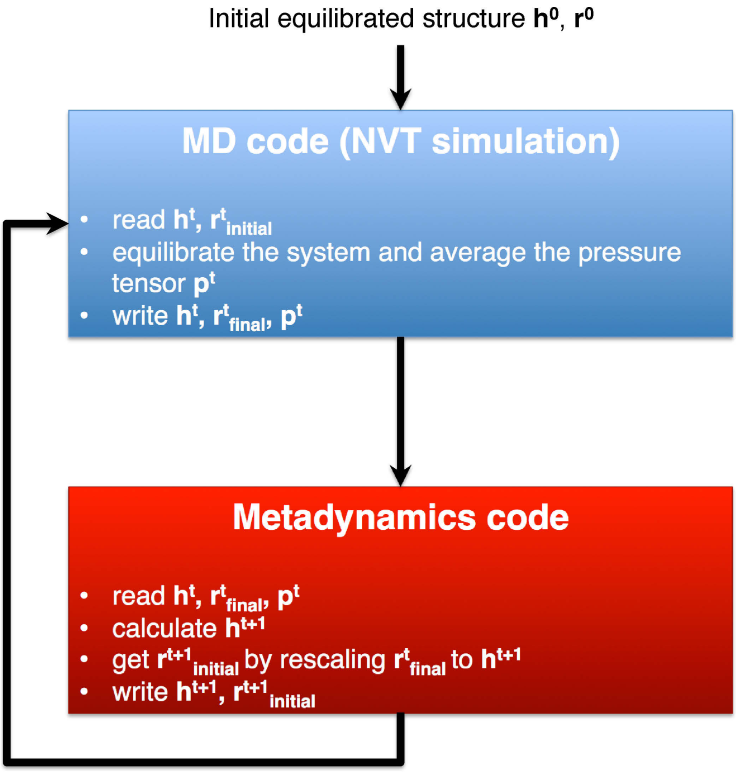
Initial equilibrated structure h0, r0
MD code (NVT simulation)
• read ht, rtinitial
• equilibrate the system and average the pressure tensor pt
• write ht, rtfinal, pt
Metadynamics code
• read ht, rtfinal, pt
• calculate ht+1
• get rt+1initial by rescaling rtfinal to ht+1
• write ht+1, rt+1initial

Figure 2.6 – Flow diagram of a metadynamics simulation: communications between MD integrator and the metadynamics driver are shown.

a given equilibrium crystal structure characterized by a matrix $\boldsymbol{h^0}$

$$\mathcal{G}(\boldsymbol{h}) \approx \mathcal{G}(\boldsymbol{h^0}) + \frac{1}{2}(\boldsymbol{h} - \boldsymbol{h^0})^T \boldsymbol{A}(\boldsymbol{h} - \boldsymbol{h^0}) \tag{2.30}$$

where the Hessian matrix

$$A_{ij} = \left.\frac{\partial^2 \mathcal{G}(\boldsymbol{h})}{\partial h_i \partial h_j}\right|_{\boldsymbol{h^0}} \tag{2.31}$$

is calculated from the $\boldsymbol{h}$ matrix fluctuations in a constant-pressure simulation. At the equilibrium matrix $\boldsymbol{h}$ has positive real eigenvalues $\{\lambda^i\}$ and can be diagonalized by an orthonormal matrix $\boldsymbol{O}$. The central point of this modified methodology is to introduce new collective coordinates which bring all degrees of freedom in the 6D space of deformations to the same energy scale. The new coordinates are chosen in the form

$$s_i = \sqrt{\lambda^i} \sum_j O_{ij}(h_j - h_j^0) \tag{2.32}$$

and this way the well become spherical

$$\mathcal{G}(\boldsymbol{h}) \approx \mathcal{G}(\boldsymbol{h}^{\mathbf{0}}) + \frac{1}{2}\sum_i s_i^2 \tag{2.33}$$

The thermodynamic force in the new coordinates $\partial\mathcal{G}/\partial s_i$ is simply related to equation (2.27)

$$\frac{\partial\mathcal{G}}{\partial s_i} = \sum_j \frac{\partial\mathcal{G}}{\partial h_j} O_{ij} \frac{1}{\sqrt{\lambda^i}} \tag{2.34}$$

The metadynamics simulation can then be performed in the s-coordinates in the same way as the original one.

The last, but extremely important point discussed in this brief overview on metadynamics, regards the choice of the Gaussian parameters δs and W, which correspond to the width and the height of the Gaussian respectively (equally, the resolution in space and energy). It is particularly difficult to guess *a priori* what is the relevant scale of both quantities, since no information about the landscape such as position and height of barriers is available. Usually, it is a good approximation to relate the two parameters such that $W \sim \delta s^2$. Furthermore, the Gaussian width has to be as large as possible, in order to be considerably larger than the thermal fluctuation $\delta s^2 \gg \sqrt{k_{\mathrm{B}} T}$ and save CPU time, but small enough to ensure a good resolution and avoid overfilling of relevant free energy wells.

2.3 Transition Path Sampling

In the previous Section, it has been shown how thanks to the help of the metadynamics algorithm, complex free energy landscapes can be rapidly explored. Nevertheless, the power of this technique lies in its excellent prediction capacity, whereas the informations on the actual free energy path connecting different local or global minima is, in general, fragmentary and blurred. Different methods have been developed in order to unravel transition mechanisms and to find the most probable reaction path, which in simple cases can correspond to the minimum energy path, but which in general have to be 'selected' out of different pathways connecting minima of the system under study. In the following, a general overview on the basic principle of a distinct method used to study transition mechanisms in solid state systems, namely the Transition Path Sampling [37–41], will be given.

2.3.1 Rare Event in Complex Systems

The concept of *rare event* has been touched upon already in the Sections above. As we have seen, many activated natural processes and transformations occur at a time scale and with a reduced frequency, which poses problems to numerical simulations. Connecting different attraction basins, which may correspond to different chemical species like reactants and products of a chemical reaction, or different polymorphs or phases of a condensed material, or even conformations of a polymer, is not only a matter of overcoming reaction barriers, but also finding the real kinetic and at given thermodynamic conditions, out of all the possible connection solutions along the free energy landscape.

Since the observation of a dynamic transition is computationally problematic with plain MD, and since several informations about the transition mechanism details are bypassed by the metadynamics algorithm as it has been presented above, a better

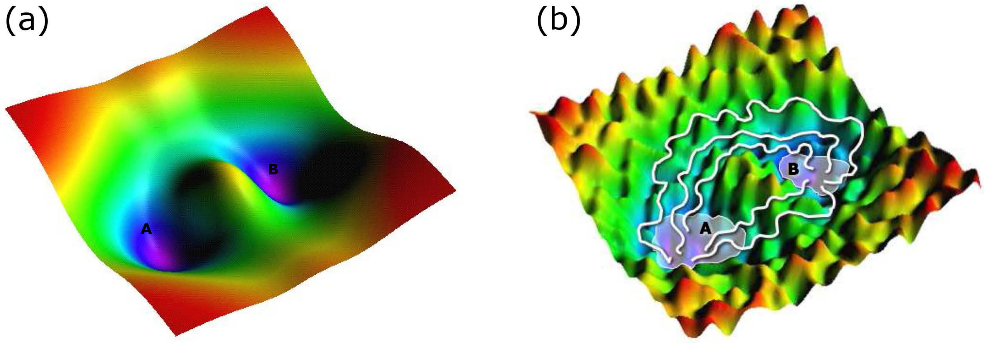

Figure 2.7 – Energy landscapes for a simple (a) and complex (b) system. In the first case a single stationary point, representing the saddle point of the transition, divides the the attraction basins A and B, whereas in the second case more points become relevant and a single transition pathway is impossible to identify.

apporach to clarify the transition process is to focus on the dynamical bottleneck the system passes through, which makes the event rare. For a simple system, see Fig. 2.7 (a) from Ref. [41], this can be done by enumerating the stationary points on the potential energy surface [42, 43]. In this case, local minima exemplify stable (or metastable) states and saddle points, activated states from which the system may access different minima. In complex systems, which have in general "many chaotically varying degree of freedom interacting with one other" [44], the situation is dramatically different (Fig. 2.7 (b)). Also in this case, long-lived stable states are separated by an energy barrier, but now stationary points exemplifying this barrier, comprise only a small fraction of the total set of saddle points. Hence, an incomplete enumeration of stationary points is insufficient to locate transition states of interest. In addition, for complex systems, the probability that the transition is completely characterised by a single sequence of configuration, such as minimum energy path, is really small and in general a large set of markedly different pathways may be relevant.

For a condensed material, the bottlenecks are typically associated with phases nucleation. The hopping of atoms from one interstitial site to another in a solid is another physical example of a rare event, as it involves an activation energy. As shown in Fig. 2.8, the periods of time spent within each basin, A and B , are different but distinctly longer than the time needed to cross over. Once the threshold is crossed, the system has a large kinetic energy compared to $k_\mathrm{B}T$. The energy is transferred to different degrees of freedom causing a very fast relaxation into the second basin. Therein, the system starts again fluctuating within microstates forming the basin B. The nature of the bottleneck in this case depends upon the energy required to distort the local lattice structure and thereby opens possible pathways between interstitial sites.

The aim of our investigation in solid state phase transitions, is to identify:

- **Transition mechanism** between the initial, the final and the intermediate attraction basins, by the determination of atomic movements associated with phase nucleation and growth.

- **Intermadiate states**, typical of nucleation and growth phase transitions. Local deformations or the formation of low dimensional structures interfacing the coexistent phases are the main causes of the formation of such metastable phases.

- **Kinetic** of the transition. Thermodynamic products are not always the actual products of real transitions, kinetic can drive the system to a local minima instead of a global one.

The principal aspect to be taken care of in this kind of analysis, is to identify and select relevant degrees of freedom, or reaction coordinates of the transition under investigation, as distinguished from orthogonal variables, whose fluctuations may be regarded as random noise.

The simplest approach to collecting such kinetical informations and acquire an atomistic description of the dynamical process is the use of straightforward Molecular Dynamics. Nevertheless, the long waiting times consumed during the system thermal

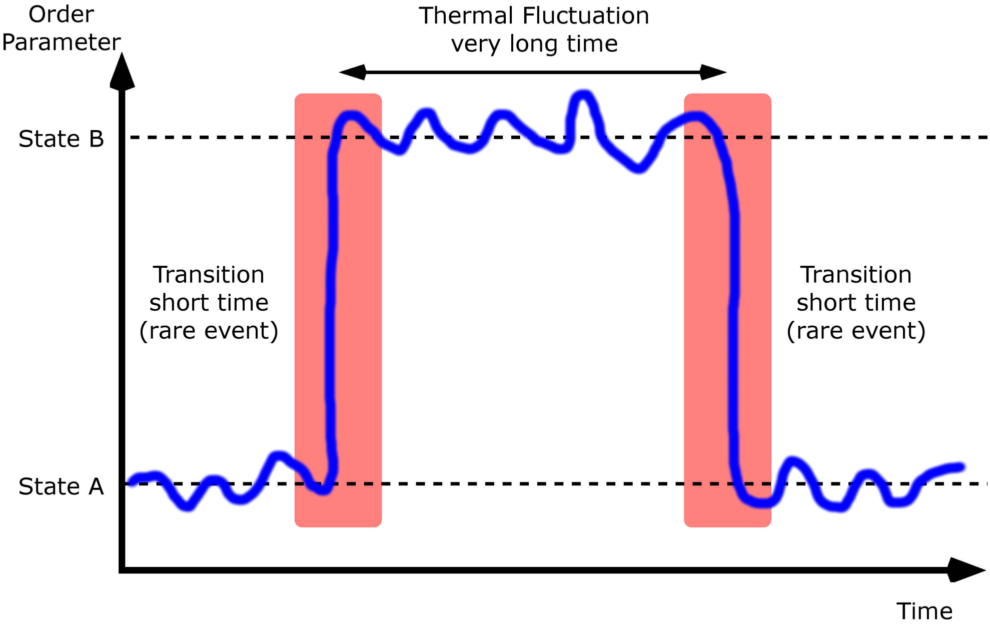

Figure 2.8 – Time evolution of a dynamic transition from different states, A and B. Most of the time the system will fluctuate in one basin or the other, and just rarely it will switch between the two states. A and B can be distinguished using an order parameter like the coordination number of an atom.

fluctuation within stable basins prevent for such simplistic approach and entail the use of a superior theoretical method.

2.3.2 Transition State Theroy

The traditional way to get around the problem of long simulation times to perform representative sampling of pathways, is to focus on the dynamical bottleneck of the rare event. Along this line, classical transition state theory (TST) has been developed [45, 46]. In a rare event, it is the transition state surface or threshold that is rarely visited and thus rarely crossed. If its location is known, however, one may construct a scheme where the system is first moved reversibly to the transition state surface and then many fleeting trajectories are initiated from that surface. Thus, if the dynamic process is reversible, each crossing point corresponding to a trajectory A → B , should result into a trajectory B → A on reversing the momenta. Consequently, each point on the TST dividing surface has equal probability of ending in either A or B.

As already mentioned in the previous Section, in a dynamic event dominated by energetic effects and not entropic ones, the use of algorithms considering gradients of the potential energy surface allows for the identification of a transition state surface. Saddle points can be systematically determined by the enumeration of stationary points on the PES. Local minima exemplify attraction basins while saddle points indicates transition states. Different minima can be accessed from saddle points via small fluctuations [42,43]. If the location of the surface is known, one may construct a scheme where the system is first moved reversibly to the transition state surface. Many fleeting trajectories are then initiated. The first step consists in determining the reversible work and thus the probability of reaching the transition state surface. In the second, however, one can use the set of subsequent trajectories to determine the probability to successfully cross the threshold. To complete the transition picture, the mechanism is inferred by comparing stable states to the transition states. This approach was pioneered by Anderson [47], Bennett [48], and Chandler [49]. Since then, TST was employed and systematically improved in order to get the best approximation of the dynamical process statistics.

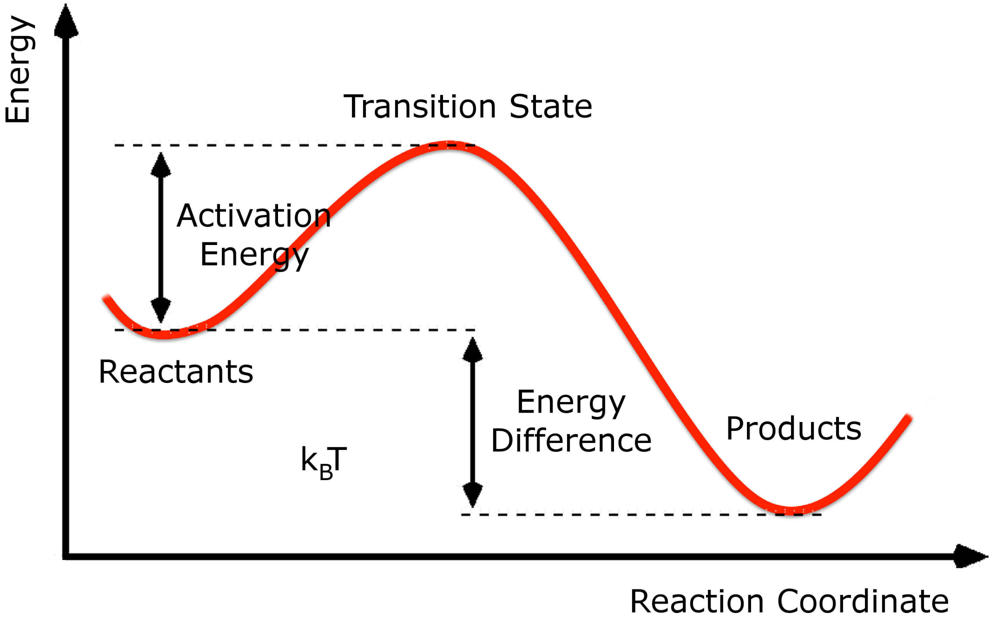

Figure 2.9 – Ideal illustration of the transition state scheme: reactants and products separated by an highest energy transition state.

However, the biggest limitation of this technique stems from the fact that with TST kinetic information may be obtained, but the choice of the reaction coordinate for the transition is still the crucial point for the description of this dynamic event. In other words, the *a priori* knowledge of the true transition path is required. Chemical or physical intuition can guide one to guess which degree of freedom may be the most relevant. Unfortunately, in complex systems such a choice is far from being trivial.

Another method is thus needed to accurately determine the reaction coordinate to use, or a theory that simply does not rely on a reaction coordinate to study the rare event. The central idea behind the Transition Path Sampling algorithm, is to focus on the short time window relative to the rare event, i.e. the phase transition, and sample an initial trajectory connecting two attraction basins, in order to identify the real kinetic path by collecting the transition path ensemble connecting the hypothetical A and B states. In this way the tedious and irrelevant long waiting times, can be avoided and the focus is entirely set on the fast transition.

2.3.3 Sampling the Transition Path Ensemble

It has been shown how transition state theory and its modern variants can be very successful in simple and small systems with smooth topography of potential energy landscapes (of the sort of Fig. 2.7 (a)). The efficiency of such methods relies on the correctness of the choice of reaction coordinates which describes the progress of the process. For numerous problems, reaction coordinates are not known and very difficult to anticipate. The situation is further complicated because the energy surface can exhibit a large number of local minima, maxima and saddle points. In this case, saddle points cease to be characteristic points of the free energy barrier.

For small systems involving a few atoms, transition states can be numerically located using algorithms that systematically search for saddle points in PES. For higher-dimensional systems, however, PES contains many saddle points as illustrated in Fig. 2.7 (a). The explicit enumeration of saddle points in PES (configuration space) can be done for system of ten or fewer atoms. However, one can by no means distinguish those which are dynamically relevant for the transition process. For systems containing large number of atoms, PES topologies are rough on the scale of thermal energies, $k_B T$, and dense in saddle points. Therefore, there is generally an uncountable number of transition states. The accurate determination of relevant points is not possible. Instead, one wants to locate and sample an ensemble of transition states. Transition path sampling accomplishes this task [37–40, 50].

The basic idea to achieve this is a generalization of standard Monte Carlo procedures [51, 52]. The focus is set on the chains of states (dynamical trajectory) rather than on individual states [53]. In standard procedures, Monte Carlo calculations perform a random walk in configuration space. This walk is biased such that a configuration x is visited in proportion to its probability $p(x)$, in order to ensure that the most important regions of the space are adequately sampled. There is no needing for initiating the walk from a certain configuration, on the contrary different configurations including atypical ones, i. e. with low probability $p(x)$, can be chosen as starting point. After equilibration moves, the bias drives the system to the most relevant regions of configuration space. This important feature for the success of the Monte Carlo Sampling is called *Importance Sampling,* and can be generalized to trajectory space as well.

In an ergodic system, there is a unique probability for the occurring of any possible trajectory that connects A to B in a given time t. This property can be used to construct a distribution functional for dynamical paths, upon which the statistical mechanics of trajectories is based. Such a functional can be helpful in the construction of partition functions for ensembles of trajectories satisfying given constraints. This change in perspective allows for a direct access to a set of markedly different pathways that may be relevant for the process. We generally refer to the set of all these trajectories as the *transition pathway ensemble.* The power of the transition path sampling method is that, rather then needing prior knowledge of the transition mechanism or reaction coordinates in order to identify such statistical ensemble, it can help to define it. Since the pathways collected by TPS are fully dynamical trajectories, it is possible to extract kinetic information from sampling simulations. The first step in the application of the TPS consists in the definition of an appropriate path ensemble. A set which contains reactive paths that begin in a particular stable state, A, and end in a different stable state B.

Defining the Initial and Final Regions

While transition path sampling does not require *a priori* knowledge of the transition mechanism (no reaction coordinate), the correct characterization of the initial and final regions is mandatory. An easy-to-use way is the consideration of a low dimensional *order parameter* q, however, the identification of such an order parameter that truly discriminates between A and B is sometimes not trivial.

A successful order parameter must fulfill a two criteria:

- it should be able to tolerate typical equilibrium fluctuations within basins of attraction. Otherwise, many important transition pathways might be missing in the transition path ensemble.
- region A and B (spanned by h_A and h_B, respectively) should not extend off basins of corresponding basins of attraction (no overlap between A and B). Otherwise, the transition path sampling would wrongly collect $A \rightarrow A$ and $B \rightarrow B$ as reactive pathways.

Dynamical Path Probability

In principle, the evolution of a dynamic system along the time coordinate is continuous, but for our purpose it is more convenient to discretize the time evolution and view a trajectory of length T as an ordered sequence of states:

$$x(T) \equiv \{x_0, x_{\Delta t}, x_{2\Delta t}, ..., x_T\} \tag{2.35}$$

A small time increment Δt separates consecutive states or time slices, thus $x_{i\Delta t}$ is a complete snapshot of the system at time $i\Delta t$. Consequently, the representation of the trajectory consists of $L = T/\Delta t + 1$ states. For a molecular system that evolves following the Newton's equations of motion, each state $x \equiv \{r,p\}$ consists of positions r and momenta p of all particles.

The statistical weight, $P[x(T)]$ indicates the probability to observe a given path $x(T)$. It depends on the probability of its initial conditions and on the specific propagation rules describing the time evolution of the system. If the process is Markovian, i. e. the probability to move from x_t to $x_{t+\Delta t}$ after one time step Δt depends only on x_t and not on the history of the system prior to t, the total path probability can be written as the product of single time step transition probabilities $p(x_t \rightarrow x_{t+\Delta t})$,

$$P[x(T)] = \rho(x_0) \prod_{i=0}^{T/\Delta t-1} p(x_{i\Delta t} \rightarrow x_{(i+1)\Delta t}) \tag{2.36}$$

Here, the prefactor on the right hand side, $\rho(x_0)$, represents the probability distribution of the initial conditions. These distribution can be defined according to the ensemble of the system to study. It depends on atomic positions and momenta and other conditions of temperature and pressure.

Reactive Path Probability

In transition path sampling the interest is restricted to reactive pathways connecting A to B, i. e. trajectories starting at time zero in region A and ending in region B at time T,

$$P_{AB}[x(T)] \equiv h_A(x_0)P[x(T)]h_B(x_T) \tag{2.37}$$

where, $h_A(x)$ and $h_B(x)$ represent characteristic population functions of regions A and B, respectively. These functions are used to establish whether a given state x is inside A (or B) or off basins:

$$h_{A,B}(x) = \begin{cases} 1 & \text{if} \quad x \in A, B \\ 0 & \text{if} \quad x \notin A, B \end{cases} \tag{2.38}$$

Due to the restriction applied to the pathways in the transition path probability (Eq. (2.37)), a non-reactive path (not beginning in A or not ending in B) has a statistical weight of zero. A path connecting A to B, however, has a non-zero weight that depends on the unrestricted path probability $P[x(T)]$. The transition path appears, thus, a selection of reactive trajectories from the ensemble of all possible pathways without changing trajectories relative probabilities.

The transition path ensemble, weighted and filtered via the probability functional in Eq. (2.37), is a set of true dynamical trajectories free of any bias by unphysical forces or constraints. Detailed informations about the mechanism and the transition kinetics are produced via an exhaustive sampling of such pathways. The definition of this ensemble is very general and valid for all Markovian processes (a given future state, at any given moment, depends only on its present state, without any history dependence on past states. This memorylessness property is required for sampling ergodic systems), and can be applied for different types of dynamics (deterministic, stochastic, Brownian, etc ...).

Deterministic Dynamics

The Lagrangian on which newton's equations of motion are based for a deterministic system, has the form:

$$\Gamma(r,p) = \{\partial H/\partial p, -\partial H/\partial r\} \tag{2.39}$$

Therefore, the time evolution of such system can be described by a set of ordinary homogeneous differential equations

$$\dot{x} = \Gamma(x) \tag{2.40}$$

The definitions mentioned above apply for different dynamics, such as extended Lagrangian dynamics of Car and Parrinello [54], and in different ensembles [51]. The solution of Eq. (2.40) gives the propagator time dependent function $\phi_t(x_0)$ and, since the time evolution of the system is deterministic, the state of the system x_t at time t will be completely determined by the state x_0 at time 0,

$$x_t = \phi_t(x_0). \tag{2.41}$$

For such deterministic dynamics the short time transition probability can be expressed as a Dirac delta function:

$$p(x_t \to x_{t+\Delta t}) = \delta[x_{t+\Delta t} - \phi_{\Delta t}(x_t)]. \tag{2.42}$$

This gives the probability of being in $x_{t+\Delta t}$ at time $t + \Delta t$ provided that you were in x_t at time t. Accordingly, the path probability is given as follows,

$$P_{AB}[x(T)] = \rho(x_0)h_A(x_0) \prod_{i=0}^{T/\Delta t-1} \delta[x_{(i+1)\Delta t} - \phi_{\Delta t}(x_{i\Delta t})]h_B(x_T) \tag{2.43}$$

Monte Carlo in Path Space

The transition path sampling is an importance sampling of trajectories akin to the importance sampling of configurations of standard Monte Carlo techniques. Depending on its statistical weight, a certain pathway of the transition path ensemble, will be visited with an higher or lower frequency during the random walk. The methodology of sampling transition pathways in trajectory space is similar to probability distribution sampling in Monte Carlo procedures [55]. Two are the principle steps to accomplish the random walk; starting from a trajectory $x^{(o)}(T)$ ("(o)" stands for "old") with a weight $P_{AB}[x^{(o)}(T)] \neq 0$, a new trajectory $x^{(n)}(T)$ is generated. This step is termed *trial move*. Following, the newly generated path is accepted with an acceptance probability balanced by the frequency of the reverse move. This step is termed *detailed balance*.

The detailed balance condition implies the following:

$$P_{AB}[x^{(o)}(T)]\pi[x^{(o)}(T) \to x^{(n)}(T)] = P_{AB}[x^{(n)}(T)]\pi[x^{(n)}(T) \to x^{(o)}(T)] \tag{2.44}$$

where, $\pi[x(T) \to x'(T)]$ is the probability to move from the old to the new path. It is expressed as product of generation probability P_{gen} and acceptance probability P_{acc}:

$$\pi[x(T) \to x'(T)] = P_{gen}[x(T) \to x'(T] \times P_{acc}[x(T) \to x'(T)]. \tag{2.45}$$

From (2.44) the following condition is obtained:

$$\frac{P_{acc}[x^{(o)}(T) \to x^{(\mathrm{n})}(\mathrm{T})]}{P_{acc}[x^{(n)}(T) \to x^{(o)}(T)]} = \frac{P_{AB}[x^{(n)}(T)]P_{gen}[x^{(n)}(T) \to x^{(o)}(T)]}{P_{AB}[x^{(\mathrm{o})}(\mathrm{T})]\mathrm{P_{gen}}[\mathrm{x^{(o)}(T) \to x^{(n)}(T)}]}. \tag{2.46}$$

To satisfy this condition and considering that $P_{acc}[x^{(o)}(T) \to x^{(n)}(T)]$ cannot exceed 1, we can use the Metropolis rule [56]:

$$P_{acc}[x^{(o)}(T) \to x^{(n)}(T)] = min\left[1, \frac{P_{AB}[x^{(n)}(T)]P_{gen}[x^{(n)}(T) \to x^{(o)}(T)]}{P_{AB}[x^{(o)}(T)]P_{gen}[x^{(o)}(T) \to x^{(n)}(T)]}\right]. \tag{2.47}$$

Since the old trajectory $x^{(\mathrm{o})}$ is reactive, i. e. $h_A[x_0^{(\mathrm{o})}] = 1$ and $h_B[x_T^{(\mathrm{o})}] = 1$, the acceptance probability can be written as:

$$P_{acc}[x^{(o)}(T) \to x^{(n)}(T)] = h_A[x_0^{(n)}]h_B[x_T^{(n)}] \times \min\left[1, \frac{P[x^{(n)}(T)]}{P[x^{(o)}(T)]}\frac{P_{gen}[x^{(n)}(T) \to x^{(o)}(T)]}{P_{gen}[x^{(o)}(T) \to x^{(n)}(T)]}\right], \tag{2.48}$$

Accordingly, only trajectories that connect A to B are accepted.

So far, we have described TPS as a realization of two processes. The core process is the system dynamics, that takes place in the phase space x of the system. The outer process is the path sampling that is built as a Markov process (Section 2.3.3) in the transition path space $x(T)$. We move now on to see how this Monte Carlo random walk in path space is realized in practice.

Shooting Moves for Deterministic Dynamics

What is crucial in the TPS algorithm, is the possibility of generating new trajectories starting from an existing one. Although many schemes can be considered [41], the shooting algorithm is practically the most efficient method.

In a shooting move, we randomly select a phase space point $x_{t'}^{(\mathrm{o})}$ along an existing (old) pathway, $x^{(\mathrm{o})}(T)$. The modification of this single state can be accomplished by slightly changing the atomic momenta. From the yielding state $x^{(\mathrm{n})}(T)$, two trajectory segments are *shot off* in both directions of time ($+t$ and $-t$), forward to time T and backward to time 0. The corresponding generation probabilities are:

$$P^f_{gen}[x^{(o)}(T) \to x^{(n)}(T)] = \prod_{i=t'/\Delta t}^{T/\Delta t-1} p\left(x^{(n)}_{i\Delta t} \to x^{(n)}_{(i+1)\Delta t}\right) \tag{2.49}$$

$$P^b_{gen}[x^{(o)}(T) \to x^{(n)}(T)] = \prod_{i=1}^{t'/\Delta t} \bar{p}\left(x^{(n)}_{i\Delta t} \to x^{(n)}_{(i-1)\Delta t}\right). \tag{2.50}$$

Eq (2.49) represents the dynamical path weight for the forward trajectory. To generate probability of the backward segment of trajectory the inverted probability $\bar{p}(x \to x')$ has been used. The probability to obtain the modified state, or the *shooting point* $x_{t'}^{(n)}$ combined with the generation probabilities of the forward and backward segments of the new trajectory, results in the generation probability of the new trajectory:

$$P_{gen}[x^{(o)}(T) \to x^{(\mathrm{n})}(\mathrm{T})] = \mathrm{p_{gen}}[\mathrm{x}_{\mathrm{t'}}^{(\mathrm{o})}] \prod_{\mathrm{i=t'/\Delta t}}^{\mathrm{T/\Delta t-1}} \mathrm{p}\left(\mathrm{x}^{(\mathrm{n})}_{\mathrm{i\Delta t}} \to \mathrm{x}^{(\mathrm{n})}_{\mathrm{(i+1)\Delta t}}\right) \times \prod_{i=1}^{t'/\Delta t} \bar{p}\left(x^{(n)}_{i\Delta t} \to x^{(n)}_{(i-1)\Delta t}\right) \tag{2.51}$$

This formula is a general expression of the shooting algorithm. In order to simplify it we make two assumptions and focus more on deterministic dynamics: microscopic reversibility ($\bar{p}(x \to y) = p(\bar{x} \to \bar{y})$) ($\bar{x}$ and $\bar{y}$ denote the transformation of x and y under time-reversal) and symmetric slice modification ($p_{gen}(x_t^{(o)} \to x_t^n) = p_{gen}(x_t^{(n)} \to x_t^o)$). If the stationary distribution of the modified state includes conserved quantities such as total linear and angular momentum, a consistent generating algorithm reduces further the acceptance rule into

$$P_{acc}[x^{(o)}(T) \to x^{(n)}(T)] = h_A[x_0^{(n)}]h_B[x_T^{(n)}] \tag{2.52}$$

The simplicity of the acceptance probability in Eq. (2.52) entails an algorithmic simplicity for shooting moves. Determining where the new pathway begins and ends (in basin A rather then B), together with the calculation of relative weights of old and new phase space points, allows for the direct evaluation of P_{acc}. The acceptance criterion in Eq. (2.52) holds even when the dynamics is non Hamiltonian.

The construction of a symmetrical algorithm that modifies a state $x_{t'}^{(o)}$ into $x_{t'}^{(n)}$ deserves a particular attention. The modification has to be consistent with the initial conditions distribution $\rho(x)$, that might contain additional constraints. In the case of linear constraints, such as total momentum and angular momentum, we can construct the following algorithm. In this procedure we assume that only momenta are changed. We consider the space point $x_{t'}^{(o)} = \left\{ r_{t'}^{(o)}, p_{t'}^{(o)}, \xi_{t'}^{(o)} \right\}$, where $\xi_{t'}^{(o)}$ represents additional variables of generalized dynamics,

1. Randomly select a time slice $x_{t'}^{(o)}$ on an existing path $x^{(o)}(T)$
2. Modify the selected time slice momenta by adding a random displacement δp from a one dimensional Gaussian distribution according to $p' = p_{t'}^{(o)} + \delta p$. The random displacement must be symmetric with respect to reverse move
3. Impose linear constraints such as vanishing total linear and angular momentum
4. Accept the new shooting point with probability $\min[1, \rho(x_{t'}^{(n)})/\rho(x_{t'}^{(o)})]$. If rejected, restart from 2
5. If accepted, rescale the momenta in order to obtain the desired total energy
6. Integrate backward and forward in time
7. If the path is reactive (starts from A and ends in B) accept and the new trajectory is used, otherwise reject and restart from 1

The shooting algorithm generates new trajectories by perturbation of old path, for the random walk in trajectory space. Anyway, the acceptance of the move is strictly related to the magnitude of phase space displacement δx, δp in our case. If $\delta x \to 0$, the old path is simply reproduced with and acceptance equal to 1, but also very low displacements lead to the sampling of the same path, and the harvested pathways are correlated. If δx is very large, however, the collected pathways are different but the acceptance rate will be very low because of the instability of reactive

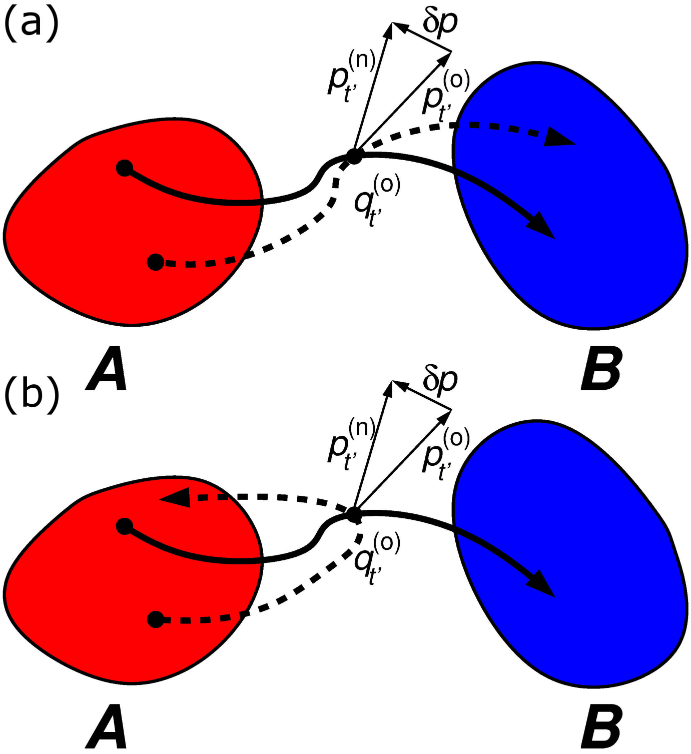

Figure 2.10 – In a shooting move, at a random time slice $x_{t'}^{(o)}$ of the old path (solid line), momenta $p_{t'}^{(o)}$ are changed by a small amount δp. Integrating backward and forward the equations of motion starting from the modified state $x_{t'}^{(n)}$, the new trajectory $x^{(n)}(T)$ is yielded (dashed line). (a) If the new trajectory still connect A to B, than is accepted, otherwise (b) is rejected.

trajectories $A \to B$. Unstable simply means, that the generation of $A \to A$ and $B \to B$ trajectories is statistically more probable. The production of decorrelated trajectories using as less as possible Monte Carlo cycles is at the aim of any efficient sampling algorithm. An acceptance of $40 - 60\%$ indicates an efficient sampling [57].

2.4 Density Functional Theory

So far, the treatment of simulation system has been done considering atoms as solid particles subject to external potentials that regulate their static and dynamic behaviour. This kind of approximation works generally well for several systems and problematics, however there are intrinsically more complex aspects of the atomistic world, which needs a more accurate description. *Ab initio* techniques allow for the description of a quantum system with first-principle considerations only, relying on the mathematical model taken as representation of the real system itself. In this way all the electronic, and related properties of an atomic or molecular system can be determined. Clearly, the quality of the final result strictly depends on the choice of the initial model and from a practical point of view, it is possible to apply a certain *ab initio* method only to a limited class of problematics, because of the computational difficulties that may be encountered. The quantum description of the atomistic and molecular world relies on the solution of the Schrödinger equation [58]

$$\hat{H}\Psi = E\Psi \tag{2.53}$$

here reported in its not time-dependent, static formulation. In the equation, E represents the total energy and Ψ the wave function. It is the central quantity in quantum mechanics; it contains spin and spatial coordinates and in general all the informations about the system. $\hat{H}$, the Hamiltonian, is a differential operator containing kinetic and potential terms referred to electrons-electrons, nuclei-nuclei and electrons-nuclei interactions. Nonetheless, the complexity of the equation (mainly due to many-body interactions) allows for its exact resolution only in the case of atoms with few electrons, e.g. hydrogen and helium. To approach more complicated systems, as the ones studied in material science, mathematical approximations sometimes based on physical intuitions have to be done. Over the years, a large number of techniques have been developed. The first approximate solutions of the Schrödinger equation, are due to Hartree and Fock methodologies [59–61] who start the development of quantum mechanics techniques off. Thereafter, a large number of these techniques were set up and nowadays we have several of them: some are for general descriptions of the system, others for rather specific purposes, some are outdated, other ones have been improved over the years and still used with big success [62–64].

Here, we focus on the so-called Density Funcional Theory (DFT) [65], that is one of the most successful computational technique of the last 2-3 decades, because of its great power in the thorough description of relatively large quantum systems. In the next Section we will also briefly discuss the tight-binding formulation of DFTB [66]. Several approximations considered in such technique allows for a dynamic quantum treatment of large systems, which can be hard to compute with plain DFT.

2.4.1 The electron density

The main idea in DFT is to focus on the electron density function $\rho(r)$ of a system, instead of trying to guess its complicated wave function. From the Eq. (2.53) and through many considerations, including that the Hamiltonian below contains just mono- and bi-electronic terms, the total energy of a system can be expressed as

$$\begin{aligned} E &= \langle\Psi|\hat{H}|\Psi\rangle = \langle\Psi|\hat{T}+\hat{V}+\hat{W}|\Psi\rangle = T+V+W \\ &= \int dr \left(-\frac{1}{2}\nabla^2\rho(r,r')\right)\Bigg|_{r'=r} + \int dr\ v(r)\rho(r) + \frac{1}{2}\int dr_1 \int dr_2 \frac{\rho(r_1,r_2)}{r_{12}} \end{aligned} \tag{2.54}$$

where we can distinguished the different contribution to the total Hamiltonian $\hat{H}$:

- The kinetic energy T, defined with the one-body density matrix $\rho(r,r')$
- The external potential V, for the description of which we need the simple density function $\rho(r)$
- The inter-electronic energy repulsion W, expressed via the two-body density function $\rho(r_1,r_2)$

These quantities can be directly calculated from the wave function and this kind of expression for the total energy (Eq. (2.54)), suggests that the knowledge of the electron density is somehow sufficient to the description of the entire system. Unfortunately, only the external potential V can be described just by means of the density function, whereas T and W need more involved terms to be determined. Since this intuition, most of the work has been done in approximating the T and W contributions that are not functional (a functional is a function of a function) of the simple electron density function.

Historically, Thomas and Fermi [67, 68] were the first who proposed to express the total energy of a system of interacting electrons as a function of the associated charge density. Their consideration of a free electron gas in which interactions are given by a coulombian potential $v(r)$ due to the nucleus, brought them to express the total energy as a functional of the density

$$\begin{aligned} E[\rho] &= T_F[\rho] + J[\rho] + V[\rho] \\ &= T_F[\rho] + \int dr\ v(r)\rho(r) + \frac{1}{2}\int dr_1 \int dr_2 \frac{\rho(r_1)\rho(r_2)}{r_{12}} \end{aligned} \tag{2.55}$$

From this simple formulation, where only the classical coulomb interaction $J[\rho]$ is considered and the inter-electronic exchange and correlation terms are by definition neglected, it is possible to derive an expression for the kinetic energy where only the electron density function appears:

$$T_F[\rho] = C_F \int dr\ \rho(r)^{5/3} \tag{2.56}$$

This functional is local and describes in a correct way only the kinetic term of an homogeneous electron gas. It is clear that for molecules and atoms where the density ρ varies significantly depending on r, the model merely failed, however, the work of Fermi and Thomas has to be seen as a pioneeristic attempt of working only with the electron density function.

Some years later, Dirac first and von Weizsäcker [69, 70] then, refined the previous model including the exchange functional of the electron density $K[\rho]$, which represents the quantum equivalent of the classical coulomb interaction between electrons ($J[\rho]$) and the gradient of ρ into the kinetic term

$$\begin{aligned} E[\rho] &= T_{FW}[\rho] + J[\rho] + V[\rho] - K[\rho] \\ &= C_F \int dr\ \rho(r)^{5/3} + \frac{\lambda}{8} \int dr\ \frac{\nabla\rho \cdot \nabla\rho}{\rho} + \int dr\ v(r)\rho(r) \\ &\quad + \frac{1}{2} \int dr_1 \int dr_2 \frac{\rho(r_1)\rho(r_2)}{r_{12}} - C_x \int dr\ \rho(r)^{4/3} \end{aligned} \tag{2.57}$$

Despite these improvements, good results using only the electron density ρ were not obtained until the enunciation of two fundamental theorem, based on which the Tomas-Fermi model can be seen as an approximation, of an otherwise exact theory: the Density Functional Theory.

2.4.2 The Hohenberg-Kohn Theorems

In 1967, Hohenberg and Kohn finally established that the complicated and thus hard-to-compute many-electron wave function, which contains $3N$ variables (where N is the number of electron, each of which with 3 spatial coordinates), can be substituted with the functional of the electron density, containing only 3 variables.

The statement that the external potential (monoelectronic) $V = \sum_{i=1}^{N} v(r_i)$, defines the electron density of the fundamental state, appears obvious: in the Hamiltonian, $\hat{H} = \hat{T} + \hat{V} + \hat{W}$, only the potential is specific for a certain system, while the kinetic and bi-electronic terms have the same expression for each molecule with N electrons. This means that, known the number of particles N and the potential V, solving the Schrödinger equation and determining the ground state, a *unique* density ρ is obtain via integration of $N-1$ electron coordinates. The fundamental question is then: Is the *viceversa* also true, does the electronic density ρ univocally determines the external potential V and hence, all the properties? The answer is not trivial, but Hohenberg and Kohn found a brilliant solution to this problem.

First Hohenberg-Kohn Theorem

The external potential $v(r)$ of a system is univocally determined, within a trivial additive constant, by the electron density $\rho(r)$.

This theorem establishes an injective correspondence between $v(r) \Longleftrightarrow \rho(r)$ and its demonstration is extremely simple and based on the variational theorem, valid only for non degenerate fundamental states. Let's assume to have two different systems with the same N. They have different external potentials v_1 and v_2, i. e. different Hamiltonians $\hat{H}_1$ and $\hat{H}_2$ and ground state wave functions Ψ_1 and Ψ_2 but, by contradiction same density functions ($\rho_1 = \rho_2$). Starting from $\hat{H}_1|\Psi_1\rangle = E_1|\Psi_1\rangle$ and $\hat{H}_2|\Psi_2\rangle = E_2|\Psi_2\rangle$ we have:

$$E_1 < \langle\Psi_2|\hat{H}_1|\Psi_2\rangle = \langle\Psi_2|\hat{H}_2|\Psi_2\rangle + \langle\Psi_2|\hat{H}_1 - \hat{H}_2|\Psi_2\rangle \tag{2.58}$$

$$E_1 < E_2 + \langle \Psi_2 | V_1 - V_2 | \Psi_2 \rangle = E_2 + \int dr \; (v_1 - v_2)\rho(r) \tag{2.59}$$

in the last Eq. (2.59), the hypothesis that $\rho_1 = \rho_2$ has been used. The same procedure brings to an equivalent expression for E_2

$$E_2 < E_1 + \langle \Psi_1 | V_1 - V_2 | \Psi_1 \rangle = E_1 + \int dr \; (v_2 - v_1)\rho(r) \tag{2.60}$$

The sum of Eqs. (2.59) and (2.60) gives the illogical result $E_1 + E_2 < E_1 + E_2$, proving that the two densities have to be different, $\rho_1 \neq \rho_2$. With these considerations, Hohenberg and Kohn established that the energy of the ground state only depends from the electronic density

$$E_v[\rho] = F_{HK}[\rho] + \int dr \; v(r)\rho(r) \tag{2.61}$$

where $F_{HK}[\rho]$ is the *universal functional* (universal means, not dependent from the system, but only from the observable that has to be described), whose analytical expression is unknown but whose existence is certain.

$$F_{HK}[\rho] = T[\rho] + W[\rho] = T[\rho] + J[\rho] + \text{non classic terms} \tag{2.62}$$

Second Hohenberg-Kohn Theorem

Considering the relation $\rho(r)_1 \Longleftrightarrow v_1$ from the first HK theorem, and assuming that there is a $\rho(r)_2$, such that $\rho(r)_2 \geq 0$, than: $E_{v1} \leq E_{v2}$.

This theorem established the variational character of the energy functional. Again, the demonstration is based on the variational theorem. With the simple assumption that ρ_2 corresponds to the density of an other system with external potential $v_1 \neq v_2$ ($\Psi_1 \neq \Psi_2$), so that

$$E_{v1}[\rho_1] = \langle \Psi_1 | \hat{H}_2 | \Psi_1 \rangle \leq \langle \Psi_2 | \hat{H}_1 | \Psi_2 \rangle \tag{2.63}$$

where the correspondence $\rho_2 \rightarrow v_2 \rightarrow \Psi_2$ has been applied. In this way the search of ρ corresponds to the search of that density which minimises $E_v[\rho]$. Applying the Langrange multipliers method we can look for the stationary energy referred to the variation of ρ with the constrain $\int \rho(r)dr = N$

$$\frac{\partial}{\partial \rho} \left\{ E_v[\rho] - \mu \left[\int \rho(r)dr - N \right] \right\} = 0 \tag{2.64}$$

$$\mu = \frac{\partial E_v[\rho]}{\partial \rho(r)} = v(r) + \frac{\partial F_{HK}[\rho]}{\partial \rho(r)} \tag{2.65}$$

This latter expression represents an *exact* equation for the electronic density, but it can be solved only when the F_{HK} functional is known and exact. The central problem of the theory, is that the functional is generally approximated in the reality, thus DFT is not always supported by the variational principle.

2.4.3 The Kohn-Sham Equations

The main problem of the approximation of the universal functional was the precise calculation of the kinetic energy. For this reason the theory remained too rough to give adeguate results, until in 1965 Kohn and Sham [65] proposed a clever way to bypass this issue, introducing the concept of non interacting system and expressing the density by means of orbital (auxiliary functions).

Let us consider a system of N *non interacting electrons*. In this case the expression for the energy is

$$E[\rho] = \int dr\ v(r)\rho(r) + F_s[\rho] \tag{2.66}$$

where $F_s[\rho]$ is the universal functional for non interacting electrons. Clearly, this functional is constituted by a pure kinetic energy part:

$$F_s[\rho] \equiv T_s[\rho] \tag{2.67}$$

where $T_s[\rho]$ is the kinetic energy for non interacting electrons. If we apply the variational principle to the approximate expression for the energy

$$E[\rho] = \int dr\ v(r)\rho(r) + T_s[\rho] \tag{2.68}$$

we obtain:

$$\partial E[\rho] = \left[v(r) + \frac{\partial T_s[\rho]}{\partial \rho(r)} \right] \partial \rho(r) = 0 \tag{2.69}$$

The kinetic energy for the system of N non interacting electrons, can be defined in terms of the spin orbitals ψ_i for each electron:

$$T_s[\rho] = \sum_{i=1}^{N} \langle \psi_i | -\frac{1}{2}\nabla^2 | \psi_i \rangle \tag{2.70}$$

The electronic density for such a system is:

$$\rho(r) = \sum_{i=1}^{N} \sum_{s} |\psi_i(r,s)|^2 \tag{2.71}$$

It has to be noticed that this decomposition of the electronic density is allowed by the property of N-representability. The functional $T_s[\rho]$ above, is not, however, a functional of the electronic density function, since the Eq. (2.70) is based on the knowledge of the wave function (the problem has thus not been simplified). The main statement of the Kohn-Sham scheme stems from the fact that: *for each interacting system, $W \neq 0$ it exists a local mono-electronic potential v_s, such that the exact density ρ of the interacting system is equal to ρ_s of the non interacting system with external potential v_s.*

The procedure of minimization of the energy $E[\rho]$ with respect to the mono-electronic orbitals ψ_i, that has been shown to derive directly form the non interacting density ρ_s via this simple logic chain $v \to \rho \xrightarrow{KS} \rho_s \xrightarrow{HK} v_s \to \psi_i \to T_s[\rho]$, leads to the following set of *mono-electronic* Euler equations:

$$\left[-\frac{1}{2}\nabla^2 + v_s(r)\right]\psi_i = \epsilon_i \psi_i \tag{2.72}$$

Let us move now to the *interacting*, N particles system. We can rewrite $F[\rho]$ extracting the kinetic energy term for non interacting electrons $T_s[\rho]$:

$$F[\rho] = T_s[\rho] + \frac{1}{2}\int dr \int dr' \frac{\rho(r)\rho(r')}{|r-r'|} + E_{xc}[\rho] \tag{2.73}$$

where E_{xc} is an other central quantities in DFT and represent all the difficult-to-calculate parts of our functional. It is defined as:

$$E_{xc}[\rho] = W[\rho] - J[\rho] + T[\rho] - T_s[\rho] \tag{2.74}$$

and know as exchange-correlation functional. It contains:

- The differences between the exact (and unknown) functional for the real kinetic energy $T[\rho]$ and the one for the non interacting $T_s[\rho]$, that is presumably small
- The non-classical parts of the electron-electron interaction term that include the exchange and correlation energies.

The total expression for the energy is thus

$$E[\rho] = \int dr\ v(r)\rho(r) + T_s[\rho] + \frac{1}{2}\int dr \int dr' \frac{\rho(r)\rho(r')}{|r-r'|} + E_{xc}[\rho] \tag{2.75}$$

and applying again the variational principle we get

$$\partial E[\rho] = \left[v(r) + \int dr' \frac{\rho(r')}{|r-r'|} + \frac{\partial E_{xc}[\rho]}{\partial\rho(r)} + \frac{\partial T_s[\rho]}{\partial\rho(r)}\right]\partial\rho(r) = 0 \tag{2.76}$$

Let define the effective potential v_{eff}:

$$v_{eff}(r) = v(r) + \int dr' \frac{\rho(r')}{|r-r'|} + \frac{\partial E_{xc}[\rho]}{\partial\rho(r)} \tag{2.77}$$

where we can express the exchange and correlation potential as $v_{xc}(r) = \partial E_{xc}[\rho]/\partial\rho(r)$ that is unknown, but regardless of how complicated it can be, it is always a local one. The total energy functional can be expressed therefore, as

$$E[\rho] = \int dr\ v_{eff}(r)\rho(r) + T_s[\rho] \tag{2.78}$$

Now, invoking the variational principle and determining the stationarity conditions, the following Eulero expression is obtained:

$$\mu = \frac{\partial}{\partial\rho}\int dr\ v_{eff}(r)\rho(r) + \frac{\partial T_s[\rho]}{\partial\rho(r)} \tag{2.79}$$

or

$$\mu = v_{eff}(r) + \frac{\partial T_s[\rho]}{\partial \rho(r)} \tag{2.80}$$

that are the equivalent expressions used to derive the non interacting system (Eq. (2.72)) eigenvalue equation, but now referred to a system subject to an effective potential v_{eff}, which takes into account electron-electron interactions. Thus, the optimal density for the description of our system is the one obtained iteratively from the solution of these mono-electronic equations:

$$\left[-\frac{1}{2}\nabla^2 + v_{eff}(r)\right]\psi_i = \epsilon_i \psi_i \tag{2.81}$$

This is the canonical form of the Kohn-Sham equations (KS). First of all, they are valid only for the ground state, since the Hohenberg and Kohn theorems can be demonstrated only in this case and then, they determine the exact density ρ (from which the total energy $E[\rho]$ is calculated) only if a correct exchange and correlation potential is set up. It is clear, that v_{xc} can be seen as the “carpet”, under which “the dust”, corresponding to all the terms we can not calculate exactly (namely the real kinetic energy and the quantum term of the inter electron interactions), is swept. Most of the work that has been done since the Kohn-Sham equations formulation, regards the quest of reasonable exchange-correlation potential v_{xc}. We will not go into the details neither of how these potentials can be determined nor of their main expressions but, for these purposes, we refer to the literature [71–76].

Solution of the KS Equations

The Kohn-Sham equations (2.81) have to be solved iteratively. This technique has been originally introduced by Hartree [59, 60] in its approximated solution of the Schrödinger equation and can be extended to fit the KS equations solution. The functions $\{\psi_i^{(n)}\}$ (where n, counts the iterative cycles) called basis set, have the big advantage in DFT, not to be atomic orbitals (that vice versa, is mandatory in Hartree-Fock and post HF methods) but in principle just ‘random’ functions. With these functions, the initial electron density $\rho^{(n)}$ is guessed and the external potential $v_{eff}^{(n)}$ (Eq. (2.77)), and thus the KS Hamiltonian, are defined. Thereafter, the solution of the KS equations brings to a new set of orbitals $\{\psi_i^{(n+1)}\}$ that identify a new density $\{\psi_i^{(n+1)}\}$ and a new potential. This procedure, called sefl-consistent field (SCF) is iterated until $E[\rho]^{(n+m)} - E[\rho]^{(n+m-1)} \ll \epsilon$, with ϵ being the convergence threshold. In Fig. 2.11 a schematic picture of the SCF algorithm is reported.

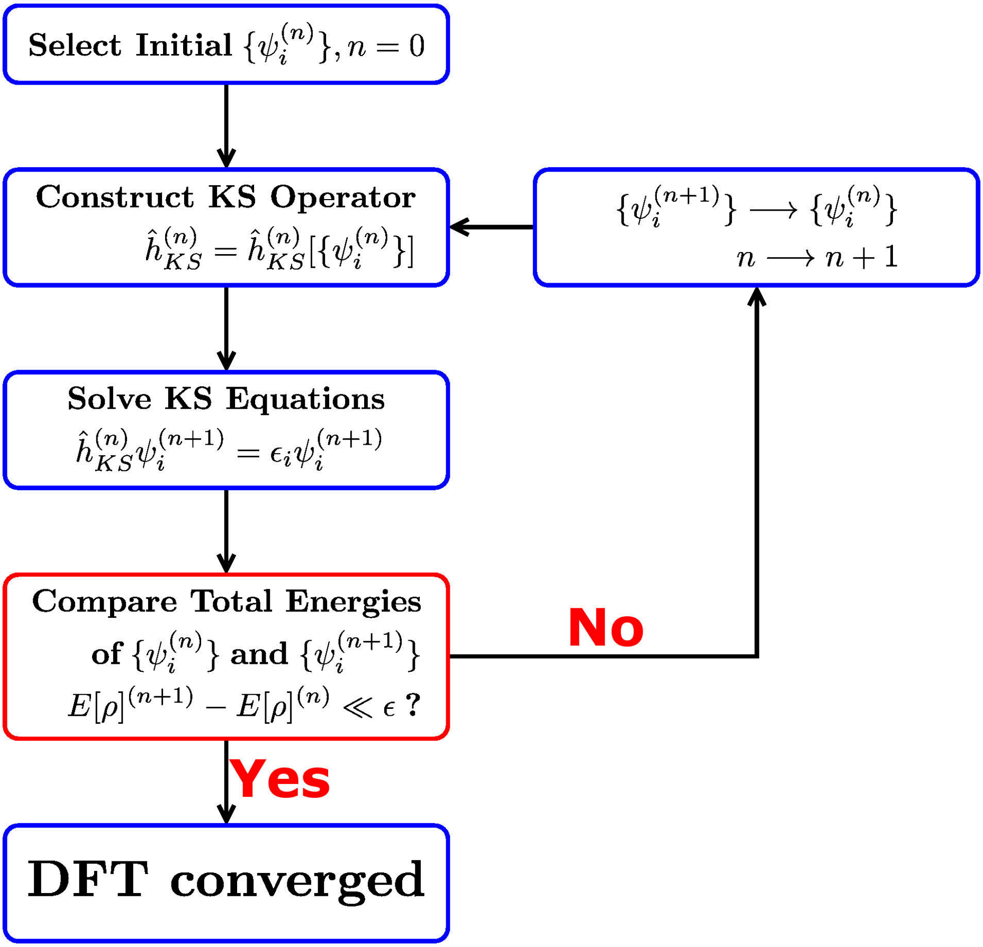
Select Initial $\{\psi_i^{(n)}\}, n = 0$
Construct KS Operator
$\hat{h}_{KS}^{(n)} = \hat{h}_{KS}^{(n)}[\{\psi_i^{(n)}\}]$
$\{\psi_i^{(n+1)}\} \longrightarrow \{\psi_i^{(n)}\}$
$n \longrightarrow n+1$
Solve KS Equations
$\hat{h}_{KS}^{(n)}\psi_i^{(n+1)} = \epsilon_i\psi_i^{(n+1)}$
Compare Total Energies
of $\{\psi_i^{(n)}\}$ and $\{\psi_i^{(n+1)}\}$
$E[\rho]^{(n+1)} - E[\rho]^{(n)} \ll \epsilon$?
No
Yes
DFT converged

Figure 2.11 – Schematic workflow of a Self-Consistent Field (SCF) procedure: iterative resolution of the Kohn-Sham equations.

2.5 Introduction to The Tight-Binding Approach

The idea behind the tight-binding (TB) approximation of the DFT theory, is to set up a robust, fast and portable method to afford calculation of atomic and electronic structures in larger molecular and condensed systems. The standard formulation of the theory is due to Slater and Koster [77], that in 1954 proposed to represent the exact many-body Hamiltonian operator (H) of the system under study, with a parametrized H matrix, whose element are fitted to the electronic band structure of a suitable reference system. Later, the formulation was extended to the calculation of the total energy [78], introducing a splitting of it

$$E_{tot} = E_{bs} + E_{rep} \tag{2.82}$$

such that E_{bs} represents the sum over the occupied orbital of the energies derived from the diagonalization of the electronic Hamiltonian and E_{rep} refers to a short-range repulsive two-body interaction. Despite the long records of success of this technique like it was originally formulated [79], the main issue was to increase the transferability of the method, since the accuracy of the scheme was tuned for particular problematics, failing in the treatment of other ones where the bonding situations were not covered by the parametrization. In the following, a general overview of the TB scheme used in this work is reported. However, for a deeper description of how the method has been improved over the years, Refs. [80, 81] should be consulted.

Basis of DFTB theory

Tight-binding DFT has to be seen as a stationary approximation of the DFT theory. It has been proven that Eq. (2.82) is a valid approximation of the total energy and that the non-self-consistent treatment of the KS equations together with the definition of a repulsive pairwise term is a good initial guess of the charge distribution [82–84]. Second order effects arising from a charge redistribution can be often neglected, but there are peculiar chemical situation, in which an adjustment of the charge distribution itself via a self-consistent field procedure is needed.

The total energy functional of the electron density $\rho(r)$, for a system of M electrons in the field of N nuclei can be expressed within DFT as

$$\begin{aligned} E[n(r)] &= \sum_i^{occ} \langle\psi_i| - \frac{1}{2}\nabla^2 + v_{ext} + \frac{1}{2}\int dr' \, \frac{\rho(r')}{|r-r'|}|\psi_i\rangle \\ &+ E_{\mathrm{XC}}[\rho(r)] + \frac{1}{2}\sum_{\alpha,\beta}^{N} \frac{Z_\alpha Z_\beta}{|R_\alpha - R_\beta|} \end{aligned} \tag{2.83}$$

where the first sum is over the occupied KS orbitals $\{\psi_i\}$, the second one is the exchange and correlation (XC) contribution, and the last represents the ion-ion core repulsion, E_{ii}. Let's now substitute the charge density in Eq. (2.83) with a superposition of a reference density $\rho_0' = \rho_0(r')$ and a small fluctuation $\delta\rho' = \delta\rho(r')$ and then rewrite everything in a second order Taylor expansion of the DFT energy:

$$\begin{aligned}
E[n(r)] &= \underbrace{\sum_i^{occ}\langle\psi_i| -\frac{1}{2}\nabla^2 + v_{ext} + \int dr' \, \frac{\rho_0'}{|r-r'|} + v_{\mathrm{XC}}[\rho_0]|\psi_i\rangle}_{1} \\
&- \underbrace{\frac{1}{2}\int\int dr' \, \frac{\rho_0'(\rho_0+\delta\rho)}{|r-r'|}}_{2} - \underbrace{\int v_{\mathrm{XC}}[\rho_0](\rho_0+\delta\rho)}_{3} \\
&+ \underbrace{\frac{1}{2}\int\int dr' \, \frac{\delta\rho'(\rho_0+\delta\rho)}{|r-r'|}}_{4} + \underbrace{E_{\mathrm{XC}}[\rho_0+\delta\rho]}_{5} + \underbrace{E_{ii}}_{6} \qquad (2.84)
\end{aligned}$$

where term 2 corrects for the double counting in the new Hartree term, 3 corrects for the XC contribution and term 4 comes from the first Hartree term in Eq. (2.83) into a part relative to ρ_0 and to $\delta\rho$. Eq. (2.84) can be, finally, rewritten as a second order Taylor expansion of the DFT energy:

$$\begin{aligned}
E[n(r)] &= \sum_i^{occ}\langle\psi_i|\hat{H}_0|\psi_i\rangle - \frac{1}{2}\int\int dr' \, \frac{\rho_0'\rho_0}{|r-r'|} + E_{\mathrm{XC}}[\rho_0] \\
&- \int v_{\mathrm{XC}}[\rho_0]\rho_0 + E_{ii} \\
&+ \frac{1}{2}\int\int dr' \left(\frac{1}{|r-r'|} + \left.\frac{\delta^2 E_{\mathrm{XC}}}{\delta\rho\delta\rho'}\right|_{\rho_0}\right)\delta\rho\delta\rho' \qquad (2.85)
\end{aligned}$$

where $\hat{H}_0$ is the Hamiltonian operator resulting from the reference density ρ_0.

2.5.1 Standard DFTB, non-SCC Approach

Traditionally, the standard DFTB approach tends to neglect the last term of Eq. (2.85) and the KS equation are solved non-self-consistently (non-SCC) within a frozen-core approximation. Thus, only the single-particle Hamiltonian and the pairwise, repulsive, short range term (that contains also the non-trivial exchange and correlation contribution) are included in the total energy expression

$$E_0^{\mathrm{DFTB}} = \sum_i^{occ}\langle\psi_i|\hat{H}_0|\psi_i\rangle + E_{rep} \qquad (2.86)$$

and precisely the usual repulsion energy is replaced by repulsive diatomic potentials. The procedure to follow in the non-SCC approach is here reported:

- Express the reference density ρ_0, as a summation of atomic densities:

$$\rho_0 = \sum_i^N \rho_0^i$$

- Expand KS orbital ψ_i in Slater basis of valence pseudoatomic orbitals χ_i:

$$\psi_i = \sum_{\mu} c_{\mu i}\chi_i$$

- Calculate DFTB energy by solving a generalized DFTB eigenvalue problem with $\mathbf{H^0}$ computed by atomic and diatomic DFT (due to several approximations, only two-center Hamiltonian matrix elements are explicitly evaluated)

$$\mathbf{H^0 C} = \mathbf{SC}\epsilon \quad \text{with} \quad \begin{aligned} S_{\mu\nu} &= \langle \chi_\mu | \chi_\nu \rangle \\ H^0_{\mu\nu} &= \langle \chi_\mu | \hat{H}_0 | \chi_\nu \rangle \end{aligned}$$

- Determine the repulsion energy E_{rep} as a function of distance by taking the difference of the SCF-LDA cohesive and the corresponding TB band-structure energy for a suitable references:

$$E_{rep} = \left\{ E^{\text{SCF}}_{\text{LDA}}(R) - \sum_i^{occ} n_i \epsilon_i(R) \right\}\Bigg|_{\text{reference structure}}$$

- Calculate the total energy, by using terms obtained in the last to points and summing them according to Eq. (2.86).

2.5.2 Self-Consistent Charge Extension

The procedure described in the previous Section works fine as long as the electron density of the many-body structure is well approximated by a sum of atomic like densities. By the way, when the chemical bonding situation is controlled by delicate charge balancing between different-constituted parts of the system of interest (heteronuclear molecules, polar semiconductors), the standard DFTB lose accuracy in the proper description of the total energy. Therefore, an improved scheme has been set up [81] to extend the approach for the treatment of system where considerable long-range electrostatic interactions are presents. The new procedure, called SCC-DFTB, is schematically reported in the following:

- Explicitly take into account the second order part of the total energy (last ten of Eq. (2.85)). After some rearrangement, it can be expressed as:

$$E_{\text{2nd}} = \frac{1}{2}\sum_{\alpha,\beta}^{N} \Delta q_\alpha \Delta q_\beta \gamma_{\alpha,\beta}$$

  where induced-charges term allows for a proper description of charge-transfer phenomena and $\gamma_{\alpha,\beta}$ account for the Hartree and XC contributions.

- The new DFTB total energy is then:

$$E_2^{\text{DFTB}} = \sum_i^{occ} \langle \psi_i | \hat{H}_0 | \psi_i \rangle + \frac{1}{2}\sum_{\alpha,\beta}^{N} \Delta q_\alpha \Delta q_\beta \gamma_{\alpha,\beta} + E_{rep} \tag{2.87}$$

and here the atomic charges depend on the one-particle wave function ψ_i, thus a self-consistent procedure is required to find the minimum of the expression above

- Induced charge q_α on atom α is determined from Mulliken population analysis:

$$\Delta q_\alpha = \frac{1}{2}\sum_i^{occ} n_i \sum_{\mu\in\alpha}\sum_\nu^N c_{\mu i}c_{\nu i}S_{\mu\nu} - q_\alpha^0$$

- Kohn-Sham eigenenergies are obtained from a generalized, self-consistent SCC-DFTB eigenvalue problem

$$\begin{aligned} \mathbf{H^0C} = \mathbf{SC}\epsilon \quad & \text{with} \quad S_{\mu\nu} = \langle\chi_\mu|\chi_\nu\rangle \\ & \text{and} \quad H^0_{\mu\nu} = \langle\chi_\mu|\hat{H}_0|\chi_\nu\rangle + \frac{1}{2}S_{\mu\nu}\sum_\xi^N(\gamma_{\alpha\xi}+\gamma_{\beta\xi})\Delta q_\xi \end{aligned}$$

2.5.3 Gradient for the DFTB methods

Since we used this technique in the field of molecular dynamic calculations, it is worth mentioning how interatomic forces can be calculated for both $0th$ and $2nd$ order approximations. By taking the first derivative of both final energies (2.86) and (2.87) with respect to the nuclear coordinates, we obtain for the non-SCC formulation

$$F_\alpha = -\sum_i^{occ} n_i \sum_{\mu\in\alpha} c_{\mu i}c_{\nu i}\left[\frac{\partial H^0_{\mu\nu}}{\partial R_\alpha} - \epsilon_i\frac{\partial S_{\mu\nu}}{\partial R_\alpha}\right] - \frac{\partial E_{rep}}{\partial R_\alpha} \tag{2.88}$$

and equivalently for the SCC one

$$\begin{aligned} F_\alpha &= -\sum_i^{occ} n_i \sum_{\mu\in\alpha} c_{\mu i}c_{\nu i}\left[\frac{\partial H^0_{\mu\nu}}{\partial R_\alpha} - \left(\epsilon_i - \frac{H^1_{\mu\nu}}{S_{\mu\nu}}\right)\frac{\partial S_{\mu\nu}}{\partial R_\alpha}\right] && (2.89) \\ &- \Delta q_\alpha \sum_\xi^N \frac{\partial\gamma_{\alpha\xi}}{\partial R_\alpha}\Delta q_\xi - \frac{\partial E_{rep}}{\partial R_\alpha} && (2.90) \end{aligned}$$

3

Novel carbons

Carbon is one of the most amazing elements in nature. Although it represents the fourth more abundant element in the universe, it is present only with a percentage of 0.02 as a rocking-form element in the earth's crust. Strikingly, this relatively "rare element", is the fundamental basement of life on our planet and represents the 43% of our dry body weight. In material science, most of the interest comes from the copious variety of polymorphs that it shows in the solid state despite the apparently simple [He]$2s^2 2p^2$ electronic valence configuration. Numerous phases are exhibited depending on the distinct sp^2, sp^3 or both $sp^2{-}sp^3$ hybridisation: diamond, lonsdaleite, graphite, graphene, nanotubes, fullerenes, amorphous carbon and foams. Among these allotropes mechanical, optical and electronic properties are substantially different and with that carbon-based materials are at the moment outstanding candidates in disparate kind of technological applications.

Diamond is the hardest known natural material with a hardness (H) of 60-120 GPa [85] coming from its crystalline structure of tetrahedrally bonded carbon atoms arranged in a covalent sp^3 lattice. It appears transparent due to its wide fundamental indirect gap of 5.5 eV [86], but unlike most electrical insulators it is an exceptional conductor of heat (thermal conductivity has been measured to be 2200 W/mK [87]). Lonsdaleite is the hexagonal modification of diamond, is less stable and has a smaller electronic gap with respect to its cubic counterpart. On the other hand, it has been recently proved [88], that this carbon allotrope is harder than diamond resisting to an indentation strength, normal to the $< 100 >$ surface, 58% higher than the corresponding value of diamond. Graphite is the modification of carbon which is stable under normal conditions. It has a structure consisting of planar layers, stacked with an ABAB sequence (with stacking faults of ABC stacking sequence) kept together by a weak attractive Van der Waals force. Within each layer, carbon atoms are sp^2 covalently bonded into a characteristic honeycomb lattice. A high electrical conductivity exists only in the plane of the layers, thanks to the delocalisation of π-electrons, and not perpendicular to them. For these reasons graphite appears dark and is a brittle material. Graphene is a single layer of graphite found to be stable just recently [89]. It is a semi-metal with incredibly high carrier mobilities, exceeding 15000 $\mathrm{cm}^2 \cdot \mathrm{V}^{-1} \cdot \mathrm{s}^{-1}$, and extremely low electron resistivity of 10-6 $\Omega\cdot$ cm [90] and therefore it is considered an appealing candidate in electronic applications. From the mechanical point of view, graphene appears also to be one of the strongest materials ever tested, with an incredible Young's modulus of 1 TPa and an extreme tensile strength of 130 GPa [91]. Single-walled carbon nanotubes can be ideally considered as graphene strips rolled up in a cylindrical nanostructure. The electronic properties of these carbon polymorphs are strictly related to the unrolled counterpart. A chiral vector (linear combination of the n, m rolling vectors) discriminates between different nanotubes that can accordingly, be classified as armchair (m=n), zig-zag (n, 0) and chiral (m≠n). For a given (m,n) nanotube, if m=n, the nanotube is metallic, if n−m is multiple of 3 then the nanotube is semiconducting with a narrow band gap, otherwise it is a moderate semiconductor. Multi-walled carbon nanotubes are different kinds of tubes consisting of multiple rolled graphene's layers and they are usually zero-gap materials. In general carbon nanotubes exhibit similar properties to graphene: high carrier mobility, fine gap tunability, extremely high Young's and tensile strength. Thanks to their relatively low production cost, especially in their aggregated state (bundles), they are already used in the mass production of super light and super resistant materials. Amorphous carbon and carbon foams are both consisting of mixture of sp^2 and sp^3 carbon atoms. They display a wide range of properties that are primarily controlled by the different bond hybridizations possible in such materials. Consequently, the different species of amorphous carbon can range from those with high transparency and diamond-like hardness, to those which are opaque, soft and graphitic-like. Applications are diverse and include the use of amorphous carbon in field emission cathodes, microelectromechanical systems (MEMS), electronic devices, medical and optical coatings [92] synthesis. Foams appear as a cluster-assembly of carbon atoms held together in a three dimensional net [93]. It is an inexpensive, lightweight, fire-resistant, impact-absorbing material that can be thermally insulating or conducting, and whose electrical resistivity can be varied over many orders of magnitude.

Despite the great variety of modifications described in the previous paragraph, carbon polymorphism is evidently ways far to be totally explored and the recent effort in the quest of carbon modifications with new or improved properties is the sign of an always vivid interest in these materials. Predicting novel materials and anticipating iterating properties, is a task of top priority. For periodic solids, metadynamics has shown to perform very well, as it allows to efficiently discover novel polymorphs by bridging length- and timescale. In this Chapter we will see how the application of metadynamics techniques can be crucial in the solution of problems related to synthetic products, whose characterisation and structural solution are only partially achieved. In particular, carbon cold compression resulted in a hard and transparent material, distinct from diamond, whose crystal structure remains unresolved. In the following results of metadynamics simulations on carbon cold compression will be illustrated, which leads to novel hard carbon candidates.

3.1 Superhard Carbon Materials: Cold Compression of Graphite

Materials whose hardness is comparable or can exceed that of carbon diamond, are generally referred to as superhard materials [94]. From the experimental point of view, hardness depends mostly on many specificities of the sample, like concentration and type of defects, morphology and grain size, such that the hardness of diamond can vary from 60-120 GPa [85]. In theoretical works, the solid-state problematic is approached with modern computational techniques, where the description of mechanical properties of crystals is based on numerical calculations of the interatomic forces. The systematic quest of a new hard material goes hand in hand with the ability to predict the hardest phase of a certain crystal. In order to find a minimum on the free-energy multidimensional surface varying atomic positions and lattice vectors, we should be able to calculate hardness for a specific crystal structure, which in general represents an involved task. Strictly related to hardness and essential in the study of the mechanical properties of materials, is the bulk modulus B, found for diamond to be 420-460 GPa [94–96]. The correlation between hardness and bulk modulus in the solid-state, has driven theoretical efforts to focus on materials with high bulk moduli in order to identify novel superhard topologies. Bulk moduli are related to the crystal total energy E and the cell volume V, by definition $B = d^2E/dV^2$. Therefore, the natural condition to have a superhard material, is also to find a system with a maximum energy increasing with a minimum cell volume change.

The plausible routes for the synthesis of superhard carbon materials are several. Carbon nanotubes and fullerenes are two excellent building block in nanotechnology. They are considered one- and zero-dimension precursors of new carbon phases, since upon compression and at high temperature they undergo a transition to tridimensional frameworks. Both experimentally [97] and theoretically [98] polymerisation of C_{60} has been observed under pressure. The resulting compound contained large numbers of sp^2 and sp^3 hybridised carbons. Carbon nanotubes aggregates have been also studied extensively [99, 100]. This nanotubular condensed phases can be divided in two groups, the molecular aggregates, where the interaction between the tubes is a Van der Waals one, and aggregates where additional covalent sp^3 bonds are formed. The formation of polymorphs in the latter case, is usually associated with a mild compression. Examples of sp^3 structures deriving from nanotubes compression, have been found also with a molecular dynamic approach [101].

Even though the production of novel superhard carbons via the compression of carbon-based nanomaterials is promising, there are still big controversies over different conversion mechanisms between various forms of carbon. In this Section we will focus on the compression of graphite as a feasible synthetic way towards novel mechanically hard carbons.

3.1.1 Introduction

Compression of graphite at high pressure and temperature produces diamond [102]. Graphite cold compression on the contrary produces a hard and transparent product, different either from cubic or hexagonal diamond [103–109] but not fully characterized so far. Evidences of the phase transition can be found above 14 GPa as obvious changes in the electrical resistivity [110, 111], optical reflectivity and transmittance [103, 104, 112], Raman modes [106, 112, 113], x-ray diffraction (XRD) pattern [105, 107, 108], hardness [108] and the near K-edge spectroscopy [108] occurs. This new phase is, strikingly, a superhard carbon modification as evidenced by the broadening of ruby fluorescence lines and its ability to indent diamond anvils [108]. Many recent studies deal with the nature of this metastable product. Several energetically competing carbon phases were proposed, W- and M-carbon [30], $bctC_4$, as plausible structure solutions, based on estimating transition pressures, goodness of fit of x-ray diffraction data, and band gaps [114–116]. The intrinsic problem of stacking faults in the pristine graphite, and Raman evidence of amorphization suggest a mixture of different phases in the compressed material. The two energetically most preferable candidates so far (M- and W- carbon) can be described (in terms of topology) as corrugated graphene sheets interconnected by an alternating sequence of odd rings (pentagons and heptagons) fused into a $5+7$ pattern. This odd-ring topology formally results from connecting puckered graphene layers aligned in a particular way. On the other hand, further compressing M- or W- carbon can produce different diamond polytypes. Therefore, a larger variety of intermediate hard structures can in principle be expected. To further unfold the structural diversity of sp^3 carbon phases, dedicated approaches are required. The approach was based on metadynamics simulations of structural transformations [23, 24] and topological enumeration to efficiently scan the configuration space.We report on energetic,mechanical, and electronic properties of four unique tetrahedral carbon phases, and insist on a different underlying graphitic pattern connected with the formation of a particular topology. We show how distinct topologies with $5+7$ (odd-odd), but also $5+8$ (odd-even) and $4+6+8$ (even-even-even) ring patterns can do for different mechanical responses.

3.1.2 Methods

Efficient theoretical approaches to hypothetical carbon modifications, based, e.g., on random techniques, genetic (evolutionary) algorithms, or accelerated molecular dynamics (MD) [117] result in important discoveries supporting experiments [118, 119]. In some approaches the use of graph theoretical methods [120] represents a means of increasing the sampling efficiency of carbon configurations. It was indeed a graph-theoretical approach that allowed to derive all possible sp^3 carbon allotropes with four atoms per cell (including the recently rediscovered bct C_4) [120]. Metadynamics, on the other hand, explores the energy landscape along collective reaction coordinates, which in the case of high-pressure polymorphs is represented by the simulation box itself. While metadynamics does not require prior knowledge of the energy landscape under investigation, its sampling efficiency improves on combining many independent runs started from different initial configurations. Additionally, the number of atoms per simulation box is critical for capturing a particular atomic configuration. Diamond and lonsdaleite are important metastable forms of carbon. They can appear in the same metadynamics run only if the number of atoms in the box is at least four and multiples thereof. Similarly, including a minimum of three atoms (or multiples thereof) is sufficient to find a dense carbon with quartz topology, recently suggested from evolutionary algorithms [121].

To systematically include known and find new carbon forms, metadynamics runs were performed on simulation boxes comprising three, four, six, eight, twelve and sixteen carbon atoms, respectively. A similar approach has been shown to work well in connection with plain MD to search for ice phases [122, 123]. Quasirandom

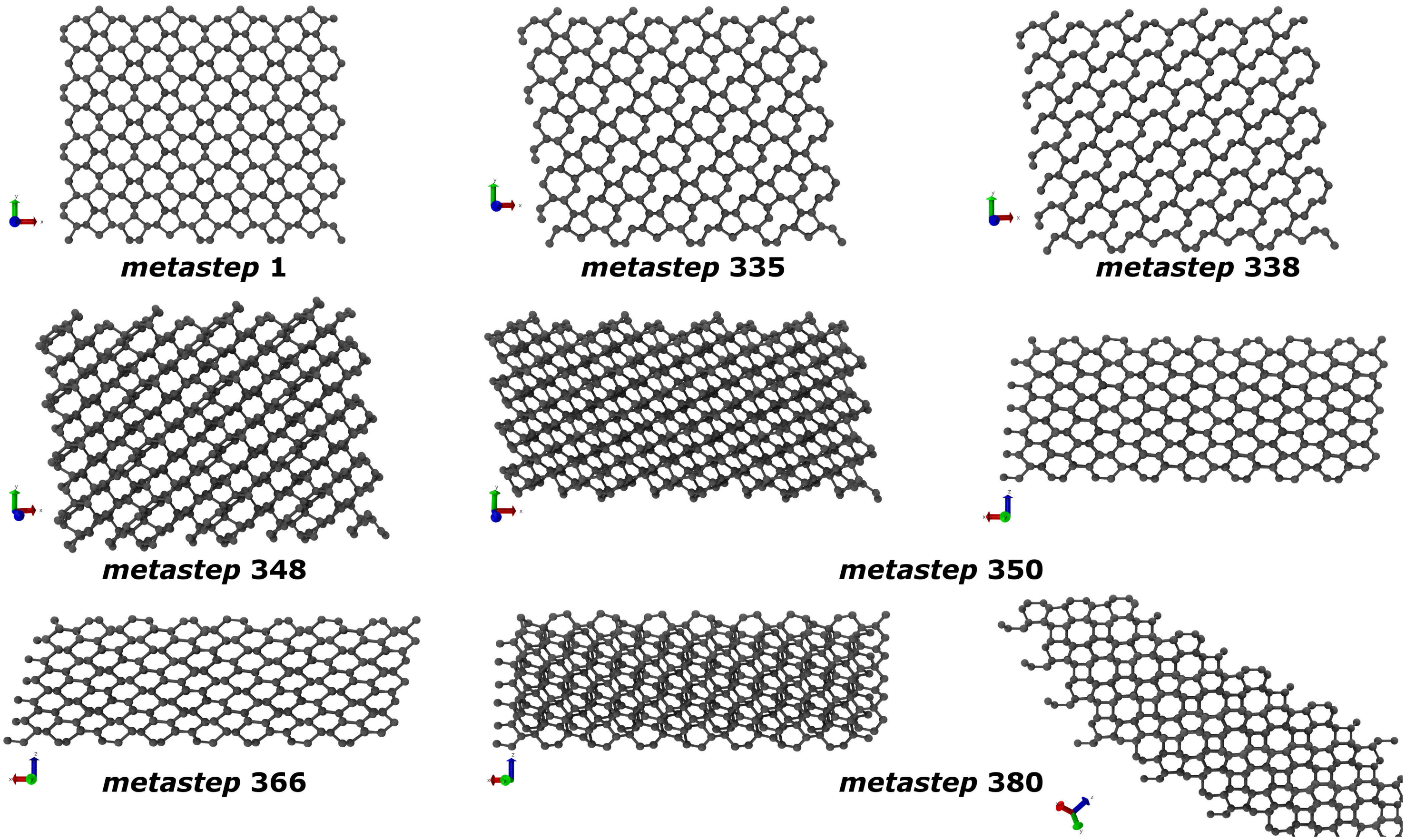
metastep 1
metastep 335
metastep 338
metastep 348
metastep 350
metastep 366
metastep 380

Figure 3.1 – Example of meta-trajectory. From a quasirandom carbon sp^3 structure at metastep 1 to the final oC16-II at metastep 380, different intermediate modifications are encountered. Each metastep corresponds to 0.5 ps for a total of 190 ps of simulation time. At metastep 350 and 380 two snapshots of the same structures are reported with different orientations.

four-connected nets were used as starting configurations. We note here that the application of metadynamics in this case is slightly different from its typical use for simulation of crystal-crystal structural phase transitions, as recently reviewed in Refs. [124] and [125]. While in both cases the simulation cell is used as an order parameter, here one instead starts from a disordered configuration in a small cell and searches for low-energy configurations representing crystalline structures with a given number of atoms in the unit cell. Each run typically consisted of ∼25000 metasteps. Within each metastep MD was performed in the NVT ensemble for at least 0.5 ps at 300 K. An example of a metatrajectory can be seen in Fig. 3.1. In these preliminary scans the tight-binding Tersoff potential [15] was used, which ensured rapid and reliable structure evolution thanks to its good description of sp^2/sp^3 carbons. Molecular dynamics in the NVT ensemble was performed with the CP2K code [126,127]. Structure diversity was judged by calculating vertex symbols, which contain information on all the shortest rings meeting at each atom, and coordination sequences, as implemented in the TOPOS package [128]. Both topological descriptors are widely used, e.g., for the topological characterization of zeolites [128]. Metadynamics trajectories contained many foamlike structures with mixed sp^2-sp^3 carbon atoms and a few sp^3 allotropes. In the case of unique tetrahedral structure types, inferred from their topology, ideal space groups and asymmetric units were identified with the Gavrog Systre package [129] In a subsequent set of runs, candidate structures were studied with respect to their transformability into diamond by metadynamics simulations using SIESTA [130, 131] as the density functional theory (DFT)/MD layer.

In the initial metadynamics runs the choice of large pressure values is less critical. It is rather the number of atoms in the simulation box that decides whether a particular topology can be visited at all within a single metadynamics run. The structures presented in the following were harvested from metadynamics runs performed at 0 and 5 GPa, with six, eight, and sixteen atoms in the simulations box.

On idealized structures variable-cell conjugate-gradient relaxation was performed within density functional theory [generalized gradient approximation (GGA), Perdew-Burke-Ernzerhof (PBE)] as implemented in the SIESTA package [130,131]. Electronic states were expanded by a double-zeta basis set with polarization functions (DZP). Core states ($1s^2$)were described by norm-conserving Troullier-Martins pseudopotentials [132]. The charge density was represented on a real-space grid with an energy cutoff of 200 Ry. Forces were relaxed to less than 0.01eV/Å. Convergence with respect to the number of k points was carefully checked.

3.1.3 Results and Discussion

Small boxes of two and three atoms produced cubic diamond and quartz, respectively. With four atoms both cubic and hexagonal diamond (lonsdaleite) were collected. From six, eight, and sixteen atoms metadynamics three unique structures were found, two monoclinic (mC12 and mC32, Fig. 3.2) and one orthorhombic (oC16-I, Fig. 3.2). From further propagating oC16-I in metadynamics runs at 100 GPa, oC16-II ($Cmmm$) was found.

Their symmetries and structural parameters are summarized in Table 3.1. All phases correspond to a stacking of corrugated graphene layers interconnected by an

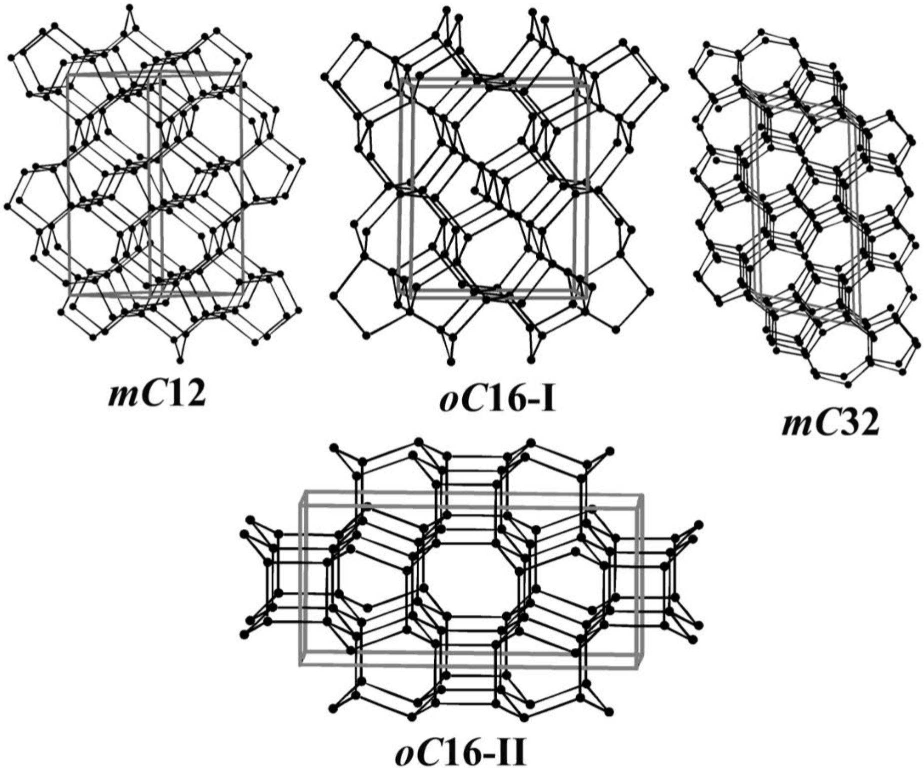

Figure 3.2 – Crystal structures of unique carbon phases. *o*C16-I and *m*C32 are characterized by a 5 + 7 odd-odd ring pattern. *m*C12 represents a distinct 5 + 8 odd-even ring topology, while *o*C16-II contains even rings only, 4 + 6 + 8.

alternating sequence of pentagons and heptagons (*o*C16-I and *m*C32, Fig. 3.2), as for M- and W-carbon. Alternatively, pentagons and octagons, or squares and octagons can also be placed between puckered graphitic layers as it is realized in *m*C12 and *o*C16-II, respectively (Fig. 3.2). Physical properties of the unique allotropes are compared with those of known structures in Table 3.2. In terms of volume per atom, *o*C16-I is the densest, hardest structure, closely followed by *o*C16-II and *m*C12. With a calculated band gap of 4.5 eV, *o*C16-I is also the structure closest to diamond.

The stability of different carbon phases in a wide pressure range is presented in Fig. 3.3. At elevated pressures, the found allotropes become more stable than graphite [Fig. 3.3(b)]. The transition pressures are similar for the *m*C32 and *o*C16-I structures (19.7 and 23.4 GPa, respectively) and much higher (by 10 GPa) for *m*C12. *m*C12 and particularly *o*C16-I are stabilized upon increasing pressure. Furthermore, the stability of *o*C16-I remains basically constant (up to 400 GPa) whereas M- and W-carbon rapidly become energetically unfavorable above 100 GPa. Bulk moduli B_0, were calculated by (least-squares) fitting of the energy versus volume curve to the third-order Birch-Murnaghan equation of state [133]

Table 3.1 – Crystal structure information for novel carbon phases at 0 GPa

Pearson Symbol	Space Group Cell	Wyckoff position	x	y	z
mC12	$C2/c$				
	a= 3.4242; b=8.5218;	$4e$	0	0.80280	3/4
	c= 3.7012; β=138.96°	$8f$	0.84662	0.91988	0.95940
mC32	$C2/m$	$8j$	0.46444	0.68220	0.12680
	a=9.7242; b=4.2932;	$8j$	0.94998	0.68122	0.59997
	c=4.8617; β=103.96°	$8j$	0.30907	0.68472	0.43555
		$8j$	0.18908	0.68609	0.87688
oC16-I	$C222_1$	$4a$	0.43209	1/2	0
	a=6.6698; b=5.5609; c=2.5119	$4b$	1/2	0.08196	1/4
		$8c$	0.81701	0.76297	0.11960
oC16-II	$Cmmm$	$8p$	0.66672	0.68505	0.0
	a=8.8134; b=4.2743; c=2.5281	$8q$	0.58903	0.81586	1/2

$$E(V) = E_0 + B_0 V_0 \left[\frac{V_\mathrm{n}}{B_0'} + \frac{1}{1 - B_0'} + \frac{V_\mathrm{n}^{1-B_0'}}{B_0'(B_0' - 1)} \right], \tag{3.1}$$

where B_0' is the first pressure derivative of the bulk modulus. The energy for a given volume was calculated by doing variable cell conjugated-gradient (fixed volume) relaxation. Simulating the hardness of a material is not a trivial task. The relationship between the atomistic simulation environment and the macroscopic hardness can be related to the hardness of the constituent bonds of the crystal itself as shown in the model of Li K. *et all.* [134]. To describe the nature of chemical bonding they used the electronegativity (EN) that in general provides primary information on microscopic electronic structure during chemical bonding, by which some important bond parameters such as bond length and ionicity can be well described. The derivation of the theoretical equivalent of the Knoop hardness is pretty tedious and here, only the final expression is reported. For a crystal with n types of bonds, its hardness is then expressed as:

$$H_k(\mathrm{GPa}) = \frac{423.8}{V} n \left[\prod_{\mathrm{a,b=1}}^{\mathrm{n}} N_{ab} X_{ab} e^{-2.7\mathrm{f}_{\mathrm{i(ab)}}} \right]^{1/\mathrm{n}} - 3.4, \tag{3.2}$$

where V is the volume and N_{ab} is the number of covalent bonds per unit cell, X_{ab} is the average EN for a specific a-b covalent bond. $e^{-2.7\mathrm{f}_{\mathrm{i(ab)}}}$ is a correction factor for polar covalent bond and the parametric part of the expression above are chosen to well agree with experimental hardness.

Bulk moduli (B_0) and hardnesses (H) are shown in Table 3.2. Strikingly, oC16-I is harder than M- and W-carbon, although it is less stable below 129.2 GPa (Fig. 3.2).

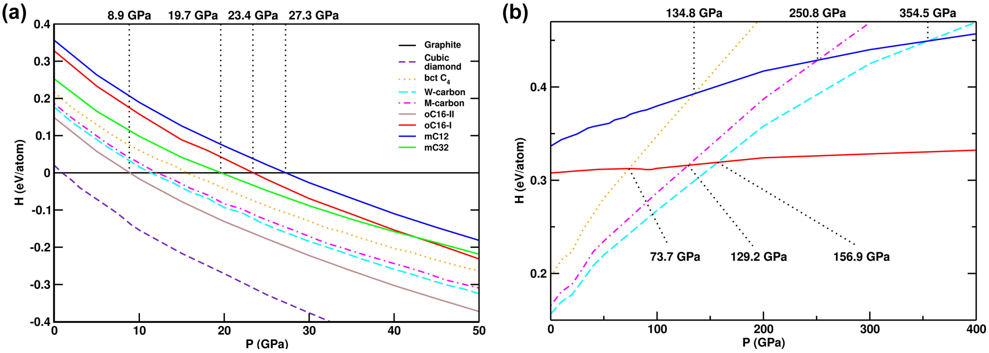

Figure 3.3 – (a) Enthalpies (relative to graphite) of different carbon allotropes; (b) enthalpies of certain sp^3 carbon allotropes (relative to diamond) in the high-pressure range. The colors (lines) are the same as in (a).

On the contrary, *o*C16-II features a lower enthalpy, but its gap is nonetheless intermediate between lonsdaleite and bct C_4, which is structurally also the case. By inspection of Fig. 3.2, the motifs of lonsdaleite and bct C_4 can be easily recognized.

The electronic band structures of *m*C12, *o*C16 (I and II), and *m*C32 at 50 GPa are shown in Fig. 3.4. The structures are insulating with indirect band gaps in the range 2.8-4.5 eV. The gaps do not depend on the pressure up to 50 GPa. All the gaps are smaller than in diamond, but similar to those of *M*- and bct-carbon. Phonon dispersion curves were calculated within a pressure range up to 100 GPa. No

Table 3.2 – Calculated equilibrium volume (V_0), bulk modulus (B_0) and band gaps (E_g). All values refer to zero pressure.

Structure	Method	V_0 (Å^3)	B_0 (GPa)	E_g(eV)	H(GPa)[a]
Diamond	This work	5.79	424.2	4.19	87.3
	PBE (Ref. [121])	5.70	431.1	4.20	
mC12	This work	5.91	399.5	2.82	84.4
oC16-I	This work	5.82	411.0	4.50	85.8
mC32	This work	6.16	384.5	3.47	70.2
oC16-II	This work	5.95	408.4	3.15	84.4
W-carbon	This work	6.04	391.8	4.35	83.1
M-carbon	This work	6.06	392.6	3.51	82.7
	PBE (Ref. [121])	5.97	392.7	3.60	
Bct C_4	This work	6.11	393.4	2.60	82.0
	PBE (Ref. [121])	6.01	411.4	2.70	

---

[a] According to the method of Lyakhov and Oganov (Ref. [135]).

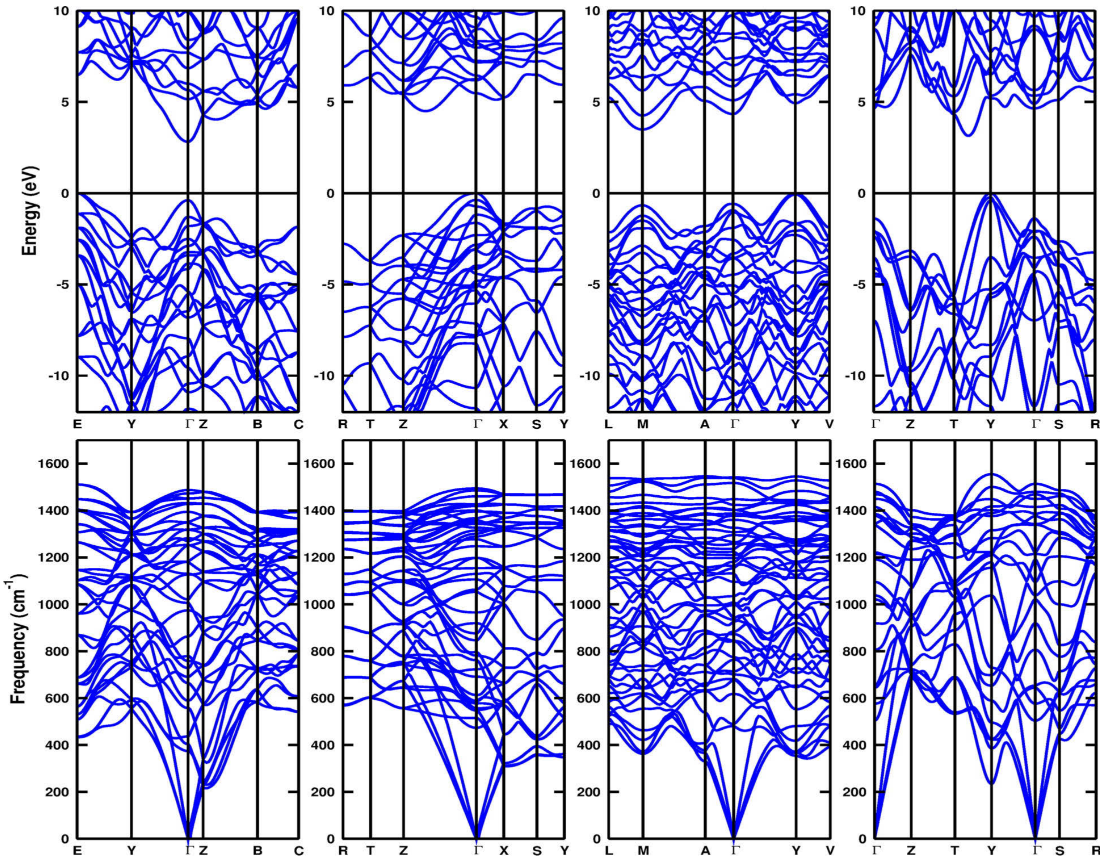

Figure 3.4 – (a) Electronic band structures (top) and phonon dispersion curves (bottom) for (from left to right) *m*C12, *o*C16-I,*m*C32, and *o*C16-II carbon phases.

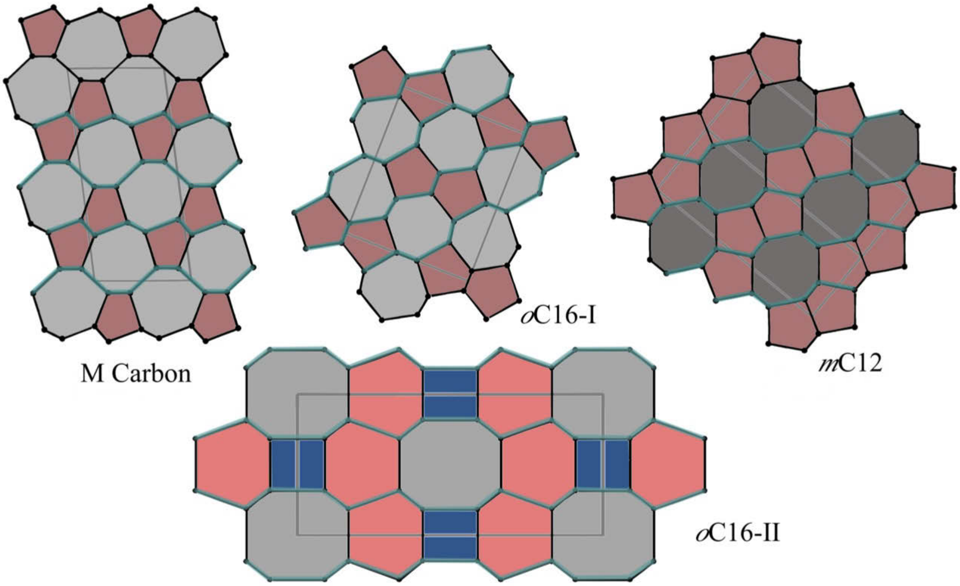

Figure 3.5 – Comparison of M-carbon with oC16-I, mC12, and oC16-II with respect to their underlying puckered graphitic stacking. Layers are highlighted in turquoise(mediumgray).

imaginary frequencies were observed throughout the whole Brillouin zone, confirming the dynamical stability of the intermediate sp^3 structures (Fig. 3.4). Isothermic-isobaric molecular dynamics simulations (300 K, 1 atm, 3 ps) also confirmed the stability of the found phases.

Figure 3.5 shows the relation between the discovered structures and the graphene layer stackings they are derived from. This information can be obtained by deconstructing the structures and looking for graphitic layers within the lattices. For the unique structures, the matching we are presenting is supported by the metadynamics runs, where a (fully or partially) graphitic structure is a typical precursor of the sp^3 phases, along the simulation time coordinate.

In general, we notice that hardness and band gap are diversely distributed among the phases. In the effort of providing an answer to the outstanding question of hard and transparent sp^3 carbon, oC16-II and oC16-I appear as better candidates as hitherto suggested, the former particularly for its stability, for a really transparent band gap and hardness the latter. In Fig. 3.6 we present the simulated x-ray diffraction (XRD) patterns of oC16-I and oC16-II. With reference to the experimental pattern [108], the relevant regions between 8.5° and 10° as well as 14.5° and 17° are similarly populated. Intermediate peaks between 10° and 14° can better distinguish between the two structures, but are, however, depleted in the experiments [108] such that the experimental match is substantially the same for oC16-I and oC16-II.

Since superhard graphite is not synthesized from the gas phase, which would probably produce oC16-II as the only product due to its lowest enthalpy, in the real

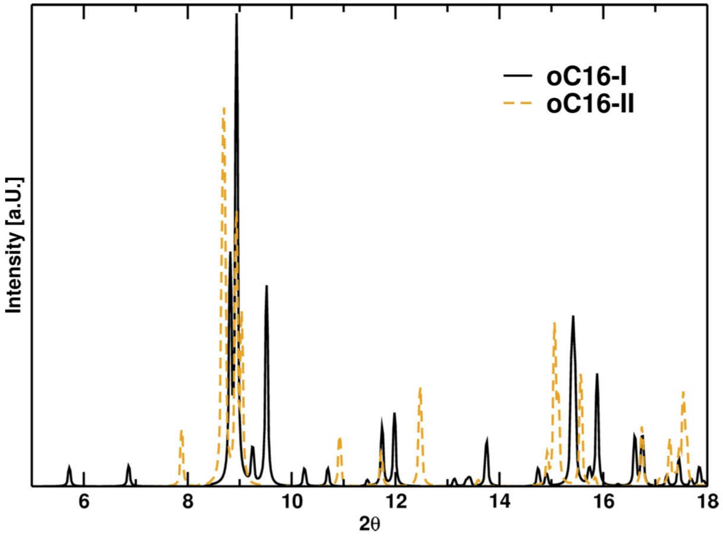

Figure 3.6 – Simulated XRD pattern for *o*C16-I and *o*C16-II carbon phases ($\lambda = 0.3329$Å). The structural data are those of Table. 3.2.

experiment much will depend on the nature of the starting graphitic material, and on the particular nucleation history, which would favor one pattern at the stage of phase growth. In this context, the overall stability of a particular structure is not the only parameter. The importance of this point of view has been recently pointed out [136] and dedicated investigations are ongoing.

In conclusion, we have found four sp^3 carbon materials, derived from combining metadynamics and topology to achieve higher scan efficiency. Two structures, *o*C16-I and *o*C16-II, stand out for hardness and band gaps, and should be considered in assessing the nature of the product of graphite cold compression.

3.2 Hybrid Graphene-based Systems

Since its synthesis, graphene has been widely studied to explore potential applications in nanoelectronics. Its outstanding properties, as the lightest and strongest material, compared with its ability to conduct heat and electricity better than anything else, have stimulated extensive research effort especially to utilize it in electronic devices and related applications [137–139]. Initially this will mean that graphene is used to help improving the performance and efficiency of current materials and substances, but in the future it will also be developed in conjunction with other two-dimensional (2D) crystals to create some even more amazing compounds to suit an even wider range of applications. However, the absence of a fundamental gap in the electronic structure of semimetallic planar graphene [140] prevents its use in most electronic devices. Nonetheless, successful methods to tune the band gap of graphene have been reported in recent studies, for example by using bilayer graphene [141, 142] or by a general 1D confinement [143,144]. In addition, graphene's exceptional properties generate a keen interest in the next step leading to the next generation of Si-based hybrid electronics. Several studies have explored the behavior of the graphene monolayer interacting with different substrates, for example, SiC [145, 146] and SiO_2 [147, 148]. For pure Silicon, except for a recent report of successful exfoliation of graphene on ultraclean Si(111) [149], most studies focused on Si(100) [150,151], where the symmetry difference between the overlayer and the substrate raises concerns about epitaxy and contact quality. Surprisingly, just little work has been done to investigate the interaction between graphene monolayers and the C(111) cubic diamond surface [152] and at the same time, only a limited number of studies have investigated the interaction between the graphitic monolayer and pure Si(111).

3.2.1 Graphene@C(111) Interface

We studied the interaction of a single layer of graphene with a bare surface (111) of diamond. Calculations on the electronic structure and electronic transport in this hybrid system, give evidence for its usefulness in nanoelectronic applications. The C(111) surface of diamond is known to reconstruct [153, 154]. Theoretical [153] and experimental [154,155] evidence indicates that the reconstruction is well characterized by the Pandey π-chain model [156]. Formation of these quasi-1D chains within the topmost layer is accompanied by significant structural and bonding changes in the topmost four layers. A similar reconstruction has also been observed at the (111) surfaces of Si and Ge with the same diamond lattice [157,158]. Recent observations [159] indicate that this surface reconstruction may initiate a step-by-step conversion of the topmost diamond layer to graphene under ultrahigh vacuum conditions at temperatures above 1300 K. The structure of the graphene/diamond hybrid system, which we propose here, is illustrated in Fig. 3.7.

As an alternative to this "bottom-up" perspective in the synthesis of this hybrid system, we propose a complementary "top-down" approach by pressing a graphene monolayer onto the (111) surface of diamond. We believe that covalent graphene-diamond bonding may be induced in this way, since the interface morphology is related to the morphology of graphite that had been subject to cold compression presented in the previews Section [30]. M-carbon [160, 161], a new carbon allotrope that was postulated previously and observed to form as the main product of the cold compression process, displays an alternating sequence of odd carbon rings (pentagons and heptagons) that covalently connect adjacent graphene layers in a characteristic '5 + 7' pattern. This ring pattern connecting the graphene overlayer with the diamond substrate can also be seen in Fig. 3.7 (a), which depicts the graphene-diamond interface in side view.

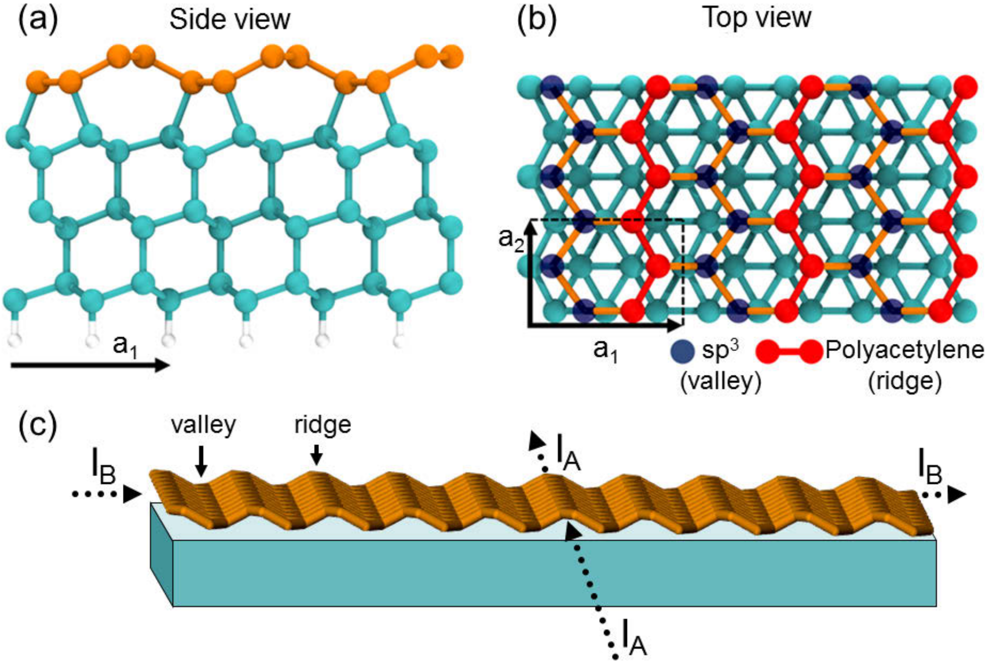

Figure 3.7 – Optimum geometry of wavy graphene on the C(111) surface. (a) Side view and (b) top view of the equilibrium structure of the slab. The ridges of free-standing C atoms forming polyacetylene chains can be distinguished from sp^3 C atoms covalently bonded to the diamond surface. (c) Perspective view of the hybrid system, illustrating transport direction along the ridges (A) and normal to the ridges (B).

3.2.2 Methods of Electronic Transport Calculation

The equilibrium morphology of the graphene-diamond interface was determined by means of *ab initio* Density Functional Theory (DFT) calculations. We found that the small mismatch between graphene and the diamond C(111) surface causes deformation of graphene to a wavy structure. This morphology, which was found to be more stable than planar graphene subject to in-layer compression, contains free-standing polyacetylene chains. Due to a sterically suppressed Peierls distortion, these chains contain delocalized π-electrons at the Fermi level. The polyacetylene chains at the ridges are separated by valley regions, which are covalently σ-bonded to the substrate, as seen in Fig. 3.7. As we will show, this bonding configuration severely affects the electronic structure of pristine, free-standing graphene. The superstructure in the hybrid system causes a pronounced anisotropy in the ballistic transport characteristic of the graphene overlayer. Optimum geometry, stability and electronic properties of the hybrid system were investigated at the DFT level of theory, as implemented in the SIESTA simulation package [130, 131]. The (111) surface was modeled by a 6-layer slab of cubic diamond with the (111) surface, saturated with hydrogen at the bottom and connected to a graphene monolayer at the top. To avoid interactions between the simulation cell replicas, the slabs were separated by a 15 Å thick vacuum region. The optimized geometry is shown in Fig. 3.7 (a). We used the Local Density Approximation to DFT with the Ceperley-Alder [162] exchange-correlation functional as parameterized by Perdew and Zunger [163], norm-conserving Troullier-Martins pseudopotentials [132] and a localized basis set of double-ζ orbitals including polarization functions. The charge density was represented on a real-space grid with an energy cutoff of 200 Ry. Geometries were relaxed until a maximum force of 0.02 eV/Å on the atoms was reached. The reciprocal space was sampled with a fine $60 \times 1 \times 60$ Monkhorst-Pack k-points grid [164]. Quantum transport calculations for this system were performed using the nonequilibrium Green's function scheme (NEGF) as implemented in the TranSIESTA code [165]. The schematic structure in Fig. 3.7 (c) shows the two transport directions we considered, namely (A) along or (B) normal to the ridges of the wavy graphene. We used a two-probe model and calculated electronic transport for the optimized structures using a single-ζ basis that included polarization functions, 200 Ry for the energy mesh cutoff and a $120 \times 1 \times 4$ k-points grid.

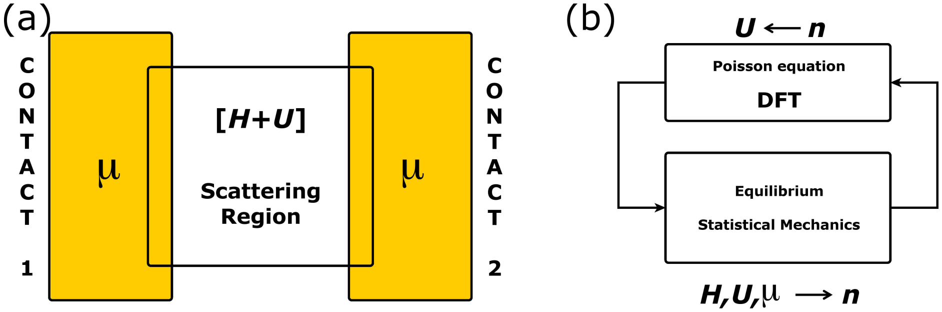

Figure 3.8 – (a) A device in equilibrium. (b) Self-consistent procedure for the analysis of electronic devices in equilibrium. Derivation of the potential can be done applying the Poisson equation, if we referred to a statistical mechanics approach or using directly *ab initio*techniques, as DFT in our case.

Nonequilibrium Green's function formalism has been widely used to study electronic transport at the atomistic level. In this thesis work, just the general outline of the methodology will be reported, but the review of Prof. Supriyo Datta [166] is warmly recommend for a deep and exhaustive insight into the quantum transport theme. For the propose of this thesis the case of device at equilibrium (Fig. 3.8) and out of the equilibrium (Fig. 3.9) will be briefly treated in the following.

Let's consider the Schrödinger-Poisson solver for the system at the equilibrium shown in Fig. 3.8 (a). The first step is to identify an adequate Hamiltonian, H, that gives the proper description of the isolated device. Thus, if the scattering region can be described only with electrons in a parabolic conduction band, then we could use the effective mass Hamiltonian $H \equiv -(\hbar^2/2m)\nabla^2$. In case we need a more accurate description of the valence band, the sp^{3}s* H is more commonly used or, in the case of a molecular conductor, we would use the 6-31 G* Hamiltonian [166, 167]. Once the scattering region is connected to the contacts (leads) there will be some charge transferred into or out of the device, which gives rise to a potential, $U(r)$, that has to be calculated self-consistently. The Schrödinger-Poisson solver (Fig. 3.8 (b)) iterates between the Poisson equation which gives the potential for a given electron density $n(r)$ relative to that required for local charge neutrality (which is equal to the ionized donor density, $N_D(r)$ in an n-type semiconductor)

$$\nabla \cdot (\epsilon \nabla U) = q^2[\mathrm{N_D} - n] \tag{3.3}$$

and the law of equilibrium statistical mechanics which tells us that the electron density $n(r)$ for a given potential profile $U(r)$ is obtained from

$$n(r) = \sum_{\mathrm{i}} |\Psi_{\mathrm{i}}(r)|^2 f_0(\epsilon_{\mathrm{i}} - \mu) \tag{3.4}$$

by filling up the eigenstates $\Psi_i(r)$ of the Schrödinger equation

$$[H + U]\Psi_{\mathrm{i}}(\mathrm{r}) = \epsilon_{\mathrm{i}}(\mathrm{r})\Psi_{\mathrm{i}}(\mathrm{r}) \tag{3.5}$$

according to the Fermi function

$$f_0(E - \mu) \equiv (1 + \mathrm{e}^{\frac{E-\mu}{k_{\mathrm{b}}T}})^{-1} \tag{3.6}$$

μ being the Fermi level. In our case, since we approach the electronic transport problem with a DFT level of theory, the Poisson potential is supplemented with an exchange-correlation potential $U_{xc}(r)$. The problem we wish to address in this work is that of a scattering region connected to two contacts with two different Fermi levels μ_1 and μ_2 (Fig. 3.9 (a)). What is the electron density, n? We can no longer use eq. 5.4 since there are two different Fermi levels. It would seem that the energy levels in the device would be occupied with a probability f_i which has a value intermediate between the source Fermi function $f_0(\epsilon_i - \mu_1)$ and the drain Fermi function $f_0(\epsilon_i - \mu_2)$:

$$n(r) = \sum_{\mathrm{i}} \Psi_{\mathrm{i}}(r)\Psi^*_{\mathrm{i}}(r) f_{\mathrm{i}} \tag{3.7}$$

However, this problem requires a more sophisticated approach. Different states can be occupied in a correlated manner described by a density matrix,

$$n(r) = \sum_{\mathrm{i,j}} \Psi_{\mathrm{i}}(r)\Psi^*_{\mathrm{j}}(r)\rho_{\mathrm{ij}} \tag{3.8}$$

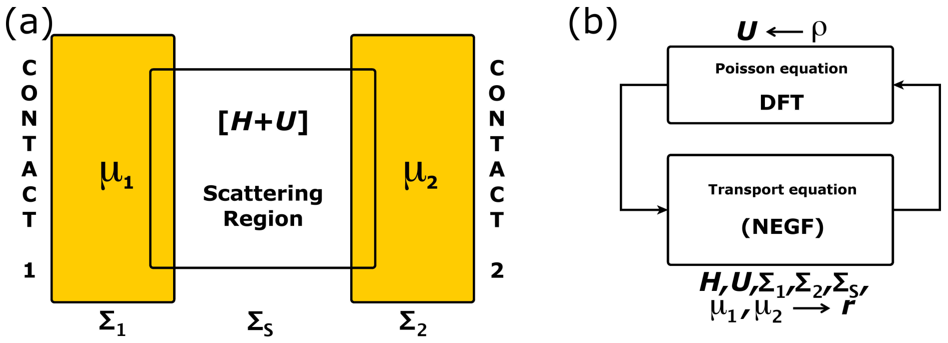

Figure 3.9 – (a) A device driven out of equilibrium by two contacts with different chemical potentials μ_1 and μ_2. (b) Self-consistent procedure for determining the density matrix ρ from which all quantities of interest (electron density, current intensity, etc) can be calculated.

The central issue in non-equilibrium statistical mechanics is to determine this density matrix ρ_{ij}.

The general procedure of the iterative algorithm to get physical quantities of interest (for example the current intensity) is shown in Fig. 3.9 (b). Once the the potential of the entire device is obtained with a DFT approach, it is used together with the total Hamiltonian $H = H_1 + H_S + H_2$, the self-energies $\Sigma_1, \Sigma_S, \Sigma_2$ (which define the interaction between the contacts and the scattering region) and the chemical potentials μ_1 and μ_2 in the NEGF formalism to get a new density matrix for this system out of the equilibrium. The procedure is then iterated until the converge of the density is reached.

In the following only equilibrium cases will be treated. The TranSIESTA code uses essentially Green's Function to couple the formally semi infinite contacts to the scattering region [165, 168] and then calculates the density matrix that will define the new potential. The procedure is, again, iterative and at the end, the final transmission probability is calculated using the Landauer-Büttiker formula [169].

3.2.3 Results and Discussion

The optimized graphene/C(111) superlattice with the smallest 2×1 cell of the substrate is shown in Fig. 3.7. The rectangular surface unit cell, delimited by the lattice vectors $\mathbf{a}_1$ and $\mathbf{a}_2$, contains 4 carbon atoms in the graphene layer, 12 C atoms in the substrate slab representing cubic diamond, and 2 H atoms saturating the bottom of the C(111) slab. In order to identify the most stable adsorption geometry, we have investigated the relative stability of 2×1, 4×1 and 6×1 supercells of the substrate lattice that provide additional structural degrees of freedom. Our results show that the '5+7' bonding topology associated with covalent graphene-diamond bonds occurs in all adsorption geometries, including the largest supercells. Carbon atoms in the valleys of the wavy graphene structure change their character from sp^2 to sp^3 upon forming covalent bonds to the diamond surface, with 1.59 Å long bonds comparable to 1.54 Å long covalent bonds in cubic diamond. The C-C bond length in detached graphene ridges is close to 1.43 Å. This indicates presence of sp^2 hybridized carbon chains, where a sterically suppressed Peierls distortion keeps the electrons delocalized.

Deforming planar graphene to a wavy structure to achieve epitaxy requires an energy investment of ≈0.74 eV, which is less than when subjecting the layer to in-plane compression. Buckling brings along a significant energy gain, since it is accompanied by the formation of strong σ bonds between the overlayer and the substrate. The attachment process is exothermic, thus thermodynamically viable, if $\Delta E = E_{\text{tot,graphene/diamond}} - (E_{\text{tot,graphene}} + E_{\text{tot,diamond}}) < 0$. In this expression, $E_{\text{tot,graphene/diamond}}$ is the total energy of the relaxed wavy graphene on C(111), $E_{\text{tot,graphene}}$ that of the optimized graphene monolayer, and $E_{\text{tot,diamond}}$ represents the total energy of the C(111) slab. We found it useful to define the average adsorption energy per carbon atom as $E_{\text{ad}} = \Delta E/N_{\text{c}}$, where N_{c} is the number of carbon atoms in the graphene layer per unit cell. Our numerical result $E_{\text{ad}} = -0.151$ eV indicates that the energy invested in the buckling process is more than compensated by the formation of strong σ bonds. To get a deeper insight into the energetics of this system, we compared the stability of our structure to that of previously proposed alternative geometries [152] H, T and B that contain planar graphene in the overlayer. We find $E_{\text{ad}} = -0.0208$ eV for the 'staggered configuration' H, $E_{\text{ad}} = -0.0196$ eV for the 'eclipsed configuration' T, and $E_{\text{ad}} = -0.0185$ eV for the 'shifted configuration' B, in qualitative agreement with Ref. [152]. The significantly stronger bonding found for wavy graphene on diamond confirms that our proposed graphene-C(111) hybrid structure should better represent the observable equilibrium geometry.

Next, we have carefully analyzed the electronic structure and determined ballistic electron transport in the optimized structure with the smallest 2×1 unit cell. We found the corrugation of about 0.73 Å of the wavy graphene normal to the surface to be enough to electronically decouple the ridge atoms in wavy graphene from carbon atoms at the surface of diamond. The electronic density of states (DOS) and projected density of states (PDOS) at ridge and valley sites of graphene in our system are shown in Fig. 3.10. In comparison to the DOS of planar graphene, shown by the dotted blue line in Fig. 3.10 (a), which reflects the Dirac cone structure at E_F, the DOS of wavy graphene, shown by the dashed red line in Fig. 3.10 (a), is higher near near E_F due to the reduced $pp\pi$ interactions in the direction normal to the ridges. Furthermore, peaks in the DOS at ± 2 eV from the Fermi level, reminiscent of van Hove singularities, are an indication of quasi-1D confinement. More detailed insight can be gained by analyzing the projected density of states for carbon atoms at the ridges and in the valleys of the wavy graphene layer, defined in Fig. 3.10 (c). Careful inspection of the projected density of states reveals that the two inequivalent sites contribute in a similar way to the total DOS. Unlike planar graphene, where the region around E_F has exclusive p_z character, we find a significant contribution of p_x orbitals to electronic state near E_F in wavy graphene. When wavy graphene attaches to diamond, C atoms in the valley bond covalently to the substrate and do not contribute electronically to states near the Fermi level. As seen in Fig. 3.10 (b), the character of states near E_F becomes dominated by p_z orbitals of C atoms at the ridge. These contributions add up to the total DOS of the hybrid system, shown by the black solid lines in Figures 3.10 (a) and 3.10 (b). Unlike semimetallic graphene or insulating diamond, the hybrid graphene/diamond system is metallic. The van Hove-like singularities in

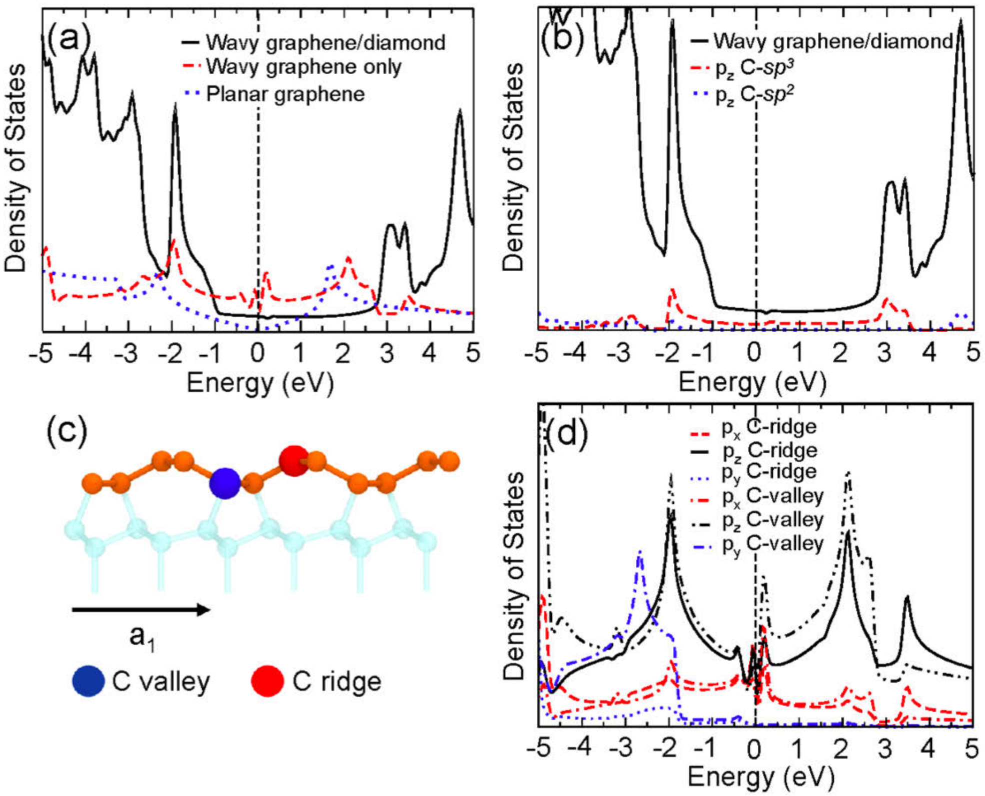

Figure 3.10 – Electronic structure of graphene/C(111). (a) Electronic density of states (DOS) of graphene/C(111) (solid black line), free-standing wavy graphene (dashed red line) and free- standing planar graphene (dotted blue line). (b) DOS of graphene/C(111) (solid black line) and the projected electronic density of state (PDOS) onto p_z orbitals of graphene C atoms at the ridge (dashed red line) and in the valley (dotted blue line). (c) Characterization of the ridge and valley sites in the side view of the graphene/C(111) structure. (d) PDOS associated with p_x (red lines), p_y (blue lines) and p_z (black lines) states of graphene C atoms in valley and ridge sites. $E = 0$ denotes the position of the Fermi level in (a), (b) and (d).

the DOS near the Fermi energy indicate presence of 1D structures, which we identify as chains of carbon atoms along the ridge with a delocalized π-electron system.

Results of our quantum transport calculations are summarized in Figure 3.11. We considered two transport geometries, namely geometry A in Figs. 3.11 (a-c) describing transport along the ridges and geometry B in Figs. 3.11 (d-f) describing transport normal to the ridges. We used semi- infinite leads consisting of two cell replicas of free-stranding wavy graphene in geometry A and of one cell replica in geometry B. The scattering region was constructed of three unit cells of wavy graphene on C(111). One additional wavy graphene cell has been added at each side in order to reduce unwanted backscattering effects at the lead-scattering junction. The dangling bonds of the diamond slab have been saturated with H atoms. In our calculation, both leads and the scattering region are periodic normal to the transport direction.

The calculated transmission spectra G(E) of the graphene/diamond system are compared to transport results for free-standing wavy and planar graphene in Fig. 3.11 (c) for geometry A and in in Fig. 3.11 (f) for geometry B. Our results for geometry A indicate a small increase in transmittance along the ridges of free-standing wavy graphene in comparison to free-standing planar graphene in a ≈0.5 eV wide energy window around EF. We observe transmittance reduction outside this energy window. Further suppression of transmittance occurs, when wavy graphene is bonded to the diamond substrate, indicating that the C(111) surface acts as a weak scatterer. Nonetheless, the system remains metallic, as already suggested by our DOS results presented in Fig. 3.10(a). As anticipated, the 1D transport channel is formed by the π-electron system of the carbon chains along the ridges.

The situation is dramatically different in geometry B, where the transport direction

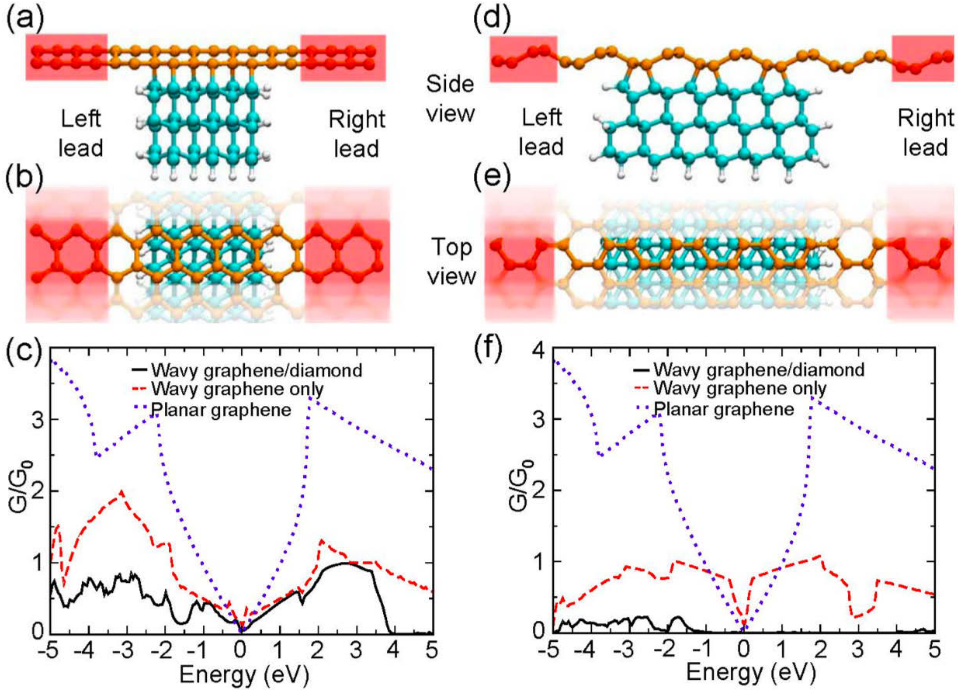

Figure 3.11 – Geometry and numerical results of quantum transport calculations. Transport along the ridges in geometry A (a-c) is compared to transport normal to the ridges in geometry B (d-f). (a,d) Top and (b,e) side view of the structure used in the calculations. A central graphene/C(111) scattering region is connected to two semi-infinite leads consisting of free-standing wavy graphene. (c,f) Transmission spectra with drain-source bias $V_{ds} = 0$ for the two geometries, with $E = 0$ representing carriers injected at the Fermi level.

is normal to the ridges. Also in this geometry, our results in Fig. 3.10 (f) indicate enhanced transmittance of free-standing wavy graphene near E_F in comparison to free-standing planar graphene. This enhancement can be attributed to the contribution of $pp\sigma$ states, notably the p_x orbitals, to the DOS of wavy graphene at the Fermi energy. Attaching the wavy graphene overlayer to the C(111) surface changes the transport behavior drastically, as it opens a $\approx$5.5 eV wide transport gap, which is very close to the fundamental band gap of diamond. This strong change indicates that the diamond substrate, when covalently bonded to the wavy graphene overlayer, acts as a strong scattering center that efficiently suppresses transport near E_F in geometry B. Hence, the hybrid system displays a striking anisotropy in its transport behavior. In the direction along the ridges, the graphene/diamond system behaves as a metal due to the conducting π-system eigenchannels. In the direction normal to the ridges, the system behaves as a wide-gap insulator, since the conducting channels are separated by insulating regions containing only sp^3 carbon atoms in the direction of transport.

To summarize, in this Section our study on the equilibrium morphology, stability and electronic structure of the interface between a graphene monolayer and the diamond C(111) surface using *ab initio*density functional calculations has been reported. We found that the optimum epitaxial interface morphology contains a wavy graphene structure that is covalently bonded to the substrate. The detached ridges of the wavy graphene overlayer behave electronically as free-standing polyacetylene chains with delocalized π-electrons, separated by regions with sp^3 carbon atoms covalently bonded to the (111) diamond surface. We have also performed quantum transport calculation in order to elucidate how the deformation of the graphene layer and its bonding to the diamond substrate changes its conductance in comparison to a free-standing planar graphene monolayer. Our results show a strong anisotropy in the transmittance, with high carrier mobility along the ridges and a wide transport gap in the direction normal to the ridges. The high mobility regions at the ridges are polyacetylene chains containing delocalized ? electrons, These regions are separated by graphene valleys containing sp^3 carbon atoms that are covalently bonded to the diamond substrate. The intriguing, strongly anisotropic transport properties qualify the hybrid graphene-C(111) system as a viable candidate for a new generation of high-performance electronic nanodevices for applications including topological logic switches in future nanoscale circuitry.

3.2.4 Graphene@Si(111) Interface

In the previous Section we presented our study on the hybrid graphene-C(111) system and we identified it as a possible candidate for the next generation of electronic devices. Despite the outstanding transport features, it is well known that the high cost of production of pure diamond, prevents the possibility of electronic application based uniquely on carbon diamond. The role of Si-based devices, in this scenario, is still of primary importance. However, it is now common knowledge that Moore's law, which has correctly represented the unprecedented progress of Si-based electronics for decades, can no longer be sustained as device dimensions approach the atomic scale [170]. One way to proceed next is to augment Si circuitry by taking advantage of the exceptional carrier mobility in graphitic nanostructures including graphene or nanotubes [171, 172]. Successful utilization of hybrid devices involving graphene and silicon necessitates the microscopic understanding of the morphology, electronic structure, and transport at the Si-graphene interface.

Here we study the electronic properties and quantum conductance at the graphene-Si(111) interface. We use *ab initio*density functional theory to determine the equilibrium morphology of the interface and the nature of Si-graphene bonds. We find that the lattice mismatch between graphene and Si(111) can be accommodated by buckling the graphene overlayer and creating an array of free-standing graphene strips separated by regions covalently bonded to the substrate. Our ballistic transport calculations identify the effect of a covalently connected Si substrate on transport in the graphene overlayer and describe quantitatively the injection of carriers across the interface.

3.2.5 Methods

To gain insight into the equilibrium structure, stability, and electronic properties of a graphene monolayer on the Si(111) surface, we performed density-functional theory calculations as implemented in the SIESTA code [130, 131]. The surface was represented by a periodic array of six-layer Si(111) slabs separated by an 8 Å thick vacuum region, which were connected to a graphene monolayer at the top and terminated by hydrogen at the bottom, as seen in Fig. 3.12 (a). We used the Ceperley-Alder [162] exchange-correlation functional as parametrized by Perdew and Zunger [163], norm-conserving Troullier-Martins pseudo-potentials [132], and a double-ζ basis including polarization orbitals. The reciprocal space was sampled by a fine grid [164] of $6 \times 12 \times 1$ k-points in the Brillouin zone of the primitive surface unit cell and its equivalent for larger supercells. We used a mesh cutoff energy of 100 Ry to determine the self-consistent charge density, which provided a precision in total energy of ≤ 2 meV/atom. Transport properties were investigated using the nonequilibrium Green's function approach as implemented in the TranSIESTA code [165]. Ballistic transport calculations for optimized structures were performed using a single-ζ basis with polarization orbitals, a 200 Ry mesh cutoff energy, and a $4 \times 60 \times 1$ k-points grid.

3.2.6 Results and Discussion

Even though silicon and carbon are very similar in many ways, graphene is not epitaxial with any silicon surface. Previous theoretical studies of graphene on the Si(100) surface [150], which has a different symmetry, have assumed that the large lattice mismatch may be accommodated by stretching or compressing laterally the graphene overlayer. Since the in-plane compressibility of graphene is rather low, the energy cost to enforce epitaxy in this way by far exceeds the energy gained by graphene bonding to silicon, indicating that graphene should not bond to Si(100).

Also on the Si(111) surface, which has the same sixfold symmetry as the graphene overlayer, there is a large 11.6% lattice mismatch between the overlayer and the substrate. On this substrate, however, there is an alternative way to maintain epitaxy that does not involve in-layer compression and still benefits from interface bonding.

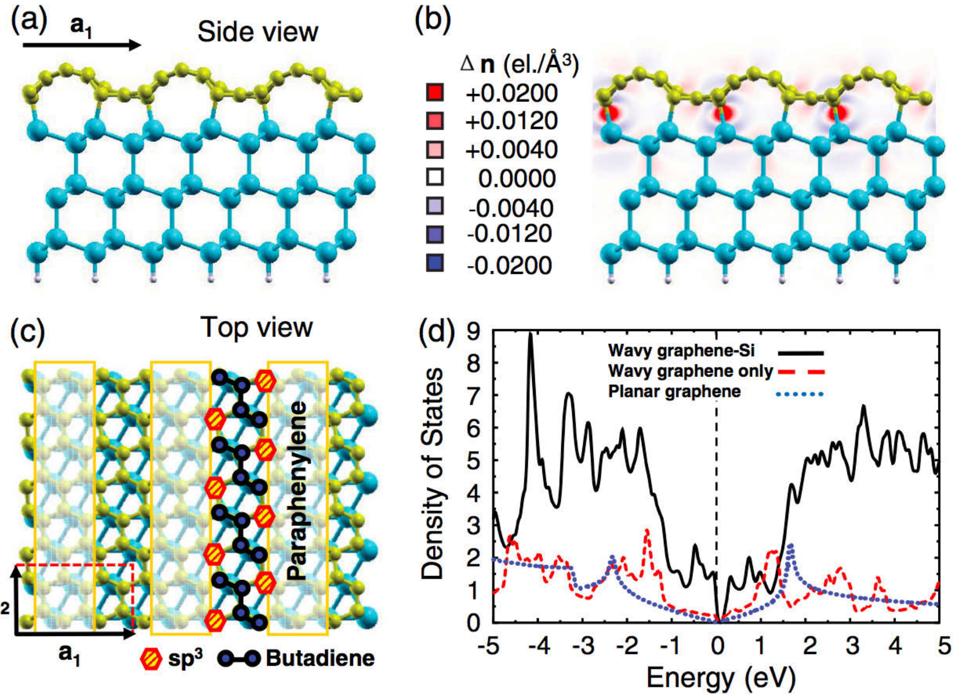

Figure 3.12 – Optimum geometry and electronic structure of wavy graphene on the Si(111) surface. (a) Equilibrium structure of the slab and (b) electron density difference $\Delta n(\mathrm{r})$ in a plane normal to the surface. (c) Top view of the structure. The ridges of C atoms forming paraphenylene chains can be distinguished from sp^3 C atoms covalently bonded to Si and C atoms in butadienelike units that are not covalently bonded to Si. $\mathbf{a}_1$ and $\mathbf{a}_2$ are the Bravais lattice vectors defining the 2×1 surface unit cell. (d) Electronic density of states (DOS) of wavy graphene-Si(111) (solid black line), wavy graphene only (dashed red line), and planar graphene (dotted blue line). $E = 0$ denotes the position of the Fermi level.

When attached to Si(111), the graphene overlayer with the larger lattice constant may buckle and transform to a superlattice that we call wavy graphene. The graphene-Si(111) superlattice with the smallest 2×1 unit cell is shown in Figs. 3.12 (a) and 3.12 (c). We should emphasize that the non-planar, wavy structure of graphene in our study is stabilized by strong bonds between sp^3 hybridized atoms in the overlayer and the substrate, which is very different from thermodynamically induced rippling observed in graphene on metal substrates [173]. Whereas the bare Si(111) surface is known to undergo a 7×7 surface reconstruction [174], no such structural change occurs at the graphene-Si(111) interface, since the dangling bonds of surface silicon atoms have been saturated by forming strong σ bonds to the graphene overlayer, as seen in Fig. 3.12 (b). The rectangular surface unit cell delimited by the lattice vectors $\mathbf{a}_1$ and $\mathbf{a}_2$ contains 12 C atoms in the graphene layer, 12 Si atoms arranged in six slab layers, and two terminating H atoms.

The major benefit of the wavy structure is the coexistence of ribbon-shaped conducting graphene ridges that are detached from the substrate and separated by ribbons of carbon atoms bonded to the substrate, enabling carrier injection across the interface. The detached graphene ridges contain embedded paraphenylene chains partly resembling polyperinaphtalene and are labeled in this way in Fig. 3.12 (c). The separating regions contain sp^3 carbon atoms covalently connected to the Si substrate and short carbon chains resembling butadiene.

Clearly, changing the period of the wavy graphene structure offers a new structural degree of freedom to the graphene overlayer. We have investigated the relative stability of 2×1, 4×1, and 6×1 supercells of the graphene-Si interface by keeping the bottom four Si layers of the slab in the optimum Si bulk geometry. Contrary to the case of the graphene-C(111) system, presented in the previous Section, here the situation differs considering supercells of different size. Our numerical results allow for a quantitative analysis of all energy terms associated with the Si-graphene bonding. We find that especially the sp^3 carbon atoms bind strongly to Si atoms directly underneath, with the 2.0 Å long Si-C bonds comparable to the 1.9 Å long covalent bonds in SiC. The covalent bond character is also reflected in the electron accumulation in the bond region, as seen in the electron density difference $\Delta n(r) = n_{\mathrm{tot}}(r) - n_{\mathrm{graphene}}(r) - n_{\mathrm{Si(111)}}(r)$ plotted in Fig. 3.12 (b). If we were to attribute the entire graphene-Si interaction to these bonds, each of them would contribute 1.62 eV towards the binding energy. Obviously, maximizing the number of such C-Si bonds is beneficial for the stability of the interface.

To achieve epitaxy, there is an initial energy investment associated with the transformation of a free graphene monolayer to a wavy graphene structure matching the substrate. Even though buckling is less costly than in-plane compression, the net energy cost cannot be neglected due the large flexural rigidity and low in-plane compressibility of graphene. We find that this energy investment decreases with increasing lattice constant $\mathbf{a}_1$ or the corresponding size n of the $n \times 1$ supercell, favoring large supercells. The relatively most stable structure of graphene bonded to silicon results from an energetic compromise between maximizing the number of Si-C bonds and minimizing the buckling energy. Because of the dominant role of the strong Si-C bonds, we find that the structure with the small 2×1 supercells represents the best energetic compromise.

Graphene will form stable bonds with the silicon substrate if the adsorption process is exothermic, i.e., if $\Delta E = E_{\mathrm{tot,graphene/Si}} - (E_{\mathrm{tot,graphene}} + E_{\mathrm{tot,Si}}) < 0$. As in the case of the gaphene-C(111) system, $E_{\mathrm{tot,graphene/Si}}$ is the total energy of the relaxed wavy graphene structure on Si(111), $E_{\mathrm{tot,graphene}}$ is that of the equilibrium planar graphene monolayer, and $E_{\mathrm{tot/Si}}$ is the total energy of the relaxed Si(111) surface. Defining the average adsorption energy per carbon atom as $E_{\mathrm{ad}} = \Delta E/N_{\mathrm{c}}$, where N_{c} is the number of carbon atoms per unit cell, we find $E_{\mathrm{ad}} = 0.45$ eV in the optimum case, as the buckling energy dominates over the covalent bonds at the interface. We also found that partial hydrogenation of the graphene layer makes the formation of a stable graphene superlattice on Si(111) energetically much more affordable, as it reduces the adsorption energy penalty down to $E_{\mathrm{ad}} = 0.12$ eV in case of four H atoms per C_{12} unit cell. We expect that additional constraints, such as a low density of defects including substitutional impurities and vacancies at the interface, should turn $E_{\mathrm{ad}} > 0$, yielding a stable bonding geometry between graphene and the Si(111) surface. Indeed, Presence of chemisorbed hydrogen reduces the flexural rigidity of graphene and thus the buckling energy, while affecting to a lesser degree the graphene-Si bonds. The equilibrium structure of the 2×1 graphene overlayer on Si(111) with different numbers of hydrogen atoms per unit cell is presented in Fig. 3.13.

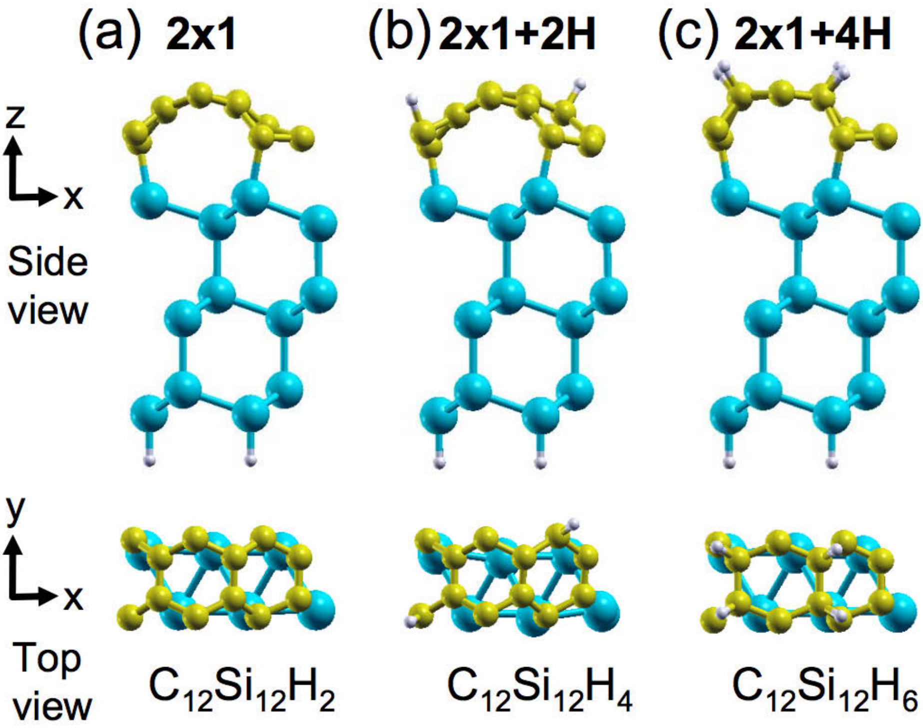

Figure 3.13 – Top and side view of the relaxed geometry of 2×1 supercells of wavy graphene on the Si(111) surface at different H coverages.

In the following, we will turn to the electronic structure and transport in the optimum 2×1 superlattice with $C_{12}Si_{12}H_2$ unit cells shown in Fig. 3.12. The calculated 1.56 Å corrugation of the wavy graphene normal to the surface is sufficient to electronically decouple the carbon atoms in the paraphenylene chains (constituting the ridges) from the Si substrate, whereas the remaining carbon atoms in the troughs should be strongly perturbed by the vicinity of Si.

The electronic density of states (DOS) of graphene in different environments is shown in Fig. 3.12 (d). In comparison to the free-standing graphene monolayer, which is a semimetal with a smooth DOS near E_F, the DOS of free-standing wavy graphene displays more peaks that resemble van Hove singularities in 1D systems and are caused by a reduction of $pp\pi$ interactions normal to the ridges. Apart from the only 0.03 eV wide band gap near E_F, the DOS of wavy graphene is enhanced with respect to its planar counterpart in the ≈2 eV wide energy range around E_F that is significant for transport. An even larger DOS enhancement near E_F is seen for wavy graphene bonded to the Si(111) surface. Interaction with the substrate increases the fundamental band gap width to 0.13 eV, in analogy to graphene in contact with other semiconductor surfaces including SiC [175] and diamond [152]. Results of our Mulliken population analysis indicate a small electron transfer from silicon to graphene. Such a charge redistribution, which is expected based on the higher electronegativity of C as compared to Si, turns the interface to a *pn* junction. We find that the extra 0.2 electrons per carbon atom are distributed rather evenly across the wavy graphene layer. These results all indicate that the hybrid graphene-Si(111) system may display interesting quantum transport behavior.

In order to determine how contact to a silicon substrate may affect conduction in a graphene monolayer, we performed quantum transport calculations of wavy graphene on Si(111) and present our results in Fig. 3.14. As in the case of graphene-C(111), we distinguished transport normal to the ridges in transport geometry A shown in Figs. 3.14 (a) and 3.14 (b), from transport along the ridges in transport geometry B shown in Figs. 3.14 (d) and 3.14 (e). We constructed the semi-infinite leads of wavy graphene using one cell replicas in geometry A and two cell replicas in geometry B. The scattering region consists of three replicas of the 2×1 wavy graphene-Si(111) unit cell augmented by one additional unit cell of wavy graphene on each side to properly describe the evanescence of scattering states into the lead region. All Si dangling bonds on the surfaces perpendicular to the transport direction have been saturated by H atoms. Both leads and the scattering region are infinitely wide and periodic normal to the transport direction.

Transmission spectra $G(E)$ of a contiguous graphene layer in different environments are shown in Fig. 3.14 (c) for transport geometry A and in Fig. 3.14 (f) for transport geometry B. In both cases, we compare the quantum conductance of wavy graphene in contact to Si(111) to that of free-standing wavy or planar graphene monolayers. Our results for geometry A indicate that transmittance normal to the graphene ridges in free-standing wavy graphene is reduced to some degree in comparison to planar graphene. The transmission spectrum of wavy graphene displays more peaks than that of planar graphene, reflecting the changes in the DOS in Fig. 3.12 (d) including a narrow transport gap of $\leq$0.05 eV. Si acts as a weak scatterer when connected to wavy graphene. This further reduces the conductivity of the wavy graphene layer and opens an ≈0.35 eV wide transport gap, somewhat larger than the 0.13 eV wide fundamental band gap of the system seen in Fig. 3.12 (d).

Electron transmission along the ridges of wavy graphene in transport geometry B shown in Fig. 3.14 (f) is greatly enhanced with respect to geometry A. Especially impressive is the conductivity enhancement in a free-standing wavy graphene monolayer over its free-standing planar counterpart within a broad energy range, with the exception of a very narrow transport gap found also in geometry A. Even though attachment of the wavy graphene monolayer to Si reduces the net conductance of the system, this conductance is still higher than that of free-standing planar graphene in the ≈1 eV wide energy window near E_F that is most important for transport.

Results in Fig. 3.14 for transport geometry A and B confirm our hypothesis about the formation of anisotropic preferential transmission channels in wavy graphene,

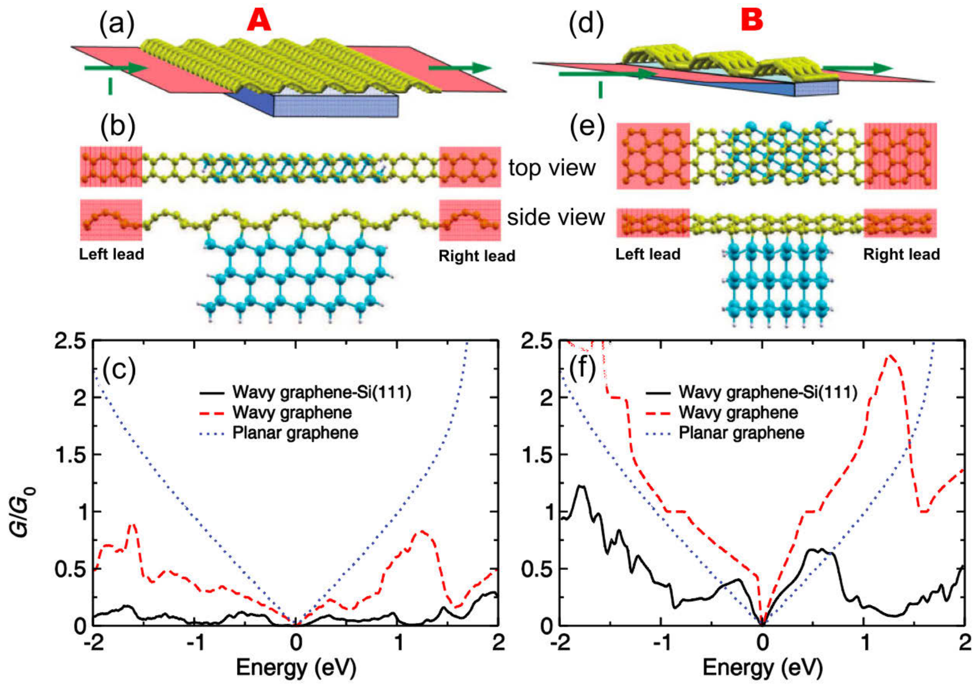

Figure 3.14 – Setup for the quantum transport calculations for contiguous wavy graphene layers bonded to Si(111). Results for quantum transport normal to the ridges in transport geometry A (a)-(c) are compared to those along the ridges in transport geometry B (d)-(f). (a), (d) Schematic geometry for the calculations distinguishing perfect graphene leads from the central scattering region, with the direction of the current I shown by the arrows. (b), (e) Atomic structure of the scattering region and its connection to the leads in the top and side views. (c), (f) Quantum conductance G in units of the conduction quantum G_0 as a function of injection energy, with $E = 0$ corresponding to the Fermi level. The conductance is given per unit cell normal to the transport direction, shown in panels (b) and (e).

which are responsible for conduction enhancement along the conductive ridges containing embedded paraphenylene chains and suppression of conduction normal to these ridges.

To investigate the possibility of charge injection from graphene to silicon, we constructed transport geometry C by removing a ridge from wavy graphene in the scattering region of geometry A, as seen in Figs. 3.15 (a) and 3.15 (b). We followed the approach for geometry A in constructing the graphene leads and saturating all Si dangling bonds on the surfaces perpendicular to the transport direction by H atoms. In the absence of the silicon substrate, there is obviously no transport due to the gap in a disrupted free-standing wavy graphene monolayer. If there were no possibility to inject carriers across the silicon-graphene interface, this would also be true for the disrupted mono- layer bonded to silicon. Our results in Fig. 3.15 (c) suggest otherwise, as we do find transport channels passing through the silicon substrate. Obviously, carrier injection across the graphene-silicon interface is possible, albeit only into and from energetically allowed states below and above the 1.1 eV wide fundamental band gap of Si. As in the other transport geometries, the transport gap is larger than the fundamental band gap.

Finally, we followed up on our results for geometry B, which suggest enhanced conductance along ridges of wavy graphene, and studied the effect of laterally disconnecting the beneficial paraphenylene-based conductance channels. Transport geometry D shown in Figs. 3.15 (d) and 3.15 (e) has been generated from geometry B by removing every other ridge of wavy graphene, creating an array of armchair graphene nanoribbons (GNRs) that are bent about their axis. These systems have been discussed widely as a viable alternative to zero-gap graphene [30,31]. We constructed the graphene leads for GNRs and passivated the Si dangling bonds by hydrogen following the approach used for geometry B. Also, the GNR edges were passivated by hydrogen.

Our transport results for an array of disconnected armchair GNRs in transport geometry D are presented in Fig. 3.15 (f). The reference system, an array of planar 5-AGNRs, shows a constant conductance $G = 1G_0$ corresponding to one conductance channel in a $\geq$2 eV wide energy range around E_F, with the exception of an $\approx$0,3 eV wide transport gap. These findings agree with previously published electronic structure results [176, 177]. Transport properties of free-standing 5-AGNRs that are bent about their axis are very similar to the planar GNRs in a 1-2 eV wide energy range around the narrow band gap. Attaching these GNRs to the Si(111) substrate causes a significant drop in conductance, especially in the conduction band region. This result is in stark contrast to the related transport geometry B that contains the same conductive paraphenylene-based ridges as geometry D, but does not separate them into nanoribbons.

The main message of our transport calculation is that especially in transport geometry B, the wavy graphene monolayer connected to a Si(111) surface may efficiently transport carriers along the graphene-silicon interface. Our results for geometry C indicate that the wave function overlap between the overlayer and the substrate is sufficiently large to permit partial carrier injection from graphene into the valence or conduction band of the silicon substrate. Our results suggest that wavy graphene attached on Si(111) substrate combines high mobility along the ridges with efficient carrier injection into Si in the contact regions. Anisotropy of its transport features is observed and this makes also the hybrid graphene-silicon system, a suitable candidate for a new generation of high-performance electronic circuitry.

It is intriguing to compare the electronic and transport properties of graphene on diamond C(111) surface to those of graphene bonded to the Si(111) substrate. The systems differ in two major aspects. For one, the lattice constant of carbon-diamond is significantly smaller than that of silicon, which results in a different interface morphology and a larger fraction of graphene atoms covalently bonding to the substrate. The presence of a larger number of sp^3 bonds per unit cell in the case of the graphene-C(111) hybrid system, allow for a exothermic formation process, with an E_{ad} of -0.151 eV/atom, while the graphene-Si(111) system shows a positive E_{ad} of 0.45 eV/atom (chemisorption of H can lower this energy to 0.12 eV/atom). Even though graphene forms a wavy structure both on diamond and on silicon to maintain epitaxy, the structure of the free-standing ridges is different. In graphene on

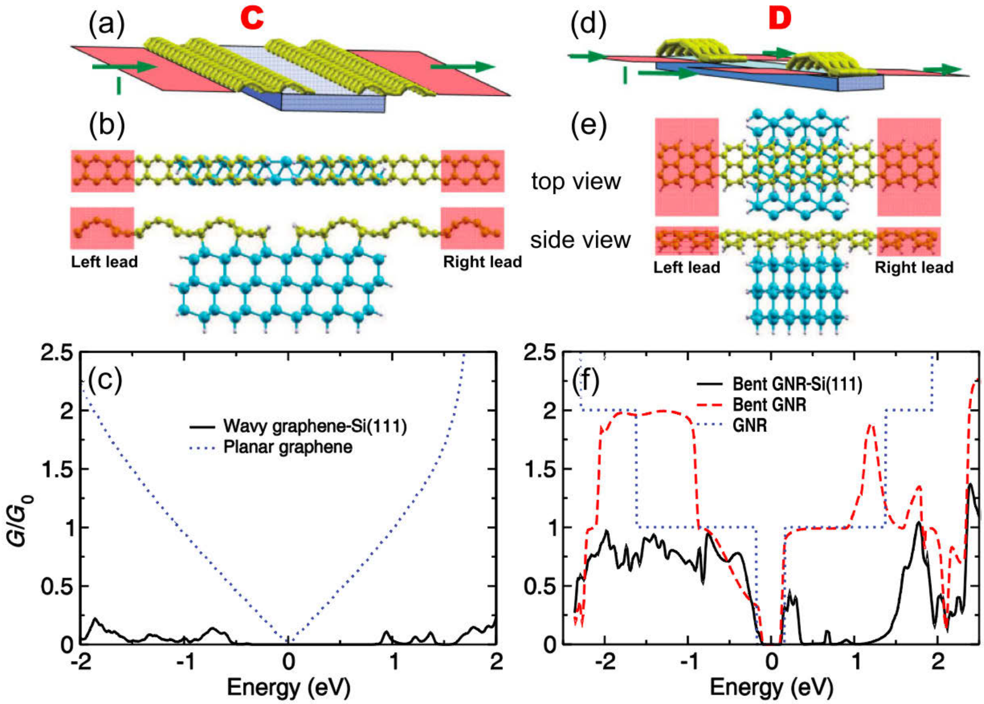

Figure 3.15 – Geometry and quantum transport calculations for semi-infinite wavy graphene layers and graphene nanoribbons bonded to Si(111). Results in (a)-(c) are for transport geometry C analogous to that of Fig. 3.14 (a), with the graphene monolayer disrupted by removing a ridge in the scattering region. Results in (d)-(f) are for transport geometry D analogous to that of Fig. 3.14 (d), where removal of every other ridge resulted in the formation of bent graphene nanoribbons. (a), (d) Schematic geometry for the calculations distinguishing free-standing perfect graphene leads from the central scattering region, with the direction of the current I shown by the arrows. (b), (e) Atomic structure of the scattering region and its connection to the leads in the top and side views. (c), (f) Quantum conductance G in units of the conduction quantum G_0 as a function of injection energy, with $E = 0$ corresponding to the Fermi level. The conductance is given per unit cell normal to the transport direction shown in panels (b) and (e).

Si(111), the ridges contain paraphenylene chains, whereas graphene ridges on C(111) contain polyacetylene chains with a system of delocalized π-electrons. The different ridge and valley morphologies of graphene on Si(111) and C(111) are responsible for differences in the transport along the ridge direction. Unlike on C(111), the valleys of graphene on Si(111) contain not only sp^3 carbon atoms, but also short butadiene segments. Since both Si and C (diamond) as substrate material have a fundamental band gap, transport through the scattering region normal to the ridges is limited by the interface region containing valley C atoms bonded to the substrate, resulting in a significant conductance reduction. In the graphene/diamond hybrid system, these regions contain only sp^3 carbon atoms, which completely block transmission within a wide transport gap that coincides with the fundamental gap of the substrate. The different morphology of the graphene valleys on Si(111) allows a partial transmission of electrons at energies within the fundamental band gap of the substrate.

4

Novel germaniums

Germanium is a scarce but not rare element in the Earth's crust (in average about 1.6 ppm) [178]. Despite being part of group-IVa as carbon ([Ar]$3d^{10}4s^{2}4p^{2}$), Ge allotropes are generally considered just two: α-germanium, semiconducting with the same structure of cubic diamond and β-germanium, metallic, stable at high pressure and with the same structure of β-tin. It has been shown that is possible to synthesize low dimensional homologues of carbon nanostructures. Recently J. Cheng *et al.* [179] for example, found a viable route for a simple and low-cost synthesis of Ge nanoparticles/graphene. These compounds show huge capacity, high room-temperature Li diffusivity and extremely low volume change during the Li ion insertion/extraction process as Li ion batteries anodes. Furthermore, 1D Ge-based materials have been easily grown in porous anodic aluminium oxide template by low-temperature chemical deposition [180]. These nanowires and nanotubes present amazing features, mainly due to the rhythmic conductance fluctuations that should allow an easier control of the current flow compare to Si and Sn homologues [181]. This suggests Ge monodimensional structures as outstanding candidates in nanoelectronic devices. Amorphous germanium (a-Ge) is an other, well known, modification of this element used as coating material or more often as template for a "disorder-to-order" transition in the synthesis of new metastable polymorphs [182]. The phase diagram of germanium is further complicated by a family of tetrahedral structures [183–185] and high pressure ones [186–189].

The fundamental character and technological relevance of tetrels (group-IVa elements) have thus motivated further systematic investigations on their polymorphism [190–194]. Apart from carbon polymorphs, that have been widely treated in the previous Chapter, semiconducting silicon and germanium are extremely versatile for micro- and nanoelectronic applications. For many technological targets, such as thermoelectricity [183, 195] or superconductivity [192, 196] applications, germanium seems to be the best candidate, even superior to silicon due to showing several advantages [197]: higher carrier mobility, more pronounced quantum-confinement effects, that allow a fine band gap control, and a good compatibility with high-dielectric constant materials. Metallization occurs in silicon and germanium upon compression [190], even if there is an intrinsic difference in the transition pressures of Ge, higher than in Si, due to its core d-electrons [198]. In Ge lowering of phonon frequencies promotes electron-phonon coupling towards superconductivity [191, 192]. The possibility of metallic germanium under room conditions is very intriguing and intensively debated [191, 199], while superconductivity in elemental Ge appears under pressure [192]. In the lower pressure range, improved optical properties via band-gap tuning can be achieved in a different polymorph. Engineering Ge-based viable new compounds with superior properties entails, thus, a detailed understanding of structural changes [117].

4.1 Novel metallic and semiconducting structures prediction

Upon compression, the Ge semiconductor diamond phase transform to β-tin ($tI4$, space group $I4_1/amd$) at about 10 GPa [186], and then to $Imma$ phase [187], simple hexagonal ($P6/mmm$) [188], orthorhombic $Cmca$ phase and finally upon further compression, above 180 GPa, to the hexagonal-close-pack arrangement ($P63/mmc$) [189]). Elemental germanium adopts, moreover, a large number of open framework structures. From mild oxidation of precursor Zintl compounds germanium can be obtained in the allotropic II-type clathrate Ge($cF136$ sp. gr. $Fd\bar{3}m$). Under pressure, $cF136$ transforms into β-tin type and γ-silicon type ($cI16$, sp. gr. $Ia\bar{3}$) over an intermediate, only moderately denser structure of trigonal symmetry, $hR8$ (sp. gr. $R\bar{3}$) [184], which is also accessible from another metastable phase, $tP12$ (sp. gr. $P4_12_12$) [200]. In a nutshell, during the last few years, new dense and open phases of germanium have been experimentally observed and theoretically predicted. Nevertheless, a systematic approach to including known and finding novel germanium forms is still outstanding, and of top priority in order to explain recent experiments [191].

4.1.1 Refining the Ge phase diagram

At ambient conditions, structural transformations are hampered by the relatively high potential barriers due to covalent interactions. Understanding high-pressure induced structural changes of the modification of group-IVa elements, is therefore tightly connected to the possibility of engineering viable new compounds. Here we have exhaustively explored the energy landscape associate with different crystalline structures of germanium, both at ambient condition and upon compression. By means of metadynamics, we efficiently sample all the possible transformations along specific collective reaction coordinates, which in the case of high pressure polymorphs is conveniently represented by the simulation box itself. Besides the already known dense phases of germanium, we found two novel allotropes (green in Fig. 4.1).

The first one is a monoclinic modification of germanium ($mC16$) slightly less dense than diamond, is an indirect band gap semiconductor and is unprecedented for tetrel elements. The second one is a five-coordinated (square pyramidal) metallic intermediate structure ($tI4$, sp. gr. $I4/mmm$), which incurs in the diamond ($cF8$) $\rightarrow$ β-tin phase ($tI4$) transition, and which has been postulated to exist in homologue silicon (bct-5) [201]. We report on transformation paths, energetic, mechanical and electronic properties. For the metallic bct-5 phase, we calculated superconducting temperatures down to ambient pressure compared to β-tin phase, based on the electron-phonon cou-

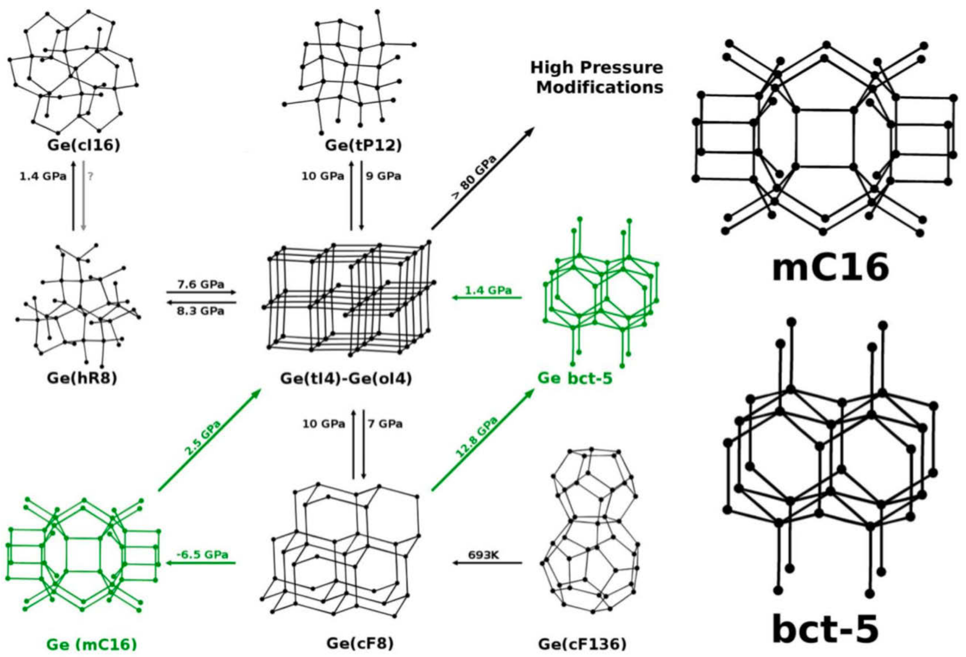
Ge(cI16)
Ge(tP12)
High Pressure Modifications
mC16
1.4 GPa
?
10 GPa
9 GPa
> 80 GPa
Ge(hR8)
7.6 GPa
8.3 GPa
Ge(tI4)-Ge(oI4)
1.4 GPa
Ge bct-5
2.5 GPa
10 GPa
7 GPa
12.8 GPa
bct-5
-6.5 GPa
693K
Ge (mC16)
Ge(cF8)
Ge(cF136)

Figure 4.1 – Lower pressure region of the phase diagram of Ge, augmented by two novel phases $mC16$ and bct-5, found by *ab initio* metadynamics runs. bct-5 shows characteristic square pyramidal 5-fold coordination of Ge atoms. In monoclinic $mC16$ four-rings are a characteristic feature. The arrows indicate the direction of metadynamics evolution. The pressures were evaluated based on the common tangent construction (see below, Fig. 4.3).

pling mechanism [202].

4.1.2 Methods

As we also reported in Section 3.1.2, for the prediction of novel polymorphs of the elements, metadynamics [23, 24, 125] is particularly suitable and presents different advantages with respect to other technique used in the same research field [118, 119]. Indeed, the method is independent of the level of theory used, it does not require prior knowledge of the energy landscape, its sampling efficiency can be enhanced by parallel runs started from different configurations and it allows, thus, for a fast exploration of the energy surface along one or more collective reaction coordinates. All metadynamics runs were performed with at least eight atoms in the simulation box which served as a collective (6-dimensional) variable. This minimal box approach was successfully used in our prediction of novel carbon polymorphs. The size of the minimal box ensured commensurability of all already known phases (except for the clathrate II-type phase, which requires a minimum of 34 atoms) either open or dense. Each metadynamics metastep consisted of a molecular dynamics run in the NVT ensemble for 0.5 ps (timestep 2 fs) at 300 K.

Metadynamics was performed with different molecular dynamics layers. A Density Functional Tight Binding (DFTB) [203] level of theory, as implemented in the Γ-point-only DFTB module of the CP2K code [126,127], ensured rapid and accurate sampling in the low-pressure regime, characterized by four-connected Ge atoms. For higher-pressures SIESTA [130,131] was used as the DFT molecular dynamics layer, allowing for k-point runs. Electronic states were expanded by a single-ζ basis set constituted of numerical orbitals with a norm-conserving Troullier-Martins [132] pseudopotential description of the core electrons. Single-ζ basis set dramatically reduces computational times providing nonetheless, the right topology and energy differences of all the Ge allotropes under study. The charge density was represented on a real-space grid with an energy cutoff of 200 Ry. A Monkhorst-Pack k-point mesh of $2 \times 2 \times 2$ ensured the convergence of the electronic part. High-pressure metadynamics was performed based on DFT. Lower pressure regions were initially explored by DFTB, followed by DFT metadynamics upon discovery of interesting novel polymorphs. In the lower pressure range the transferability between DFTB and DFT is unflawed. To validate the method a set of preliminary test runs were performed. Similarly to metadynamics applied to silicon [204], the correct sequence of reported phases [192] of Ge could be reproduced as reported in Fig. 4.2.

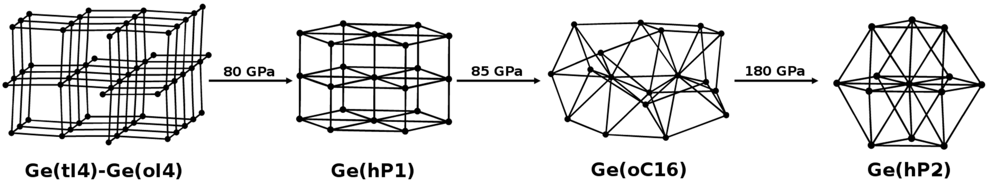

Figure 4.2 – High pressure Ge modifications sequence. $tI4$ and $Imma$ are reported in the same structure because they are visually undistinguishable (transition pressure of the former into the latter is ~10 GPa). From the left to the right all the high-pressure "cascade" is reported: $Imma \rightarrow sh \rightarrow Cmca \rightarrow hcp$.

Electronic structure, phonon dispersion curves and superconducting properties were calculated with the Quantum Espresso (QE) [202,205] package. The superconducting critical temperature T_c was evaluated based on the Allen and Dynes modification of the McMillan formula. This required calculating the electron-phonon coupling strength λ via the Eliashberg function. The Coulomb potential value was μ =0.1. A q-mesh of $12 \times 12 \times 12$ was used for the evaluation of the dynamical matrix, while a Monkhorst-Pack k-point mesh of $16 \times 16 \times 16$ ensured convergence of the electronic part.

The structures visited during each run were characterized by their vertex symbols, which contain the information on all the shortest rings meeting at each atom, and coordination sequences, as implemented in the TOPOS package [128]. In case of new structures ideal space group and asymmetric units were identified with the Gavrog Systre package [129]. Subsequently a variable-cell geometry optimization was performed (DFT-GGA, PBE functional [74]) in a plane-wave pseudopotential framework [205] using Vanderbilt ultrasoft pseudopotential with non-linear core correction [206]. A k-point mesh of $8 \times 8 \times 8$ ensured convergence of the electronic part, while a plane-wave basis set with an energy cut-off of 30 Ry was applied.

The electron localization function (ELF) [207] is a widely used tool to study chemical bonding in molecules and solids. The ELF monitors the correlation of the movement of parallel spin electrons in real space [208]. In this study the ELF calculations were performed by using the ELF module as implemented [209] in the all-electron, full-potential local orbital (FPLO) minimal basis method [210]. In FPLO each atomic orbital nl with principal quantum number n and angular momentum l is represented by one basis function only. The basis functions are obtained by solving an effective Schrödinger equation which contains the spherically averaged crystal potential and an artificial confining potential [211]. The confining potential makes the basis functions more localized than the atomic orbitals. The FPLO method does not have any atomic (or muffintin) spheres so that the whole space is treated in a uniform manner. In the scalar relativistic calculations within the LDA scheme (Perdew and Wang [212]) Ge(3d, 4s, 4p, 4d) represented the basis sets. Lower-lying states were treated as core states.

4.1.3 Results and Discussion

The $mC16$ structure (Fig. 4.1, C2/m, a =7.6094 Å , b =7.9746 Å , c =6.5668 Å , β =104.10°) arised from a metadynamics run started from diamond (8 atoms box, P=1 bar, T=300 K). Ge atoms occupy three Wyckoff positions: (4i) 0.70984 0.50000 0.67434, (4i) 0.60981 0.50000 0.29080, (8j) 0.65012 0.76388 0.11596. Strikingly, $mC16$ is less dense than diamond (see Fig. 4.3), although topologically as dense as diamond or lonsdaleite. Its bulk modulus amounts to 51.2 GPa that is slightly lower than that of the diamond type-structure (60.7 GPa), estimated from the fit to the third order Birch- Murnaghan equation of state. Applying pressure to the mC16 allotrope in an additional metadynamics run resulted into a direct transition to the β-tin phase. Decompressing the latter is known to generate metastable phases typically denser than diamond Ge. Therefore, a viable route to $mC16$, like for other recent germanium allotropes, could rather be the oxidation of suitable germanium Zintl salt precursors, i.e. via chemical synthesis.

Upon compression diamond transforms into β-tin and it subsequently follows the same transition sequence of silicon phases. Along the diamond → β-tin transition, metadynamics (64 atoms box, P=10 GPa, T=300 K, Gaussian width δs =4.5 (GPa Å^3)$^{(1/2)}$, Gaussian height W= δs^2) visited an intermediate of bct-5 topology ($I4/mmm$, a =3.5491 Å, c =5 6.4478 Å, Ge(4e) 0.0 0.0 0.19273). The bct-5 bulk modulus is 58.7 GPa, slightly lower than that of the β-tin phase (68.2 GPa). This five-connected structure has been proposed for silicon [201], but has never been observed so far.

The total energy/volume curves of Fig. 4.3 suggest bct5 as a conventional product of diamond compression (here "conventional" denotes a positive equilibrium pressure, whereby an "unconventional" product requires a "negative" pressure). However, under hydrostatic conditions β-tin is formed from diamond, while decompression leads to other germaniums, although indications of minority phases exist. Low-temperature nonequlibrium decompression further influences phase formation towards

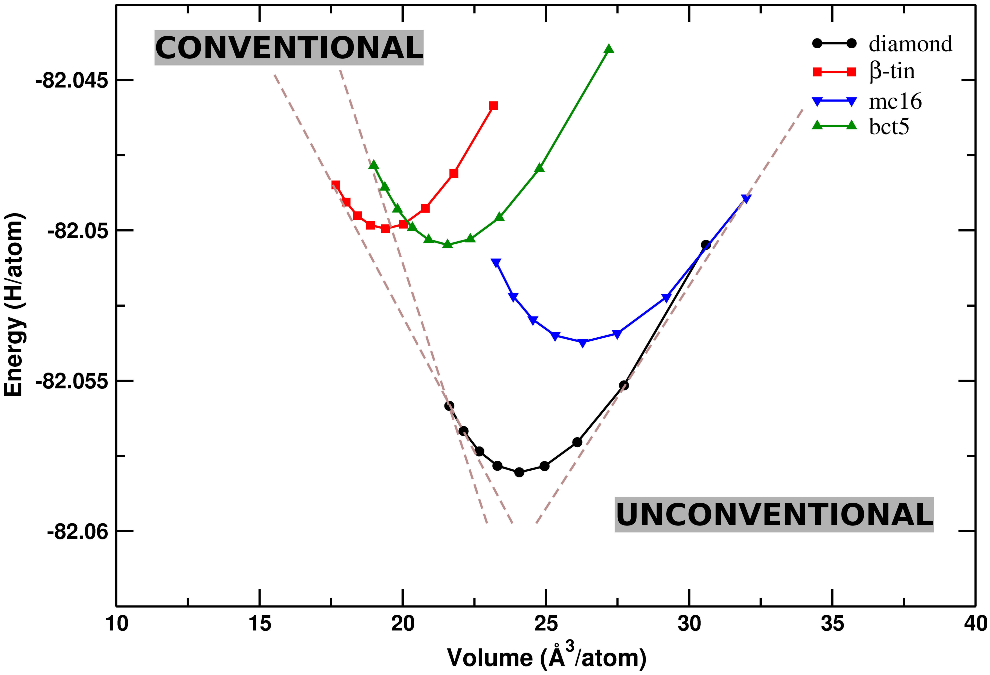

Figure 4.3 – Equation of states of Ge $mC16$ and bct-5, compared to cubic diamond and β-tin type. bct-5 features a reduced volume per atom compared to diamond type ($cF8$), while the total energy minimum lies lower than β-tin. $mC16$ on the contrary is less dense and energetically close to the diamond type. The tangents used for evaluating equilibrium pressures of Fig. 4.1 are highlighted.

amorphous [213] and novel germaniums [214].

The transformation affects only one box parameter, suggesting nonhydrostatic shearing as the protocol of choice towards bct-5, also supported by the magic-stress approach which led to bct-5 in silicon [201]. Alternatively, low-temperature compression may be considered. The evolution of the enthalpy profile of metadynamics runs from diamond Ge (Fig. 4.4) shows bct-5 as a narrow plateau around metastep 160. Metadynamics runs started from bct-5 (Fig. 4.4, black curve) confirms it as a proper intermediate along the transition, which can be quenched down to room pressure, and which is mechanically stable (see below). Mechanistically, the coordination number increases from 4 to 5 on shortening one bond, followed by flattening of the pristine tetrahedron and formation of the square pyramidal geometry of bct-5, Fig. 4.3 (b). The four bonds in the pyramid basis are 2.62 Å long, the axial one 2.48 Å.

The evolution of the bonding situation from Ge diamond to β-tin over bct-5 is shown in Fig. 4.5. Calculation of the ELF [207] shows four, one+four and two+four bond attractors, respectively. The five "bonds" in this orbital-deficient, electron-deficient metallic bct-5 result from the sp Ge valence shell. This bonding scenario is reminiscent of the recently discovered superconducting Zintl phase $CaGe_3$ [215],

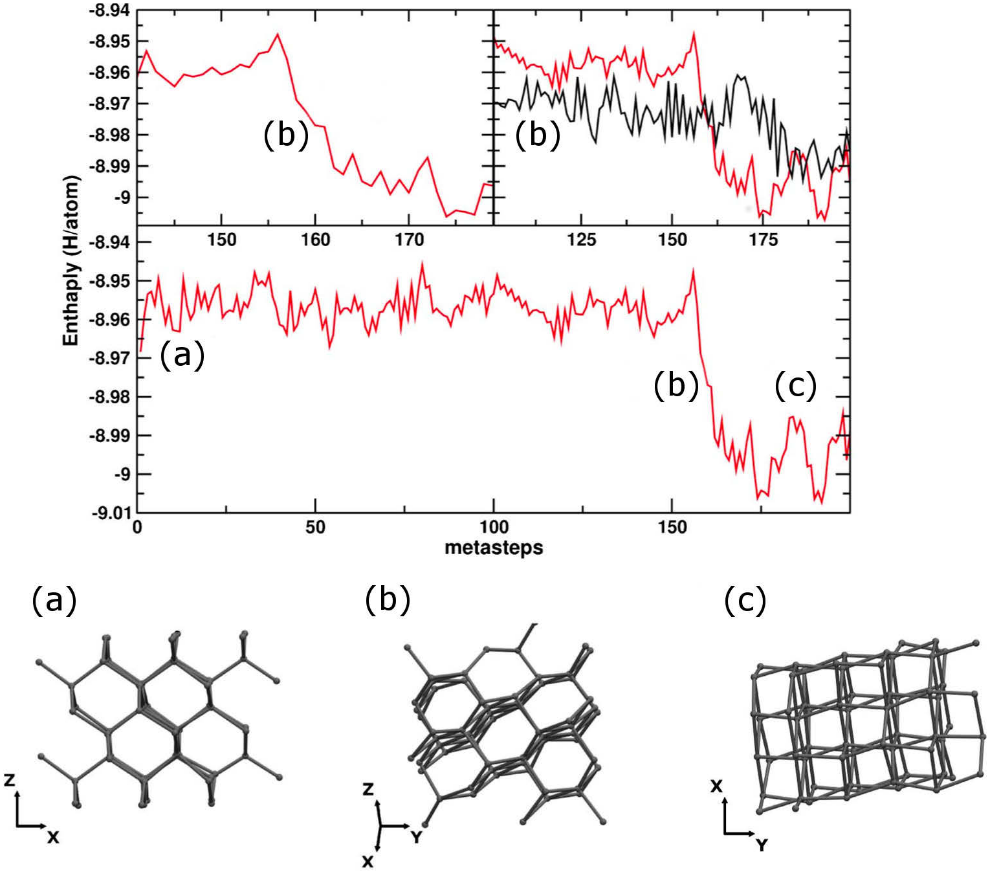

Figure 4.4 – Metadynamics (DFT) runs on a 64 Ge atoms box (P=10.0 GPa, T=300 K). bct-5 appears as a stepwise feature in the enthalpy profile of the run started from diamond (red line). Runs commenced from bct-5 (black line) evolve into β-tin. Configurations corresponding to distinct points along the runs are detailed below the graph. Energy units are eV.

isosymmetric with bct-5.

The electronic band structures and phonon dispersions of $mC16$ and bct-5 are shown in Fig. 4.6. The tetrahedral $mC16$ phase is semiconducting with an indirect band gap of 1.43 eV (PBE-GGA [74]), while bct-5 is metallic and stable down to 0 GPa. Isothermic-Isobaric molecular dynamics (1 bar, 300 K, 2.5 ps) confirmed the stability of bct-5. $mC16$ is characteristic due to the presence of four-membered rings. However, this does not imply overall structure destabilization [216]. The expectation of a strained geometry is in fact not supported by total energy calculations, which place $mC16$ among the energetically lowest Ge allotropes. The indirect band gap and the low density (compared to the diamond type) make this germanium an attractive material. The need for a "negative" pressure makes a chemical path plausible.

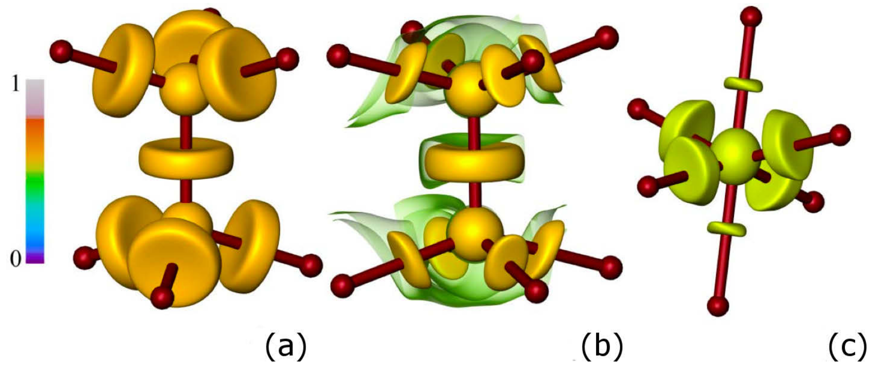

Figure 4.5 – Evolution of the bonding situation from diamond to β-tin type over bct-5. The ELF map is showing four bond attractors for diamond Ge (a, η =0.58), one+four bond attractors for bct-5 (b, η =0.53, transparent green isosurface η =0.48), two+four bond attractors for β-tin (c, η =0.51).

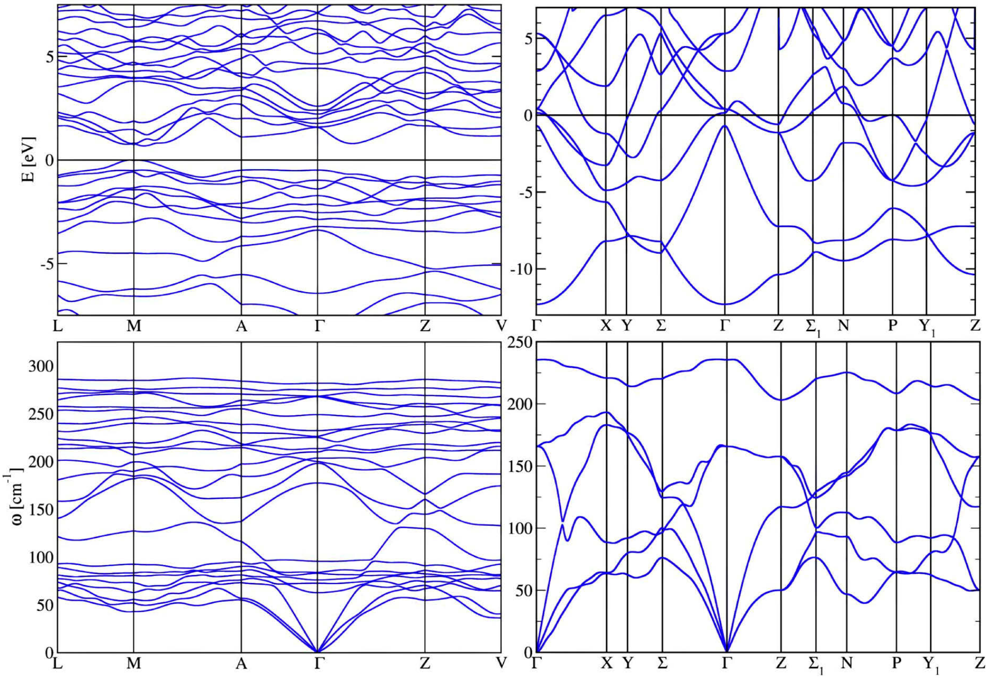

Figure 4.6 – Band structures and phonon spectra (0.0 GPa) of mC16 (left) and bct-5 (right). mC16 is a narrow-gap semiconductor (band gap 5 1.43 eV), while bct-5 is metallic. Both are mechanically stable. Brillouin zone choice (bct-5) according to Ref. [2].

The prominent property of bct-5 is the conservation of metallic character down to ambient conditions. Calculations and experiments have shown an increase of the superconducting temperature on lowering pressure, with superconductivity still present at 6.9 GPa ($T_c \approx 6.0$ K) [191], outside of the existence range of β-tin. This points to the existence of another superconducting phase. The evolution of T_c as a function of pressure for bct-5 and β-tin is shown in Fig. 4.7. The calculated value of T_c for bct-5 at 6.9 GPa is T_c=6.1 K (β-tin T_c=7.7 K). The ongoing debate on the feasibility of "strange" metals other than β-tin [191, 199], and particularly the need for further explanations of the survival upon decompression of "metallic" metastable phases (not reliably identified as any known Ge phase up to now) open the door for a serious consideration of the role of the bct-5 in the lower pressure range, as a metallic state that qualifies for higher T_c values (via the McMillan relation).

In conclusion, we have seen in this Section how with metadynamics runs we were able to find and later characterize two novel Ge polymorphs. The first one, $mC16$, is an indirect gap semiconductor, and its structure is unprecedented for the tetrel family. The second bct-5 polymorph was suggested for Si. Our simulations lean strong relevance to bct-5 in the lower pressure range, as a new metallic superconducting with relevant superconductive features phase capable of stability at room conditions. We expect our predictions to stimulate further experimental work.

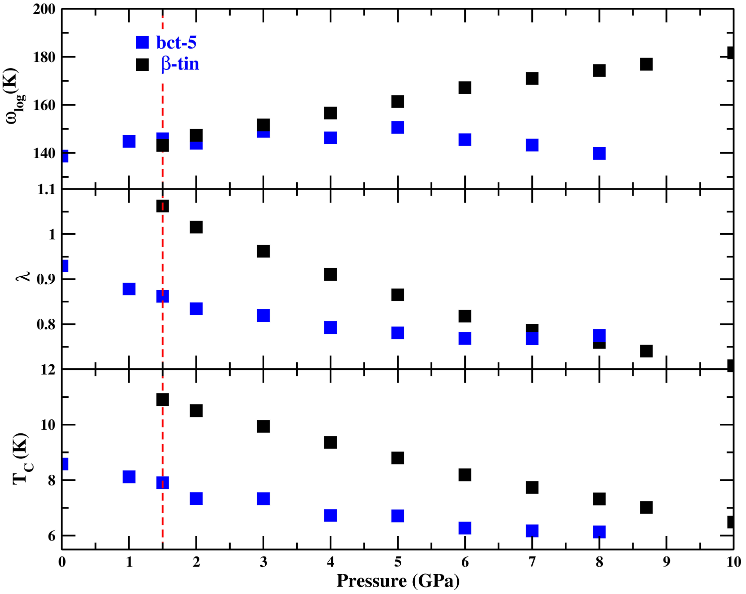

Figure 4.7 – Evolution of ω, λ and T_c as a function of pressure for bct-5 and β-tin, calculated based on the electron-phonon coupling model. The calculated equilibrium pressure between bct-5 and β-tin marks the boundary between the phases. Notice the flattening of bct-5 T_c after 5 GPa as phonons soften. The model predicts an increase of T_c in the lower pressure region.

4.2 Unrevealing the interconversion mechanism of Ge($hR8$) and Ge($cI16$) polymorphs

Our accelerated molecular dynamic techniques allow for a fast scan of the potential energy surface, however, our capacity of directing novel covalent bond geometries is still limited by an incomplete understanding of the rules governing the formation of metastable phases [217]. This entails an understanding, as complete as possible, of the transformation kinetics and microscopic mechanisms associated with material synthesis [218]. This knowledge is needed to judge on the synthesizability of a particular compound, which is not ensured by barely ascertaining that a particular compound can exist in principle. The quest for microscopic mechanisms is nowadays greatly empowered by methods able to provide the appropriate time and space resolution and the mandatory backtracking of the time evolution of a system to key elementary atomistic steps of material reactivity. While the resolution of experimental setups is greatly increasing, major breakthrough for material synthesis can be expected from routinely including the atomistic level of detail into designing synthetic approaches. Simple systems, and chemical elements in particular, represent the perfect ground on which an initial grammar of reactivity rules can be commenced.

As presented in the previous Section Ge tends to adopt different topological modification both with an open (ambient pressure) and dense (high pressure) framework. Among the semiconducting Ge networks, the $hR8$ allotrope comprises four-coordinated Ge only, while 2 different sites Ge1 (Wyckoff position $6c$) and Ge2 (Wyckoff position $18f$) are indicated by the crystallographic analysis [184]. This contrasts with $cF8$, $tI4$ or $cI16$, which can be generated from one site only. In the extended phase diagram of germanium, $hR8$ is at the gateway between relatively denser ($cF8$, $tI4$, $cI16$) and open-framework ($cF136$) structures [184]. The $hR8$ structure may in fact be decomposed into a Ge2 framework hosting Ge1 guest chains [184]. Under compression, a structural evolution towards higher symmetric structures is common. Site splitting rarely occurs and when it does so, exotic metals like for example Ti [219] are involved. Beyond the bare crystallographic data, we interpreted this as a manifestation of chemical reactivity and we moved on to unfolding the chemically relevant steps responsible for this differentiation. Clearly, a particular rearrangement of covalent bonds into a different pattern is controlling the formation and stability of a metastable phase here.

4.2.1 Introduction

Using state-of-art molecular dynamics techniques combined with density-functional tight-binding (DFTB) level of theory [220] for expressing interatomic forces, we have investigated the mechanism connecting $hR8$ to $cI16$, two intriguing structural patterns, and group IV (Si, Ge) characteristic assemblies (Fig. 4.8), which appear in the Ge phase diagram as metastable phases.

The investigation of phase transition mechanisms remains a very important but challenging task [221]. This is due to the specificities of the phenomenon of phase transition, which is difficult to assess both experimentally and by theory. Recent computational methods allow for shedding light onto transformation mechanisms and

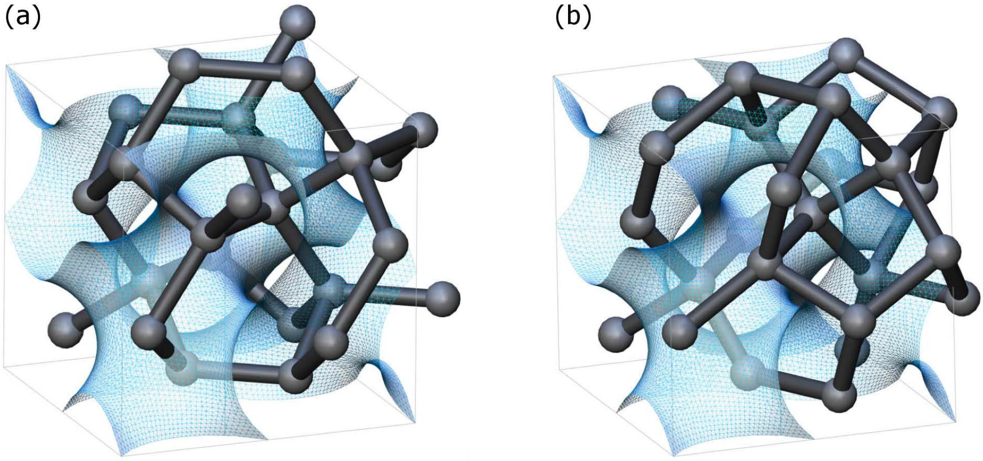

Figure 4.8 – Crystal structures of the (a) $cI16$ and (b) $hR8$ Ge allotropes ($hR8$ is represented in a pseudo-cubic cell for better comparison with $cI16$). Their networks follow the shape of the gyroid (transparent blue), except for a set of bonds, which trespass the surface in a way that is peculiar for $cI16$ and $hR8$, respectively. Flipping these bonds formally converts $cI16$ into $hR8$. One such flip is visible in the foreground, causing inversion of a Ge tetrahedron.

reactive intermediates, though [222]. A detailed atomistic map of reactive events that transform one structure into the other is the commencement of a chemical understanding of phase transitions in crystalline matter, now overdue [160].

Symmetry provides, to some extent, guidance thanks to group-subgroup relationships [223]. However, in a situation of framework reconstruction, relevant details of bond nucleation stay undisclosed. Heuristic matching of minimal surfaces (or approximants thereof) with crystalline matter has a long record of stimulating examples [224]. The networks of $cI16$ and $hR8$ develop around the gyroid [225], a surface of intrinsic $Ia\bar{3}d$ symmetry. All Ge atoms are found on either side of the surface, as well as the majority of covalent bonds. Only some Ge-Ge bonds trespass the gyroid, in a way that is different and characteristic for $cI16$ and $hR8$, respectively (Fig. 4.8). Chemical intuition suggests that the process of their mutual structural rearrangement is “economical” and well-balanced in terms of bond-breaking and bond-forming patterns. However, how does the transformation of a framework into another one actually work, and what is the role of chemistry therein, given that covalent bonds have to be re-formed? These are the questions we address in this work.

4.2.2 Methods

To determine the proper reaction pattern between solid-sold first-order phase transitions, the Transition Path Sampling (TPS) molecular dynamics technique is a method of proven success [226–228]. The sample of an initial transition path (ITP) that connect the two basins of interest is performed following a Monte Carlo algorithm

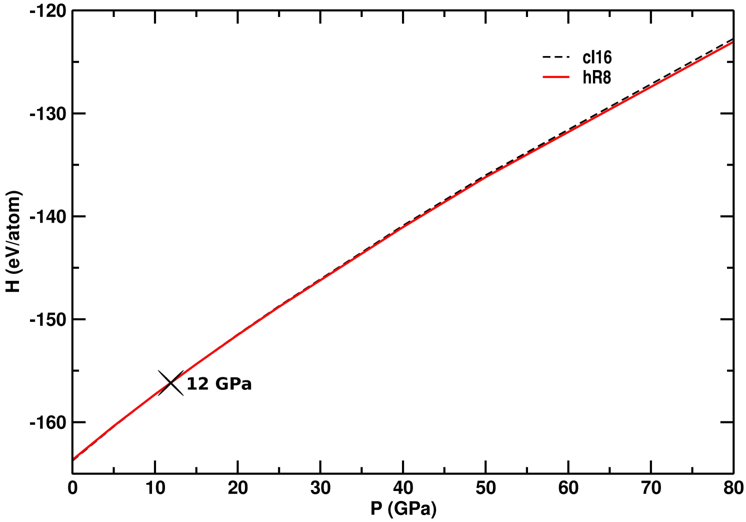

Figure 4.9 – Enthalpy vs. Pressure of Ge($cI16$) and Ge($hR8$). The intersection point represents the transition pressure within the DFTB potential considered.

(MC) [50, 229] in the space of trajectories, like it is described above, Chapter 2. The ITP is iteratively driven to a most probable transformation regime. The sampling procedure is kept in a way to ensure complete independence between the TPS algorithm an the level of theory used to temporally propagate the system. Generally speaking, if the ITP is derived from a symmetry-based model, the converged calculation regime after TPS is typically characterized by nucleation and growth.

The $hR8 \rightarrow cI16$ phase transition was investigated with TPS. The iterations were performed within the NPT ensemble (P = 12 GPa, T = 300 K) and implemented by applying momentum modifications on selected trajectory snapshots, keeping total energy, momentum and angular momentum unchanged according to the shooting scheme. The pressure corresponded to the equilibrium pressure of the DFTB potential, which fulfills the condition $E_1 + pV_1 = E_2 + pV_2$, where the indices distinguish between $hR8$ and $cI16$ (Fig. 4.9). Propagating the new configuration in both directions of time provided a new trajectory that was examined for the $hR8$-$cI16$ (or $cI16$-$hR8$) process, respectively. If this condition was not met, the trajectory was rejected and the shooting process iterated. The distinction between initial and final state was made based on coordination sequences (see below). MD simulations were carried out using DFTB [220], Γ-point-only module of the CP2K package [126, 127]. The accuracy of electronic density representation was checked against DFTB k-point calculations [230]. The Ge DFTB energetic score is in agreement with DFT local-density approximation (DFT-LDA) calculations (Table 4.1 [231]), but the equilibrium volumes are slightly overestimated. The time step t = 0.2 fs ensured a good time reversibility. The mechanistic analysis was based on more than 50 transition pathways collected after trajectory convergence. The latter was inferred from the stability of the

Table 4.1 – Energetics of Ge Structures.

	DFTB(eV/atom)	Volume(Å^3/atom) DFTB	 Exp	DFT(eV/atom) FPLO[a]	Volume(Å^3/atom)
$cF8$	0.00	25.86	22.56[b]	0.00	22.54
$cI16$	0.1489	23.83	20.81[c]	0.126	20.98
$hR8$	0.1758	23.58	20.30[d]	0.138	20.36

---

[a] Ref. [210, 212]
[b] Ref. [232]
[c] Ref. [185]
[d] Ref. [184]

mechanistic features emerging during TPS MD. Different from the initial, concerted mechanistic models, the stable regime shows local events of bond flipping.

The ITP was constructed based on matching the two allotropes ($cI16$ and $hR8$) in a common $R\bar{3}$ space group within an 8-atom rhombohedral unit cell. Clearly, subgroup degradation was only necessary for the $cI16$ phase ($Ia3 \rightarrow R\bar{3}$). The simulation box was chosen as a supercell obtained from a minimal one by the transformation matrix (022/202/220), which resulted in a pseudo-cubic cell with 128 atoms. To quantitatively differentiate between the networks, we calculated coordination sequences (up to the 5th shell), which were also used to monitor structure evolution in the TPS simulations (coordinations sphere analysis of the converged final trajectory is shown in Fig. 4.10). Recall that a coordination sequence [233] is a set of integers $\{n_1, n_2, \ldots n_i, \ldots\}$, where n_i indicates the number of atoms separated from a central one by a minimal path of i bonds. For $cI16$ the coordination sequence reads (for each atom): $\{4, 12, 27, 49, 77, \ldots\}$. In $hR8$, Ge1 sites are characterized by the sequence $\{4, 12, 24, 51, 72, \ldots\}$ while Ge2 sites show a denser environment $\{4, 12, 26, 49, 77, \ldots\}$. Coordination sequences clearly discriminate between the two structures starting from the 3rd coordination sphere. Within this model, bond changes are taking place along three directions ([$\bar{1}$11], [1$\bar{1}$1], [11$\bar{1}$]), without preference. Along [111] no bond breaking is observed. The reconstruction as the model codes it is thus “degenerate” in 3 directions.

Wannier centers and Wannier orbitals were used to characterize bond evolution during phase transitions. The Fourier transform of Bloch states into Wannier functions is defined up to a phase factor. Characteristic of a Wannier function are its center and spread. A convenient set of maximally localized Wannier functions (MLWFs) [234] was obtained by minimizing the total quadratic spread of the Wannier orbitals, as implemented in the WANNIER90 program [235]. For the MLWFs of Fig. 5, sp^3 projection functions were used. This choice consistently produces four “bonds” in $cI16$ and $hR8$, and is sensitive to bond elongation/shortening [236].

4.2.3 Results and Discussion

In the converged TPS regime, a typical transformation path shows structural variations along two directions only, distinguished by colors (red and blue) in Fig. 4.11.

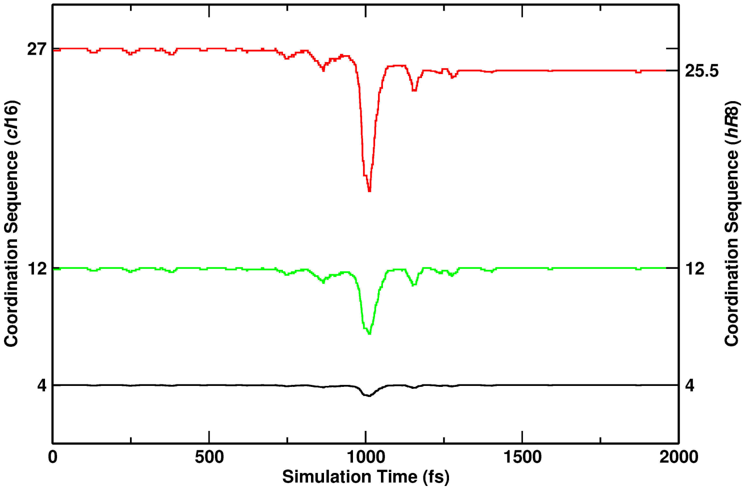

Figure 4.10 – Coordination sequence calculated along the time coordinate for the converged transition trajectory.

The reconstruction relates two distinct groups of localized bond systems, which are similarly oriented in the initial and final structures, Fig. 4.11 (a), (d).

Striking is the formation of two sets of Ge chains around the reactive transition intermediate (Fig. 4.11 (b)). These chains, which result from the condensation of isolated bonds, are tilted with an angle of ~ 60° against each other and are entangled and interconnected into a web. Blue chains are oriented along [$\bar{1}11$] (referred to as the simulation box) (Fig. 4.11 (b)) and are responsible for the transformation $hR8 \leftrightarrow cI16$ by shortening and elongating alternate sets of bonds. Red chains (along [111]), on the contrary, are forming in the course of the transition but do not rearrange from one structure into the other. Localized "red" bonds, similarly dislocated in both limiting structures, are momentarily resonating into a chain structure.

Along the transition, an intermediate, four-connected, metastable configuration is visited ($hR32$) (Fig. 4.11 (c)), isosymmetric with $hR8$ but requiring certain bonds within some of the reactive [$\bar{1}11$] chains to be flipped. Details on this novel metastable configuration, quenchable to ambient pressure based on phonon calculations and finite temperature molecular dynamics simulations (DFTB/DFT), can be seen in Fig. 4.12. Structural and cell parameters (sp. gr. $R\bar{3}$, a= 117.058 pm, α = 117.02°) were optimized with SIESTA [130, 131] and reported in Table 4.2.

The blue-marked dumbbells in $hR8$ (Fig. 4.11 (d)) involve Ge1 sites only, while red ones are made by Ge2 sites. Red and blue become equivalent in $cI16$. Changes within blue chains are thus responsible for site differentiation. Their difference is rooted in the steps around the reactive intermediate, which we are analyzing in detail now.

The bond flip mechanism among different reactive (blue) chains as well as within a single chain is markedly asynchronous. Fig. 4.13 shows a close-up of the bond reorganization of a single chain as a function of time. Noteworthy is the formation of

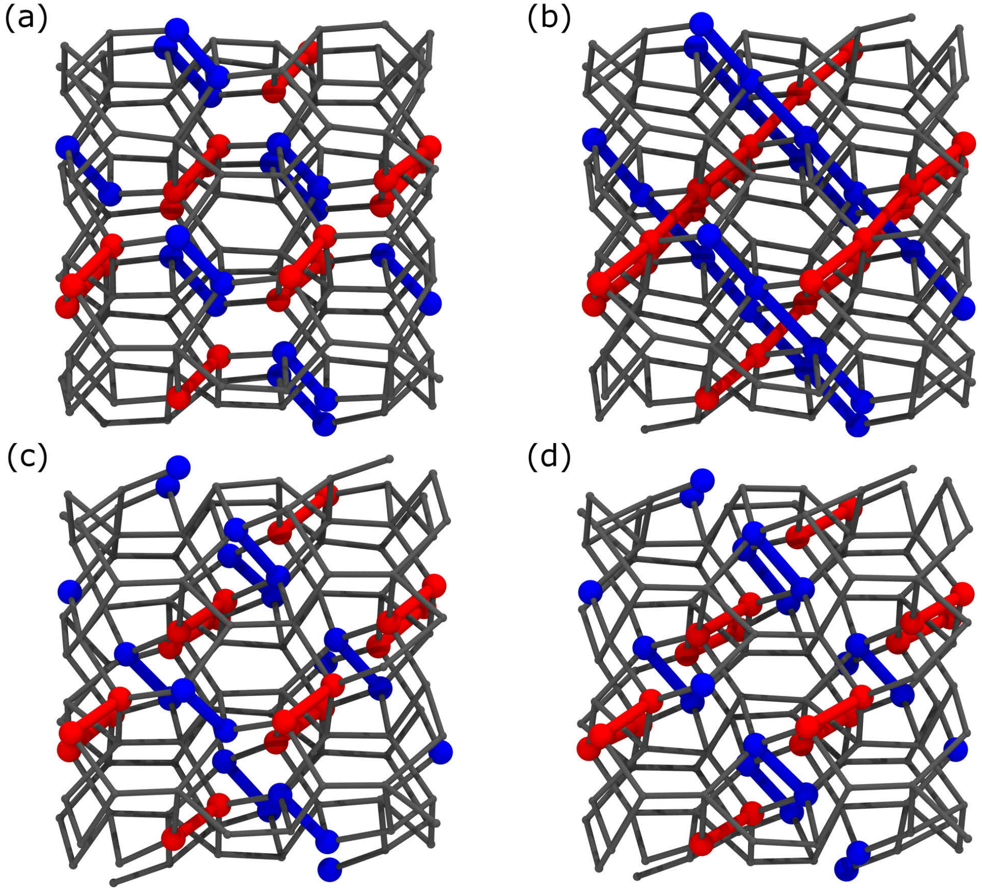

Figure 4.11 – Configurations appearing along the transformation. (a) Ge($cI16$), (b) reactive intermediate, (c) a novel metastable phase Ge($hR32$) and (d) Ge($hR8$). Bonds changing from one structure to the other are highlighted in blue, while red ones show stretching along the trajectory, but they are never completely broken. (c) and (d) differ only by some bonds. They are nonetheless two distinct local minima on the chemical landscape of Ge.

trigonal-bipyramidal geometries at Ge, suggesting $sp^2 + p$ hybridized states like they are caused by a S_N2 reaction sequence mechanism, in which tetrahedral sp^3-hybridized Ge atoms get inverted. Most notable is the generation of an almost regularly spaced sequence of sp^2 Ge atoms. This sequence undergoes rapid rearrangements with the formation of new bonds, characteristic either of Ge($hR8$) or Ge($cI16$), respectively. Single bonds "nucleate" from a roughly equally spaced arrangement, triggering a sequence of bond-forming and bond-breaking events.

A global characterization of all bond changes along a trajectory is achieved by calculating Wannier functions centers (WFCs) [234]. Two atoms are associated with a single WFC (within a so-called "association length") in the presence of a chemical

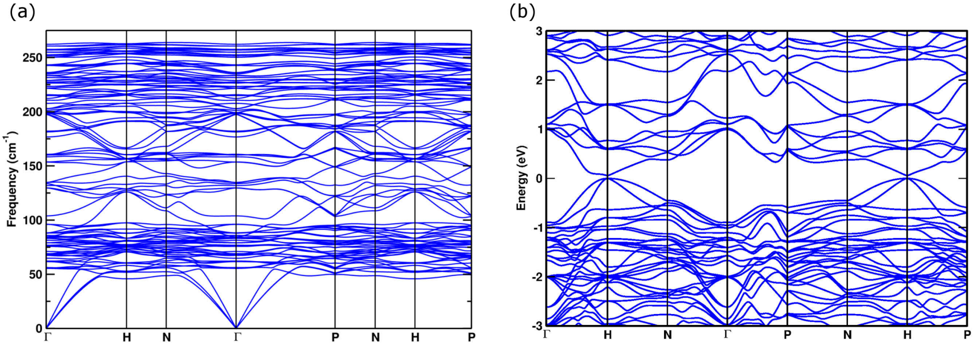

Figure 4.12 – Phonon dispersion curves (a) were calculated at 0 GPa. No imaginary frequencies were observed throughout the whole Brillouin zone, confirming the dynamical stability of the intermediate $hR32$ structure. Band structure calculations (DFTB+) indicate that $hR32$ is a semiconductor (b).

bond. Upon bond breaking, the WFC disappears or becomes shifted. For the characterization of the transition trajectories with respect to chemical bond changes, the motion of WFCs was monitored along the time coordinate of framework reconstruction. The shift of a bond within a chain (Fig. 4.13) is reflected into a jump in WFC relative position (Fig. 4.14). Just one snapshot every 20 fs was considered near the relaxed $hR8$ and $cI16$ phases. In the intermediate region, a finer time resolution (every 2 fs) was necessary. The displacement of Wannier centers serves here as collective order parameter.

Fig. 4.14 shows the time evolution of WFCs within every reactive chain. Different reactive chains are distinguished by color (green, black, purple and turquoise), while bonds within a chain are marked by symbols. Clearly, the total reconstructive process is discontinuous on the timescale of the simulation. Chain bond flippings occur at different moments in the whole material, as indicated by the mutual offset of the sigmoidal curves. For each color, different symbols jump at different times, denoting non-concerted bond shifts within chains, as already highlighted in the close-up of Fig. 4.13. Therefore, the overall bond rearrangement process spans quite a large time

Table 4.2 – Structural parameters for $hR32$.

Atom	Multiplicity	X	Y	Z
Ge1	6	0.73075	0.13191	0.38248
Ge2	6	0.74004	0.64066	0.89041
Ge3	6	0.23572	0.13597	0.88540
Ge4	6	0.23774	0.63638	0.38723
Ge5	6	0.78941	0.28964	0.28996
Ge6	6	0.70296	0.70296	0.70296

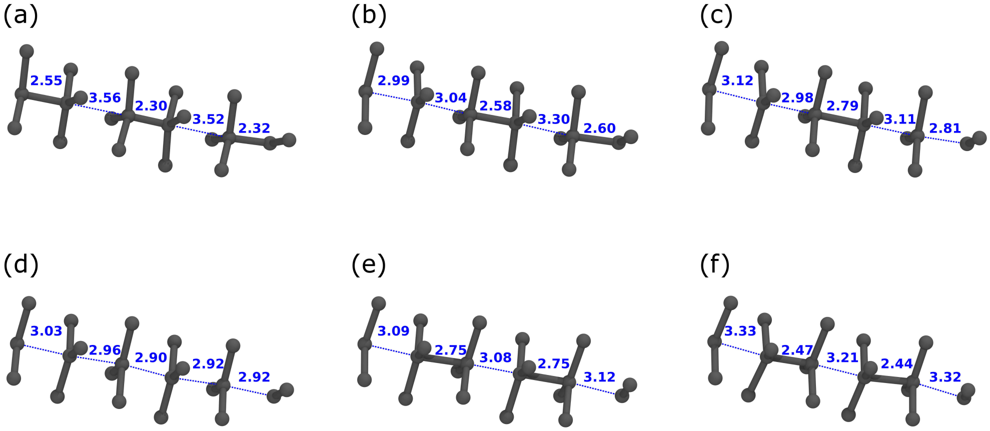

Figure 4.13 – Transition mechanism for a single reaction chain (in blue in Fig. 4.11). Snapshots of the trajectory are shown at 0.0 (a), 880 (b), 906 (c), 960 (d), 1040 (e), 2000 (f) fs.

window: the first bond flip occurs at ~750 fs while the last one is at ~1200 fs. The green curves refer to the chain of Fig. 4.13. As the first bond gets broken (green circle), the other bonds in the same chain start rearranging (green square, triangle), followed after some delay by bond shifts in neighboring chains (black, purple and turquoise). The larger WFC fluctuations around 850 fs (Fig. 4.14, green chain) and 1000 fs (green and purple chains) coincides with the formation of red chains, which is taking place just before breakage/formation of reactive (black and purple) chains, and less markedly ahead of the last chain reshuffling (~1200 fs).

This is echoed in the changes of phonon frequencies along the transition. The stretching mode of the first flipping bond becomes negative at t ~750 fs, at the onset of bond nucleation (green curve and circles in Fig. 4.14). At ~800 fs also, the frequency associated with black squares flips and turns negative, rapidly followed by other reactive chain modes. At 950 fs, in correspondence with the first fluctuation of the green curve (circle), the modes associated with the red, non-reactive chains become unstable and keep showing negative frequencies till 1050 fs, past the second fluctuation value of green and violet curves. The maximal wavenumbers of the red chains (-75 cm^{-1}) are considerably smaller than the blue chain modes (-270 cm^{-1}). Nonetheless they strongly influence phase transition by spreading the initial instability associated with single bond nucleation events over the whole material *via* chemical bonds.

The inset of Fig. 4.14, shows the potential energy profile along the reaction coordinate for a representative trajectory. For the $hR8 \rightarrow cI16$ transformation, $hR32$ is initially formed, which is structurally and energetically similar to $hR8$, before a major reconstruction towards $cI16$ takes place. This allows splitting of the overall reconstruction into two "elementary" steps, $hR8 \rightarrow hR32$, followed by $hR32 \rightarrow cI16$. The intermediate can be formed thanks to the asynchrony of chain reconstruction, as $hR8$

and $hR32$ differ by just a few bonds. To the extent that this solid transformation can indeed be understood as a set of "molecular" steps, the Hammond postulate [237], may warrant some guidance. The $hR32$ intermediate is structurally and energetically closer to $hR8$ and is formed first. The second step involves more bond reshuffling and a larger activation barrier, as it contains the core of the reconstructions. On forming $hR32$ first, $hR8$ would be the kinetic product, $cI16$ the thermodynamic one.

To visualize the $sp^3 \rightarrow (sp^2 + p) \rightarrow sp^3$ sequence of re-hybridization around Ge inside reactive chains, Wannier functions were calculated, Fig. 4.15. In $cI16$ ($t = 0$ fs) four-bonded Ge shows four equal sp^3 Wannier functions. Around $t = 880$ fs, the first bond is broken, under formation of a trigonal planar center (3 Wannier functions) and of a lone pair along the chain (contracted Wannier function, associated with one Ge only). Geometry fluctuations cause the lone pair to slightly expand and contract again ($t =$ 880-960 fs) while the intermediate arrangement is maintained. Eventually, a new bond is formed under inversion of the pristine tetrahedral arrangements at $t =$ 960-1040 fs. This is indicated by a rapid change of spread and shape of the corresponding Wannier function along the chain axis. Minor rearrangements lead to

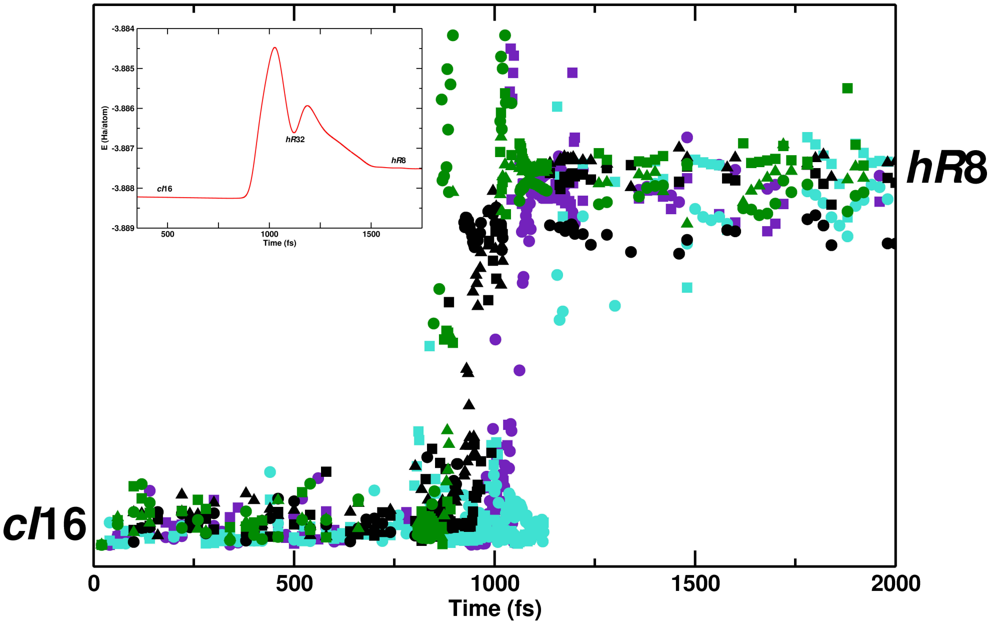

Figure 4.14 – Evolution of WFC relative distances, calculated for each bond and each reactive chains (four blue chains in Fig. 4.11 (b)) along the time coordinate of the framework reconstruction transition. Different colors (green, black, purple and turquoise) refer to distinct chains, while distinct symbols (square, circle and triangle) refer to different bonds within a single chain. Inset: potential energy profile with $hR32$ as the intermediate phase. Zeroth time frame is arbitrary set. The y axis corresponds to relative displacements of WFC along the transition and is used here as an order parameter, able to distinguish between initial and final states.

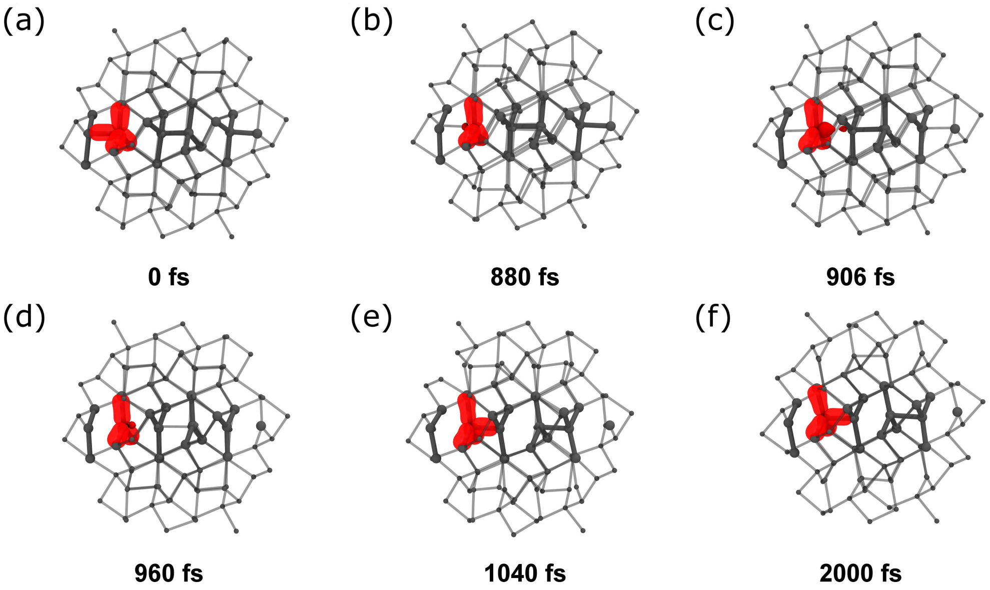

Figure 4.15 – sp^3-projected, maximally-localized Wannier functions for the Ge atom at which the transition is commenced. The evolution of bonds (transparent lobes) and lone pair (opaque lobe) are shown at different snapshots. For clarity, only the positive lobe of the MLWFs is rendered. The chain and time frames are the same as in Fig. 4.13. Zeroth time frame was set at $cI16$.

$hR8$ at $t = 2000$ fs.

Quasi-regularly spaced chains appeared in the intermediate regions of the phase transition. They reconstruct by symmetrically pairing atoms into alternating localized bonds in a sort of Bond Density Wave (BDW) [238], reminiscent of a 1D Peierls distortion. Nonetheless, our analysis has shown that different modes coexist while the networks reconstruct. Particularly, no chain acts as a truly isolated 1D system, as a non-reactive "red" mode is supporting bond rearrangement. While the rearrangement of a single chain may be termed "Peierls-patterned", a 1D chain is not acting here as the fundamental instability controlling the process.

The effect of periodic boundary conditions needs careful consideration when studying nucleation geometries. However, we believe our results to be transferable to larger systems, as the initial "nucleus" was determined to be a single bond switching, which can occur anywhere within a reactive chain. Furthermore, the non-concerted character of the bond shuffling process allows for the formation of an intermediate metastable structure ($hR32$), which we expect to be detectable in high-pressure experiments with an appropriate (de)compression protocol. This would represent a rare case of experimental verifiability of a solid-solid phase transition mechanism, and a major step towards controlling reactivity in the solid state.

In conclusion, by atomistic simulations we have characterized the $hR8$ to $cI16$ phase transition as a chemical isomerization reaction, which is taking place in the solid state. Sets of reactive chains are formed in the intermediate transition region. Within such reactive channels, distinct sets of bonds can rearrange from one structural pattern into the other one. Framework reconstruction is commenced by local bond nucleation, which is propagated along chains. The propagation step is assisted by a second set of chains, which is forming around the transition state only, but which is not accommodating any event of bond breakage or bond formation. In the reactive chains, bonds are reshuffled by Ge sp^3 tetrahedra inversions, with the formation of intermediate trigonal-planar geometries known from S_N2 type reactions.

4.3 High pressure behaviour of Ge($cF136$) clathrate

As it has been reported so far, group-IVa elements present a wide selection of interesting properties. The global energetic demand and the need for improved energy materials, have recently motivated to look for better thermoelectric materials. A somewhat forgotten class of tetrels compound, clathrates [239, 240], is enjoying a renewed interest for it shows promising properties. This has promoted extensive investigations on electronic, magnetic, spectral and transport properties of clathrates and related structural types [241–246]. The recent discovery of superconductivity in a Na-Ba-Si compound with the clathrate-I structure has considerably contributed to the boost interest in these systems [247–249]. Furthermore, clathrates are a step closer to porous silicon and to the valuable optical properties that are associate with it [250, 251]. This has led to the search for reliable and reproducible ways for the synthesis of silicon and germanium clathrates in high yields and with defined stoichiometry [252].

Although almost-empty $Na_{1-x}Si_{136}$ has already been reported [253, 254], the synthesis of guest-free germanium clathrate has been long time unsuccessful. Only recently [183] a high-yield synthesis of germanium with the empty clathrate-II structure through the oxidation of Ge_9^{4-} Zintl anions in ionic liquids under ambient conditions was proposed. The approach demonstrated the potential of ionic liquids as media for the reactions of polar intermetallic phases and the advantages of low-temperature synthesis.

Even if $\square_{24}Ge_{136}$ ($\square$ means a vacancy on a possible metal position) have been caracterized [183] both from the structural and electronic point of view, the pressure-induced structural changes of this material and its behaviour upon compression remain to a large extent an open issue. A large number of amorphous phases are encountered during the compression and just partially clarity on the final products of this procedure has been reported [184] (detailed references can be found in Section 4.1).

In this work, we extensively investigate the response to compression of the clathrate type-II structure Ge($cF136$) by means of systematic metadynamics calculations at different temperature and pressure regimes. We were able to identify two main pressure and temperature protocols. At relatively low pressure (P = 2.5 GPa) a quick transition from the clathrate open framework to the bct-5 novel phase proposed in the last Section, was observed. Nonetheless, pure bct-5 phase can be hardly stabilised and several amorphous-Ge have been found. The situation is significantly better if we operate at liquid nitrogen temperature (77 K), within reach of a typical experimental set up adopted in the study of solid state phase transitions. In this case we noticed a smoother transition to bct-5, that remains stable for a longer simulation time. A similar temperature dependece's behaviour, has been also observed in the case of higher pressure regimes (P > 5 GPa). In this case the bct-5 phase is completely bypassed and the Ge($cF136$) structure directly undergoes to β-tin ($tI4$). Stabilization of the product is again obtained on lowering the temperature. This procedure seems the most promising way for a feasible production of the electronical outstanding bct-5 modification. For the first time, simulations can be used to predict different regimes of reactivity, which yield different product under controlled, in the simulation setup explicitly addressable conditions.

4.3.1 Methods

Despite the pronounced differences in atomic volumes, the compressibility of the new clathrate Ge($cF136$), as revealed by the bulk moduli $B_0 = 76 \pm 6$ GPa [184], is significantly close to the value of cubic diamond Ge($cF8$), $B_0 = 75$ GPa [255]. Furthermore, from the energetic point of view, calculated total energies indicate that Ge($cF136$) is the lowest-lying modification among the Ge metastable ones. Energy differences with cubic diamond, indeed, are of ΔE =-0.01 eV/atom in the case of the clathrate and ΔE =-0.11 eV/atom in the case of γ-Ge ($cI16$, sp. gr. $Ia\bar{3}$), usually considered to be the energetically closer to Ge($cF8$). For these reasons, the clathrate potential energy well is extremely deep. Therefore, in order to approach the study of possible phase transitions, the use of molecular dynamic accelerated technique, like metadynamics here, is mandatory. All runs were performed with at least 34 atoms in the simulation box which served as a collective (6-dimensional) variable. This is the minimum number of atoms necessary to describe the clathrate II-type phase and all the already known phases either open or dense (comprising the new Ge($mC16$) and bct-5 ones) are included. Each metadynamics metastep consisted in a molecular dynamics run in the NVT ensemble for a simulation time of 0.5 ps (timestep 2 fs) at either 300 K or at liquid nitrogen temperature, 77 K, depending on the regime studied.

All metadynamics runs were performed with a DFT molecular dynamics layer as implemented in the SIESTA [130,131] package. The extensive and systematic calculations used to simulate several compression's protocols, were performed by expanding electronic states by a single-ζ basis set constituted of numerical orbitals with a norm-conserving Troullier-Martins [132] pseudopotential description of the core electrons. In this way a strong reduction of computational times is provided, giving nonetheless, the right topology and energy differences of all the Ge allotropes under study. The charge density was represented on a real-space grid with an energy cutoff of 200 Ry. A Monkhorst-Pack k-point mesh of $2 \times 2 \times 2$ ensured the convergence of the electronic part, particularly important in the description of amorphous high coordinated phases.

To get an overall impression of the structure evolution in the metadynamics simulations, we first calculated the average size of the shortest circuits [233] in the structures. The average circuit size for the $cF136$ structure is 5.11765 and for the β-tin it is 4.66667. As expected, the average circuit size should decrease along the transition from the clathrate phase to the β-tin phase since most of 5-rings disappear. To quantitatively discriminate between the β-tin and bct-5 networks, we calculated coordination sequences (up to the 3rd shell), which were used to characterize the structures from the metadynamics simulations. For β-tin the coordination sequence reads (for each atom): $\{6, 22, 46, 82, \dots\}$, for bct-5 it is (for each atom): $\{5, 16, 33, 58, \dots\}$. Coordination sequences were also used to estimate the percentage of a phase (either β-tin or bct-5) in intermediate structures as follows: We counted the number of atoms having the coordination sequences $\{5, 16, 33\}$ and $\{6, 22, 46\}$. Dividing the number of atoms with a coordination sequence specific for a given phase by the total number of atoms in the simulation box, we obtained the percentage of this phase in the intermediate(s).

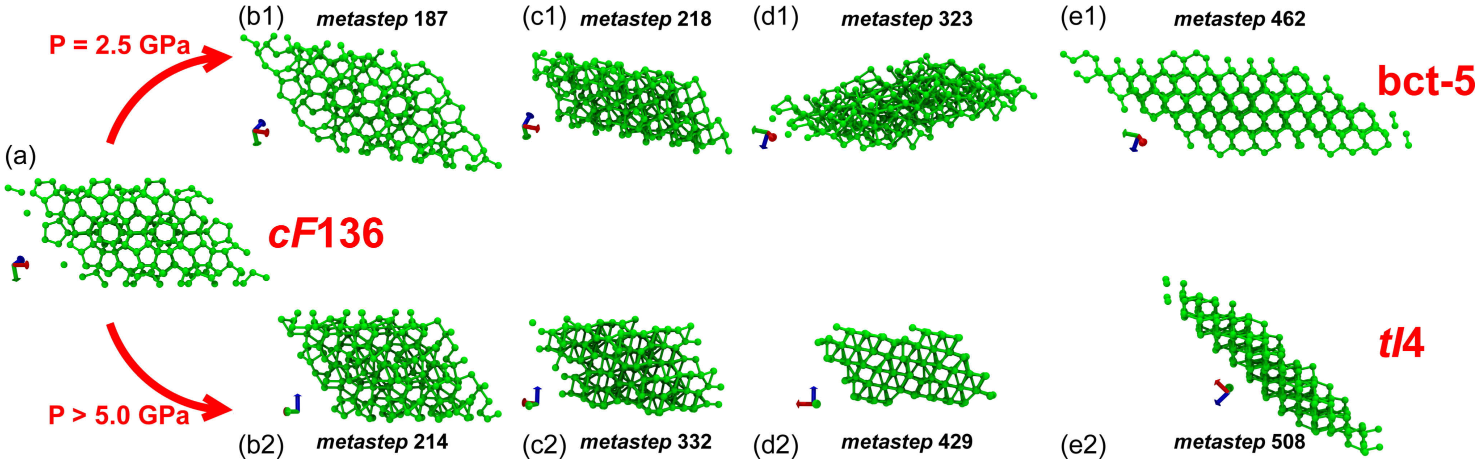
(b1) metastep 187
(c1) metastep 218
(d1) metastep 323
(e1) metastep 462
P = 2.5 GPa
bct-5
(a)
cF136
tI4
P > 5.0 GPa
(b2) metastep 214
(c2) metastep 332
(d2) metastep 429
(e2) metastep 508

Figure 4.16 – Meta-trajectories at two different pressure regimes and T=300 K. Starting from the Ge($cF136$) clathrate (a), and depending on the pressure applied, different structure are encountered. At low pressure, an intermediate clathrate Ge($mC68$) is initially found (b1), and then through a large number of amorphous phases, e. g. (c1) and (d1) the system is attracted by the bct-5 basin (e1). The meta-trajectory follows a significantly different path in the case of an high pressure transition: the amorphous structure are relatively larger than in the previous case, e. g. (b2), (c2) and (d2), and the "perfect" Ge($tI4$) structure is caught only after several steps (e2), while the bct-5 one is completely bypassed.

4.3.2 Results and Discussion

At room temperature, a strong dependence on the amount of pressure applied to the system has been observed. Upon mild compression, around 2.5 GPa, the Ge($cF136$) clathrate undergoes a transition to the bct-5 modification, whereas at higher pressure, 5.0 GPa or more, the transition is rather direct to the β-tin structure. Fig. 4.16, shows some snapshots of the meta-trajectories at different regimes. As can be noticed, there is a large number of amorphous Ge structures along each transformation, therefore, a unique analysis tool would not be enough for an exhaustive and satisfactory description of the phase transition process. To evaluate the density of each snapshots along the trajectories, the coordination sequence and ring topology (calculated as described in the Section above), have been used. These, together with the total percentage of the final phase that is formed, univocally characterize a certain phase transition. Furthermore, by means of the enthalpy profile of the transitions, we were able to follow the energy fluctuation along the transition meta-paths, which may be indicative of the existence of additional intermediate steps.

At first, we investigated the high-pressure response of Ge($cF136$) at ambient temperature. The three graphs in Fig. 4.17, report a complete analysis of the meta-trajectory that connects the type-II clathrate to the Ge($tI4$) phase. The percentage of pure β-tin species is always reported on the right-X axis (blue curve in the graphs), while each segment (distinguished by with different colours) refers to a segment of distinct structural features of the free energy surface. The high stability of the Ge($cF136$) is reflected on the long time that it takes to escape its attraction basin. Only after 100 ps ($\sim$210 metasteps) a sudden enthalpy drop (see Fig. 4.17 (c)) is observed as the system moves on into an PES area where amorphous but rather dense structures are observed (black segment): the average circuits size and enthalpy (Fig. 4.17 (a) and (c)) display minima, while the coordination sequence (Fig. 4.17 (b)) rapidly increases. Subsequently, the system decompresses ($\sim$10 metasteps) and remains amorphous (as measured by the indicators mentioned above) even if a certain tendency towards forming of the β-tin phase (blue peaks) around the 265th metastep can be discerned. A conspicuous part of the meta-trajectory consists of amorphous structures that do not show particular differences in volume or coordination (blue segments gather such systems) with respect to each other. It is worth focusing only on three narrow windows of the meta-trajectory. Between metastep 295 and 305 (labeled with a violet segment) a clear peak in the circuit size (a) can be seen, as well as a marked drop in the coordination sequence (b). In this region thermal fluctuations bring the system close to the β-tin attraction basin, but the structure remains rather expanded and stays off the basin itself (as also indicated by the absence of a percentage peak, which would indicate phase formation). Furthermore, between metastep 370 and 400 (green segment) plateaux can be recognized by inspection of the circuits size (a), coordination sequence (b) and enthalpy (c) graphs: these structures related to rock-salt (that does not actually exist for Ge and can be to some extent an artefact of the small basis set used) but pronouncedly distorted and dense, as displayed by the coordination sequence average $\{6, 18, 42\}$ against $\{6, 18, 38\}$ of a pure rock-salt phase. A similar occurrence of a denser structural motif is observed around steps 405 and 425, where a simple hexagonal structural pattern is closely matched, nonetheless

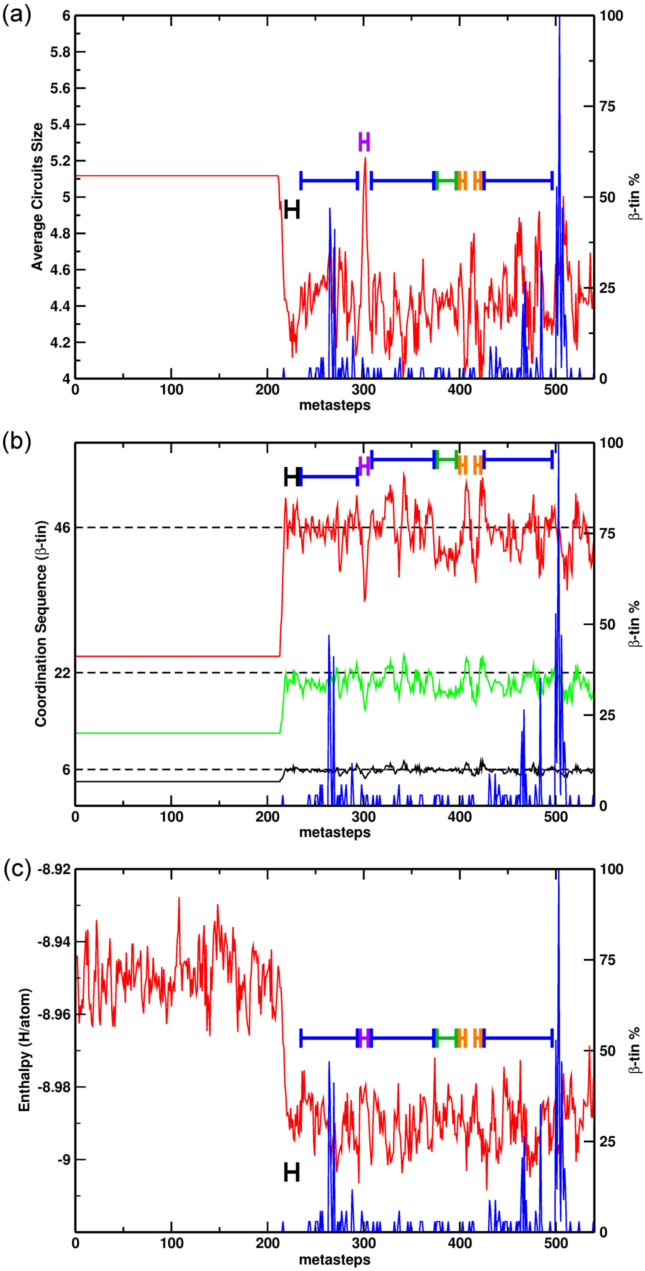

Figure 4.17 – Average circuits size (a), coordination sequence (b) and enthalpy of each meta-trajectory step for β-tin at 300 K and 5 GPa. The blue curve in each graph represent the total percentage % of β-tin in each snapshot and the segments represent a different structural "area".

with a slightly expanded volume as it can be inferred from the coordination sequence of {7.5, 25, 54} against {8, 26, 56} of the ideal $hP1$. Cell fluctuations are characterisitc of the metadynamics methods, and contribute to driving the systems to the final β-tin basin, into which the whole system has transformed (100% structural peak, see Fig. 4.17) after ~500 metasteps.

The same kind of analysis is reported in Fig. 4.18 for the case of the meta-trajectory that connects Ge clathrate to bct-5. The percentage of pure bct-5 species is reported, again, on the right-X axis (blue curve in the graphs) and each segment (differently coloured) defines part of the PES with close structural features. The relatively low pressure allows for a meta-trajectory, which is more structured, that is reach in features. As a matter of fact, after ~175 metasteps, the Ge($cF136$) structure finally deforms into an intermediate that can be partially quenched (black segment in Fig. 4.18). We identify it with the Pearson symbol Ge($mC68$) and its structure is reported in Fig. 4.16 (b1). This clathrate-like structure, significantly high in energy ($\Delta E = E_{cF8} - E_{cF136} = 0.03$ eV/atom, while $\Delta E = E_{cF8} - E_{mC68} = 0.16$ eV/atom), was optimized at zero Kelvin. Furthermore a short molecular dynamics run (t=10 ps, P=0 GPa, T=300 K) didn't show any structural deformation. Nonetheless, a pronounced negative vibrational frequency has been found in the phonon dispersion analysis: it is this soft mode that drives the system, after only ~25 metasteps, to another structural area (blue segment in Fig. 4.18). Here a single structure can hardly be extracted, on the other hand a number of intermediate configurations between Ge($cF136$) and a denser phase (somehow similar to β-tin), can be seen. Confirmation can be gained from Fig. 4.18: the average circuits size (a) for this segment is ~4.9, intermediate between ~5.1 for $cF136$ and ~4.67 for β-tin; the coordination sequence (b) is increased, meaning that the structures are denser; the enthalpy plateaux (c) stands halfway between the two (see also Fig. 4.17 (c) for comparison). Thereafter, a long part of the trajectory, ~175 metasteps (violet segment), consists of amorphous structures that occasionally show local diamond-like features (green segment), which correspond to maxima in the average circuits size and in coordination sequence, to enthalpy minima, or to structures close to rock-salt (orange segments), which eventually end in the basin of bct-5 as clearly indicated by blue peaks in each graph. In general, there is a number of attempts to grow a particular structural pattern along a metadynamics run, which may suggest failed or disfavoured paths. To which extent these features can be recast in a context of nucleation and growth remains to be elucidated. Nonetheless, the central indication of metadynamics is the one of distinct paths (over different intermediate, more or less elusive), which lead to the formation of different product, β-tin and bct-5 for instance

It appears clearly that large temperature fluctuations impair the ability of the system to promptly relax into an attraction basin corresponding to a proper phase. Structural pattern close to simple hexagonal, cubic diamond or rocksalt-related may be part of the complex landscape of intermediate structures of the transition. However, to properly separate relevant configurations to fortuitously visited non-stationary regions, a different approach may be needed. Particularly, a more precise characterization of the attraction basin of bct-5 and beta-tin is needed. Those modification are found in different metadynamics run indeed. However, the corresponding trajectories visit the respective attractors for a limited period of time only. One of the reasonable

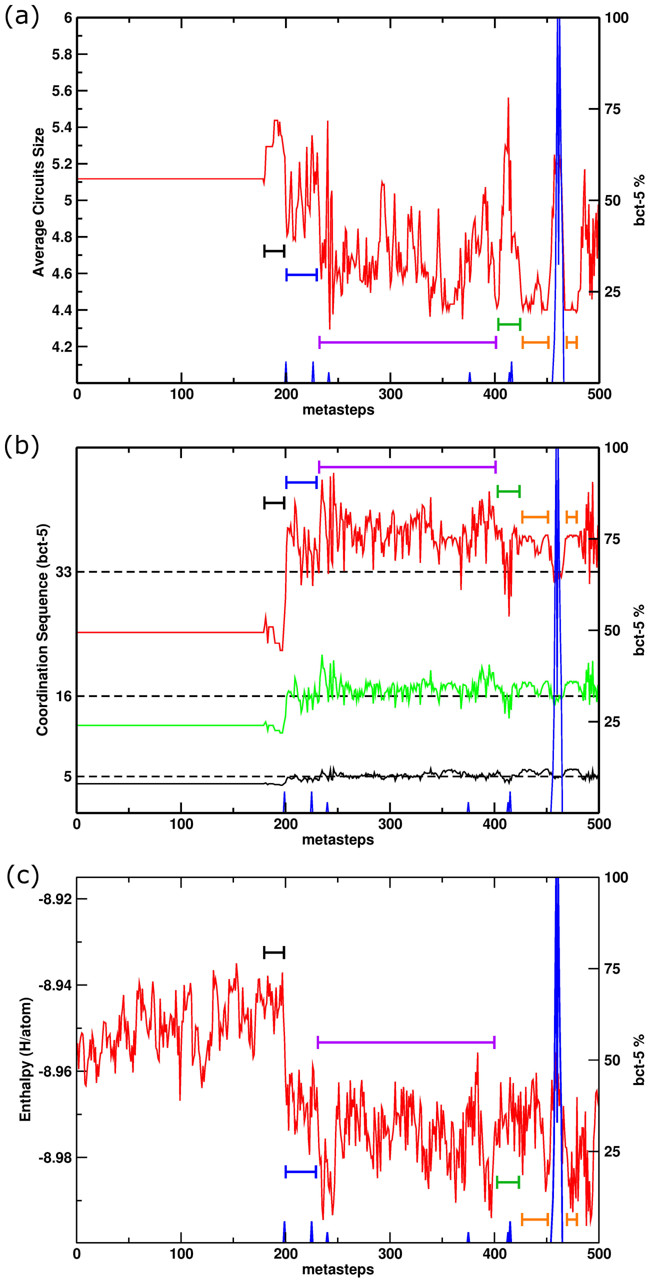

Figure 4.18 – Average circuits size (a), coordination sequence (b) and enthalpy of each meta-trajectory step for bct-5 at 300 K and 2.5 GPa. The blue curve in each graph represent the total percentage % of bct-5 in each snapshot while the segments represent a different structural "area".

choices is to lower temperatures. On the one hand, this echoes a natural experimental choice, which is meant at affecting nucleation patterns. On the other hand, a lower temperature allows for a computational setup with reduced Gaussians, which will do for a smoother trajectory. Along this line of reasonings, a set of metadynamics simulations was implemented at liquid nitrogen temperature.

Starting again with the analysis of the meta-trajectory that drives the system from the clathrate $cF136$ to the β-tin (Fig. 4.19), at 5.0 GPa of pressure, but this time at 77 K of temperature. The lower temperature has immediate consequences on the aspect of the resulting trajectory: first, the β-tin phase was clearly locked in, and remained stable for over 20 steps, as highlighted by the blue line in each graph, Fig. 4.19. Second, the transition is markedly smoother as can be deduced from the less steep drop of the enthalpy profile. As the system escapes the $cF136$ free energy well, an other open framework modification is encountered (black segment). It remained detectable for almost 10 metasteps and it is clearly denser than the initial structure, with a minimum in the average circuit size (a) and increased coordination sequence number (b). This is less of a metastable phase than rather an activated intermediate. Thereafter (blue segment), the transition begins towards the actual product and different amorphous phases are recorded on the way to it. Around the 380th metastep (violet segment), the system re-crystallizes in a β-tin like structure (maximum in average circuits size (a) and minima in coordination sequence (b) and enthalpy (c)). The system spends only a few steps therein, since the cell fluctuations bring it back to an amorphous stage (green segment), which is the gateway to the exact β-tin basin. Between two 100% peaks of β-tin phase, other amorphous phases are touched upon, while a short segment of the meta-trajectory displays feature that are close to rock-salt motifs (orange segment). Nonetheless, it can be expected that these effects can be further reduced by tuning the choice of the Gaussian parameters in the simulation setup. Due to the extremely high computational costs of such *ab initio* and systematic investigations, gaussian width and height have to be kept reasonably large: this way, it is really difficult to guess the best combination of gaussian's parameters for each trajectory. It has to be recalled that the system is truly multidimensional, as such any small perturbations may drive the system into a completely different regime, particularly with respect to non-stationary points and fortuitous intermediate configurations. The strategy here consists rather in collecting enough statistics on the occurrence of particularly structural patterns, in order to properly weight the statistical relevance of an intermediate. While methods like TPS are tuned on refining the picture of intermediate structures, metadynamics is reliable on the identification of minima, while any activated configuration that is found along the trajectories may only be the result of a more or less strong fluctuation in cell parameters.

Lowering temperature improved the product stability of $cF136$ compression in the high pressure regime. It is well known [184,199] that β-tin is unstable at low pressure. What we expected, hence, is that keeping the temperature low and decreasing pressure, it would be possible to stabilize the bct-5 modification, obtaining two reaction paths as in the case at 300 K. It appears quite clearly that a proper manipulation of the type-II clathrate could represent the gateway towards an efficient synthesis of the novel bct-5 superconducting phase. In this respect, metadynamics has been used

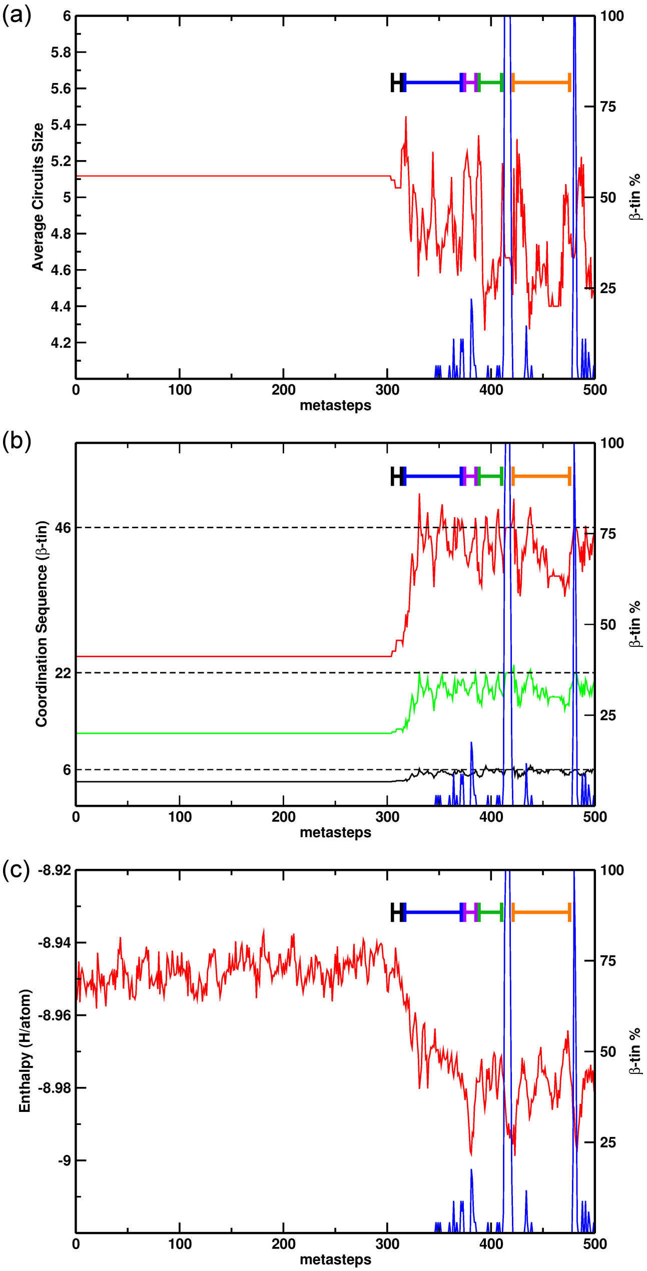

Figure 4.19 – Average circuits size (a), coordination sequence (b) and enthalpy of each meta-trajectory step for β-tin at 77 K and 5.0 GPa. The blue curve in each graph represents the total percentage % of β-tin in each snapshot and the segments highlight "areas" characterized by a particular structural pattern, including fluctuations.

here in a different way than its standard filed of application, that is the bare structure prediction. In fact, it can be used as a tool for exploring different reactivity paths for changed external conditions: detailed indications of the transition mechanism are not easily extrapolated for the reasons cited above, nonetheless several informations about the energetic and structural surroundings of each stable and meta-stable modification encountered, as intermediate structures, are discovered.

5

High-Performance Thermoelectric Materials

The energy demand and the urgency for a more articulated setup of energy management, has motivated focused efforts particularly with respect to re-collecting wasted heat, within an overall more efficient energy production and storage framework. To lower the environmental impact due to fossil fuel combustion, sustainability calls for an articulated choice of renewable sources like solar, biomass, wind, geothermal and others. Nonetheless, with about two-thirds of all used energy being lost as wast heat, a viable energy supply channel can rather be the recovery of this heat via thermoelectric generators. Sources of heat wasting are as disparate as home heating, automotive exhaust, combustion, sunlight, chemical reactions, nuclear decay and many others. Therefore, thermoelectric materials can play a key role in both primary power conversion-generation and energy conservation.

Additional advantages come from the fact that thermoelectric generators are solid-state devices mechanically inactive, hence silent, operationally reliable and portable, thus ideally suited for small-distributed power generation [256], which is known to be energy efficient with respect to centralised power plants, as there is no energy waste due to high-voltage via cable electricity distribution. Advances have been already achieved in replacing car parts and compression-based refrigeration fluids [257].

The discussion about how important can be the role of thermoelectrics in tackling the compelling “energy problem” is a hot topic in the scientific community and the answer to this question is strictly related to the efficiency of these materials [258]. Their relatively low efficiency has limited cost-effective applications in most cases [259]. However, as also reported in Chapter 4, a renewed interest in thermoelectrics began already in the 90s when the increased computational power allowed for theoretical predictions, which suggest thermoelectric efficiency enhancement through nanostructural engineering. This in turn led to experimental efforts to demonstrate the proof-of-principle and to synthesize higher-efficiency materials [260]. At the same time, complex bulk materials (such as skutterudites [261], clathrates [262] and Zintl phases [263]) have been explored and found to be very promising candidates as high efficiency thermoelectric materials.

Thermoelectric materials performances directly depends on temperature gradient (ΔE) and on an intrinsic parameter, the thermoelectric figure of merit (ZT). In order to maximise the ZT and to increase efficiency in both power generation and cooling of a certain thermoelectric material, a variety of conflicting properties need to be optimized. Thus, the challenge to create high ZT thermoelectric materials lies in achieving simultaneously high electronic conductivity (σ), large thermoelectric power (absolute value of the Seebeck coefficient, S) and low thermal conductivity (κ) in the same solid [256–259, 262, 264]. These parameters are connected to the mentioned thermoelectric figure of merit ZT,

$$ZT = \frac{\sigma S^2 \mathrm{T}}{\kappa}, \tag{5.1}$$

where T is the absolute temperature. These properties are directly related to the electronic structure of each material and are not fully independently controllable. Low carrier concentration insulators and even semiconductors have large Seebeck coefficient, but of course their conductivity is pretty small. A compromise between the two is thus unavoidable and usually the key to achieving high performance is to find the efficiency peak of the power factor σS^2. Thermal conductivity κ has two different contributions, one coming from the lattice vibrations, κ_{L} and the other from the carrier thermal conductivity, κ_{el}. Intuitively, the thermal conductivity $\kappa = \kappa_{\mathrm{L}}+\kappa_{\mathrm{el}}$ must be low as a large ΔT must be maintained; a large thermal conductivity will short the thermal circuit. The compromise between all these characteristics is clarified in Fig. 5.1, which is taken from Review [265].

Moving from these considerations, two possible approaches aimed at increasing the ZT are feasible: either the power factor is maximized and/or the thermal conductivity is minimized. In this Chapter, lattice properties of lead chalcogenides PbX (X=Se, Te) will be focused on as the reduction of κ_{L} have been proved to allow for increasing global efficiency in this class of materials. The first generation of thermoelectric devices, that were developed more then forty years ago, presented an efficiency of ~5-6% with a ZT of ~0.8-1.0 for the material they were composed of. Thanks to new approaches to the synthesis of such bulk thermoelectrics, mainly oriented to the reduction of the lattice thermal conductivity, a second generation of materials have been yield, reaching an efficiency of ~11-15%, doubling thus the first generation values. The hope for the future is to go farther in order to exceed the 20% of efficiency and to make these materials main characters in the energy era [266].

5.0.3 Lowering the Thermal Lattice Conductivity

From the phonon point of view, glasses exhibit some of the lowest lattice thermal conductivities since, in a glass, thermal conductivity is not related anymore to transport via phonons but is rather an energy random walk through a lattice. Nonetheless, the big hindrance that make them useless in thermoelectric applications, is the total lack of "electron-crystal" behaviour. In comparison with crystalline semiconductors the carrier mobility and thus electronic conductivity is severely reduced due to the increased electron scattering. Therefore, thermoelectric applications require an atypical class of materials, able to show "phonon-glass/electron-crystal" features [267]. The "electron-crystal" statement stems from the fact that crystalline semiconductors display a better compromise between high thermoelectric factor S and high electrical conductivity. The "phonon-glass" feature is needed in order to reduce as much as possible the lattice thermal conductivity.

To achieve this goal, three main strategies have been shown to be effective. The first one consists in scattering phonons within the unit cell increasing the intrinsic disorder by creating point defects as interstitials, vacancies or by alloying (solid solutions) [268]. The second approach is more related to topological separation of the electron-crystal from the phonon glass. The challenge here is to obtain a preponderant glassiness in the material without loosing the crystallinity of the electron-transport region. The last strategy amounts to increasing interfaces and phase domains in order to scatter phonons. In this direction, multiphase nanoengineering as well as mixed nanometer scale [260] composites are actually the more promising synthesis prespectives.

5.0.4 Lead Chalcogenide in Thermoelectronics

In binary lead chalcogenides thermal conductivity is dominated by the lattice contribution (κ_L), while the electronic part remains comparatively small. In this class of compounds phonon scattering is typically achieved for example by impurity modes or alloying, which effectively lower thermal conductivity [266, 269]. PbTe is a good thermoelectric material in the so-called intermediate temperature regime (500-900

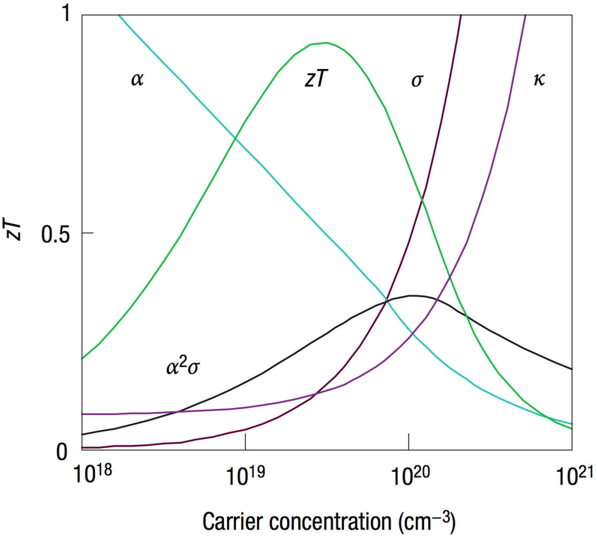

Figure 5.1 – Maximizing the efficiency (ZT) of a thermoelectric involves a compromise of thermal conductivity (κ; plotted on the y axis from 0 to a top value of 10 W m^{-1} K^{-1}) and Seebeck coefficient (α; 0 to 500 μV K^{-1}) with electrical conductivity (σ; 0 to 5.000 Ω^{-1} cm^{-1}). Good thermoelectric materials are typically heavily doped semiconductors with a carrier concentration between 10^{-19} and 10^{-21} carriers per cm^3. The thermoelectric power factor $\alpha^2\sigma$ maximizes at higher carrier concentration than ZT. The difference between the peak in $\alpha^2\sigma$ and ZT is greater for the newer lower-κ_L materials. Trends shown were modelled from Bi_2Te_3, based on empirical data in Ref. [3]

K) [270]. Single-crystalline PbTe nanowires grown by chemical vapor transport show reduced thermal conductivity [271]. The thermal conductance of 180 nm diameter, micrometer long PbTe nanowire is around 11 nW/K at 300 K, $\sim 10^3$ times smaller than for an equally thick layer of bulk PbTe [272]. Different from bulk compounds, nanocomposites, endotaxial precipitates and mesoscale grain boundary engineering are emerging paradigms for a broader scattering of phonon heat transport. Along this line Hsu *et al.* achieved exceptionally high ZT$\sim$2.2 at 800 K in LAST ($AgPb_mSbTe_{2+m}$) alloys [273]. Enhanced ZT is observed in $PbTe/PbSe_xTe_{1-x}$ quantum dot superlattice structures, with a value of ZT $\sim$2 at ambient temperature [274]. Nanostructured PbTe-PbS materials are prepared by spinodal decomposition and nucleation-and-growth techniques, with thermal conductivity values as low a $\kappa_L \sim 0.4$ W/m K [275]. Together with nanostructuring, the presence of Tl impurity levels in p-doped PbTe leads to a doubling of ZT (ZT$\sim$1.5) at 773 K [276].

In PbTe based materials the good thermoelectric performance is largely due to the low lattice thermal conductivity. However, Te is not only rare in the Earth's crust but also increasingly used in a number of other applications, such as steel metallurgy, solar cells, phase change materials for digital recording, and thermoelectric cooling devices based on Bi_2Te_3 [277]. Attractive Te-free alternatives to rock-salt PbTe are the congeneric PbSe and PbS, which have remarkably similar electronic and structural properties [278, 279]. Furthermore, even if PbSe-based materials usually have a lower figure of merit in the mid temperature range (around 500K) compared to PbTe, in doped PbSe the Seebeck coefficient does not exhibit the usual [280] "turn-over" at high temperature, but keeps increasing even at 1000K, thus making it a good alternative to PbTe especially at higher temperatures, owing also to its higher melting point [279].

5.1 PbTe-PbSe Nanoengineering

One particular technique, nanoengineering, has a long record of successes in lowering the lattice thermal conductivity in lead chalcogenide-based materials. This approach, indeed, brought to a remarkable enhancement of the figure of merit ZT by reducing the κ_L through the placement of suitable nanoscale precipitates in the matrix. Examples of this kind of improvement can be found in the study of $AgPb_mSbTe_{2+m}$ (Ref. [273]; LAST), $NaPb_xSbTe_{2+x}$ (Ref. [281]; SALT) and PbTe-PbS (Ref. [282]) materials. Alternatively, p-type $PbTe_{1+x}Se_x$ (Ref. [283]) and Tl-PbTe (Ref. [276]) also have excellent thermoelectric properties, arising from multiple valence bands and from the introduction of a density-of-states distortion in the valence band, respectively. The performance increase is generally related to the fact that nanostructuring obstructs heat transport within the material without affecting the carrier (holes or electrons) mobility [284]. However, the inclusion of interfering agents in a bulk thermoelectric materials usually affects phonons with medium and short mean free path ($\sim$3-100 nm). A further and potentially more significant reduction can be achieved scattering the phonons with longer mean free path, i.e at lower frequencies. For this purpose an additional nanostructuring at the mesoscale ($\sim$0.1-1 μm) appears essential [269]. This last point will be the object of a feasibility study, which is discussed in Section 5.2.

Despite existing paradigms, a controlled design and synthesis of thermoelectric materials remains an involved task. Atomistic simulations may represent the method of choice towards a deeper understanding of the thermoelectric phenomenon, as they provide the necessary resolution for elucidating the impact of defects, the role of interfaces, nanostructuring and morphology. Furthermore, calculations can provide benchmark values to assist the difficult experimental task of measuring thermal transport, in particular in nanoscale materials [285]. In this Section we investigate the atomistic details of (sub)nanostructuring on lowering thermal conductivity in PbTe-PbSe mixed systems, using solid solutions (alloys) as reference systems. We use equilibrium molecular dynamics (EMD) simulations to compute the thermal conductivity of several PbSe/PbTe systems. The systems considered are PbTe-PbSe solid solutions of different composition ($\mathrm{PbTe_{0.25}Se_{0.75}}$, $\mathrm{PbTe_{0.50}Se_{0.50}}$, $\mathrm{PbTe_{0.75}Se_{0.75}}$), PbTe/PbSe layered superlattices (Fig. 5.2 (a)) and PbSe (PbTe) spherical precipitates of variable diameter embedded in a PbTe (PbSe) matrix (Fig. 5.2 (b)). The latter comprises spherical inclusion of different size on the one hand (Fig. 5.2 (c)) and dense, "eight-in-a-box" nano-dot geometries (Fig. 5.2 (d)).

5.1.1 Methods of Heat Transport Calculation

The realistic modeling of material strongly benefits from the use of empirical interaction potentials of a simple given analytical form, which allow for the simulation of much larger systems over longer time scales, compared to methods based on first principles. For binary semiconducting materials a simple interatomic potential was shown to very reliably account for structural and elastic properties, and to be very accurate even in the description of phase transitions [286]. Nevertheless, the restricted number of available parameters limits this approach. Additionally, parameters adapted to binary compounds must be transferable to mixed system, which is rarely the case. To provide suitable potentials for heat transport calculations in PbSe/PbTe, transferable potentials for the binary compounds PbSe and PbTe were parameterized. The interaction between the atoms was described by a sum of Lennard-Jones (LJ) and Coulomb terms

$$U_{\mathrm{ij}}(r_{\mathrm{ij}}) = U_{\mathrm{Coul}}(r_{\mathrm{ij}}) + U_{\mathrm{LJ}} = \frac{q_{\mathrm{i}} q_{\mathrm{j}}}{4\pi\epsilon_0 r_{\mathrm{ij}}} + 4\epsilon_{\mathrm{ij}} \left[\left(\frac{\sigma_{\mathrm{ij}}}{r_{\mathrm{ij}}} \right)^{12} - \left(\frac{\sigma_{\mathrm{ij}}}{r_{\mathrm{ij}}} \right)^{6} \right], \tag{5.2}$$

r_{ij} is the distance between atoms i and j; ϵ_{ij} and σ_{ij} are the LJ parameters; q_{i} and q_{j} are partial charges on atoms i and j; and ϵ_0 is the dielectric constant of vacuum. Only LJ coefficients of pairwise equal atoms are fitted. Cross terms are obtained from Lorentz-Berthelot mixing rules. For PbSe, an existing set of parameters was taken from literature [287]. Therein, four LJ coefficients and partial charges (5 parameters in total) were fitted to lattice and elastic constants. In this work the ϵ_{ij} LJ coefficients were refitted using the GULP [288] code, for the parameters to additionally reproduce the thermal conductivity κ_{L} of PbSe at room temperature (300 K) and its temperature dependence (300-1200 K). To construct transferable parameter sets, ϵ_{ij} and σ_{ij} of Te were fitted on PbTe lattice and elastic constants using Pb parameters from PbSe, again ensuring that the parameter reliably accounted for the PbTe thermal conductivity as known from experiment. Calculated elastic and

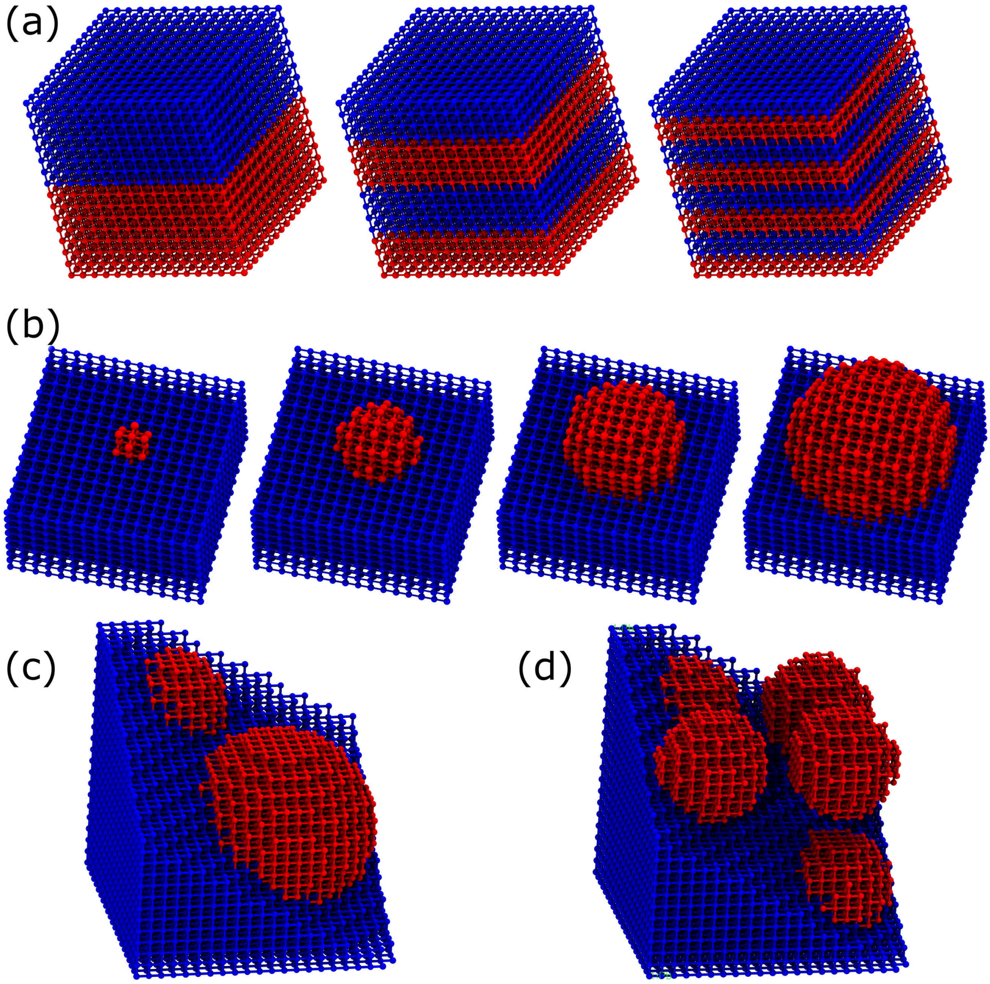

Figure 5.2 – (a) Layered structure of PbTe (in blue) and PbSe (in red) in their rock-salt modification. Layers are (from, left to right) 25, 12.5 and 6.25 thick. (b) Intercalated PbTe(Se) spheres in a PbSe(Te) matrix. Sphere radii are, from left to right 5, 10, 15 and 20 Å, respectively. (c) 25 Å and 15 Å radius spheres and (d) "eight-in-a-box" spheres of 15 Å radius.

lattice constants for both PbTe and PbSe bulk are in good agreement with previous results [289, 290]. Moreover the predicted temperature dependence of κ_{L} compares very well with available reference experimental data (Fig. 5.3 (a,b)) [4, 5]. The κ_{L} of solid solutions is also closely reproduced (Fig. 5.3 (c)) [6]. Details of the potential parameters can be found in Table 5.1 and 5.2.

The lattice thermal conductivity κ_{L}, was calculated using the statistical mechanic Green-Kubo relation based on the fluctuation-dissipation theorem [291]:

$$\kappa_{\mathrm{L}} = \frac{1}{k_{\mathrm{B}} V T^2} \int_0^\infty \frac{\langle \boldsymbol{J}(t) \cdot \boldsymbol{J}(0) \rangle}{3} \mathrm{d}t, \tag{5.3}$$

where k_{B} is the Blotzmann constant, V is the volume of the system, T is the temperature and $\langle \boldsymbol{J}(t) \cdot \boldsymbol{J}(0) \rangle / 3$ is the heat current autocorrelation function averaged over three directions. We computed heat current autocorrelation function as a function of time by means of equilibrium molecular dynamics (EMD) calculations. The heat current vector for a pair potential is defined as [292]:

$$\boldsymbol{J} = \sum_i^N \epsilon_i \nu_i + \frac{1}{2} \sum_{i,j;i \neq j}^N (\sigma_i \cdot \nu_j), \tag{5.4}$$

Where ϵ_i and ν_i are the total energy and velocity associated with to atom i, respectively. The 3x3 tensor σ_i denotes the atomic virial stress, r_{ij} interatomic distances between atoms i and j.

Different kinds of convergence tests have been performed. The truncation time (t_{tr}) chosen to evaluate the integral in the Green-Kubo relation needed to calculate the thermal conductivity was tested (Fig. 5.4 (a)) for the critical solid solution composition $\mathrm{PbSe_{0.50}Te_{0.50}}$ with 4096 atoms in the cell, considered in this work. After $t_{\mathrm{tr}} = 10$ ps the correlation of the heat flux is practically zero and than at $t_{\mathrm{tr}} = 40$ ps the values calculated for κ_{L} converged (inset in Fig. 5.4 (a)). Size-dependence effects were investigated as well. This is necessary as a small size of the simulation box may affect the computed value of the thermal conductivity. For semiconductors this is of relevance as low frequency phonons may have long mean free paths, which provide a significant contribution to κ_{L}. Supercells containing up to $\sim 10^5$ atoms, i.e. $4 \times 4 \times 4\times$ replicas of the original nanostructured systems ($\sim 10^3$ atoms), where chosen. The values calculated from supercells are equal within standard deviations (Fig. 5.4 (b)), while the difference between the smallest cell and the first supercell are within 9% . Fluctuations of κ_{L}, for each structure taken into account are therefore small, while linear regressions are parallel in the size range considered, meaning that

Table 5.1 – Potential parameters for the interatomic interaction terms in PbSe and PbTe.

	q (e)	**σ (Å)**	**ϵ/k_{B}**
Pb	1.29	3.29	29.87
Se	-1.29	4.36	88.45
Te	-1.29	4.35	318.30

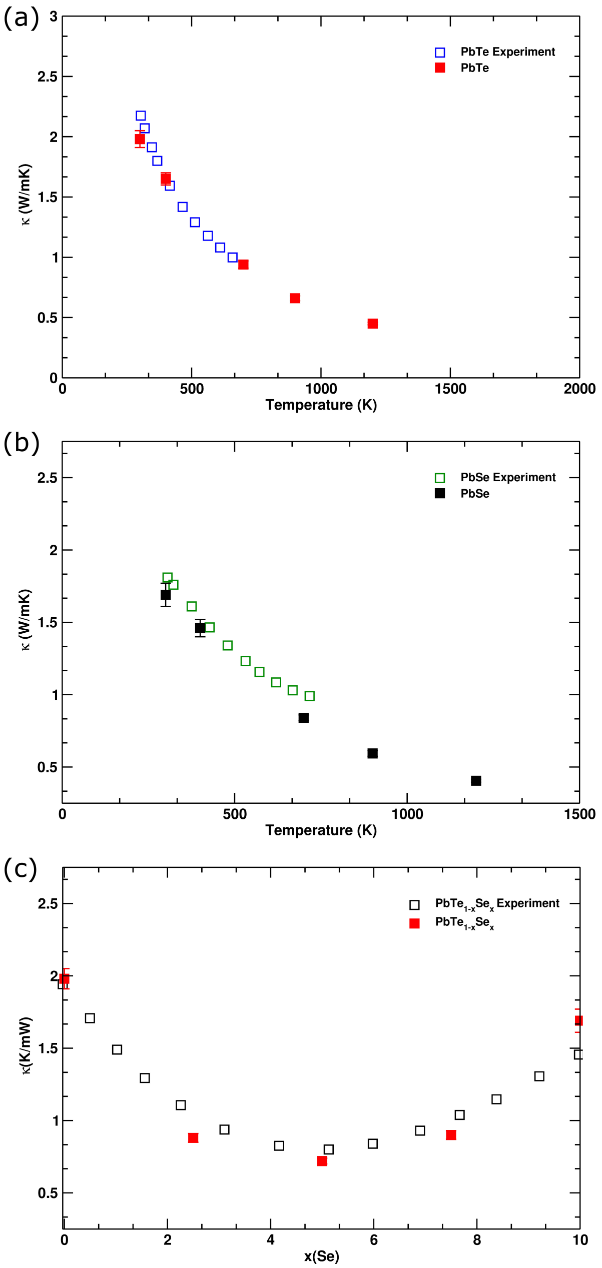

Figure 5.3 – Predicted lattice thermal conductivity of bulk PbTe (a), PbSe (b) and solid solution (c) in comparison with experimental counterpart values [4–6].

Table 5.2 – Calculated and experimental (300 K) equilibrium lattice parameters, elastic constants and bulk modulus for PbSe and PbTe.

	PbSe	**Exp.**	**PbTe**	**PbTe**
***a* (Å)**	6.2288		6.5489	
150 K	6.2463		6.5764	
300 K	6.2659	6.13[a]	6.6008	6.462[b]
$\mathbf{C}_{11}$	114.37	123.7[b]	103.32	105.3[c]
$\mathbf{C}_{12}$	17.95	19.3 [c]	16.77	7.0 [c]
$\mathbf{C}_{44}$	17.95	15.9 [c]	16.76	13.2 [c]
$\mathbf{B}_0$	50.09	54.1 [c]	45.62	39.8 [c]

---

[a] Ref. [293]

[b] Ref. [294]

[b] Ref. [295]

[c] Ref. [296]

relative values of thermal conductivity for the different geometries are reliably computed in the small cells, which therefore we are using from now on. In the case of embedded spheres of different size and dense nano-dots, a larger cell of 10648 atoms was considered. In order to correct for size effects, a reference κ_L for a $PbSe_{0.50}Te_{0.50}$ alloy of the same size was calculated. Also in this case the scaling fully agrees with the red line in Fig. 5.4 (b). All MD calculations where performed with the lammps simulation package [297].

5.1.2 Results and Discussion

In Table 5.3 we report the computed values of κ_L for the composites considered. The temperature dependence is expressed only for the case with smallest thermal constant already at ambient condition. For layered structures the temperature dependence was evaluated for the structure with the highest anisotropy at ambient condition, i.e. largest difference between cartesian components of κ_L.

Our calculations at room temperature show that alloys display lower thermal lattice conductivity than binary phases. Although κ_L does not vary much as a function of composition, $PbSe_{0.50}Te_{0.50}$ solid solution in particular shows maximal reduction, in agreement with previous works based on first principle methods [298]. In turn, the κ_L of nanostructured systems depends on the dimension of the nano-dots (Fig. 5.5 (a)). The κ_L of the samples with smaller nano-dots (radius from 0.5 to 1 nm) is in the order of bulk PbTe and PbSe, whereas a significant reduction of κ_L is obtained for larger nano-inclusions (1.5 or 2 nm). The effect of enlarging the sphere radius is more prominent in the case of PbTe spheres into a PbSe matrix than vice versa. Values of κ_L below the alloy limit may be obtained in samples with even larger nano-inclusions. Further, larger assets were considered, as cells of 4096 atoms limit the maximal host sphere radius to 2 nm, and contrasted against same-sized (10648 atoms) top-performing alloys of composition $PbSe_{0.50}Te_{0.50}$. Figure 5.5 (b), shows the trend of κ_L for these increased systems, for which the sphere radii span from 1 nm to 3 nm.

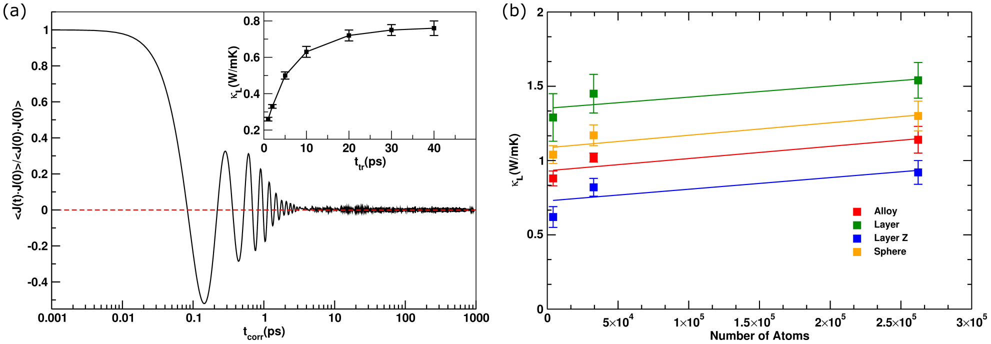

Figure 5.4 – (a) Normalized heat current autocorrelation function of $\mathrm{PbSe_{0.50}Te_{0.50}}$ alloy as a function of correlation time at 300K. The inset reports the calculated thermal conductivity as a function of the truncation time. (b) Lattice thermal conductivity as a function of the system size. Values for the best $\mathrm{PbSe_{0.50}Te_{0.50}}$ alloy (red), 12.5 Å thickness layer averaged (green) and the z component (blue) and the 20 Å radius PbTe sphere in PbSe matrix (blue) are reported.

The general features do not vary much between the two sets of data (a shift of ~0.3 W/mK in the κ_L values can be attributed to the size effects, as suggested by Fig. 5.4 (b)), indicating that the absolute dimension of the nano-dots is not the main feature for this kind of nanostructures. The spacing between spheres is rather the relevant parameter. Table 5.4, summarises values of κ_L at ambient temperature for large cell systems: single sphere inclusions, two spheres with different size (Fig. 5.2 (c)) and "eight-in-a-box" spheres PbSe(Te) nanocomposites in PbTe(Se) matrix (Fig. 5.2 (d)) are compared to the $\mathrm{PbSe_{0.50}Te_{0.50}}$ alloy with the same cell dimension. Narrowing the distance between the nano-dots (as shown in Fig. 5.6 (b)) causes the lattice thermal conductivity to decrease. With reference to Fig. 5.6 (a), the trend of κ_L reduction as a function of size eventually yields a value of κ_L smaller than the best 50% solid solution, underpinning the relevance of the (sub)nano-regime for devices.

The "eight-in-a-box" spheres PbTe nanocomposites in a PbSe matrix represents the right balance between dot size and, most importantly, inter-dot distance. The resulting enhanced phonon scattering lowers the lattice thermal conductivity to values smaller than the best alloy. Temperature dependence for these two systems has been investigated and is reported in Fig. 5.7. The decrease of κ_L in the alloy is quite monotonic, while nanostructured compounds rather displays a step-like trend. In particular, at ambient and higher temperatures the inclusion of nano-dots is expected to lower thermal conductivity to a larger extent than the best alloy compound.

Lattice thermal conductivity of layered superlattices is strongly anisotropic at room temperature, as $\kappa_{\mathrm{L_z}}$ is markedly lower than $\kappa_{\mathrm{L_x}}$ ($\kappa_{\mathrm{L_x}} \cong \kappa_{\mathrm{L_y}}$). In contrast with nanoinclusion $\kappa_{\mathrm{L_z}}$ is not a monotonic function of the superlattice spacing. The lowest $\kappa_{\mathrm{L_z}}$ is obtained for a superlattice spacing of 1.25 nm. The observed trends of κ_L as a function of size and dimensionality in PbTe and PbSe systems show analogies with Si/Ge superlattices [299]. In both cases, for ~1 nm lattice spacing 2D geometries provide a

Table 5.3 – Avarege lattice thermal conductivity computed for PbTe- PbSe B1 structures, alloys at different stoichiometric composition and PbTe(PbSe) spheres into PbSe(PbTe) matrices. Values are reported in units of W/mK. Directional thermal conductivity ($\kappa_{\mathrm{L_x}}$, $\kappa_{\mathrm{L_y}}$, $\kappa_{\mathrm{L_z}}$) computed for layered structure with different layer thickness. Dependences on Temperature are shown for selected systems.

		300 K	400 K	700 K	900 K	1200 K
B1						
PbTe		1.98 ± 0.07	1.65 ± 0.05	0.94 ± 0.03	0.66 ± 0.02	0.45 ± 0.01
PbSe		1.69 ± 0.08	1.46 ± 0.06	0.84 ± 0.02	0.59 ± 0.02	0.41 ± 0.01
Alloy						
75% of Te		0.88 ± 0.03				
50% of Te		0.72 ± 0.02	0.59 ± 0.02	0.49 ± 0.01	0.41 ± 0.01	0.33 ± 0.01
25% of Te		0.90 ± 0.03				
Sphere (Te in Se)						
5 Å radius		2.17 ± 0.07				
10 Å		2.09 ± 0.06				
15 Å		1.54 ± 0.05				
20 Å		0.91 ± 0.03	0.79 ± 0.03	0.60 ± 0.01	0.46 ± 0.01	0.35 ± 0.01
Sphere (Se in Te)						
5 Å radius		2.13 ± 0.09				
10 Å		1.89 ± 0.11				
15 Å		1.47 ± 0.06				
20 Å		1.09 ± 0.03	0.91 ± 0.02	0.66 ± 0.02	0.47 ± 0.02	0.38 ± 0.01
Layers						
25Å	x	1.80 ± 0.14				
	y	1.79 ± 0.18				
	z	0.85 ± 0.11				
12.5Å	x	1.40 ± 0.27	0.95 ± 0.13	0.78 ± 0.12	0.37 ± 0.04	0.32 ± 0.05
	y	1.44 ± 0.21	0.88 ± 0.09	0.68 ± 0.09	0.35 ± 0.03	0.29 ± 0.03
	z	0.49 ± 0.08	0.48 ± 0.07	0.41 ± 0.07	0.27 ± 0.03	0.25 ± 0.03
6.75Å	x	1.40 ± 0.12				
	y	1.32 ± 0.05				
	z	0.71 ± 0.06				

more efficient reduction of κ_{L}, but even lower thermal conductivity can be achieved using larger nano-dots. Similarly to Si/Ge systems the crossover of κ_{L} between 2D and 0D nanostructures occurs beyond 3 nm.

The value of κ_{L} of crystalline PbTe and PbSe and of simpler nanostructured materials rapidly approaches the one of the best alloy as temperature is increased (Fig. 5.8 (a,b)). In addition, as the temperature increases the anisotropy of kk of superlattices rapidly disappears. Already at 400 K the $\kappa_{\mathrm{L_z}}/\kappa_{\mathrm{L_x}}$ ratio reaches 0.51 and at higher temperature it is close to 1, since increased anharmonic three-phonon scattering takes over phonon scattering at the interfaces. Nonetheless $\kappa_{\mathrm{L_z}}$ remains below the values of the PbSe$_{0.50}$Te$_{0.50}$ alloy by as much as ~25 % (Fig. 5.8 (c)).

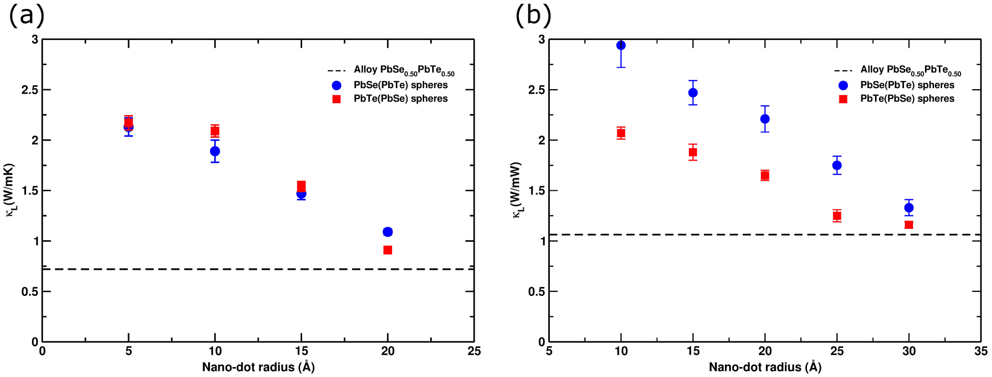

Figure 5.5 – κ_{L} dependence on PbTe(PbSe) nano-dot size in PbSe(PbTe) matrix for 4096 (a) and 10648 (b) atoms systems. The dashed lines represent the κ_{L} value for the most performing $PbSe_{0.50}Te_{0.50}$ alloys.

In order to understand the physics behind changes in thermal conductivity between our samples and bulk binary compounds, effective mean free paths of carriers as a function of frequency were computed. The size of larger systems of 10648 atoms per simulation box rapidly becomes too demanding with respect to memory allocation of the dynamical matrix. Therefore only relatively small 4096 systems were considered. We compared values for PbTe bulk (the case of PbSe shows qualitatively the same results with an obvious shift at lower frequencies due to the smaller mass of selenium) with the one obtained for the $PbSe_{0.50}Te_{0.50}$ alloy, the largest PbTe sphere (20 Å of diameter) embedded in a PbSe matrix and the 12.5 Å thick layered structure.

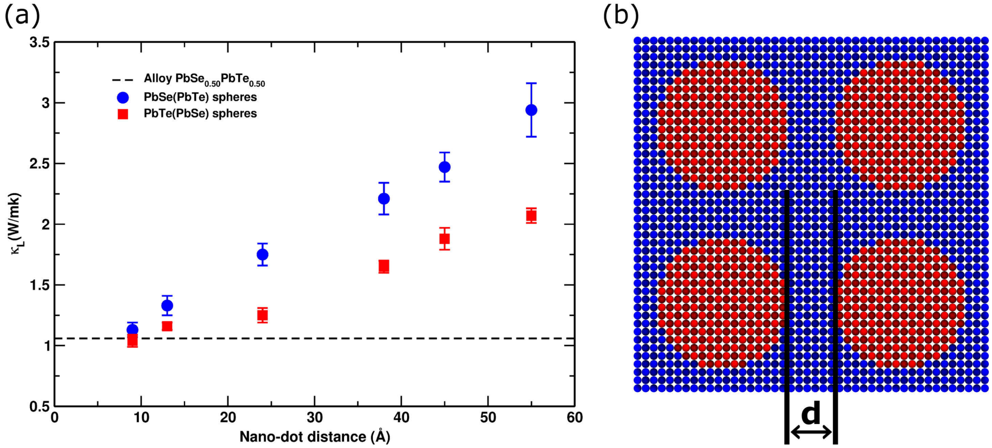

Figure 5.6 – (a) Lattice thermal conductivity dependence of PbTe(PbSe) nanocomposites as a function of nano-dot distance d (b).

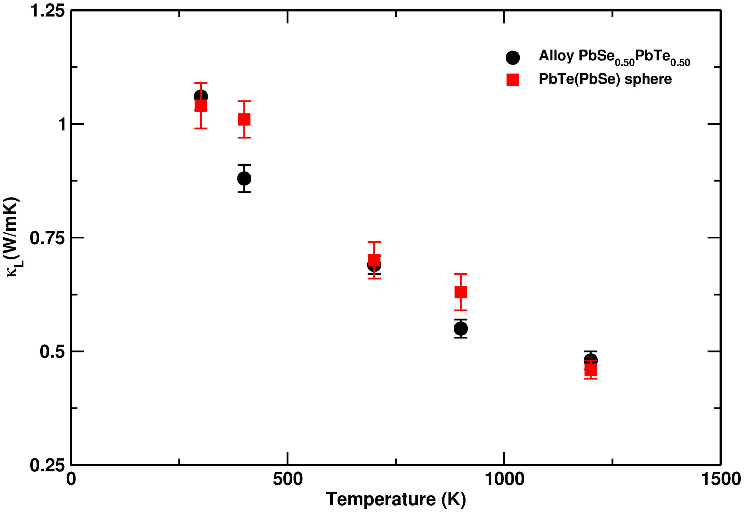

Figure 5.7 – κ_L temperature dependence of PbTe nano-dots in PbSe matrix and $PbSe_{0.50}Te_{0.50}$ alloy (both systems have 10648 atoms in the unit cell).

Table 5.4 – Average lattice thermal conductivity computed for PbTe(PbSe) spheres into PbSe(PbTe) matrices for the 10468 atom systems. Values are reported in units of W/mK. The value for the same size $PbSe_{0.50}Te_{0.50}$ alloy, is also reported.

	300K	Distance (Å)
Sphere (Te in Se)		
10 Å radius	2.07 ± 0.06	55
15 Å	1.88 ± 0.09	45
20 Å	1.65 ± 0.05	38
25 Å	1.25 ± 0.06	24
30 Å	1.16 ± 0.03	13
“eight-in-a-box”, 15 Å	1.04 ± 0.05	9
“different-size”, 15 Å and 25 Å	1.45 ± 0.09	
Sphere (Se in Te)		
10 Å radius	2.94 ± 0.22	55
15 Å	2.47 ± 0.12	45
20 Å	2.21 ± 0.13	38
25 Å	1.75 ± 0.09	24
30 Å	1.33 ± 0.08	13
“eight-in-a-box”, 15 Å	1.13 ± 0.08	9
“different-size”, 15 Å and 25 Å	1.59 ± 0.06	
Alloy		
50% of Te	1.06 ± 0.03	

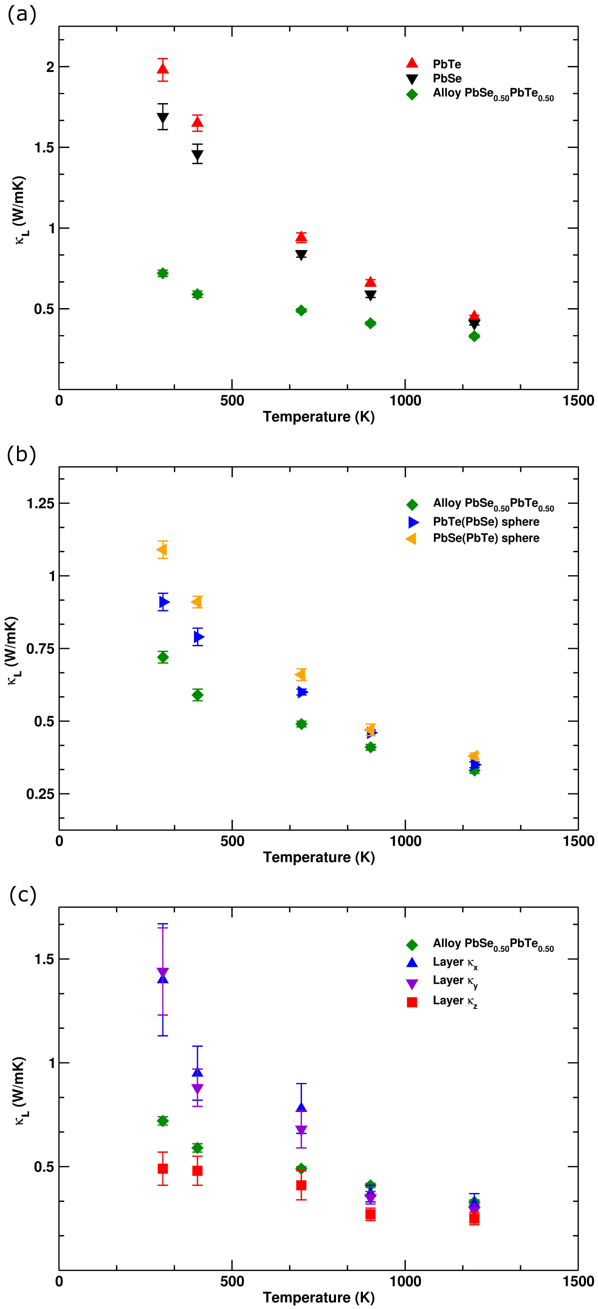

Figure 5.8 – Comparison of lattice thermal conductivity dependence on temperature between (a) bulk PbTe, bulk PbSe and $PbSe_{0.50}Te_{0.50}$ alloy, (b) between 20 Å radius PbTe(PbSe) sphere in PbSe(PbTe) matrix and $PbSe_{0.50}Te_{0.50}$ alloy and (c) between the cartesian components of the lattice thermal conductivity of the 12.5 Å thickness layered structure and the $PbSe_{0.50}Te_{0.50}$ alloy.

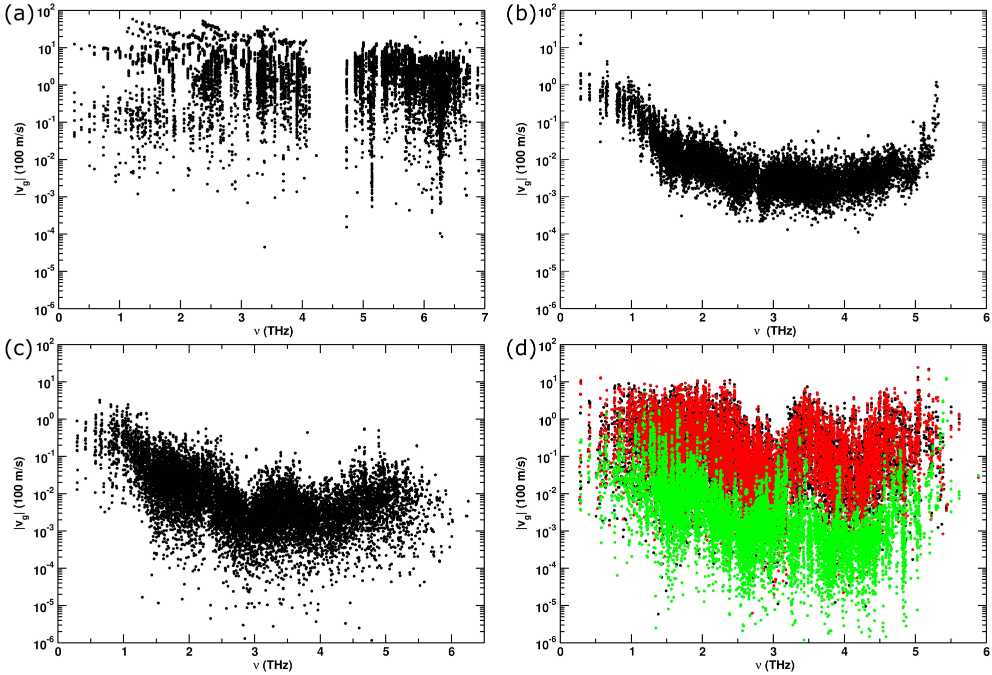

Figure 5.9 – Calculated amplitude of group velocities as a function of frequency for bulk PbTe sample (a), $\mathrm{PbSe_{0.50}Te_{0.50}}$ alloy (b), 20 Å radius PbTe sphere in PbSe matrix and for 12.5 Å thick layered structure (d).

The dynamical matrix Ω was obtained, in lattice dynamic calculations, computing derivatives of forces acting on atoms as finite differences. The matrix was computed and diagonalized in order to obtain eigenvectors e and eigenvalues ω at the Γ point ($\mathbf{q} = 0$) of the Brillouin zone relative to supercell. For several and small finite $\mathbf{r}$ points, $\Omega_{ij}(\mathbf{q}) = \Omega_{\mathrm{ij}}(\mathbf{q} = 0)\mathrm{e}^{-\mathrm{i}\Omega\mathbf{q}\cdot\mathbf{r}_{\mathrm{ij}}}$ where $\mathbf{r}_{\mathrm{ij}} = \mathbf{r}_{\mathrm{i}} - \mathbf{r}_{\mathrm{j}}$ and $\mathbf{r}$ is the atomic position. We then define effective group velocities as $\nu_{\mathbf{q}=0} = \Delta\omega/\Delta\mathbf{q}$, without taking the limit for $\mathbf{q} \to 0$(we considered 20 q values spaced by 0.0001 $\mathrm{\mathring{A}}^{-1}$, over an interval of 0.001 $\mathrm{\mathring{A}}^{-1}$ excluding the Γ point and we approximated dispersion curves by a quadratic function obtained by least quadratic fit). Computed group velocities for our systems are reported in Fig. 5.9. From the normalized autocorrelation function of the energies of each eigenmode lifetimes were calculated:

$$\tau_i = \int_0^\infty \frac{\langle E_i(\mathbf{q},t) \cdot E_i(\mathbf{q},0)\rangle}{\langle E_i(\mathbf{q},0) \cdot E_{\mathrm{i}}(\mathbf{q},0)\rangle} dt, \tag{5.5}$$

where

$$E_i(\mathbf{q},\mathrm{t}) = \frac{\omega_{\mathrm{i}}^2 S_i^*(\mathbf{q},t) S_i(\mathbf{q},\mathrm{t})}{2} + \frac{\omega_{\mathrm{i}}^2 S_i^{*\prime}(\mathbf{q},t) S_i^{\prime}(\mathbf{q},t)}{2}, \tag{5.6}$$

and

$$S_i(\mathbf{q},\mathrm{t}) = \sqrt{N}\sum_j \sqrt{\mathrm{M}_j}\mathrm{e}^{-\mathbf{iq}\cdot\mathbf{r}_{\mathrm{j,o}}}\mathrm{e}_i^*(\mathbf{q})\cdot u_j(t). \tag{5.7}$$

S' is the derivative of S, and u_j is the displacement of the atom j in our MD trajectories. Computed lifetimes are also reported in Fig. 5.10.

Once all these contributions are available, further calculations of the effective mean free path (MFP) are straightforward [300]. For a certain i mode, the MFP is given by $\lambda_i = \nu_i^g \tau_i$. Figure 5.11 shows the impact of (sub)nanostructuring on thermal conductivity. From frequencies of $\nu \approx 1$ THz on, a significant average decreasing of the mean free path with respect to bulk PbTe is clearly visible. In the interval 1 THz $\leq \nu \leq$ 3 THz, value reductions by a factor ~350 are found for the alloyed structure, ~310 for PbTe nanoparticles embedded in a PbSe matrix, while the layered structure outstands the previous ones with a large factor λ_z ~550 along the stacking direction ($\lambda_x = \lambda_y$ ~40), in agreement with the trend of lattice thermal conductivity reduction shown in Table 5.3. The same analysis allows discriminating among layered nanocomposites. Comparing the mean free path for the 6.25 Å thick layered structure to the one with a thickness of 12.5 Å (Figure 5.12), the latter is distinguished by a markedly lower thermal conductivity across the layers. This in turn is due to a reduction of the

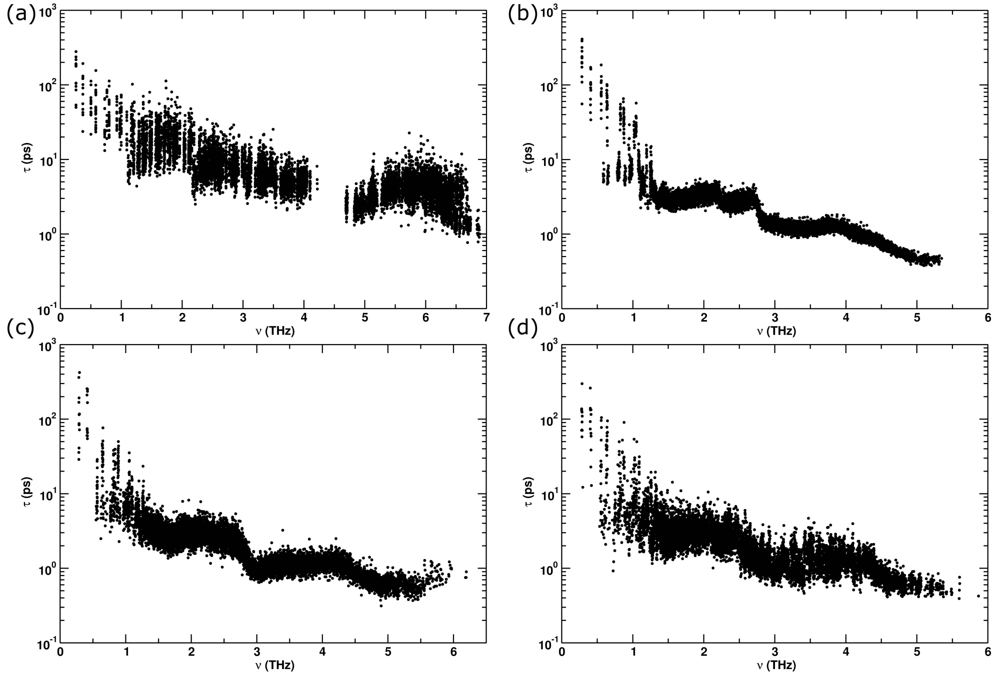

Figure 5.10 – Calculated lifetimes of vibrational modes as a function of frequency for bulk PbTe sample (a), $\mathrm{PbSe_{0.50}Te_{0.50}}$ alloy (b), 20 Å radius PbTe sphere in PbSe matrix (c) and for 12.5 Å thick layered structure (d).

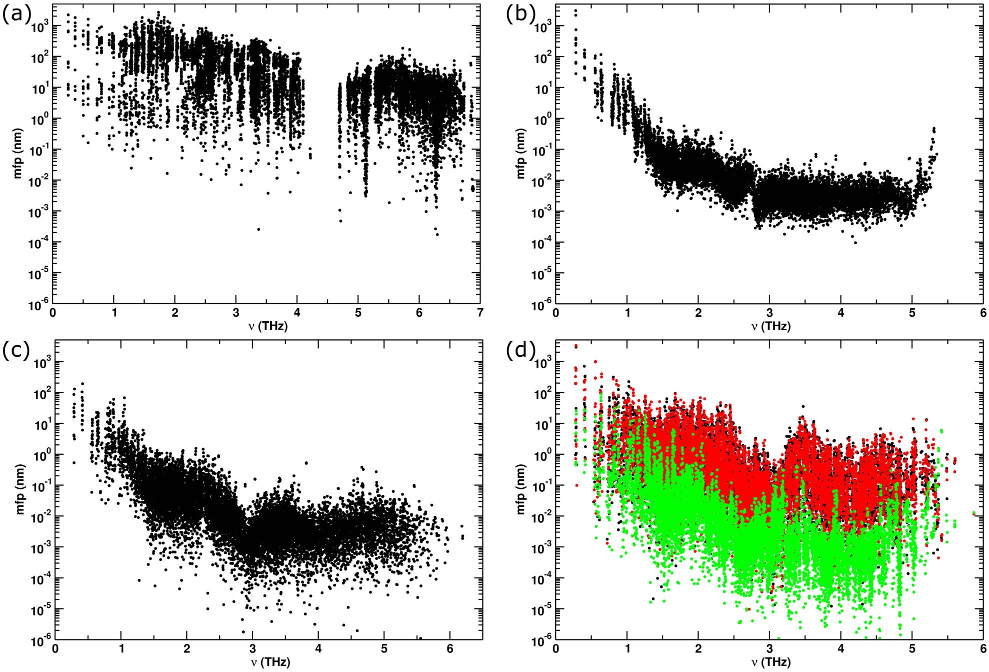

Figure 5.11 – Average mean free path of vibrational modes as a function of frequency for bulk PbTe sample (a), $PbSe_{0.50}Te_{0.50}$ alloy (b), 20 Å radius PbTe sphere in PbSe matrix and directional mean free path for 12.5 Å thick layered structure.

mean free path of intermediate frequency modes, which suggests that a selective filtering on selected portions of the frequency range can be achieved as a function of morphological features of the composite. While the right scale of (sub)nanocompositing may be difficult to guess by trial and error, the computational approach of the present work is very precise in indicating a viable route of material thermoelectric property improvements. On the one hand the enhancement of the thermoelectric figure of merit for PbTe-PbSe solid solutions [6, 265, 301] is confirmed, on the other hand a more promising and "intelligent" nanoengineering approach is emerging. At room temperature, the insertion of PbTe(Se) nanoparticles into PbSe(Te) matrix causes a reduction of κ_{L_z} up to 55% with respect to the binary compound, while in layered nanocomposites the rather modest average reduction of about 40% in the layer is remarkably enhanced above 70% perpendicular to the layers. Furthermore, the study of lager systems suggests densely packed nano-dot as nano-engineering design targets. This qualifies nanocomposites with stong anisotropic features and dense packings as potentially outstanding thermoelectrics for the energy era.

Our results indicate the overall decreasing of the thermal lattice conductivity in nanocomposites with respect to PbTe or PbSe to arise from a reduction of the mean free path of selected frequency modes. PbTe-PbSe alloys are known to enhance thermoelectric efficiency because of phonon features, which are distinct from the binary

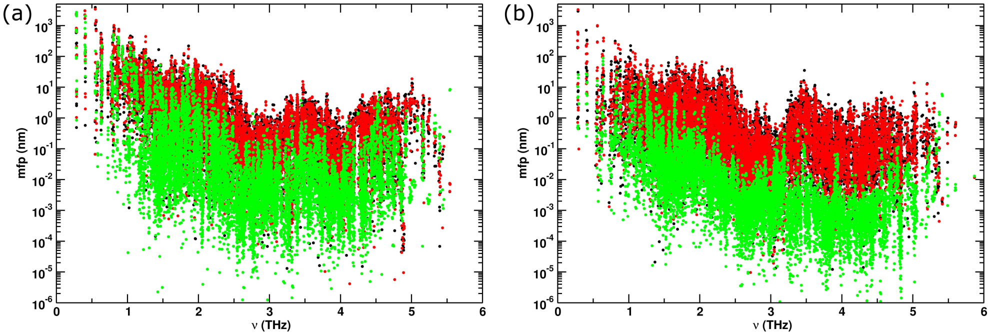

Figure 5.12 – Mean free path of vibrational modes as a function of frequency for 6.25 Å (a) and 12.5 Å (b) thick layered structure. The former shows a lowest average mfp for $\kappa_{\mathrm{L_x}}$ and $\kappa_{\mathrm{L_y}}$ (values in black and red) and the latter shows very low values for $\kappa_{\mathrm{L_z}}$ (in green) confirming not only its strikingly phonon scattering features but also an incredible anisotropy.

phases. Our computational approach sheds light on a different strategy of thermal conductivity reduction, that is engineering at the (sub)nanometer scale. Along this line it is possible to obtain structures with potentially better phonon scattering properties. Experimentally [302] κ_{L} resulted independent from layer thickness between 5 and 50 nm. Our calculations indicate that the threshold for an effect to set in has to be at shorter length values, also pinpointed by the indication of densely packed nanodots spaced by less than a few nanometers. Considering group velocities, lifetimes and mean free path of low frequency vibrational modes of different layered structures, an optimal spacing between different species (alternating PbTe and PbSe layers) can be identified, which enhances anisotropy and reduces thermal conductivity along the layer stacking direction. Low values are also found if spherical PbTe nanoparticles are growth inside a PbSe matrix (or vice versa), as an alternative means to modulate material distribution and length sequences on the (sub)nano scale.

We have seen how, by means of MD calculations, lowest lattice thermal conductivity values are characteristic of a region between solid solutions (“0” nm) and nanostructured (∼5nm) materials. Length modulations in this region (*i.e.* between 0 and 5 nm) achieve efficient scattering of intermediate frequency modes. The precise reproduction of experimental curves and the precise evaluation of the temperature dependence of thermal conductivity as a function of morphological features provide guidance for the design of novel materials with improved properties. We expect our approach to be widely applicable for thermal transport evaluation, and for designing better thermoelectric materials.

5.2 Crystal grain boundaries in rocksalt PbSe as scalable phonon scatterers

Nanostructuring is one of the best technique so far to reduce heat transport in crystalline thermoelectrics, but clearly is not the only one. As a matter of fact, while in general this represents a powerful paradigm for better thermoelectric compounds, nanostructuring can affect only portions of the phonon spectrum, i.e. those frequencies with relatively short mean free paths. A more efficient emerging paradigm of controlling phonon scattering also affecting medium to long mean free paths, is through a complete understanding of material morphology, and its consequences on thermal conductivity while length scales vary. Seminal work in this direction has been recently achieved in the system SrTe-PbTe with Na doping [269]. Therein, besides nanoscale precipitates, grains up to the micrometer scale represent the novel ingredient. The presence of grains and grain boundaries are understood as a means to trespass the ZT threshold of 2. Therefore grains and domain boundaries open novel perspectives in material engineering, since they implement a natural way of size re-scaling over different lengths. While nanoprecipitates are local, grains and their boundaries offer a way of accommodating disparate scale length in a material, without necessarily affecting composition. While they can be used together with doping and nanoscale precipitates like proved in experiments, grains should be capable of lowering thermal conductivity on their own, at “constant chemistry” so to speak.

5.2.1 Introduction

Following this line, we investigated the formation and thermal conductivity of PbSe crystals of variable, increasing size, in order to understand and systematise the impact of morphology onto transport properties. While the formation of domains is of difficult experimental assessment, as they are part of the rather elusive reactivity of solids, we have taken a fully *ab initio* approach to morphology modelling. The formation of grains and boundaries typically accompanies solid-solid reactions, and structural phase transitions in general. Exploiting the polymorphism of PbSe, which, from the ground-state structure rock-salt (B1), transforms into CsCl type structure (B2) under pressure, it is possible to obtain a range of metastable PbSe B1 structures, which contains grain bounded into domains. On varying the number of atoms considered, grain features as they affect real materials can be produced and studied in detail.

To capture the effect of grains and grain boundaries in PbSe we first investigated the mechanism of the B1-B2 structural phase transition in PbSe. The path crosses an intermediate, metastable configuration of roughly B33 type structure. When pressure is released this intermediate transforms into B1. This transformation is accompanied by the formation of grains. This part uses methods of phase transition modelling and transition path sampling molecular dynamics simulations. Thermal conductivity is calculated for ideal, i.e. grain-free PbSe, and for several B1 structures containing grains, as a function of size. This part is based on equilibrium molecular dynamics, from which thermal lattice conductivity can be derived via computation of the thermal flux as already discussed in Section 5.1.1.

5.2.2 B1-B2 Phase Transition in PbSe

PbSe crystallises in the rock-salt (B1) type structure of space group symmetry $Fm\bar{3}m$. Several works have concentrated on the prediction and detection of metastable intermediate along the transformation path from B1-B2, the CsCl type high-pressure structure. PbSe transforms into B2 at around 16 GPa, while the phase transition involves metallisation (B2 is metallic). Phases of $Pnma$ (GeS type structure) and $Cmcm$(CrB type structure) are possible intermediate along the paths [303,304]. For PbSe, accurate transport and X-ray diffraction studies under pressure identify an intermediate phase of CrB type structure at around 9.5 GPa, which is in agreement with theoretical predictions.

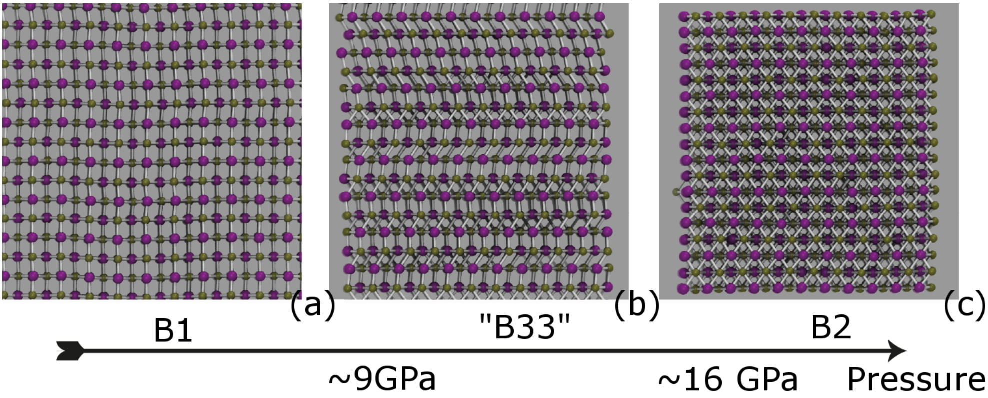

Figure 5.13 – Representative path of structural transformation from B1 to B2. The TPS identifies an intermediate of overall B33 structure, showing the typical alternation of triangular and square layers in the chosen projection. The latter can be stabilized in the lower pressure range, while higher pressure favors B2.

The assessment of a structural phase transition mechanism, including possible intermediates, can be approached with different strategies. The principle methods make use of extended Landau theory in combination with first principles calculations, metadynamics, and, as the method of choice here, molecular dynamics simulations based on the transition path sampling scheme. The power of this methods has been widely discussed during this thesis and in this specific case it yields very detailed transformation mechanisms without enforcing any collective transformation. As NaCl, PbSe transforms into B2 under pressure. Therefore, some of the previous experience accumulated on the B1-B2 polymorphism can be advantageously used here [227]. The MD-TPS method works iteratively on a so-called first trajectory (initial path), which connects B1 to B2. While the initial mechanism is typically concerted, (as it is derived from a general scheme of interpolating intermediate configuration between two limiting structures, B1 and B2 for instance), the converged regime is characterised by nucleation and growth. Here, we have commenced the simulation from a path connecting B1 to B2 in an NpT ensemble, obtained from a geometric-topological approach, based on transforming minimal surfaces [305,306]. The classical MD simulations were carried out by using the DLPOLY CLASSIC package [307]. The PbSe pair potential of Schapotschnikow *et al.* was used [287]. A relatively small simulation time step of 0.1 fs was used to ensure a good time-reversibility. The Melchionna/Nose-Hoover algorithm [20] ensured constant pressure and temperature. Therein, anisotropic shape changes of the simulation box were allowed. Several simulations were performed in the range 9-16 GPa, at 300 K, with a box of 1980 PbSe pairs. In the course of iterations, the collective characteristics of the geometric model disappeared, and a regime characterized by nucleation and growth set in. Additionally, an intermediate appeared in the converged regime, which was not contained in the geometric model. The mechanistic analysis is based on more than 300 transition pathways, collected after trajectory convergence. Fig. 5.13 was produced based on a typical trajectory collected in the converged regime. Furthermore, intermediate configurations can be visited on the eve of the transformation.

The initial B1-B2 path in PbSe was modelled as it was done for NaCl [306], which also crystallises in the same type structures and bears many common aspects with respect to its polymorphism. Three snapshots of representative initial, intermediate and final configurations are shown in Fig. 5.13 (a-c), respectively. To monitor the progress of the calculations and of the transition, a suitable order parameter is necessary. Given the compact nature of the structures, a good choice is the first coordination sphere (fCN), which is 6 in B1 and becomes 8 in B2. To precisely identify any intermediate step, also the second and third coordination spheres (sCN, tCN) were considered. In Fig. 5.14 the progress of the three CNs is monitored as a function of the progress of the transition. Three horizontal dotted lines mark the values of the first three CNs, which are distinctive for CrB (B33), that are $\{7, 22, 47\}$.

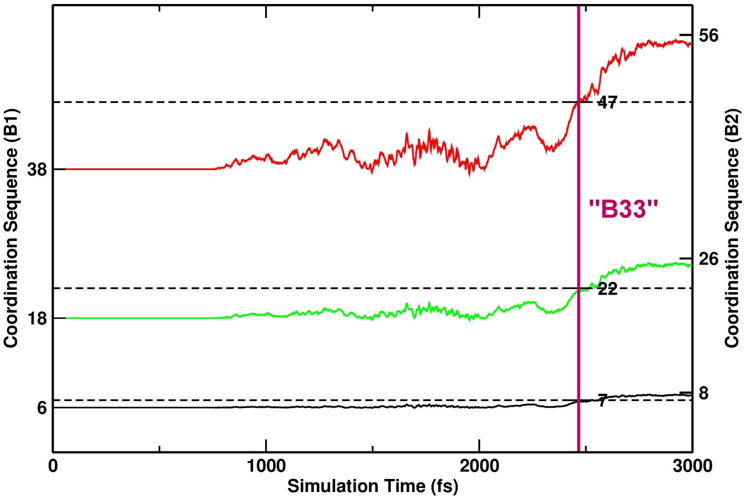

Figure 5.14 – Coordination sequence calculated along the time coordinate for the converged transition trajectory. The plateaux marked with the magenta line correspond to the “B33” intermediate.

The three CNs cross the lines quasi-synchronously, indicating that the transition is visiting an intermediate of B33 characteristics. The configuration of Fig. 5.13 (b) corresponds to this point. The typical pattern of B33 is apparent (alternating square and triangular patterned layers), however some part are not fully locked-in into this pattern. On the average B33 is emerging as an intermediate though, and can be quenched at lower pressure (~6-9 GPa, at which B2 would not form), in accordance with the experimental indications.

5.2.3 Results and Discussion

Grains and grain boundaries

The elucidation of the B1-B2 phase transition is the starting point for the construction of realistic PbSe structures with grains. In this context, realistic means that the grains are calculated from the particular setup, without prior knowledge on their geometries. For this, intermediate configurations like the one of Fig. 5.13 (b) are used as starting point for molecular dynamics calculations (they were iteratively relaxed using the conjugated gradient method, P=1 kbar, T= 0 K). The metastable nature of this configuration causes it to re-transform into the ground state, B1. This is taking place in a non collective way, having different regions transforming into B1 at different times and along different crystallographic directions, such that the process yields B1 PbSe with coherent B1 zones, separated into grains by grain boundaries. While relaxing the 3960 atom cell results into boundaries along two directions only, systematically doubling the edges of the box yields more complex grain geometries, which are increasingly isotropic. The process of enlarging the box and the resulting PbSe grain structures are shown in Fig. 5.15. The still rather anisotropic structure resulting from the 3960 atom box, which contains coherent and percolating B1 domains in a distinct direction, is shown on the right, Fig. 5.15 (b). Magnification factors of 2×2×2, 4×4×4, 6×6×6 and 12×12×12 were chosen, corresponding to 31680, 253444, 855360, 6842880 atom boxes, respectively. Each structures was propagated at p=1 kbar and T= 300 K (NpT anisotropic ensemble) until averaged structural parameters were stable. A typical run was at least 400 ps long, depending on the size. For every grain box size (up to 253444 atoms), a corresponding MD of grain-free PbSe was also prepared, obtained by periodically replicating the unit cell. This was used to evaluate the influence of the finite box size on the value of κ_{L}. The theory behind the calculation of the lattice thermal conductivity has been already extensively treated in Section 5.1.1. Again, all MD equilibrations and heat flux calculations were performed with the lammps simulation package [297].

Thermal transport in PbSe and role of grains

The effect of grains and grain boundaries on pure PbSe can be appreciated already at the lowest step of magnification. The evaluation of κ_{L} as a function of temperature for grain-free PbSe and for the smallest PbSe box containing grains (3960 atoms box) is shown in Fig. 5.16. For grain-free PbSe the curve behaves like in experiments: the value of κ_{L} drops a function of temperature, from an initial value of ~2.5 W/mK. The plot for PbSe with grains is resolved into Cartesian components of κ_{L}. The anisotropic

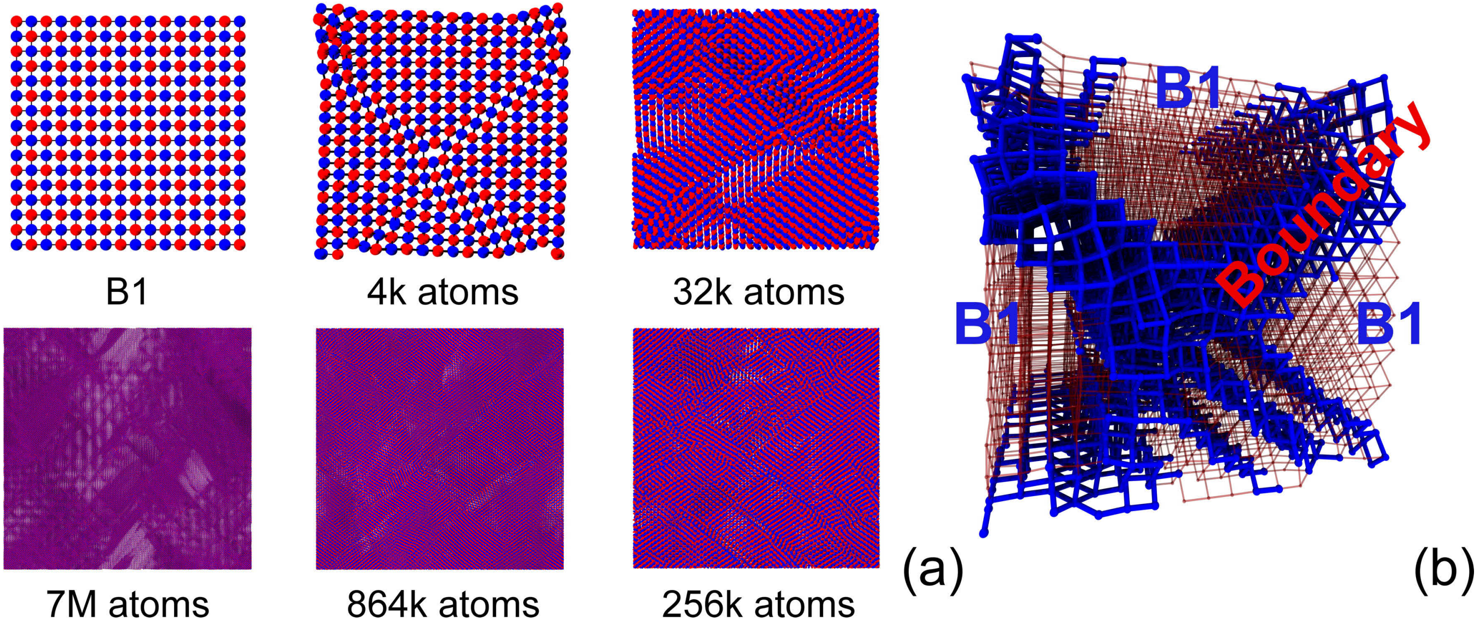
B1
4k atoms
32k atoms
7M atoms
864k atoms
256k atoms
(a)
B1
Boundary
B1
B1
(b)

Figure 5.15 – (a) Structural example of B1 grain boundaries obtained by enlarging the "B33" intermediate of Fig. 5.13 by a factor 1×1×1 (4k atoms), 2×2×2 (32k atoms), 4×4×4 (256k atoms), 6×6×6 (864k atoms) and 12×12×12 (7M atoms), and propagating it in a NpT-MD calculation. (b) Detailed representation of the smallest grain obtained (4k atoms): B1 zones are separated by crossing boundaries. A strong anisotropy can be noticed, since no interfaces are presented in the direction normal to the plane.

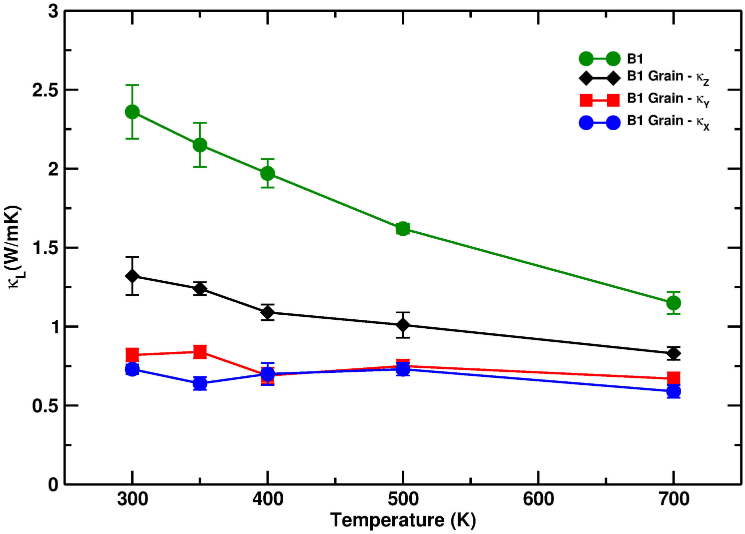

Figure 5.16 – κ_L values calculated as a function of temperature for B1 and B1 grains (3960 atoms box). Cartesian components $\kappa_{\mathrm{L_x}}$, $\kappa_{\mathrm{L_y}}$ and $\kappa_{\mathrm{L_z}}$ are reported for the grain boundaries case: anisotropy can be noticed since the z component presents lattice thermal conductivity values markedly larger than x and y components. However, the overall value of κ_L is noticeably reduced with respect to the B1 pure phase, as temperature dependence is nearly lost.

structure strongly impacts thermal conductivity. While there is an overall dropping of κ_L with respect to grain-free PbSe, the z component $\kappa_{\mathrm{L_z}}$ is only partially affected. By inspection of Fig. 5.15 (b), PbSe is coherently aligned and percolating along z. $\kappa_{\mathrm{L_z}}$ diminishes as a function of temperature, yet to a less extent with respect to grain-free PbSe. The other two components $\kappa_{\mathrm{L_x}}$ and $\kappa_{\mathrm{L_y}}$ show a different behaviour. Any structural path along x and y crosses grain boundaries, such that B1 regions are fully enclosed. Both $\kappa_{\mathrm{L_x}}$ and $\kappa_{\mathrm{L_y}}$ have low values around 0.75 W/mWk at 300 K. Strikingly, the dependence on the temperature has vanished, showing a similar response over the whole temperature range considered, 300-700 K. Grains thus affect thermal conductivity both in terms of κ_L absolute value lowering and of flattening the dependence of κ_L on temperature. This indicate a broader impact of structuring PbSe with grain than just nano precipitates. This effect is somehow reminiscent of the situation in silicon and germanium alloys [308].

To quantitatively capture this effect mean free paths (mfp) spectra were computed (see Section 5.1.2 for further details). The comparison between PbSe with and without grains is shown in Fig. 5.17 (a) and (b). Pure, features free PbSe (Fig. 5.17 (a)) shows a frequency gap between ~4.0 and ~4.5 THz. Lower frequencies are roughly distributed around 1 to 0.1 nm, while higher frequencies have lower mfp around 0.001 nm down to 0.0001 nm. By comparison with grain-free B1 PbSe, there is a substantial lowering of frequencies in the range 2.5-4.5 THz, which also implies gap closure. Already $\kappa_{\mathrm{L_z}}$

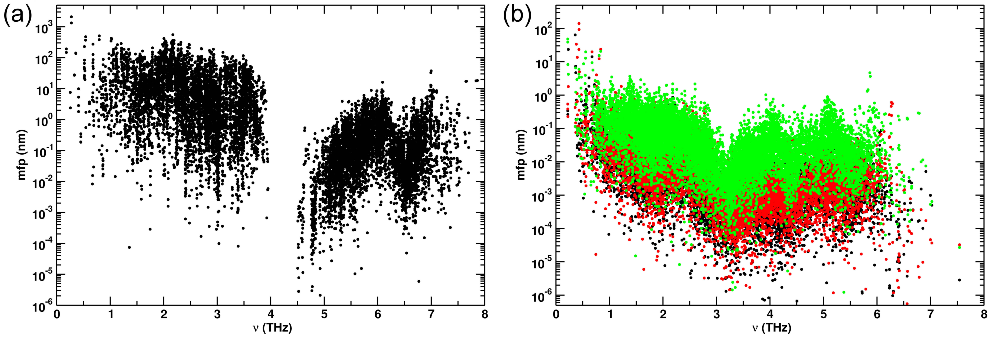

Figure 5.17 – Mean free path of vibrational modes as a function of frequency for pure B1 (a) B1 grains (b) PbSe structure (3960 atoms box). In the former a frequency gap can be noticed between 4.0 and 4.5 THz. The latter shows a lowest average mfp already for $\kappa_{\mathrm{L_z}}$ (in green) with a particular reduction for $\kappa_{\mathrm{L_x}}$ and $\kappa_{\mathrm{L_y}}$ (values in black and red) that confirms not only its strikingly phonon scattering features but also remarkable anisotropy.

(green band in 5.17 (b)) shows a reduction of the overall mfp length. Especially at lower frequencies the values have lowered. The other two components (red and black bands) show an even stronger reduction of mfp at lower frequencies. The overall effect is a global lowering of mfp lenghts over a broader range of frequencies, with particular impact on lower frequencies. Quantitatively, the averaged reduction is of a factor ∼820, ∼600, ∼120 for λ_x, λ_y, λ_z, respectively and a total reduction of a factor ∼500 with respect to the PbSe (B1) pure phase. The emerging picture is thus the one of an impact of grains on a broader range of frequencies, which is not achievable with finite objects (nano-crystals or nano-precipitates).

This is particularly evident by inspecting Fig. 5.18. Here, what we have defined as reduction factor (RF) is reported. Mean free paths associated with phonons of PbSe (B1) pure phase were divided put in one to one correspondence with λ_x, λ_y and λ_z of the grain boundaries structure. This generates peaks in the figure, which correspond to frequencies more affected by the grains. The overall picture suggests again a strong anisotropy of the system, disclosing this time more detailed features. Along the z coordinate, phonon are almost not scattered between 4.5-6 THz. In the remaining part of the phonon spectrum, the z contribution to the mfp frequency reduction is qualitatively the same as the x and y ones, with a reduction of almost an order of magnitude. It is worth focusing on very low frequencies (below 1 THz), corresponding to phonons with relatively long mean free path. Around 0.5 THz, grain boundaries in the x and y directions cause a brusque reduction of the mfp as the λ_z component is strongly reduced at ∼0.3 THz. This analysis reveals a distinctive feature of PbSe grain boundaries, that is their capacity to affect low frequencies in such a way that is hardly attainable by nanoengineering or alloying. While the size is still limited to a few thousands atoms, we now proceed to enlarging system size to understand this effect in detail.

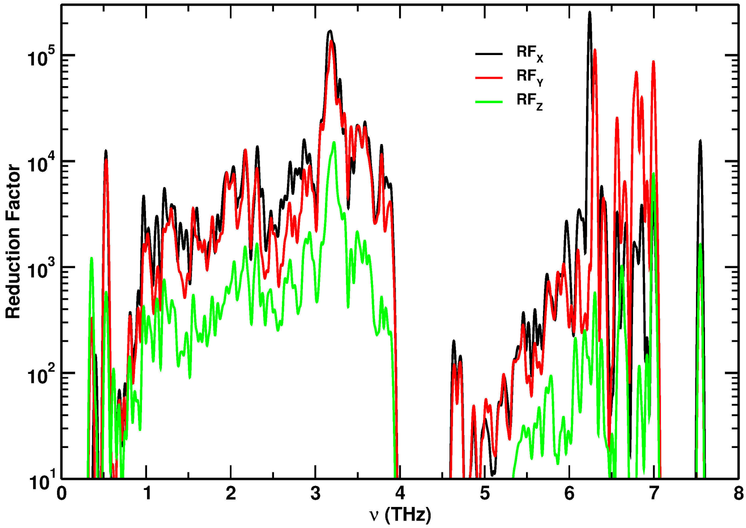

Figure 5.18 – Mean free path reduction factor (RF) resolved in Cartesian directions. In agreement with Fig. 5.17, the reduction factor displays a strong anisotropy since RF$_x$ and RF$_y$ (black and red lines) show similar values, while RF$_z$ (green line) is markedly lower.

Thermal conductivity of PbSe with extensive grain features

In this Section we compare the impact of size on lowering thermal conductivity, κ_L. Sizes of 4k, 32k and 256k atoms as displayed in Fig. 5.15 (a). The sizes span two orders of magnitude, while the grain features in the larger boxes affect all three Cartesian directions while they become more isotropic. The calculations were performed with the same protocol as for the smaller sizes. Comparing thermal conductivity over disparate scales can be flawed by size effects though. Particularly small sizes may artificially repress long mean free paths. Different from a typical approach of verifying size effects by systematically enlarging the size of the simulation box until numerical convergence of transport properties, a distinct approach was taken here. The averaged κ_L value for each size was weighted on the κ_L of a reference system of equal size, but free of any grain feature. This amounts to constructing a calibration curve as a function of size for pure, feature-free B1, at 300K. For each size the difference between the grained and grain-free system $\Delta\kappa_L$ was added to the curve. In general, without size-correction, smaller sizes tend to deliver values which underestimate κ_L. For a small system of 4k atoms the difference amounts $\sim$0.1 W/mK while already at 32K the numerical values have converged since it is the same of the 256k atoms system.

Fig. 5.19 presents the main results of this step. The three sizes are distinguished by different colours. In general, the trend is the one of a continuous decrease of thermal conductivity towards a lower limit of approximately 0.72 W/mK for the largest system considered, at 300K. The impact of the different distribution and size of grains is reflected on a flattening of the curves, and on an overall lowering of κ_L values, reduced by still sensible as size is increased. Additionally (not shown) the difference between Cartesian components has disappeared, which was still present in the 4k atoms system due to the anisotropy in grain boundary distribution. While we expect a further refinement of the absolute value of κ_L on further increasing size, only fractional corrections of the top-scoring value for the 256k atoms grain can be expected. Importantly, it is the strongly reduced to vanishing dependency on temperature, which represents the striking feature of engineering grains in B1.

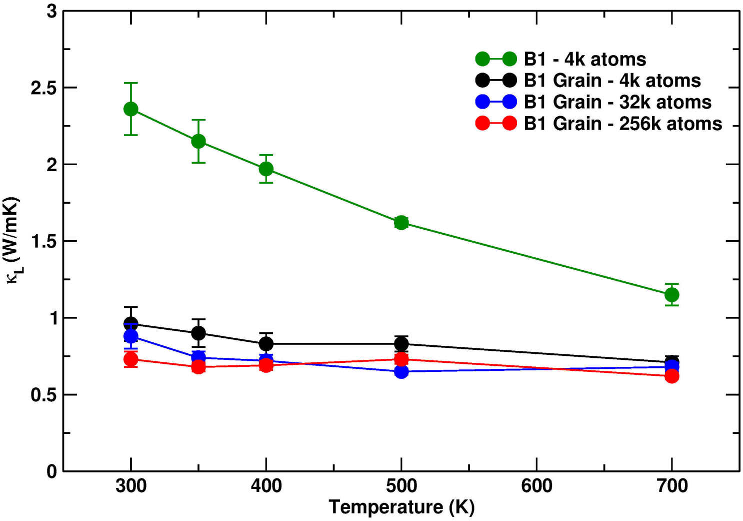

Figure 5.19 – κ_{L} values calculated as a function of temperature for B1 and B1 with grains (3960, 31680 and 253444 atoms boxes). Enlarging the system brings to a direct reduction of the lattice thermal conductivity and to a lower dependence over temperature, nearly lost for the 256k atoms grain.

Grains are rather unwelcome in semiconductor technologies. On the contrary, when it turns to suggesting a different perspective for improved thermoelectric performance, grains are superior phonon scatterers. In this work, by means of heat flux computation based on molecular dynamics techniques, B1 PbSe was systematically engineered with grains, and their impact on κ_L was evaluated. On the one hand, grain allows for a broader frequency range of phonon scattering, including frequencies as low as $\nu < 1$ THz, which are unattainable by any other nanoengineering approach. On the other hand, grains and grain boundaries are features that scale with size. Therefore, a larger, isotropic impact can be expected, like demonstrated in this work. While we have concentrated our study on isolating grain effects as a result of purely structural features, additional ingredients can be added to further improve properties, like nano-inclusions within large grains, and alloying, locally or over the whole crystal. This deserves a separate study.

Conclusions and Outlook

> *Nature, as we understand it today, behaves in such a way that it is fundamentally impossible to make a precise prediction of exactly what will happen in a given experiment. This is a horrible thing; in fact, philosophers have said before that one of the fundamental requisites of science is that whenever you set up the same conditions, the same thing must happen. This is simply not true, it is not a fundamental condition of science. The fact is that the same thing does not happen, that we can find only an average, statistically, as to what happens. Nevertheless, science has not completely collapsed. Philosophers, incidentally, say a great deal about what is absolutely necessary for science, and it is always, so far as one can see, rather naive, and probably wrong.*
>
> Richard Feyman

In the era of exponentially increasing energetic demands, the search for new, innovative materials appears as central task for interdisciplinary research within a broad welfare perspective. Our contribution as theoretical and computational chemists, focuses on atomic-scale static and dynamic processes that directly, or in second instance, are able to identify a certain macroscopical feature as critical for innovation. In this work, this attitude has been applied in the direction of prediction of novel high-performance materials notable for their mechanical hardness, optical properties, electronic transport features, superconductivity, and thermal conversion.

Initially, the long standing debate on the product of "cold compression" of graphite, has been tackled and different structural solutions have been reported. The result of our investigation is that, despite many carbon polymorphs have been suggested over the years, there are still open and unexplored routes for the synthesis of novel carbon materials. In this specific case, extremely hard compounds, as hard as diamond, have been identify (Pearson symbols $oC16$-II, $oC16$-I, $mC12$ and $mC32$). Moreover, their particular electronic structure suggests them as transparent materials with potential optical applications. The following step has consisted in the design of carbon-based hybrid materials for electronic applications. Graphene, one of the most interesting carbon modifications for electronic applications, has been coupled with bare C(111) and Si(111) diamond surfaces. The result is an atomic-scale switch, which - thanks to its geometrically oriented transmission channel - allow for electrons flow only in certain a direction, whereas a total backscattering is observed in the others. The advantages deriving from the use of devices based on such hybrid systems in the atomic circuitry has been proved in detail.

Germanium is another element with outstanding electronic properties. The study of its polymorphism revealed interesting so far unreported structure modifications. "Unconventional" decompression of Ge diamond, drives the system to a new semiconducting, topologically new material, $mC16$. More fascinating, is the discovery of the bct-5 Ge modification. It has been identified as intermediate phase along the pressure induced transition $cF8 \rightarrow tI4(\beta-\mathrm{tin})$ and it bears a metallic character even at room pressure, which is an unprecedented property for Ge modifications. Thereafter, we focused on the behaviour upon compression of the type-II clathrate $cF136$. Presenting the typical phonon-glass electron-crystal structure, this open-framework structure has attracted large attentions during the last years for its potential applications in thermoelectric devices. Our study shows how, at low pressure, Ge($cF136$) undergoes a phase transition to bct-5, which progresses over a number of amorphous modifications. As such, type-II clathrate $cF136$ appears to be the natural precursor for the bct-5 synthesis.

The last part of the work was devoted to setup a computational framework for improving thermoelectric material performance, and for suggesting a novel paradigm for material design. Due to their relative abundance and peak in performance in the mid-temperature range, lead chalcogenides are outstanding candidates as thermopower generators. Two different approaches were adopted, one based on nanostructural modeling and the other one on the identification of realistic path for domains formation. The new materials obtained, based on PbSe-PbTe nanoengineered substructures and PbSe grain boundaries, display strinkingly low lattice thermal conductivity, rooted into a superior phonon scattering capacity. The thermoelectric efficiency (figure of merit, ZT) of these kind of novel materials, inversely depends on their thermal conductivity: with lowering as extended as predicted in this work, our materials have the potential of raising the efficiency bar over the limit of ZT= 2, but they can also open novel perspectives on material design, as the approach for their construction can be turned into a blueprint for material engineering.

The increasing performance and reliability in reproducing macroscopical quantities by atomistic approaches, raise computer simulations to a principle discipline for material innovation. Depending on the system considered and on the characteristics of the targeted properties we are interested to find or improve, different methods, or a combination of them, can be used. The present work clearly shows how a simulation framework can be setup and used to address complex problems of solid state and material sciences. The impact of performing algorithms, smart methods and high-performace computers is critical for innovation, and the results of this thesis are expected to stimulate and promote further work, along the directions of this contribution.

Bibliography

[1] A. Laio and F. Gervasio, Rep. Prog. Phys. **71**, 126601 (2008).

[2] W. Setyawan and S. Curtarolo, Computational Materials Science **49**, 299 (2010).

[3] D. M. Rowe and G. Min, J. Mater. Sci. Lett **14**, 617 (1995).

[4] J. Androulakis, D.-Y. Chung, X. Su, L. Zhang, C. Uher, T. C. Hasapis, E. Hatzikraniotis, K. M.Paraskevopoulos, and M. G. Kanatzidis, Phys. Rev. B **84**, 155207 (2011).

[5] J. He, L.-D. Zhao, J.-C. Zheng, J. W. Doak, H. Wu, H.-Q. Wang, Y. Lee, C. Wolverton, M. G. Kanatzidis, and V. P. Dravid, J. Am. Chem. Soc. **135**, 4624 (2013).

[6] P. F. P. Poudeu, J. D'Angelo, H. Kong, A. Downey, J. L. Short, R. Pcionek, T. P. Hogan, and M. G. K. C. Uher, J. Am. Chem. Soc. **128**, 14347 (2006).

[7] D. C. Rapaport, *The Art of Molecular Dynamics Simulation* (Cambrige, New York, 1995).

[8] L. Verlet, Phys. Rev. **159**, 98 (1967).

[9] L. Verlet, Phys. Rev. **165**, 201 (1968).

[10] R. W. Hockney and J. W. Eastwood, *Computer simulations using particles* (Adam Hilger, Bristol, 1988).

[11] W. C. Swope, H. C. Andersen, P. H. Berens, and K. R. Wilson, J. Chem. Phys. **76**, 637 (1982).

[12] M. P. Allen and D. J. Tildesley, *Computer Simulation of Liquids* (Clarendon Press, Oxford, 1960).

[13] D. Frenkel and B. Smit, *Understanding Molecular Simulation* (Academic Press, San Diego, 1996).

[14] M. P. Allen and D. J. Tildesley, *Introduction to Modern Statistical Mechanics* (Oxford University Press, New York, 1987).

[15] J. Tersoff, Phys. Rev. B **39**, 5566 (1989).

[16] J. Tersoff, Phys. Rev. B **37**, 6991 (1988).

[17] S. W. de Leeuw, J. W. Perram, and E. R. Smith, J. Chem. Phys. **373**, 57 (1980).

[18] W. G. Hoover, Phys. Rev. A **31**, 1695 (1985).

[19] S. Nosé, J. Chem. Phys. **81**, 511 (1984).

[20] S. Melchionna, G. Ciccotti, and B. L. Holian, Mol. Phys. **78**, 533 (1993).

[21] M. Parrinello and A. Rahman, J. Appl. Phys. **52**, 7182 (1981).

[22] A. Laio and M. Parrinello, Proc. Natl. Acad. Sci. USA **99**, 12562 (2002).

[23] R. Martoňák, A. Laio, and M. Parrinello, Phys. Rev. Lett. **90**, 075503 (2003).

[24] R. Martoňák, D. Donadio, A. R. Oganov, and M. Parrinello, Nat. Mater. **5**, 623 (2006).

[25] D. Wales and J. Doye, J. Phys. Chem. **A101**, 5111 (1997).

[26] S. Gödecker, J. Phys. Chem. **120**, 9911 (2004).

[27] J. Pannetier, J. Bassasalsina, J. Rodriguez-Carvajal, and V. Caignaert, Nature **346**, 343 (1990).

[28] J. Schön and M. Jansen, Angew. Chem. Int. Ed. Engl **35**, 1287 (1996).

[29] S. Woodley, Struct. Bond. **110**, 95 (2004).

[30] A. R. Oganov and C. W. Glass, J. Chem. Phys. **124**, 244704 (2006).

[31] C. W. Glass, A. R. Oganov, and N. Hansen, Comp. Phys. Comm. **175**, 713 (2006).

[32] C. Ceriani, E. F. A. Laio, A. Gamba, R. Martoňák, and M. Parrinello, Phys. Rev. B **70**, 113403 (2004).

[33] P. Raiteri, R. Martoňák, and M. Parrinello, Angew. Chem. Int. Ed. Engl **44**, 3769 (2005).

[34] T. Ishikawa, H. Nagara, K. Kusakabe, and N. Suzuki, Phys. Rev. Lett. **96**, 095502 (2006).

[35] D. Quigley and M. Probert, Phys. Rev. E **71**, 065701 (2005).

[36] M. Parrinello and A. Rahman, Phys. Rev. Lett. **45**, 1196 (1980).

[37] P. G. Bolhuis, D. Chandler, C. Dellago, and P. L. Geissler, Annu. Rev. Phys. Chem. **53**, 291 (2002).

[38] L. R. Pratt, J. Chem. Phys. **85**, 5045 (1986).

[39] C. Dellago, P. G. Bolhuis, F. S. Csajka, and D. Chandler, J. Chem. Phys. **108**, 1964 (1998).

[40] C. Dellago, P. G. Bolhuis, and D. Chandler, J. Chem. Phys. **108**, 9263 (1998).

[41] C. Dellago, P. G. Bolhuis, and P. D. Geissler, Adv. Chem. Phys. **123**, 1 (2002).

[42] C. J. Cerjan and W. H. Miller, J. Chem. Phys. **75**, 2800 (1981).

[43] J. P. K. Doye and D. J. Wales, Z. Phys. D **40**, 194 (1997).

[44] L. P. Kadanoff, Physics Today **58**, 34 (August 2001).

[45] H. Eyring, J. Chem. Phys. **3**, 107 (1935).

[46] E. Wigner, Trans. Faraday Soc. **34**, 29 (1938).

[47] J. B. Anderson, J. Chem. Phys. **58**, 4684 (1973).

[48] C. H. Bennett, *Algorithms for Chemical Computations* (R. E. Christoffersen, Washington D. C.: Amer. Chem. Soc., 1998).

[49] D. Chandler, J. Chem. Phys. **68**, 2959 (1978).

[50] C. Dellago, P. G. Bolhuis, and D. Chandler, Faraday Discuss. **110**, 421 (1998).

[51] D. Frenkel and B. Smit, *Understanding Molecular Simulation: From Algorithms to Applications, Second Edition* (Academic Press, San Diego, California, 2002).

[52] D. Chandler, *Introduction to Modern Statistical Mechanics* (Oxford University Press, New York, 1987).

[53] L. R. Pratt, J. Chem. Phys. **85**, 5045 (1986).

[54] R. Car and M. Parrinello, Phys. Rev. Lett. **55**, 2471 (1985).

[55] D. P. Landau and K. Binder, *A Guide to Monte Carlo Simulations in Statistical Physics* (Cambridge University Press, Cambridge, 2000).

[56] N. Metropolis, A. W. Rosenbluth, M. N. Rosenbluth, A. H. Teller, and E. Teller, J. Chem. Phys. **21**, 1087 (1953).

[57] C. Dellago, P. G. Bolhuis, and D. Chandler, J. Chem. Phys. **110**, 6617 (1999).

[58] E. Schrödinger, Phys. Rev. **28**, 1049 (1926).

[59] D. R. Hartree, Proc. Cambridge Philos. Soc. **24**, 111 (1928).

[60] D. R. Hartree, Proc. Cambridge Philos. Soc. **24**, 426 (1928).

[61] V. Fock, Z. Phys. **61**, 126 (1930).

[62] R. McWeeny and B. T. Sutcliffe, *Methods of Molecular Quantum Mechanics* (Academic Press, London and New York, 1976).

[63] D. M. Hirst, *A Computational Approach to Chemistry* (Blackwell Scientific Publications, Melbourne, 1990).

[64] A. Szabo and N. L. Ostlund, *Modern Quantum Chemistry* (McGraw-Hill, New York, 1989).

[65] W. Kohn and L. J. Sham, Phys. Rev. **140**, A1133 (1965).

[66] G. Seifert, J. Phys. Chem. A **111**, 5609 (2007).

[67] L. H. Thomas, Proc. Cambridge Philos. Soc. **23**, 542 (1927).

[68] E. Fermi, Z. Phys. **48**, 73 (1928).

[69] C. F. von Weizsäcker, Z. Phys. **96**, 431 (1935).

[70] P. A. M. Dirac, Proc. Cambridge Philos. Soc. **26**, 376 (1930).

[71] T. Ziegler, Chem. Rev. **91**, 651 (1991).

[72] S. H. Vosko, L. Will, and M. Nusair, Can. J. Phys. **58**, 1200 (1980).

[73] C. Lee, W.Yang, and R. G. Parr, Phys. Rev. B **37**, 785 (1988).

[74] J. P. Perdew, K. Burke, and M. Ernzerhof, Phys. Rev. Lett. **77**, 3865 (1996).

[75] A. D. Becke, Phys. Rev. A **38**, 3098 (1988).

[76] A. D. Becke, J. Chem. Phys. **98**, 5648 (1993).

[77] P. C. Slater and G. F. Koster, Phys. Rev. **94**, 1498 (1954).

[78] D. J. Chadi, Phys. Rev. Lett. **43**, 43 (1979).

[79] C. M. Goringe, D. R. Bowler, and E. Hernandez, Rep. Prog. Phys. **60**, 1447 (1997).

[80] D. Porezag, T. Frauenheim, G. S. Th. Köhler, and R. Kaschner, Phys. Rev. B **51**, 12947 (1995).

[81] M. Elstner, D. Porezag, G. Jungnickel, J. Elsner, M. Haugk, T. Frauenheim, S. Suhai, and G. Seifert, Phys. Rev. B **58**, 11 (1998).

[82] J. Harris, Phys. Rev. B **31**, 1770 (1985).

[83] G. Seifert, H. Eschrig, and W. Bieger, Z. Phys. Chem. (Leipzig) **267**, 529 (1986).

[84] A. P. Sutton, M. W. Finnis, D. G. Pettifor, and Y. Ohata, J. Phys. C **21**, 35 (1988).

[85] V. Brazhkin, N. Dubrovinskaia, M. Nicol, N. Novikov, R. Riedel, V. Solozhenko, and Y. Zhao, Nature Materials **3**, 576 (2004).

[86] F. Occelli, P. Loubeyre, and R. LeToullec, Nature Materials **2**, 151 (2003).

[87] J. R. Olson, R. O. Pohl, J. W. Vandersande, A. Zoltan, T. R. Anthony, and W. F. Banholzer, Phys. Rev. B **47**, 14850 (1993).

[88] Z. Pan, H. Sun, Y. Zhang, and C. Chen, Phys. Rev. Lett. **102**, 055503 (2009).

[89] A. Geim and K. Novoselov, Nature Materials **6**, 183 (2011).

[90] J.-H. Chen, C. Jang, S. X. M. Ishigami, and M. S. Fuhrer, Nature Nanotechnology **3**, 206 (2008).

[91] C. Lee, X. Wei, and J. H. J. W. Kysar, Science **321**, 385 (2008).

[92] S. R. P. Silva, *Amorphous Carbon* (INSPEC, London, 2003).

[93] A. V. Rode, S. T. Hyde, E. G. Gamaly, R. G. Elliman, D. R. McKenzie, and S. Bulcock, Applied Physics A **69**, S755 (1999).

[94] E. G. Harlow, *The Nature of Diamond* (Cambridge Univ. Press, New York, 1998).

[95] J. E. Field, *The Properties of Natural and Synthetic Diamond* (Academic, London, 1992).

[96] D. R. Lide, *CRC Handbook of Chemistry Physics* (CRC Press, London, 1995).

[97] Y. Iwasa, T. Arima, R. M. Fleming, T. Siegrist, O. Zhou, R. C. Haddon, L. J. Rothberg, K. B. Lyons, H. L. C. Jr., A. F. Hebard, R. Tycko, G. Dabbagh, J. J. Krajewski, G. A. Thomas, and T. Yagi, Science **264**, 1570 (1994).

[98] C. H. Xu and G. E. Scuseria, Phys. Rev. Lett. **74**, 274 (1995).

[99] R. B. Heimann and S. E. E. andY. Koga, Carbon **35**, 1654 (1997).

[100] Y. Gogotsi, *Nanomaterials Handbook* (CRC Press, Boca Raton, 2006).

[101] Y. Omata, Y. Yamagami, K. Tadano, T. Miyake, and S. Saito, Physica (Amsterdam) **29E**, 454 (2005).

[102] T. Irifune, A. Kurio, S. Sakamoto, T. Inoue, and H. Sumiya, Nature **451**, 599 (2003).

[103] W. Utsumi and T. Yagi, Science **252**, 1542 (1991).

[104] M. Hanfland, K. Syassen, and R. Sonnenschein, Phys. Rev. B **40**, 1951 (1989).

[105] T. Yagi, W. Utsumi, M. A. Yamakata, T. Kikegawa, and O. Shimomura, Phys. Rev.

B **46**, 6031 (1992).
[106] M. Hanfland, H. Beister, and K. Syassen, Phys. Rev. B **39**, 12598 (1989).
[107] Y. X. Zhao and I. L. Spain, Phys. Rev. B **40**, 993 (1989).
[108] W. Mao, H. K. Mao, P. J. Eng, T. P. Trainor, M. Newville, C. C. Kao, D. L. Heinz, J. F. Shu, Y. Meng, and R. J. Hemley, Science **302**, 425 (2003).
[109] K. J. Takano, H. Harashima, and M.Wakatsuki, Jpn. J. Appl. Phys., Part 2 **30**, L860 (1991).
[110] E. P. Bundy and J. S. Kasper, J. Chem. Phys. **46**, 3437 (1967).
[111] J. R. Patterson, S. A. Catledge, and Y. K. Vohra, Phys. Rev. Lett. **85**, 5364 (2000).
[112] A. F. Goncharov, I. N. Makarenko, and S. Stishov, Sov. Phys. JETP **69**, 380 (1989).
[113] J. Xu, H. K. Mao, and R. J. Hemley, J. Phys. Condens. Matter **14**, 11549 (2002).
[114] Q. Li, Y. Ma, A. R. Oganov, H. Wang, H. Wang, Y. Xu, T. Cui, H.-K.Mao, and G. Zou, Phys. Rev. Lett. **102**, 175506 (2009).
[115] J. T. Wang and C. C. andY. Kawazoe, Phys. Rev. Lett. **106**, 075501 (2011).
[116] K. Umemoto, R. M. Wentzcovitch, S. Saito, and T. Miyake, Phys. Rev. Lett. **104**, 125504 (2010).
[117] A. R. Oganov, *Modern Methods of Crystal Structure Prediction* (Wiley-VCH, Berlin, 2011).
[118] A. R. Oganov, J. Chen, C. Gatti, Y. Ma, Y. Ma, C. W. Glass, Z. Liu, T. Yu, O. O. Kurakevych, and V. L. Solozhenko, Nature **453**, 863 (2009).
[119] Y. Ma, M. Eremets, A. R. Oganov, Y. Xie, I. Trojan, S. Medvedev, A. O. Lyakhov, M. Valle, and V. Prakapenka, Nature **458**, 182 (2009).
[120] R. T. Strong, C. J. Pickard, V. Milman, G. Thimm, and B. Winkler, Phys. Rev. B **70**, 045101 (2004).
[121] Q. Zhu, A. R. Oganov, M. A. Salvadó, P. Pertierra, and A. O. Lyakhov, Phys. Rev. B **83**, 193410 (2011).
[122] V. Buch, R. Martoňák, and M. Parrinello, J. Chem. Phys. **123**, 051108 (2005).
[123] V. Buch, R. Martoňák, and M. Parrinello, J. Chem. Phys. **123**, 204705 (2006).
[124] R. Martoňák, in *Modern Methods of Crystal Structure Prediction*, edited by A. R. Oganov (Wiley-VCH, Berlin, 2011).
[125] R. Martoňák, Eur. Phys. J. B **79**, 241 (2011).
[126] G. Lippert, J. Hutter, and M. Parrinello, Mol. Phys. **92**, 477 (1997).
[127] G. Lippert, J. Hutter, and M. Parrinello, Theor. Chem. Acc. **103**, 124 (1999).
[128] V. A. Blatov, IUCr CompComm Newsletter **7**, 4 (2006).
[129] O. Delgado-Friedrichs, [http://gavrog.org/], 2006.
[130] P. Ordejon, E. Artacho, and J. M. Soler, Phys. Rev. B **53**, 10441 (1996).
[131] J. M. Soler, E. Artacho, J. D. Gale, A. Garca, J. Junquera, P. Ordejon, and D. Sanchez-Portal, J. Phys. Condens.Matter **14**, 2745 (2002).
[132] N. Troullier and J. L. Martins, Phys. Rev. B **43**, 1993 (1991).
[133] F. D. Murnaghan, Proc. Nat. Acad. Sci. USA **30**, 244 (1944).
[134] K. Li, X. Wang, F. Zhang, and D. Xue, Phys. Rev. Lett. **10**, 235504 (2008).
[135] A. O. Lyakhov and A. R. Oganov, Phys. Rev. B **84**, 092103 (2011).
[136] R. Z. Khaliullin, H. Eshet, T. D. Kühne, J. Behler, and M. Parrinello, Nat. Mater. **10**, 693 (2011).
[137] K. S. Novoselov, A. K. Geim, S. V. Morozov, D. Jiang, Y. Zhang, S. V. Dubonos, I. V. Grigorieva, and A. A. Firsov, Science **306**, 666 (2004).
[138] K. S. Novoselov, A. K. Geim, S. V. Morozov, D. Jiang, M. I. Katsnelson, I. V. Grigorieva, S. V. Dubonos, and A. A. Firsov, Nature **438**, 197 (2005).
[139] Y. Zhang, Y.-W. Tan, H. L. Stormer, and P. Kim, Nature **438**, 201 (2005).
[140] A. H. C. Neto, F. Guinea, N. M. R. Peres, K. S. Novoselov, and A. K. Geim, Rev.

Mod. Phys. **81**, 109 (2009).

[141] E. V. Castro, K. S. Novoselov, S. V. Morozov, N. M. R. Peres, J. M. B. L. dos Santos, J. Nilsson, F. Guinea, A. K. Geim, and A. H. C. Neto, Phys. Rev. Lett. **99**, 216802 (2007).

[142] J. B. Oostinga, H. B. Heersche, X. Liu, A. F. Morpurgo, and L. M. K. Vandersypen, Nature Materials **7**, 151 (2008).

[143] M. Y. Han, B. Özyilmaz, Y. Zhang, and P. Kim, Phys. Rev. Lett. **98**, 206805 (2007).

[144] D. Selli, M. Baldoni, A. Sgamellotti, and F. Mercuri, Nanoscale **4**, 1350 (2012).

[145] K. V. Emtsev, F. Speck, T. Seyller, and L. Ley, Phys. Rev. B **77**, 155303 (2008).

[146] C. Xia, S. Watcharinyanon, A. A. Zakharov, R. Yakimova, L. Hultman, L. I. Johansson, and C. Virojanadara, Phys. Rev. B **85**, 045418 (2012).

[147] M. Ishigami, J. H. Chen, W. G. Cullen, M. S. Fuhrer, and E. D. Williams, Nano Lett. **7**, 1643 (2007).

[148] E. Stolyarova, K. T. Rim, S. Ryu, J. Maultzsch, P. Kim, L. E. Brus, T. F. Heinz, M. S. Hybertsen, and G. W. Flynn, Proc. Natl. Acad. Sci. U.S.A. **104**, 9209 (2007).

[149] O. Ochedowski, G. Begall, N. Scheuschner, M. E. Kharrazi, J. Maultzsch, and M. Schleberger, Nanotechnology **23**, 405708 (2012).

[150] Y. Xu, K. T. He, S. W. Schmucker, Z. Guo, J. C. Koepke, J. D. Wood, J. W. Lyding, and N. R. Aluru, Nano Lett. **11**, 2735 (2011).

[151] C.-C. Chen, M. Aykol, C.-C. Chang, A. F. J. Levi, and S. Cronin, Nano Lett. **11**, 1863 (2011).

[152] Y. Ma, Y. Dai, M. Guo, and B. Huang, Phys. Rev. B **85**, 235448 (2012).

[153] M. Marsili and O. Pulci, J. Phys. D: Appl. Phys. **43**, 374016 (2010).

[154] W. J. Huisman, M. Lohmeier, H. A. van der Vegt, J. F. Peters, S. A. de Vries, E. Vlieg, V. H. Etgens, T. E. Derry, and J. F. van der Veen, Surf. Sci. **396**, 241 (1998).

[155] S. Walter, J. Bernhardt, U. Starke, K. Heinz, F. Maier, J. Ristein, and L. Ley, J.Phys.: Condens. Matter **14**, 3085 (2002).

[156] K. C. Pandey, Phys. Rev. B **25**, 4338 (1982).

[157] F. J. Himpsel, P. M. Marcus, and R. Tromp, Phys. Rev. B **30**, 2257 (1984).

[158] A. A. Stekolnikov, J. Furthmuller, and F. Bechstedt, Phys. Rev. B **65**, 115318 (2002).

[159] S. Ogawa, T. Yamada, S. Ishizduka, A. Yoshigoe, M. Hasegawa, Y. Teraoka, and Y. Takakuwa, Jpn. J. Appl. Phys. **51**, 11PF02 (2012).

[160] S. E. Boulfelfel, A. Oganov, and S. Leoni, Sci. Rep. **2**, 471 (2012).

[161] Y. Wang, J. E. Panzik, B. Kiefer, and K. K. M. Lee, Sci. Rep. **2**, 520 (2012).

[162] D. M. Ceperley and B. J. Alder, Phys. Rev. Lett. **45**, 566 (1980).

[163] J. P. Perdew and A. Zunger, Phys. Rev. B **23**, 5048 (1981).

[164] H. J. Monkhorst and J. D. Pack, Phys. Rev. B **13**, 5188 (1976).

[165] M. Brandbyge, J.-L. Mozos, P. Ordejn, J. Taylor, and K. Stokbro, Phys. Rev. B **65**, 165401 (2002).

[166] S. Datta, Superlattices and Microstr. **28**, 253 (2000).

[167] S. Datta, *Quantum Transport: Atom to Transistor* (Cambridge Univ. Press, New York, 2013).

[168] M. P. Lopez-Sancho, J. M. Lopez-Sancho, and J. Rubio, J. Phys. F: Met. Phys. **14**, 1205 (1984).

[169] M. Büttiker, Y. Imry, R. Landauer, and S. Pinhas, Phys. Rev. B **31**, 6207 (1985).

[170] S. E. Thompson and S. Parthasarathy, Mater. Today **9**, 20 (2006).

[171] P. Avouris, Z. Chen, and V. Perebeinos, Nat. Nanotechnol. **2**, 605 (2007).

[172] K. Kim, J.-Y. Choi, T. Kim, S.-H. Cho, and H.-J. Chung, Nature **479**, 338 (2011).

[173] A. L. V. de Parga, F. Calleja, B. Borca, M. C. G. Passeggi, J. J. Hinarejos, F. Guinea, and R. Miranda, Phys. Rev. Lett. **100**, 056807 (2008).

[174] K. Takayanagi, Y. Tanishiro, M. Takahashi, and S. Takahashi, J. Vac. Sci. Technol. **A3**, 1502 (1985).

[175] S. Y. Zhou, G.-H. Gweon, A. V. Fedorov, P. N. First, W. A. de Heer, D.-H. Lee, F. Guinea, A. H. C. Neto, and A. Lanzara, Nat. Mater. **6**, 770 (2007).

[176] K. Nakada, M. Fujita, G. Dresselhaus, and M. Dresselhaus, Phys. Rev. B **54**, 17954 (1996).

[177] Y. W. Son, M. L. Cohen, and S. G. Louie, Phys. Rev. Lett. **97**, 216803 (2006).

[178] R. Höll, M. Kling, and E. Schroll, Ore Geol. Rev. **30**, 145 (2007).

[179] J. Cheng and J. Du, CrystEngComm **14**, 397 (2012).

[180] X. Li, G. Meng, Q. Xu, M. Kong, X. Zhu, Z. Chu, and A.-P. Li, Nano Lett. **11**, 1704 (2011).

[181] X. Q. Zhang, H. Li, and K. M. Liew, J. Appl. Phys. **102**, 073709 (2007).

[182] M. A. Paesler, D. E. Sayers, R. Tsu, and J. Gonzalez-Hernandez, Phys. Rev. B **28**, 4550 (1983).

[183] A. M. Guloy, R. Ramlau, Z. Tang, W. Schnelle, M. Baitinger, and Y. Grin, Nature **443**, 320 (2006).

[184] U. Schwarz, A. Wosylus, B. Bhme, M. Baitinger, M. Hanfland, and Y. Grin, Angew. Chem. Int. Ed. Engl **47**, 6790 (2008).

[185] R. J. Nelmes, M. McMahon, N. Wright, D. Allan, and J. S. Loveday, Phys. Rev. B **48**, 9883 (1993).

[186] C. Menoni, J. Hu, and I. Spain, Phys. Rev. B **34**, 362 (1986).

[187] R. J. Nelmes, H. Liu, S. A. Belmonte, J. S. Loveday, M. I. McMahon, D. R. Allan, D. Husermann, and M. Hanfland, Phys. Rev. B **53**, R2907 (1996).

[188] Y. K. Vohra, K. E. Brister, S. Desgreniers, A. L. Ruoff, K. J. Chang, and M. L. Cohen, Phys. Rev. Lett. **56**, 1944 (1986).

[189] K. Takemura, U. Schwarz, K. Syassen, M. Hanfland, N. E. Christensen, D. L. Novikov, and I. Loa, Phys. Rev. B **62**, R10604 (2000).

[190] A. Mujica, A. Rubio, A. Muñoz, and R. J. Needs, Rev. Mod. Phys. **75**, 863 (2003).

[191] H. B. Cui, D. Graf, J. S. Brooks, and H. Kobayashi, Phys. Rev. Lett. **102**, 237001 (2009).

[192] X.-J. Chen, C. Zhang, Y. Meng, R.-Q. Zhang, H.-Q. Lin, V. V. Struzhkin, and H. k. Mao, Phys. Rev. Lett. **106**, 135502 (2011).

[193] U. Schwarz, Z. Kristallogr. **219**, 376 (2004).

[194] H. Katzke and P. Tolédano, J. Phys-Condens. Mat. **19**, 275204 (2007).

[195] H. Fukuoka, S. Yamanaka, E. Matsuoka, and T. Takabatake, Inorg. Chem. **5**, 1460 (2005).

[196] K. L. Ekinci and M. L. Roukes, Rev. Sci. Instrum. **76**, 061101 (2005).

[197] C. Claeys, J. Mitard, G. Eneman, M. Meuris, and Simoen, Thin Solid Films **518**, 2301 (2010).

[198] S. P. Lewis and M. L. Cohen, Solid State Commun. **89**, 482 (1994).

[199] D. Li, Y. Ma, and J. Yan, Phys. Rev. Lett. **104**, 139701 (2010).

[200] A. Wosylus, Y. Prots, W. Schnelle, M. Hanfland, and U. Schwarz, Naturforsch. B **63**, 608 (2008).

[201] L. Boyer, E. Kaxiras, J. Feldman, J. J. Broughton, and Mehl, Phys. Rev. Lett. **67**, 715 (1991).

[202] S. Baroni, S. de Gironcoli, A. D. Corso, and P. Giannozzi, Rev. Mod. Phys. **73**, 515 (2001).

[203] T. Frauenheim, G. Seifert, M. Elsterner, Z. Hajnal, G. Jungnickel, D. Porezag, S. Suhai, and R. Scholz, Phys. Status Solidi B **217**, 41 (2000).

[204] J. Behler, R. Martoňák, D. Donadio, and M. Parrinello, Phys. Rev. Lett. **100**, 185501

(2008).

[205] P. Giannozzi, S. Baroni, N. Bonini, M. Calandra, R. Car, C. Cavazzoni, D. Ceresoli, G. L. Chiarotti, m. Cococcioni, I. Dabo, A. D. Corso, S. Fabris, G. Fratesi, S. de Gironcoli, R. Gebauer, U. Gerstmann, C. Gougoussis, A. Kokalj, M. Lazzeri, L. Martin-Samos, N. Marzari, F. Mauri, R. Mazzarello, S. Paolini, A. Pasquarello, L. Paulatto, C. Sbraccia, S. Scandolo, G. Sclauzero, A. P. Seitsonen, A. Smogunov, P. Umari, and R. M. Wentzcovitch, J. Phys-Condens. Mat. **21**, 395502 (2009).

[206] D. Vanderbilt, Phys. Rev. B **41**, 7892 (1990).

[207] A. D. Becke and K. E. Edegecombe, J. Chem. Phys **92**, 5397 (1990).

[208] M. Kohout, Int. J. Quantum Chem. **97**, 651 (2004).

[209] A. Ormeci, H. Rosner, F. Wagner, M. Kohout, and Y. Grin, J. Phys. Chem. A **110**, 1100 (2006).

[210] K. Koepernik and H. Eschrig, Phys. Rev. B **59**, 1743 (1999).

[211] H. Eschrig, *Optimized LCAO Methods and the Electronic Structure of Extended Systems* ((Springer, Berlin, 1989).

[212] J. Perdew and Y. Wang, Phys. Rev. B **45**, 13244 (1992).

[213] V. V. Brazhkin, A. G. Lyapin, S. V. Popova, and R. N. Voloshin, Phys. Rev. B **51**, 7549 (1995).

[214] A. G. Lyapin, V. V. Brazhkin, S. V. Popova, A. V., and Sapelkin, Phys. Stat. Sol. B **198**, 481 (1996).

[215] W. Schnelle, A. Ormeci, A. Wosylus, K. Meier, Y. Grin, and U. Schwarz, Inorg. Chem. **51**, 5509 (2012).

[216] A. J. Karttunen, T. F. F´assler, M. Linnolahti, and T. Pakkanen, Inorg. Chem. **50**, 1733 (2011).

[217] J. N. Wickham, A. B. Herhold, and A. P. Alivisatos, Phys. Rev. Lett. **84**, 924 (2000).

[218] P. F. McMillan, Nat. Mater. **1**, 19 (2002).

[219] R. Demchyna, S. Leoni, H. Rosner, and U. Z. Schwarz, Z. Kristallogr. **221**, 420 (2006).

[220] G. Seifert, D. Porezag, and T. Frauenheim, Int. J. Quantum Chem. **58**, 185 (1996).

[221] K. Jacobs, D. Zaziski, E. C. Scher, A. B. Herhold, and A. P. Alivisatos, Science **293**, 1803 (2001).

[222] S. Leoni and S. E. B. in, *Modern Methods of Crystal Structure Prediction; A. R. Oganov* (Wiley-VCH, Berlin, 2011), pp. 181–221.

[223] H. Katze, U. Bismayer, and P. Toledano, Phys. Rev. B **73**, 134105 (2006).

[224] H. G. von Schnering and R. Nesper, Angew. Chem., Int. Ed. Engl. **26**, 1059 (1987).

[225] S. Leoni and I. A. Baburin, Z. Kristallogr. **226**, 678 (2011).

[226] S. Leoni, Chem. Eur. J. **13**, 10022 (2007).

[227] S. Leoni, R. Ramlau, K. Meier, M. Schmidt, and U. Schwarz, Proc. Natl. Acad. Sci. U. S. A. **105**, 19612 (2008).

[228] M. Grünwald, E. Rabani, and C. Dellago, Phys. Rev. Lett. **96**, 255701 (2006).

[229] C. Dellago, P. G. Bolhuis, and P. L. Geissler, Lect. Notes Phys. **703**, 349 (2006).

[230] B. Aradi, B. Hourahine, and T. Frauenheim, J. Phys. Chem. A **111**, 5678 (2007).

[231] G. Seifert, T. Köhler, Z. Hajnal, and T. Frauenheim, Solid State Commun. **119**, 653 (2001).

[232] S. B. Qadri, E. F. Skelton, and A. W. Webb, J. Appl. Phys. **54**, 3609 (1983).

[233] M. O'Keeffe and B. G. Hyde, *Crystal Structures. I. Patterns and Symmetry* (Mineralogical Society of America, Washington, DC, 1996), Chap. 7.

[234] N. Marzari and D. Vanderbilt, Phys. Rev. B **56**, 12847 (1997).

[235] A. A. Mostofi, J. R. Yates, Y.-S. Lee, I. Souza, D. Vanderbilt, and N. Marzari, Comput. Phys. Commun. **178**, 685 (2008).

[236] P. Fitzhenry, M. M. M. Bilek, N. A. Marks, N. C. Cooper, and D. R. J. McKenzie, J.

Phys.: Condens. Matter **15**, 165 (2003).

[237] G. S. Hammond, J. Am. Chem. Soc. **77**, 334 (1955).

[238] M.-H. Whangbo, J. Chem. Phys. **75**, 4983 (1981).

[239] J. S. Kasper, P. Hagenmuller, M. Pouchard, and C. Cros, Science **150**, 1713 (1965).

[240] C. Cros, M. Pouchard, and P. Hagenmuller, J. Solid State Chem. **2**, 570 (1970).

[241] R. Nesper, K. Vogel, and P. Blöchl, Angew. Chem. Int. Ed. Engl **32**, 701 (1993).

[242] A. A. Demkov, W. Windl, and O. F. Sankey, Phys. Rev. B **53**, 11288 (1996).

[243] M. O'Keeffe, G. B. Adams, and O. F. Sankey, Phys. Rev. Lett. **68**, 2325 (1992).

[244] S. Saito and A. Oshiyama, Phys. Rev. B **51**, 2628 (1995).

[245] J. Gryko, P. F. McMillan, and O. F. Sankey, Phys. Rev. B **57**, 4172 (1998).

[246] P. M*é*linon, P. K*é*gh*é*lian, X. Blase, J. L. Brusc, A. Pi*é*rez, E. Reny, C. Cros, and M. Pouchard, Phys. Rev. B **58**, 12590 (1998).

[247] H. Kawaji, H. Horie, S. Yamanaka, and M. Ishikawa, Phys. Rev. Lett. **74**, 1427 (1995).

[248] H. Kawaji, K. Iwai, S. Yamanaka, and M. Ishikawa, Solid State Commun. **100**, 393 (1996).

[249] S. L. Fang, L. Grigorian, P. C. Eklund, G. Dresselhaus, M. S. Dresselhaus, H. Kawaji, and S. Yamanaka, Phys. Rev. B **57**, 7686 (1998).

[250] A. G. Cullis, L. T. Canham, and P. D. J. Calcot, J. Appl. Phys. **82**, 909 (1997).

[251] Y. Guyot, B. Champagnon, E. Reny, C. Cros, M. Pouchard, P. Melinon, A. Perez, and I. Gregora, Phys. Rev. B **57**, R9475 (1998).

[252] S. Bobev and S. C. Sevov, J. Am. Chem. Soc. **121**, 3795 (1999).

[253] J. Gryko, P. F. McMillan, R. F. Marzke, G. K. Ramachandran, D. Patton, S. K. Deb, and O. F. Sankey, Phys. Rev. B **62**, 7707 (2000).

[254] A. Ammar, C. Cros, M. Pouchard, N. Jaussaud, J.-M. Bassat, G. Villeneuve, M. Duttine, M. M*é*n*é*triera, and E. Reny, Solid State Sci. **6**, 393 (2004).

[255] M. W. Guinan and D. J. Steinberg, J. Phys. Chem. Solids **35**, 1501 (1974).

[256] D. M. Rowe, *Handbook of Thermoelectrics* (CRC Press, Boca Raton, 1995).

[257] F. J. DiSalvo, Science **285**, 703 (1999).

[258] C. B. Vining, Nat. Mater. **8**, 83 (2009).

[259] D. M. Rowe, *Handbook of Thermoelectrics: Macro to Nano* (CRC Press, Boca Raton, 2005).

[260] M. Dresselhaus, G. Chen, M. Tang, R. Yang, H. Lee, D. Wang, Z. Ren, J.-P. Fleurial, and P. Gogna, Adv. Mater. **19**, 1043 (2007).

[261] C. Uher, in *Recent Trends in Thermoelectric Materials Research I*, Vol. 69 of *Semiconductors and Semimetals*, edited by T. M. Tritt (Elsevier, ADDRESS, 2001), pp. 139 – 253.

[262] G. S. Nolas, J. Poon, and M. Kanatzidis, Mater. Res. Soc. Bull. **31**, 199 (2006).

[263] S. M. Kauzlarich, S. R. Brown, and G. J. Snyder, Dalton Trans. 2099 (2007).

[264] T. M. Tritt and M. A. Subramanian, Mater. Res. Soc. Bull. **31**, 188 (2006).

[265] G. J. Snyder and E. S. Toberer, Nat. Mater. **7**, 105 (2008).

[266] M. G. Kanatzidis, Chem. Mater. **22**, 648 (2010).

[267] G. A. Slack, in *Handbook of Thermoelectrics*, edited by D. M. Rowe (CRC Press, Boca Raton, 1995), pp. 407–440.

[268] C. M. Bhandari, in *Handbook of Thermoelectrics*, edited by D. M. Rowe (CRC Press, Boca Raton, 1995), pp. 55–65.

[269] K. Biswas, J. He, I. D. Blum, C.-I. Wu, T. P. Hogan, D. N. Seidman, V. P. Dravid, and M. G. Kanatzidis, Nature **489**, 414 (2012).

[270] C. Wood, Rep. Prog. Phys. **51**, 459 (1988).

[271] J. W. Roh, S. Y. Jang, Kang, S. Lee, J.-S. Noh, W. Kim, J. Park, and W. Lee, Appl. Phys. Lett. **96**, 103101 (2010).

[272] M. Fardy, A. I. Hochbaum, J. Goldberger, M. M. Zhang, and P. Yang, Adv. Mater. **19**, 3047 (2007).

[273] C. Hsu, F. Loo, F. Guo, W. Chen, J. Dyck, C. Uher, T. Hogan, E. Polychroniadis, and M. G. Kanatzidis, Science **303**, 818 (2003).

[274] T. C. Harman, P. J. Taylor, M. P. Walsh, and B. E. LaForge, Science **297**, 2229 (2002).

[275] J. Androulakis, C. Lin, H. Kong, C. Uher, C. Wu, T. Hogan, B. A. Cook, T. Caillat, K. M.Paraskevopoulos, and M. G. Kanatzidis, J. Am. Chem. Soc. **129**, 9780 (2007).

[276] J. P. Heremans, V. Jovovic, E. S. Toberer, A. Saramat, K. Kurosaki, A. Charoenphakdee, S. Yamanaka, and G. J. Snyder, Science **321**, 554 (2008).

[277] R. Venkatasubramanian, E. Siivola, V. Colpitts, and B. O'Quinn, Nature **413**, 597 (2001).

[278] I. I. Ravich, B. A. Efimova, and I. A. Smirnov, *Semiconducting lead chalcogenides* (Plenum Press, New York, 1970).

[279] D. Parker and D. J. Singh, Phys. Rev. B **82**, 035204 (2010).

[280] T. G. Alekseeva, E. A. Gurieva, P. P. Konstantinov, L. V. Prokof?eva, and M. I. Federov, Semiconductors **30**, 1125 (1996).

[281] P. F. P. Poudeu, J. D'Angelo, A. D. Downey, J. L. Short, T. P. Hogan, and M. G. Kanatzidis, Angew. Chem. Int. Ed. Engl. **45**, 3835 (2006).

[282] S. N. Girard, J. He, X. Zhou, D. Shoemaker, C. M. Jaworski, C. Uher, V. P. Dravid, J. P. Heremans, and M. G. Kanatzidis, J. Am. Chem. Soc. **133**, 16588 (2011).

[283] Y. Pei, X. Shi, A. LaLonde, H. Wang, L. Chen, and G. J. Snyder, Nature **473**, 66 (2011).

[284] K. Biswas, J. He, Q. Zhang, G. Wang, C. Uher, V. P. Dravid, and M. G. Kanatzidis, Nature Chem. **3**, 160 (2011).

[285] D. G. Cahill, W. K. Ford, K. E. Goodson, G. D. Mahan, A. Majumdar, H. J. Maris, R. Merlin, and S. R. Phillpot, J. Appl. Phys. **93**, 793 (2003).

[286] M. Grünwald, A. Zayak, J. B. Neaton, P. L. Geissler, and E. Rabani, J. Chem. Phys. **136**, 2341111 (2012).

[287] P. Schapotschnikow, M. A. van Huis, H. W. Zandbergen, D. Vanmaekelbergh, and T. J. H. Vlugt, Nano Lett. **10**, 3966 (2010).

[288] J. D. Gale, Phil. Mag. B **73**, 3 (1996).

[289] Y. Zhang, X. Z. Ke, C. F. Chen, J. Yang, and P. R. C. Kent, Phys. Rev. B **80**, 024304 (2009).

[290] B. Qiu, H. Bao, G. Q. Zhang, Y. Wu, and X. L. Ruan, Comp. Mater. Sci. **53**, 278 (2012).

[291] D. A. McQuarrie, *Statistical Mechanics* (University Science Books, Sausalito, CA, 2000), p. 642.

[292] G. Green, Y. Cho, J. Hartnett, and A. Bar-Cohen, *Advances in Heat Transfer* (Elsevier, New York, 2006), p. 212.

[293] T. Chattopadhyay, H. G. von Schnering, W. A. Grosshans, and W. B. Holzapfel, Physica B+C **356**, 139 (1986).

[294] R. Dalven, Infrared Phys. **9**, 141 (1969).

[295] N. S. Landolt-Börnstein, *Semiconductors: Group IV Elements, IV-IV and III-V Compounds.* (Springer, New York, 2005), Vol. 41.

[296] A. J. Miller, G. A. Saunders, and Y. K. Yogurtçu, J. Phys. C **14**, 1569 (1981).

[297] S. J. Plimpton, J. Comp. Phys. **117**, 1 (1995).

[298] Z. T. Tian, J. Garg, K. Esfarjani, T. Shinga, J. Shiomi, and G. Chen, Phys. Rev. B **85**, 184303 (2012).

[299] I. Savić, D. Donadio, F. Gygi, and G. Galli, Appl. Phys. Lett **102**, 073113 (2013).

[300] Y. He, D. Donadio, J.-H. Lee, J. C. Grossman, and G. Galli, ACS Nano **5**, 1839 (2011).

[301] A. F. Ioffe, *Semiconductor Thermoelements and Thermoelectric Cooling* (Infosearch, London, 1957).

[302] Y. K. Koh, C. J. Vineis, S. D. Calawa, M. P. Walsh, and D. G. Cahill, Appl. Phys. Lett **94**, 153101 (2009).

[303] T. Chattopadhyay, A. Werner, and H. G. von Schnering, Revue Phys. Appl. **19**, 807 (1984).

[304] S. V. Ovsyannikov, V. V. Shchennikov, A. Y. Manakov, A. Y. Likhacheva, Y. S. Ponosov, V. E. Mogilenskikh, A. P. Vokhmyanin, A. I. Ancharov, and E. P. Skipetrov, Phys. Status Solidi B **246**, 615 (2009).

[305] S. Leoni and R. Nesper, Acta Cryst. A **56**, 383 (2000).

[306] S. Leoni and D. Zahn, Z. Kristallogr. **219**, 339 (2004).

[307] W. Smith and T. R. Forester, J. Mol. Graphics **14**, 136 (1996).

[308] Y. He, D. Donadio, and G. Galli, Nano Lett. **11**, 3608 (2011).

School participations, Oral presentations

Schools

1. CINECA-Summer School on Parallel Computing, Bologna, Italy (July 2010)
2. DEISA-TeraGrid HPC School, Acireale, Italy (October 2010)
3. PRACE Autumn School, Bruyères-le-Châtel, France (October 2011)

Presentations

1. 50th EHPRG Meeting, Thessaloniki, Greece (20/9/2012); *Structure Prediction: What Can We Learn from Transformation Mechanisms*, Oral Contribution
2. IMPRS Retreat, Seminarhotel Frohberg, Germany (27/10/2012); *Structure prediction and modeling: quest for new materials*, Oral Contribution
3. Seminar in Prof. G. Cuniberti Group, TUD, Germany (22/11/2012); *Structure Prediction*, Invited Speaker
4. 245th ACS National Meeting and Exposition, New Orleans, USA (10/04/2013); *PbSe-PbTe nanocomposites. Superior thermoelectrics by computational thermal conductivity engineering*, Oral Presentation
5. 2013 APSSCCM/AIRAPT JOINT CONFERENCE, Seattle, USA (07/07/2013); *Unrevealing transition mechanism: novel carbons and metallic germaniums. Accelerated Molecular Dynamics for novel materials quest*, Oral Presentation
6. 51th EHPRG Meeting, London, UK (02/09/2013); *Structure Prediction for High-Performance Energy Materials. Molecular Dynamics Techniques for novel materials quest*, Oral Presentation
7. SOUTH WEST COMPUTATIONAL CHEMISTS MEETING, Southampton, UK (24/09/2013); *Structure prediction techniques for novel high performance energy materials*, Oral Presentation

Acknowledgements

This work has been completed in the group of Prof. Gotthard Seifert at the Technische Universität Dresden from summer 2010 to winter 2013.

I would like to thank Prof. Gotthard Seifert to give me the opportunity of working on this interesting topic, in his research group. All the members of this group gave me constant support and let me feel part of a team.

I would like to thank Dr. Stefano Leoni for his constant guide, for the precious advises, the continue assistance during all my work and especially for his friendship.

I would like to thank Dr. Matteo Baldoni and Dr. Francesco Mercuri for their help, inspirating discussions and free time spent together.

I would like to thank Prof. Roman Martoňák, Dr. Davide Donadio, Dr. Igor Baburin and Dr. Salah Eddin Boulfelfel to share with me their knowledge on material science and accelerated molecular dynamic techniques.

I would like to thank Prof. David Tománek, Z. Zhu and C. Tayran for their collaboration on the study of graphene hybrid systems.

A special thanks to my family, especially my mother, and all my friends that supported and stood me for the entire duration of my PhD studies.

Versicherung

Hiermit versichere ich, dass ich die vorliegende Arbeit ohne unzulässige Hilfe Dritter und ohne Benutzung anderer als der angegebenen Hilfsmittel angefertigt habe, die aus fremden Quellen direkt oder indirekt übernommenen Gedanken sind als solche kenntlich gemacht. Die Arbeit wurde bisher weder im Inland noch im Ausland in gleicher oder ähnlicher Form einer anderen Prüfungsbehörde vorgelegt.

Die vorliegende Dissertation wurde unter Betreuung von Herrn Prof. Gotthard Seifert in der Zeit von Juni 2010 bis Dezember 2013 am Institut fr Physikalische Chemie und Elektrochemie, Technische Universität Dresden angefertigt.

Es haben keine früheren erfolglosen Promotionsverfahren stattgefunden.

Ich erkenne die Promotionsordnung der Fakultät Mathematik und Naturwissenschaften der TU Dresden vom 23.02.2011 in vollem Umfang an.

Dresden, den